José Manuel Domínguez-Esquivel
Manuel Ramos *Editors*

Advanced Catalytic Materials: Current Status and Future Progress

Springer

Advanced Catalytic Materials: Current Status and Future Progress

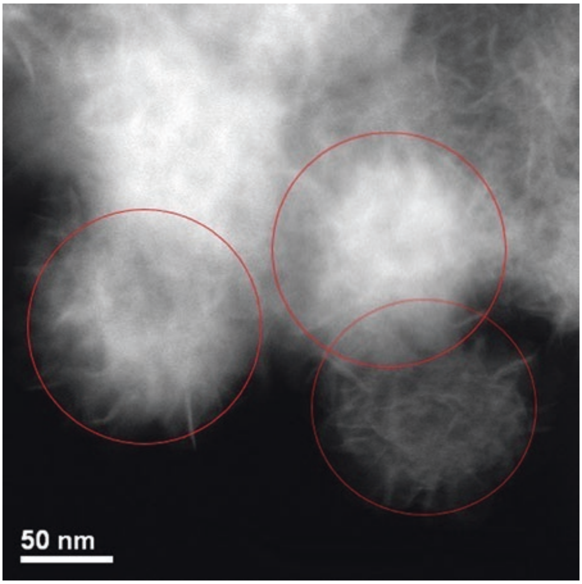
50 nm

José Manuel Domínguez-Esquivel
Manuel Ramos
Editors

Advanced Catalytic Materials: Current Status and Future Progress

Springer

Editors
José Manuel Domínguez-Esquivel
Dirección de Investigación
Instituto Mexicano del Petróleo
Mexico City, Mexico

Manuel Ramos
Departamento de Física y Matemáticas
Universidad Autonoma de Ciudad Juárez
Ciudad Juárez, Chihuahua-México, Mexico

ISBN 978-3-030-25991-4 ISBN 978-3-030-25993-8 (eBook)
https://doi.org/10.1007/978-3-030-25993-8

© Springer Nature Switzerland AG 2019
This work is subject to copyright. All rights are reserved by the Publisher, whether the whole or part of the material is concerned, specifically the rights of translation, reprinting, reuse of illustrations, recitation, broadcasting, reproduction on microfilms or in any other physical way, and transmission or information storage and retrieval, electronic adaptation, computer software, or by similar or dissimilar methodology now known or hereafter developed.
The use of general descriptive names, registered names, trademarks, service marks, etc. in this publication does not imply, even in the absence of a specific statement, that such names are exempt from the relevant protective laws and regulations and therefore free for general use.
The publisher, the authors, and the editors are safe to assume that the advice and information in this book are believed to be true and accurate at the date of publication. Neither the publisher nor the authors or the editors give a warranty, express or implied, with respect to the material contained herein or for any errors or omissions that may have been made. The publisher remains neutral with regard to jurisdictional claims in published maps and institutional affiliations.

This Springer imprint is published by the registered company Springer Nature Switzerland AG
The registered company address is: Gewerbestrasse 11, 6330 Cham, Switzerland

Preface

This book comprehends a compendium of ten chapters. Chapter 1 presents a comprehensive introduction made by Prof. Dr. Russell R. Chianelli from Materials Research and Technology Institute of the University of Texas at El Paso, covering some fundamental aspects of metallic nanoparticles, transition metal sulfides and carbides, and more related to catalytic process mainly with emphasis of energy production in low contaminant liquid fuels and an ideal approach constituted by the following steps: theory + synthesis + characterization + commercialization. Chapter 2 presents the synthesis of novel catalytic materials like titania nanotubes and transition metal carbides, nitrides, and sulfides by a group from the University Federal do Ceará, Brazil, in collaboration with the Universidad Regional Amazónica (IKIAM). Chapter 3 is dedicated to computation methods using *d*ensity *f*unctional *t*heory methods to describe electronic structure and other catalytic properties mainly in transition metal sulfides with special emphasis on molybdenum disulfide (MoS_2) catalyst for hydroprocessing reactions. Chapter 4 corresponds to catalytic evaluation and performance by laboratory test under hydroprocessing conditions, mainly the effects of support over pure transition metal sulfide catalytic materials, as presented by a strong research group of Chemical Engineering Faculty of the Universidad Nacional Autónoma de México at Mexico City Campus. Chapter 5 presents advanced electron microscopy methods for atomistic study of structure/function relationships. Chapter 6 presents a novel approach developed by a group at the University of Calgary in Canada for in situ upgrading by applying nano-catalyst fluid injection at reservoir conditions. Chapter 7 presents a complete characterization of spherical shape catalytic materials with an electron tomography technique done in collaboration with Argonne National Laboratory and Instituto Mexicano del Petróleo. Chapter 8 presents the usage of ceria oxide metal doping materials for methanol reforming and water split as presented by a group from the Instituto Nacional de Investigaciones Nucleares in Mexico. Chapter 9 presents the photocatalytic activity of titanium oxide low-dimension materials which is a work contribution by a group from Mechanical Engineering of the University of Houston, USA. Chapter 10 presents a new family of ternary phase catalytic materials for hydrodesulphurization reactions by a group from the Chemistry Department of the University of Texas.

The book corresponds to topics that have been addressed for more than 30 years of science and experimentation on the physical and chemical study of catalytic materials, reactions, electronic structure, characterization, and methods for the development of fundamental aspects to produce low contaminant liquid fuels to supply the worldwide energy demands. We believe this book presents a strong basis for undergraduate, graduate, and early career researchers who are currently dedicated to study physical and chemical catalytic low-dimension materials and systems.

In the name of all author contributors, we thank specially the Springer Nature publishers group for supporting our book proposal and for allowing us to publish this compendium of chapters. We thank all the funding agencies and academic institutions like the following: Consejo Nacional de Ciencia y Tecnología, México; Canada Foundation for Innovation (CFI); Institute for Sustainable Energy, Environment, and Economy (ISEEE); Schulich School of Engineering at the University of Calgary; Universidad Nacional Autónoma de México; Instituto Mexicano del Petróleo; Universidad Autónoma de Ciudad Juárez; and Instituto de Nanociencia de Aragon (INA) of the Universidad de Zaragoza in Spain. We also thank the State Key Laboratory of Coal Conversion of the Institute of Coal Chemistry funded by the Chinese Academy of Sciences, Universidad Federal do Ceará, and CNPq grant numbers 473568/2012-8, 470793/2013-9 for their economical support, the Venezuelan Institute for Scientific Research, the Universidad Regional Amazónica IKIAM at Ecuador, the University of Houston, the University of Texas at El Paso, Argonne National Laboratory, and the Instituto Nacional de Investigaciones Nucleares. The compilation of this book was part of a research project funded by the Mexican Science Council [CONACyT-México] under solicitation grant #177077 for SENER-hydrocarbons administrated by Instituto Mexicano del Petróleo with internal register #Y.61006.

Finally, we thank the reader for the interest in this scientific written material, and we hope to achieve a positive impact on their specific research activities.

Ciudad de México, Mexico José Manuel Domínguez-Esquivel
Chihuahua, Mexico Manuel Ramos

Contents

Chapter 1
One Brief Introduction to Catalytic Materials

Russell R. Chianelli

The field of catalysis is an ancient scientific art practice that dates back centuries to this day, as well described by Wismiak [1]. It was the need for ammunition in WWI and the need for trucks, tanks, and aircraft that accelerated the development of modern catalytic technologies. Catalysis plays a fundamental role in petroleum refining and basic petrochemical industries creating new routes in the development of industrial processes [2]. Moreover, catalysis has become indispensable to the solution of environmental pollution problems and therefore a positive impact on public health [3]. Worldwide concerns for preservation of the environment have motivated the development of "*green*" energy production in which the catalytic world plays an important role on those catalyst-based technologies, by achieving a better utilization of petroleum resources, to produce cleaner liquid fuels and derivatives to supply the enormous demand for commercial and public transportation [4]; the latter has caused great environmental concerns to make severe regulations mainly to lower sulfur, nitrogen, and aromatic content in commercial liquid fuels, to achieve better air quality mainly in large populated areas such as Shanghai, Mexico City, New York, London, Frankfurt, Paris, and São Paulo among other large urban areas [5, 6]. Heterogeneous catalysts currently come in three forms: metals, oxides, and sulfides. However, oxides and carbides are currently under study for similar catalytic purposes and processes in novel applications [7–9].

The study of heterogeneous catalytic materials involves a multidisciplinary approach:

Theory + Synthesis + Characterization + Commercialization

R. R. Chianelli (✉)
Materials Research and Technology Institute, University of Texas at El Paso,
500W University Ave. Physical Science Building 201A, El Paso, TX, USA
e-mail: chianell@utep.edu

J. M. Domínguez-Esquivel, M. Ramos (eds.), *Advanced Catalytic Materials: Current Status and Future Progress*, https://doi.org/10.1007/978-3-030-25993-8_1

In applying that strategy, it is essential to understand the relationship between catalytic activity and its molecular and solid-state structure, meaning the catalyst structure/function relationships for active and stabilized catalytic reactivity state. Up to now, one can find in the literature several reports, including new methods of synthesis, catalytic evaluation, and optimization of catalytic reaction conditions [10–15]. Recent evidence dictates that catalytic activity and selectivity depend on size and shape when compared with bulk composition of the catalytic material [16–21]. The field of transition metal sulfide (TMS) catalysis arose in earnest after the end of World War I (WWI), initiating a large-scale industrial use of catalysts to produce nitrates because German regions were cut off by blockage from the guano sources that were used to produce nitrates for explosives [22]. The introduction of the catalytic Haber process to fix nitrogen is a well-known story [23]. Technological advances leading to air and tank warfare at the end of WWI led to a race to produce liquid fuels with local coal resources to reduce dependence on imported petroleum with vulnerable supply lines. Following the lead of the Haber process researchers investigated the hydrogenation of coal with metal catalysts. After processing the metal had been converted to TMS catalytic materials. This was the beginning of the field of catalysis by TMS; more technical details can be found as described by Weisser and Landa [24]. The race to provide liquid fuel supplies produced intensive research efforts particularly in countries like Germany and France; many research efforts were made by I.G. Farbenindustrie (IGF) and Badische Anilin- und Soda-Fabrik (BASF) in Germany and between 1920 and 1930 these companies tested over 6000 catalysts [25]. Scientists such as Paul Sabatier, Friedrich Bergius, and M. Pier were leaders in investigating the TMS for fuel and chemical production; later P. Sabatier was considered the "Father of Modern Catalysis" for his early work in TMS catalysis that led to a Nobel Prize in 1912 [26]. Bergius won the Nobel Prize in 1931 for his work on coal hydrogenation. Much of the work in this period was secret and appeared only in the patented literature. The field of petroleum processing also arose in this period and the records became obscure during WWII reemerging primarily in the US and European petroleum industry after the war. Since that time TMS catalysis for fuel upgrading has played a major role in petroleum catalysis particularly in removing pollutants such as sulfur and nitrogen from liquid fuels. TMS catalysts will continue to play an increasingly important role in fuel processing as emphasis switches to cleaner and sustainable fuel supplies. In addition, TMS catalyzes many other reactions that have not been thoroughly explored. The major reactions catalyzed by TMS are hydrogenation of olefins, ketones, and aromatics; hydrodesulfurization (HDS); hydrodenitrogenation (HDN); hydrodemetallation (HDM); hydrocracking; dealkylation; and ring opening of aromatics. But the TMS catalysts have many other uses as well, including reforming, isomerization of paraffins, dehydrogenation of alcohols, Fischer–Tropsch and alcohol synthesis, hydration of olefins, amination, mercaptan and thiophene synthesis, and direct coal liquefaction [27–31]. Also, transition metal sulfide catalytic materials when used for hydrodesulfurization (HDS) process involving the removal of sulfur content in crude oil petroleum feeds, after hours/days of operation, become more carbide due to addition of carbon molecules at its surface, forming a molybdenum carbide phase

($MoS_{2-x}C_x$); this carbide effects have been studied and determined by meaning of synchrotron techniques at Stanford Synchrotron Radiation Lightsource (SSRL) as described by De la Rosa et al. [32].

The understanding and commercialization catalysis by metals were advanced significantly by John H. Sinfelt at the Corporate Research Laboratory (CRL) of Exxon Research and Engineering Company, in his book entitled "*Catalysis: An Old but Continuing Theme in Chemistry*" [33]; Sinfelt who won President's National Medal of Science under President Jimmy Carter (1979), indicates a periodic trend for noble metals and heptane hydrogenation; his work led to insertion of basic understanding of catalysis by noble metals as supported on alumina oxides (Al_2O_3), which later became a mainstay in the field of heterogenous catalysis until today [33] (Fig. 1.1).

An environmental breakthrough then occurred when petroleum companies were required to take the Federal Test Procedures (FTP). A team at CRL led by Sam Tauster created a three-way conversion (TWC) noble metal catalyst that solved the problem and became standard in every automobile; their data is presented in Fig. 1.2.

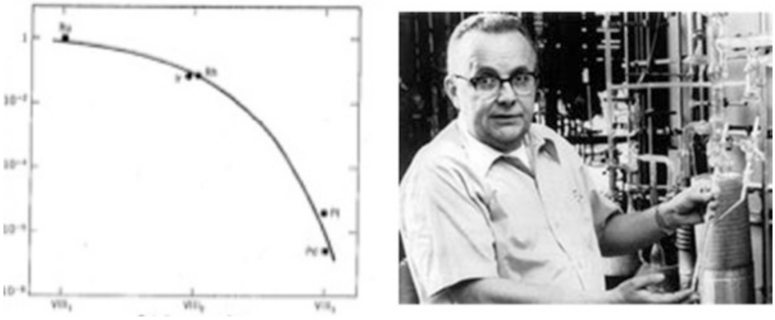

Fig. 1.1 Left: Catalytic activity of group VIII noble metals for heptane hydrogenation activity vs. periodic position. Right: Picture of John Sinfelt at Exxon Research and Engineering Labs in New Jersey, USA. Images taken with rights and permissions from ref. [33]

Fig. 1.2 Data on three-way conversion (TWC) noble metal catalyst, reprinted with the permissions of Copyright© (1978) from American Chemical Society as published in ref. [34]

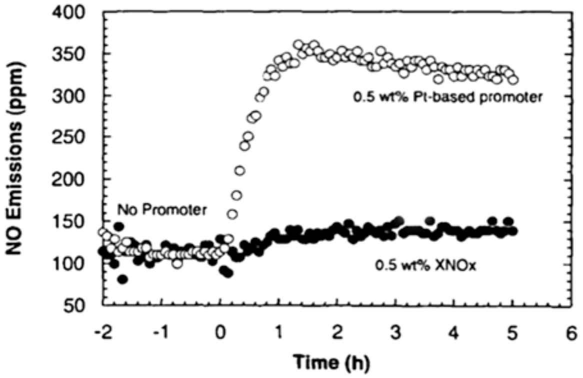

The catalytic activity can be related to surface defects in the crystallographic lattice as described by Simkovich and Wagner [35]; its catalytic properties and stability of ionic defects are determined by the bulk atomic configuration and its particular electronic structure [36]; this means that electronic structure and crystallography of stable TMS phases under catalytic environment need to be understood in order to depict fundamental origins of catalytic effects in the metal sulfides and other bimetallic phases (i.e., core–shell platinum/palladium nanoparticles and clusters). In all cases of reaction-stabilized catalytic materials it is essential to understand the structure of the catalysts and particularly of the interaction of multiple phases which include promoters, as described by Ponec [37]. The catalytic platinum nanoparticles were extensively studied by Sinfelt in order to understand reactivity and stability under catalytic conditions for nitrogenation and oxidation reactions [10], coining a term called *polymetallic cluster catalysts* [38]; his conclusions indicate that platinum bimetallic catalytic particles were more active than bulk platinum catalyst as it is presented in Fig. 1.3.

The insights into catalytic activity for commercial KX-130 (Exxon® commercial product) which is highly dispersed platinum metal bimetallic catalysts versus platinum/alumina (Pt/Al_2O_3) reforming catalyst indicates that a highly paraffinic naphtha feedstock can be converted to a product of 102.5 research octane number at 500 °C and 11 atmospheres of pressure. Although the composition of KX-130 is still proprietary it is the result of the study John H. Sinfelt Group VIII-Group1B highly dispersed platinum metal bimetallic catalysts can be found extensively described by Sinfelt [39]. Now, it is essential to mention that extensive studies as completed in TMS catalyst lead to a special emphasis on the understanding of its electronic structure and relationship to the crystallographic structure, and sulfur vacancies for deep understanding of catalytic activity and selectivity. In doing so, one study regarding *periodic effects* (electronic structure of *d*-electrons mainly) was conducted, the underpinning for any fundamental understanding related to the

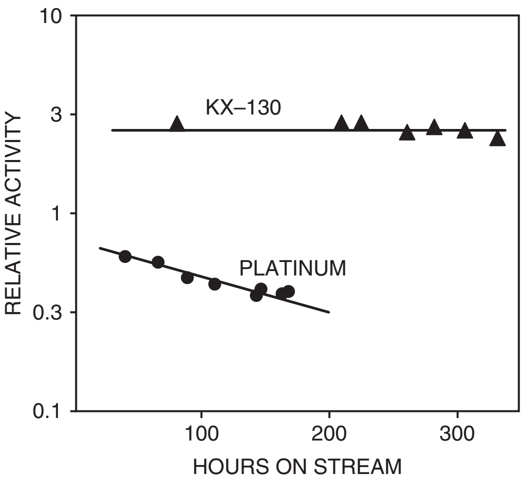

Fig. 1.3 Catalytic activity of KX-130 vs. platinum bimetallic catalysts; image taken with rights and permissions from ref. [38]

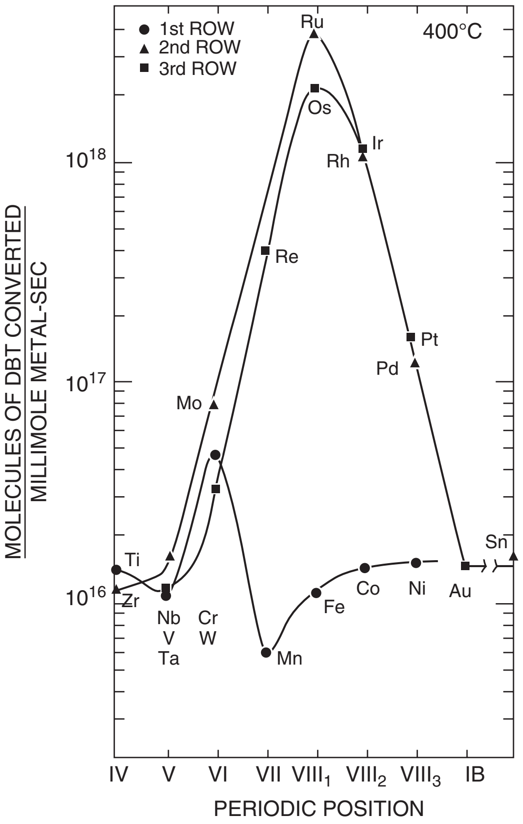

Fig. 1.4 Volcano curve representing the periodic trends for HDS test in transition metal sulfides, reprinted with copyrights and permissions from ref. [27] [Copyright©1981, Elsevier Inc.]

electronic structure; a typical “volcano” plot between the HDS activity for dibenzothiophene and the periodic position emerged and was found when achieving experimental test, as shown in Fig. 1.4. Group VIII TMS such as Ru, Rh, Os, and Ir were the most active as presented by Pecoraro and Chianelli [27]. Similar trends were later observed for hydrogenation reactions and HDN, as well as for the hydrotreating of heavy gas oil. These trends are of fundamental relevance, because they emphasize both the importance of the 4*d* and 5*d* electrons and the metal sulfur bond strength in transition metal catalysts [27–29].

Those periodic trends as shown in Fig. 1.4 for hydrodesulfurization (HDS) of dibenzothiophene molecule (DBT) in TMS catalytic materials were measured with an exception of Curie temperature (T_c) due to its radioactive nature, and indicate that ruthenium and osmium are the most TMS catalytic active, as we first assigned to a Pauling% “*d*-character” as presented in Fig. 1.5.

The stability and crystallographic composition of stabilized TMS catalyst become more complex as bulk material becomes low-dimension nanoparticles; in the case of binary systems, there are two main classes: (1) isotropic sulfides dominated by group VIII sulfides where several structures exist in this group, such as

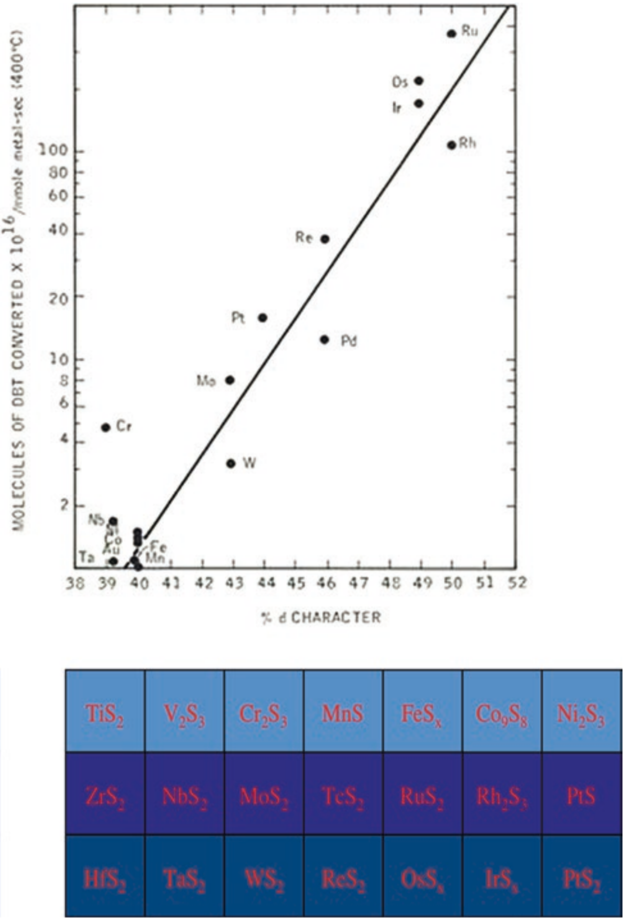

3d	TiS_2	V_2S_3	Cr_2S_3	MnS	FeS_x	Co_9S_8	Ni_2S_3
4d	ZrS_2	NbS_2	MoS_2	TcS_2	RuS_2	Rh_2S_3	PtS
5d	HfS_2	TaS_2	WS_2	ReS_2	OsS_x	IrS_x	PtS_2

Fig. 1.5 Plot to describe the Pauling% *d*-character for catalytic TMS materials, reprinted with rights and permissions of ref. [28] [Copyright©1986, Elsevier Inc.]

pyrite (RuS_2), pentlandites (Ni_3S_2), and others. The coordination of the metals in this group by sulfur is generally sixfold symmetry, octahedrally arranged, but some special structures, such as Co_9S_8, can also contain mixed sixfold and fourfold tetrahedral coordination. Some structures, such as PdS and PtS, also contain metals in distorted sixfold coordination. (2) The other layered sulfides predominate in groups IV to VII except for MnS, which are isotropic. The main structural feature of this class is a strong chemical anisotropy that greatly affects their catalytic properties; per example molybdenite structure (MoS_2), molybdenum is in trigonal prismatic coordination. Other layered sulfides are octahedrally coordinated or distorted octahedrally coordinated (ReS_2) with the metal surrounded by six sulfur atoms. It should also be noted that some TMS sulfides have structures that fall in between isotropic and layered sulfides. Rh_2S_3 is an example and others are completely amorphous,

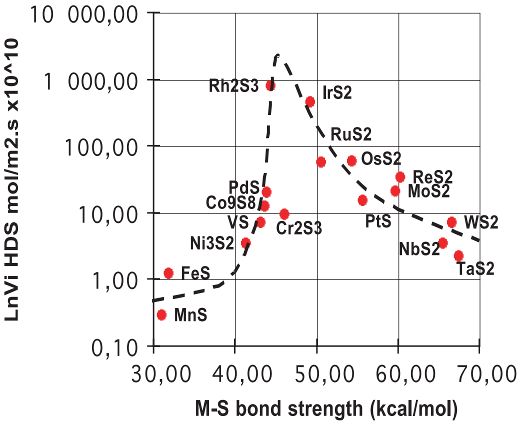

Fig. 1.6 Plot to describe bond strength vs. HDS conversion in catalytic TMS materials, reproduced with rights and permissions from ref. [40] [Copyright©2002, Elsevier Inc.]

such as IrS_x and OsS_x. The question is this: What is the basis for these periodical trends? Why do we have a correlation to Pauling% *d*-character as described before? These questions are appropriate for all classes of catalysts, metals, oxides, and sulfides, and one answer can take us to the Sabatier's principle [40], which describes the case of the TMS, the metal-sulfur bond strength that states how strongly or weakly the reacting molecules such as DBT can be reacting/bonding to the catalyst near its surface, as presented in Fig. 1.6. The strength must be intermediate or the reactant bonds too tightly and the products can't leave; this led us to coin a term as "*Goldilocks effect*," as presented in Fig. 1.7, where a comparison of transition metal sulfides with sulfur chemical bond strength in kcal/mol is shown.

The bond strength that is optimum is roughly 45 kcal/mol [40], providing a basis for understanding the synergic effects of promoted systems such as a combination between cobalt sulfide (Co_9S_8) and molybdenite (MoS_2), but also some other stoichiometric combinations present no catalytic effect, and are usually classified as non-promoted or "*poison*" species for both MoS_2 or WS_2 crystallographic structures.

As seen in Fig. 1.7, a mixture of 50/50 between MoS_2 and Co_9S_8 can coexist and it implies that what we called "*contact synergy*" occurred as originally suggested by Delmon about 22 years ago [41]. At the moment, it is well understood that in stabilized TMS catalytic materials both phases can exist, and this implies that in the contact synergy mode the bond strength will average. In the case of MoS_2/Co_9S_8, experiments and computer-assisted calculations estimate can be approximately 50 kcal/mole, meaning a relevance of electronic structure shared near MoS_2/Co_9S_8 interface promoting catalytic activity. The latter can be understood as 4*d* and 5*d* electron clouds with respect to "Pauling% *d*-character." Thus, we can schematically explain, as schematically shown in Fig. 1.8; the mechanism of promotion or poisoning occurred due to electron affinity between two species in contact [42]. However, as stated before the contact synergy between interactions of both sulfide phases is implied.

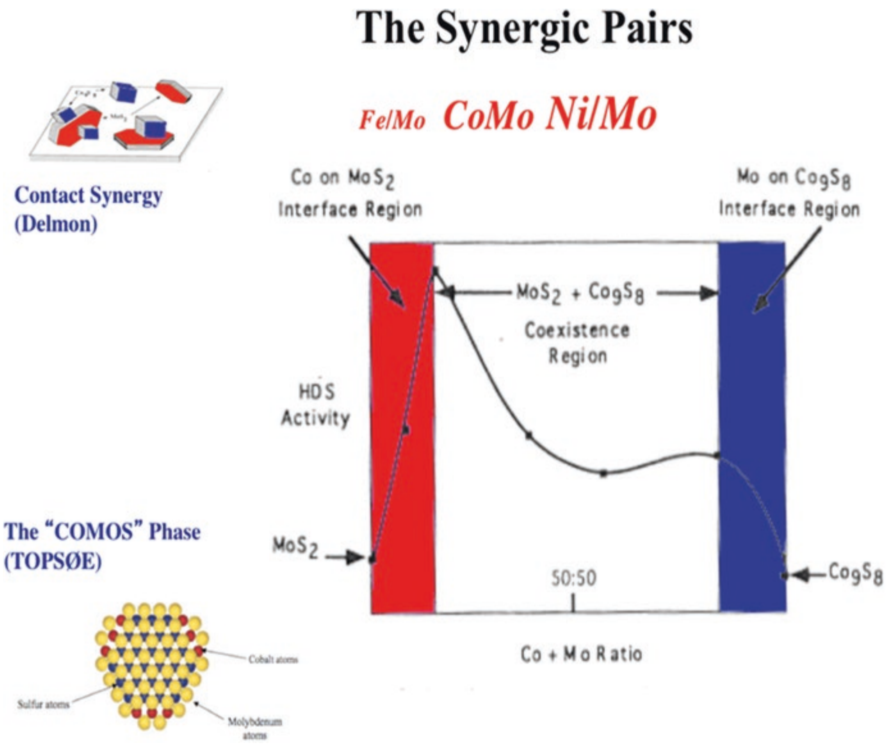

Fig. 1.7 Goldilocks effect as depicted by Co + Mo ratios. Above right: A schematic description of Delmon model. Below left: A typical cobalt promoted MoS_2 cluster described by H. Topsøe for layered TMS catalytic materials

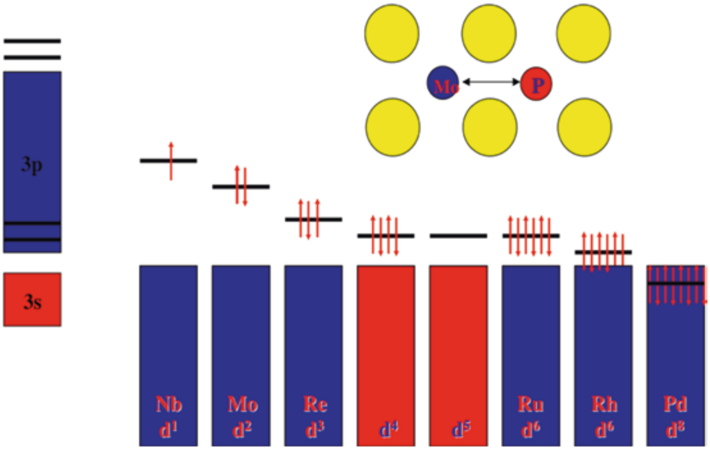

Fig. 1.8 Pauling% *d*-character schematic representation, in an attempt to describe the Goldilocks effect in the electronic structure of catalytic TMS materials, adapted from ref. [42] [Copyright©1984, Elsevier Inc.]

1.1 Electronic Theory of the Promotion Effect

In the past, it was possible to demonstrate that synergy by contact is an electronic effect through donation of electrons from promoter species such as cobalt (Co) or nickel (Ni) into molybdenite sulfide structure (MoS_2) arousing electron affinity near the metal-sulfur bond; Harris and Chianelli reported that the periodic trends of transition metal sulfide catalysts and the synergetic effects can be explained in terms of the filling of the transition metal sulfides *d*-band, supporting a theoretical approach in which several electronic factors appear to be related to catalytic activity; in other words: the orbital occupation of the highest occupied molecular orbital (HOMO) [42]. Thus, experimental evidence indicates that to be a good catalyst, the sulfide should have a HOMO filled with as many electrons as possible and be of t2g symmetry instead of eg. According to Berhault et al. a degree of covalence in metal-sulfur bond and metal-metal can make one sulfur atom shared between Co and Mo more basic and also more labile [43]. This result suggests an enhanced quality of the active sites due to the electronic promotion by cobalt. Harris et al. described in detail with earlier computer-assisted electronic structure calculations and assumed that a nearly complete localization of electron density in the metal t2g orbitals in RuS_2 and Rh_2S_3 may be partly responsible for their intrinsic high HDS catalytic activity [42]. And recently, using a combination of computer-assisted density functional theory (DFT) numerical electronic structure calculations and high-resolution transmission electron microscopy Ramos et al. had depicted the promotion effect by proposing a "*promotion interface model*" as presented in Fig. 1.9 [44] (more details about the DFT calculations are presented in Chap. 3 of this book).

The proposed interface model is exactly an electronic promotion as predicted before by theorizing experimental results. This model is supported by experiment and is currently generally accepted in the catalytic community. It is also important to consider how liquid fuel energy industry prepares the catalysts in operational units; industrially speaking, TMS is sulfided directly in the hydrotreating unit in the presence of hydrogen and sulfur-containing compounds; four different sulfiding processes are used and are distinguishable accordingly both to the nature of the sulfiding agent and to their in situ/ex situ modes of activation. Three of these methods are in situ sulfidation (by the sulfur content of the crude oil feedstock itself, H_2S, dimethyl disulfide) and one is an ex situ mode (alkyl polysulfides impregnated onto the oxidic precursor). The dimethyl disulfide process is the most extensively used until nowadays. In the chemical reaction hydrodesulfurization of dibenzothiophene, the catalysts synthesized with high-pressure hydrothermal method have achieved high conversion, generating the typical products of HDS of DBT: biphenyl and cyclohexylbenzene; in many cases those mixtures of metals have been extensively studied by the scientific catalytic community [15, 32, 39, 44].

Finally, this particular book is a compendium of many efforts from specialized groups around the world dedicated to serve as theoreticians and experimentalists in

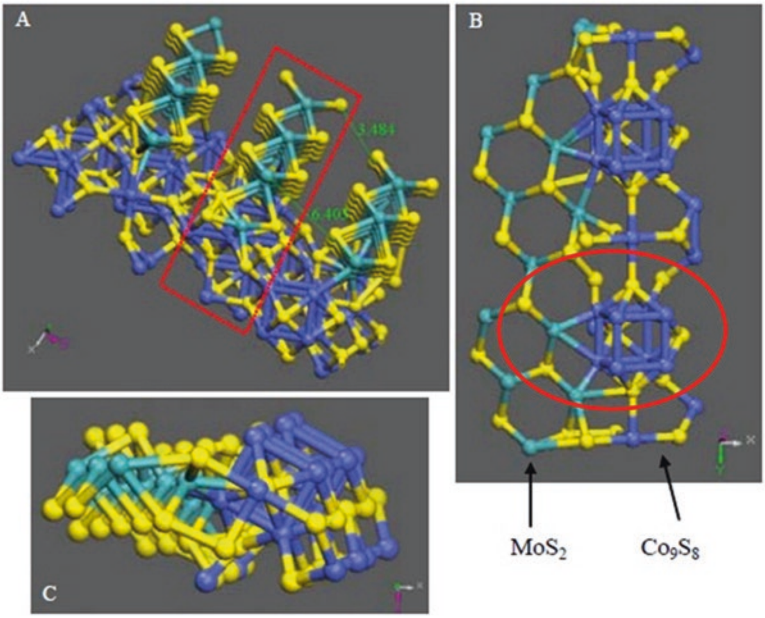

Fig. 1.9 Computer-assisted molecular model proposed by Ramos et al. to determine the synergic contact between cobalt sulfide and molybdenum disulfide in catalytic TMS materials (red circle determines the direct bonding between cobalt and molybdenum atoms, which is considered as *d*-electron promotion effect). Image adapted from ref. [44] [Copyrights© Royal Society of Chemistry]

the field of catalytic materials and liquid fuels and other sources of energy production. In the following chapters contributor authors will describe many similar effects in the wide variety of catalytic subjects.

References

1. J. Wismiak, The history of catalysis from the beginning to the Nobel Prizes. Educ. Quim. **21**(1), 60–69 (2010). ISSN 0187-893-X
2. N.K. Guillaume, R.V. Keller, Catalysts, mechanisms and industrial processes for the dimethylcarbonate synthesis. J. Mol. Catal. A Chem. **317**(1–2), 1–18 (2010)
3. R.N. Colvile, E.J. Hutchinson, J.S. Mindell, R.F. Warren, The transport sector as a source of air pollution. Atmos. Environ. **35**, 1537–1565 (2001)
4. F.C. Menza, H.M. Seip, Acid rain in Europe and the United States: an update. Environ. Sci. Pol. **7**, 253–265 (2004)
5. W. Dai, Y. Zhou, S. Wang, W. Su, Y. Sun, L. Zhou, Desulfurization of transportation fuels targeting at removal of thiophene/benzothiophene. Fuel Process. Technol. **89**(8), 749–755 (2008)
6. M. Gemmer, B. Xiao, Air quality legislation and standards in the European Union: background, status and public participation. Adv. Clim. Change Res. **4**(1), 50–59 (2013). https://doi.org/10.3724/SP.J.1248.2013.050

7. M.J. Ledoux, C. Pham-Huu, R.R. Chianelli, Catalysis with carbides. Curr. Opin. Solid State Mater. Sci. **1**(1), 96–100 (1996)
8. Jacques C. Védrine, Concluding remarks and challenges of heterogeneous catalysis on metal oxides, *Metal Oxides in Heterogeneous Catalysis*, Metal Oxides (Elsevier, Amsterdam, 2018), pp. 551–569
9. H.H. Hwu, J.G. Chen, Surface chemistry of transition metal carbides. Chem. Rev. **105**(1), 185–212 (2005)
10. J.A. Schwarz, C. Contescu, A. Contescu, Methods for preparation of catalytic materials. Chem. Rev. **95**(3), 477–510 (1995)
11. G. Pontikakis, C. Papadimitriou, A. Stamatelos, Kinetic parameter estimation by standard optimization methods in catalytic converter modeling. Chem. Eng. Commun. **191**, 1473–1501 (2004)
12. G.F. Froment, The kinetics of complex catalytic reactions. Chem. Eng. Sci. **42**, 1073–1087 (1987)
13. V. Chandra Srivastava, An evaluation of desulfurization technologies for sulfur removal from liquid fuels. RSC Adv. **2**, 759–783 (2012)
14. J. Gallagher, It takes two. Nat. Energy **3**, 252 (2018)
15. M.-C. Daniel, D. Astruc, Gold nanoparticles: assembly, supramolecular chemistry, quantum-size-related properties, and applications toward biology, catalysis, and nanotechnology. Chem. Rev. **104**, 293–346 (2004)
16. M. Chhowalla, H.S. Shin, G. Eda, L.-J. Li, K.P. Loh, H. Zhang, The chemistry of two-dimensional layered transition metal dichalcogenide nanosheets. Nat. Chem. **5**, 263–275 (2013)
17. J.V. Lauritsen, J. Kibsgaard, S. Helveg, H. Topsøe, B.S. Clausen, E. Lægsgaard, F. Besenbacher, Size-dependent structure of MoS_2 nanocrystals. Nat. Nanotechnol. **2**, 53–58 (2007)
18. R.R. Chianelli, Fundamental studies of transition metal sulfide hydrodesulfurization catalysts. Catal. Rev. **26**(3–4), 361–393 (1984). https://doi.org/10.1080/01614948408064718
19. M. Ramos, F. Galindo-Hernández, I. Arslan, T. Sanders & J.M. Domínguez, "Electron tomography and fractal aspects of MoS2 and MoS2/Co spheres", Scientific Reports 7: 12322. https://doi.org/10.1038/s41598-017-12029-8
20. B.R. Cuenya, Synthesis and catalytic properties of metal nanoparticles: size, shape, support, composition, and oxidation state effects. Thin Solid Films **518**(12), 3127–3150 (2010)
21. C.N.R. Rao, G.U. Kulkarni, P. John Thomas, Peter P. Edwards, Size-dependent chemistry: properties of nanocrystals, World Scientific Series in 20th Century Chemistry, in *Advances in Chemistry* (World Scientific Publishing, Singapore, 2003), pp. 227–233. https://doi.org/10.1142/9789812835734_0021
22. R.R. Chianelli, G. Berhault, B. Torres, Unsupported transition metal sulfide catalysts: 100 years of science and application. Catal. Today **147**(3–4), 275–286 (2009)
23. M. Appl, The Haber–Bosch process and the development of chemical engineering, in *A century of chemical engineering*, (Plenum Press, New York, 1982), pp. 29–54. ISBN 978-0-306-40895-3
24. O. Weisser, S. Landa, *Sulfide catalysts: their properties and applications* (Pergamon Press, Oxford, 1973)
25. W. Abelshauser, *German industry and global enterprise: BASF: the history of a company* (Cambridge University Press, Cambridge, 2004), pp. 15–19. ISBN: 0521827264
26. Paul Sabatier—Biographical. NobelPrize.org. Nobel Media AB 2018. Thu. 2018
27. T.A. Pecoraro, R.R. Chianelli, Hydrodesulfurization catalysis by transition metal sulfides. J. Catal. **67**(2), 430–445 (1981)
28. S. Harris, R.R. Chianelli, Catalysis by transition metal sulfides: a theoretical and experimental study of the relation between the synergic systems and the binary transition metal sulfides. J. Catal. **98**(1), 17–31 (1986)
29. R.R. Chianelli, Periodic trends transition metal sulfide catalysis: intuition and theory. Oil Gas Sci. Technol. **61**(4), 503–513 (2006)

30. A. Ivanovskaya et al., Transition metal sulfide hydrogen evolution catalysts for hydrobromic acid electrolysis. Langmuir **29**(1), 480–492 (2013)
31. H. Topsøe, B.S. Clausen, R. Candia, C. Wivel, S. Mørup, In situ Mössbauer emission spectroscopy studies of unsupported and supported sulfided Co-Mo hydrodesulfurization catalysts: evidence for and nature of a Co-Mo-S phase. J. Catal. **68**(2), 433–452 (1981)
32. M.P. De la Rosa, S. Texier, G. Berhault, A. Camacho, M.J. Yacaman, A. Mehta, S. Fuentes, J.A. Montoya, F. Murrieta, R.R. Chianelli, Structural studies of catalytically stabilized model and industrial-supported hydrodesulfurization catalysts. J. Catal. **225**, 288–299 (2004)
33. J.H. Sinfelt, Catalysis: an old but continuing theme in chemistry. Proc. Am. Philos. Soc. **143**(3), 388–399 (1999)
34. S.J. Tauster, S.C. Fung, R.L. Garten, Strong metal-support interactions. Group 8 noble metals supported on titanium dioxide. J. Am. Chem. Soc. **100**(1), 170–175 (1978)
35. G. Simkovich, C. Wagner, The role of ionic point defects in the catalytic activity of ionic crystals. J. Catal. **1**(6), 521–525 (1962)
36. A. Nilsson et al., The electronic structure effect in heterogeneous catalysis. Catal. Lett. **100**(3–4), 111–114 (2005)
37. V. Ponec, On the role of promoters in hydrogenations on metals; α, β-unsaturated aldehydes and ketones. Appl. Catal. A Gen. **149**(1), 27–48 (1997)
38. J.H. Sinfelt, Polymetallic cluster catalysts platinum. Metals Rev. **20**(4), 114–119 (1976)
39. J.H. Sinfelt, *Bimetallic Catalyst, Discovering, Concepts, and Application* (Wiley, Hoboken, 1983. ISSN: 0001-1541), pp. 1547–5905
40. R.R. Chianelli, G. Berhault, P. Raybaud, S. Kasztelan, J. Hafnere, H. Toulhoat, Periodic trends in hydrodesulfurization: in support of the Sabatier principle. Appl. Catal. A Gen. **227**(1–2), 83–96 (2002)
41. B. Delmon, A new concept explaining catalytic synergy between two solid phases. React. Kinet. Catal. Lett. **13**, 203 (1980). https://doi.org/10.1007/BF02068567
42. S. Harris, R.R. Chianelli, Catalysis by TMS: the relation between calculated electronic trends and HDS activity. J. Catal. **86**, 400–412 (1984)
43. G. Berhault, M. Lacroix, M. Breysse, F. Maugé, J.C. Lavalley, H. Nie, L. Qu, Characterization of acidic sites of silica-supported transition metal sulfides by pyridine and 2,6 dimethylpyridine adsorption: relation to activity in CH_3SH condensation. J. Catal. **178**, 555 (1998)
44. M.A. Ramos, G. Berhault, D.A. Ferrer, B. Torres, R.R. Chianelli, Combined HRTEM and molecular modeling of the MoS2-Co9S8 interface to understand the promotion effect in bulk HDS catalytical structures. Catal. Sci. Technol. **2**, 164–178 (2012)

Chapter 2
Synthesis of Novel Catalytic Materials: Titania Nanotubes and Transition Metal Carbides, Nitrides, and Sulfides

Davi Coelho de Carvalho, Josue Mendes Filho, Odair Pastor Ferreira, Alcineia Conceição Oliveira, Elisabete Moreira Assaf, and Yanet Villasana

2.1 Introduction and Scope

2.1.1 Overview

Catalysis is responsible for most of the advances in modern chemistry and industry. Food, fuels, chemical, pharmaceuticals, plastic, fibers, and fertilizers are examples of the impact of catalytic reactions on mankind, considering that chemical industry has been built after paramount advances in catalysis science and technology for the transformation of fossil and other resources into high-value products.

However, as the demand for efficient materials for catalytic processes has increased rapidly over the last century, this caused a huge growth in the search for new catalytic materials in comparison with the improvement of the traditional catalysts. Recently, much attention has been paid to the preparation of novel catalytic materials to address for challenging catalytic reactions and processes leading to

---

D. C. de Carvalho · A. C. Oliveira (✉)
Departamento de Química Analítica e Físico-Química, Universidade Federal do Ceará, Fortaleza, Ceará, Brazil
e-mail: alcineia@ufc.br

J. M. Filho (Deceased) · O. P. Ferreira
Departamento de Física, Universidade Federal do Ceará, Fortaleza, Ceará, Brazil

E. M. Assaf
Instituto de Química de São Carlos, Universidade de São Paulo, São Carlos, SP, Brazil

Y. Villasana
Grupo I+D+i Biomass to Resources, Universidad Regional Amazónica IKIAM, Tena, Ecuador

Venezuelan Institute for Scientific Research, Caracas, Venezuela

J. M. Domínguez-Esquivel, M. Ramos (eds.), *Advanced Catalytic Materials: Current Status and Future Progress*, https://doi.org/10.1007/978-3-030-25993-8_2

environmental friendly technologies to meet current demand of products, energy, and services in a situation of social and economic sustainability. Properties of new catalytic materials depend on a large extent not only on the synthesis method, which defines the catalyst surface structure and porosity, but also on the final treatments such as calcinations which allow building their structures. The most important and widely used methods are sol–gel, precipitation, impregnation, chemical vapor deposition, mechanical mixtures, complexation, gelation, crystallization, hydrothermal treatment, and ion exchange, among others. Through these methods, innovative catalytic materials including metal organic framework (MOF), inorganic nanotubes (INT), carbon nanotubes (CNT), hydrotalcites (HT), zeolites, perovskites, pnictides, graphene, hierarchically porous materials, spinel oxides, hexaaluminates, composite oxides, carbides, nitrides, sulfides, and so on have been studied. Supports, precursors, promoters, and additives also have an essential role in catalytic material synthesis since they can modify acid-base properties, metal-support interactions, particle sizes and shapes, and surface species, and probably incorporate synergetic effect, which subsequently have an impact on catalytic performance, in terms of yields, stability, and selectivity.

Inorganic oxides have been used as catalytic supports due to their high thermal stability and also their ability to preserve or enhance the properties of the bulk active phase. Alumina, silica, titania, and zirconia are commonly used for an extensive variety of catalytic reactions as supports. Titanium functionalities generally provide redox and acid-base properties, which can enhance the interactions between the solid surface and hydrocarbon molecules, e.g., methane, carbon monoxide, and carbonyl compounds, among others. The possible structures of the titanium can be included in bulk TiO_2 in rutile or anatase phases and titanate nanotubes. Originally, interest in the latter materials has been mainly focused on their use as gas sensors, water treatment, solar energy cells, medicine, electrochemistry, hydrogen storage, and new catalysts or catalyst supports and in environmental protection, as well. In this aspect, titanate nanotubes with elevated textural properties are recently receiving a great deal of attention by virtue of their specific structures and unique properties in adsorption studies and catalytic supports. Since these solids were found to exhibit good catalytic activity in reactions, other inorganic nanotubes such as vanadates, sulfates, selenides, tungstates, molybdate nanotubes of silica, alumina, perovskites, ceria, and palladium have been widely investigated and utilized for polymerization, photocatalytic activity, anodization, Knoevenagel reaction, oxidations, acid-base reactions, as well as reduction of methyl orange and Cannizzaro reactions.

Furthermore, inorganic oxides with elevated surface areas have been widely used as supports of conventional catalysts for the upgrading and transforming of crude oil through hydrotreatment and hydrocracking reactions. Usually, these supports consist of alumina, silica-alumina, or zeolites with a surface area of about 200 m^2g^{-1}. Textural properties have significant incidence on the diffusion of reactants through pores and active sites, particularly for voluminous molecules, as those present in a complex matrix such as crude oil (resins and asphaltenes). On the other hand, the active phase of these conventional catalysts is commonly based on transition metal sulfides (TMS) of Mo, promoted with Co or Ni. However, processing of nonconventional crude oils (heavy or extra-heavy) differs substantially from processing of conventional crude oils (medium and light crude oil), due to the presence of large amounts of asphaltenes and high contents of S, N, and metals, which rapidly deactivate these conventional catalysts, by sintering, poisoning, and pore mouth clogging. As a consequence, some efforts have been made to improve deactivation resistance of hydrotreatment catalysts in terms of S, N, metals, and coke resistance, and also lifetime in the process, by changing active phases and textural properties of supports. In this regard, recently carbides and nitrides have been considered as an alternative for the hydrotreatment of heavy crude oils since they can successfully perform hydrodesulfurization (HDS) and hydrodenitrogenation (HDN) reactions and are more resistant to coke than conventional TMS.

For these reasons, the aim of this chapter is to discuss the synthesis of novel catalytic materials and their application in a variety of catalytic processes, emphasizing on the structure/function relationships obtained by titania nanotubes and also transition metal carbides and nitrides (TMC and TMN, respectively). These exciting modern advances are moving from the fundamental and practical setting to the pilot-plant stage. Thus, technologies are currently being developed that will enable us to use these materials in catalytic plants by replacing the traditional catalysts. The approaches for using titanate nanotubes as catalysts or catalyst supports include some of the advantages such as their low cost, environmentally friendly aspects, stability, and lifetime. TMC and TMN have shown to be resistant to severe deactivation and also being highly active during hydrotreatment and hydrocracking reactions due to their resemblance with noble metals in terms of electronic properties.

This chapter sets out to demonstrate that the synthesis of novel catalytic materials has driven the majority of the studies of catalysis up to now, rather than the improvement of the benchmark catalysts; there are significantly more investigations on the synthesis of new solids for catalytic reactions besides other applications. Section 2.2 discusses the overall forecast for new catalytic materials related to this approach. Section 2.2.1 discusses the methods of synthesis, as this provides the basis for how to design innovative catalytic materials. Conventional solids are synthesized by physical or chemical methods and these strategies are also widely utilized to obtain newly porous materials. Inorganic nanotubes including titanate nanotubes themselves are promising candidates to be industrial catalysts. Therefore, Sect. 2.2.2 considers the general aspects concerning the inorganic nanotubes, including their routes of production, which can be used as-synthesized or modified. Also, the types of inorganic nanotubes, their characterizations, and some applications will be emphasized. Section 2.2.2.1 discusses the synthesis routes to obtain titanate nanotubes describing their characterizations and their uses. Section 2.2.2.2 explains the reasons for what the as-synthesized titanate nanotubes can be applied in the production of valuable chemical intermediates through reactions such as polymerization, photocatalytic activity, anodization, Knoevenagel reaction, oxidation and reduction of methyl orange, Cannizzaro reaction, CO oxidation, hydroformylation of vinyl acetate, and phenol oxidation. On the other hand, Sect. 2.2.3 discusses about catalytic profile of TMC and TMN and their generalities; moreover, in next Sect. 2.2.3.1 synthesis, characterization, and applications are briefly described for bulk and supported TMC and TMN finally in Sect. 2.2.3.2 their specific application as catalysts for the hydrotreatment of model molecules and crude oil is discussed.

Finally, Sect. 2.3 provides the summary and conclusions for this chapter. Significantly, this manuscript describes the fundamental chemistry on the methods of synthesis to obtain catalysts, inorganic nanotubes, TMC, and TMN; their applications in catalytic reactions; and the needs for future new catalytic material development.

2.2 Forecast for New Catalytic Materials

The constantly growing world demand for materials to be applied as catalysts has shown that there is a need of improving the traditional catalysts or produce new solids for catalytic reactions. Coupling this with rising instability in the price of reactants, devices, preparation of the materials, and uncertainty of supply as well, many research groups have been encouraged to other drivers in the search for alternative routes to prepare materials. This search also includes a very important multidisciplinary research scope for novel strategies for material syntheses, as new catalytic materials [1–7]. Advances in computational chemistry and pursuit for a deep understanding of factors involved during catalytic reactions have motivated the development of methods to simulate an entire catalytic process considering thermodynamic parameters, leading to prediction of trends in reactivity and performance, and then tailoring of catalytic structure, this being transduced into savings in synthesis and catalytic tests [8–14], as it will be seen in other chapters of this book.

A close look in the search of new catalytic material theme over the past 10 years reveals that the researches typically focused on the synthesis of innovative materials to meet demand for experimental setups and technological aspects of the catalytic reactions. Moreover, an aggressive growth is expected to continue, driven primarily by investments in preparation of material domains after 2015 (Fig. 2.1).

If these growth speculations are met, new catalytic materials would account for more than 19,519 publications of the catalytic field search by 2015. In other words, hundreds of papers are expected to be published in this field. Noteworthy, the above-mentioned projections have arisen based on the development and design of new catalytic materials such as MOF, INT, CNT, hierarchically porous materials, HT, zeolites, pnictides, graphene, perovskites, spinel oxides, hexaaluminates, graphene, composite oxides, transition metal carbides, and nitrides [1–7, 11–17]. In addition, the search is associated to the development of synthetic routes throughout the methods involving sol–gel, precipitation, impregnation, chemical vapor deposition, mechanical mixtures, complexation, gelation, crystallization, nanocasting, hydrothermal treatment, temperature-programmed reaction with reactive gases, and ion exchange, among others [17–25].

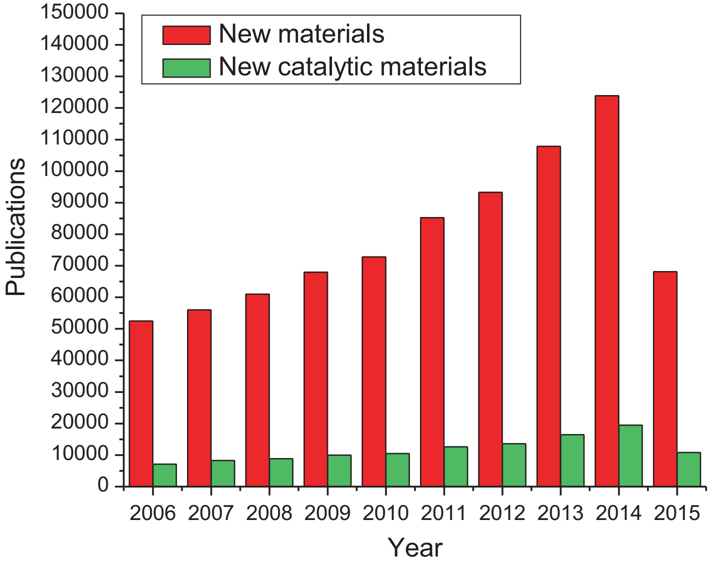

Fig. 2.1 Forecast for the applications of new catalytic materials. The period is 2006–2015

2.2.1 Methods of Synthesis to Design New Catalytic Materials

According to the Schwarz et al. [20], the catalytic materials exist in various forms and their preparations follow different protocols with a huge number of possible synthesis routes, frequently larger than the number of known catalysts. Hence, it is important to bear in mind that the new catalysts have been developed and shown promise in solving challenges encountered by the hydrocarbon transformation reactions in the industry. Therefore, as catalysis is the basis of the chemical industry [21], the improvement of properties and the discovery of new functionalities for the catalysts are achieved by a well-controlled and a better understanding of the preparation methods. Moreover, the idea of tailoring materials for specific applications has been widely spread as a consequence of the need for new materials that can handle challenging processes with a minimum of environmental impact, almost reaching zero by-products and using abundant materials in the world, with the vision of promoting the mitigation rather than adaptation to global climate change, especially on those processes identified by their highly negative impacts on the environment, as it occurs for the fuel and petrochemical industry [5, 26–31].

Thus, several methods have been developed in an attempt to attend these requirements including precipitation, impregnation, coprecipitation, sol–gel, chemical vapor deposition, mechanical mixtures, nanocasting, complexation, gelation, crystallization, hydrothermal treatment, and ion exchange, among others [1–7, 23, 32–39].

The most common methods used to prepare catalysts are divided into two families, the precipitation and impregnation procedures, as illustrated in Fig. 2.2.

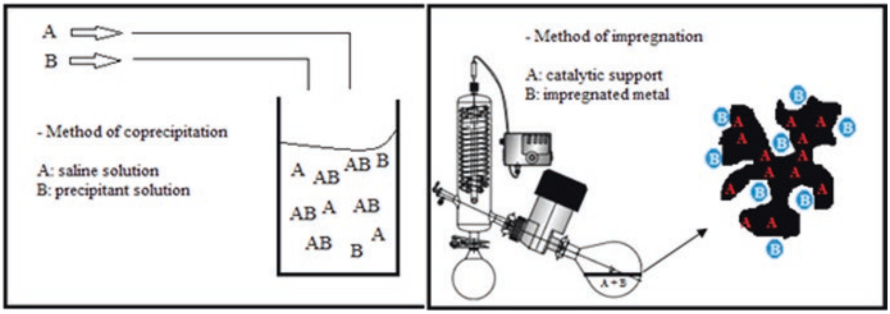

Fig. 2.2 Schematic representation of precipitation and impregnation routes to prepare catalysts

The precipitation from a homogeneous solution route is a technique based on the fact that one or more soluble salts, which contain the metal of interest, are neutralized by addition of a base for generation of precipitate or coprecipitate of the corresponding metal oxide gels [32]. As a result of the process, relative supersaturation is kept low with phase separation from the homogeneous liquid solution. The resulting precipitate is transformed into the following preparation stages into new solid phase through heating procedures, being the active catalyst. It has been claimed that the precipitation route includes the variant coprecipitation through two or more salt precursors used with ending calcination treatment steps, which transform amorphous precipitates to crystalline materials [20].

The classical impregnation route consists of the synthesis strategy whereby a certain volume of solution containing the precursor of the active element is contacted with the solid carrier material (silica, alumina, magnesia, active carbon, titania, etc.) [20, 32, 33]. The suspension is formed, being afterwards heated to remove the solvent and to disperse the metal on the carrier [32]. When the volume of the metal salt solution taken by the carrier is either identical or lesser than its pore volume, the technique is designed as incipient wetness [20]. The impregnation route also comprises different techniques such as ion exchange, deposition and grafting, among others.

The ion exchange consists of exchanging either hydroxyl groups or protons of the carrier with cationic and anionic species in solution [32]. The adjustment of the pH is a key factor to have an electronic interaction between the support and the metal precursor.

The traditional sol–gel method consists of the formation of a sol followed by the formation of gel [34]. This method is mainly based on the chemistry of hydrolysis and polymerization reactions and uses colloidal dispersion or inorganic precursors to produce novel materials. The method can use a wide variety of precursors, but the alkoxides are the most commonly used. Moreover, the alkoxides react with nucleophilic reagents giving rise to new precursors that exhibit different molecular structure, functionality, and reactivity [32, 34].

Other methods to prepare catalytic materials, for instance chemical vapor deposition, mechanical mixtures, nanocasting complexation, gelation, crystallization, hydrothermal treatment, and ion exchange, are well described in the literature [20–

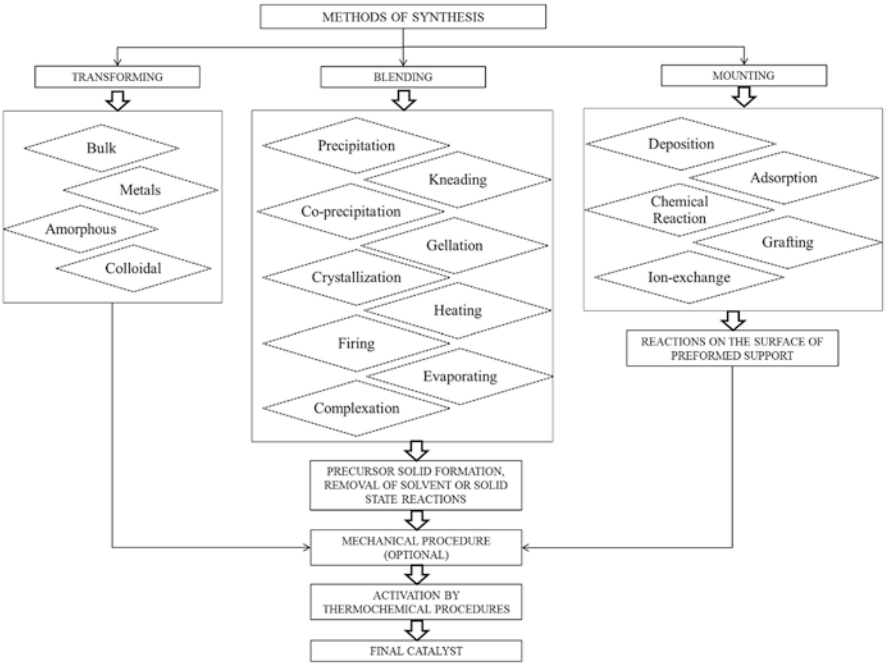

Fig. 2.3 Schematic diagram showing the methods of blending, transforming, and mounting the catalysts (adapted from ref. [20])

23, 32–43]. The main preparation routes are summarized in Fig. 2.3. These methods allow defining the properties of the catalyst via blending, transforming, and mounting steps to obtain the final catalyst to be applied in the reactions.

Importantly, through the abovementioned methods, novel materials such as metal organic framework (MOF), inorganic nanotubes (INT), carbon nanotubes (CNT), hierarchically porous materials, hydrotalcites (HT), picnides, zeolites, perovskites, spinel oxides, hexaaluminates, graphene, composite oxides, and so forth have been developed. The advantages and disadvantages of using these methods are shown in Table 2.1.

Despite these catalyst preparation methods producing materials with advantageous structural and porosity features, some of these synthetic routes require a sequence of several complex processes, many of them not completely understood.

2.2.2 *Inorganic Nanotubes: General Aspects*

Synthesis of inorganic nanotubes (INT) has recently drawn considerable interest in the research areas of solid-state chemistry and nanomaterials. The INTs are nanostructured materials derived from layered inorganic compounds possessing

Table 2.1 Distinct preparation methods to obtain new catalytic materials [20, 44–49]

Method of synthesis	Advantage	Disadvantage
Coprecipitation [20, 44, 46]	Convenient, simple process, provides a large range of scale, can be highly selective and virtually quantitative	Precipitate can be contaminated easily, can spend a long time to digest, to filter, or to wash the precipitate
Impregnation [20, 44, 45]	Fast process, the excess solvent is removed by drying easily and addition of active precursor into the porous carrier	Increasing the weight loading results usually in lower solution pH, carrying out support disruption and substitution of ions into the support lattice
Sol–gel [20]	Allows control of the textural properties, homogeneity, and chemical composition	Synthesis more complicated that requires greater energy expenditure
Chemical vapor deposition [20]	Fine-tuning of the pore size and using low-pressure conditions to allow direct deposition of the active material onto catalyst material	Surface poisoning, dissolution, and mainly redistribution of the active material during activation of the solid
Complexation [20]	The use of organic molecules with several chemical functionalities is important for formation of the three-dimensional network during the sol–gel step	The removal of the organic ingredient is very important during the catalysis activation
Crystallization [20]	Simple process and excellent purity obtained after the crystalline growth	Variation of temperature can cause instability and difficulty to the growth of the crystalline structure
Hydrothermal treatment [20, 49]	Low cost and simplicity of operation	Large amount of energy expended to produce a little sample
Ion exchange [20, 44]	Able to modify the size and way until achieving the internal pores	It is a prerequisite to keep the charge compensating ions for stability of the crystalline structure

structures comparable to those of graphite [43, 47]. For instance, Fig. 2.4 illustrates the MX_2 (M = Ta, Zr, Mo, W, Cd, Nb, Hf; X = S, Se) metal dichalcogenides, which are inorganic compounds with a metal-layered sandwiched structure between two chalcogen layers, with the metal in a trigonal pyramidal or octahedral coordination mode [43]. What makes these structures interesting is that they comprise unsaturated bonds at the edges of the layers, similar to that presented in graphite. It is important to figure out that especially in case of the dichalcogenide layers, there is instability towards bendings and these solids have a high propensity to roll into curved structures [43, 48].

In recent years, these INTs have moved towards being the subject of intense multidisciplinary studies in reason of their one-dimensional nanostructure, excellent physiochemical properties, and versatile applications such as sensors, adsorbents, solar cells, catalyst supports, medicine, photocatalysis, drug delivery, and electronics, among other applications [43, 47–52].

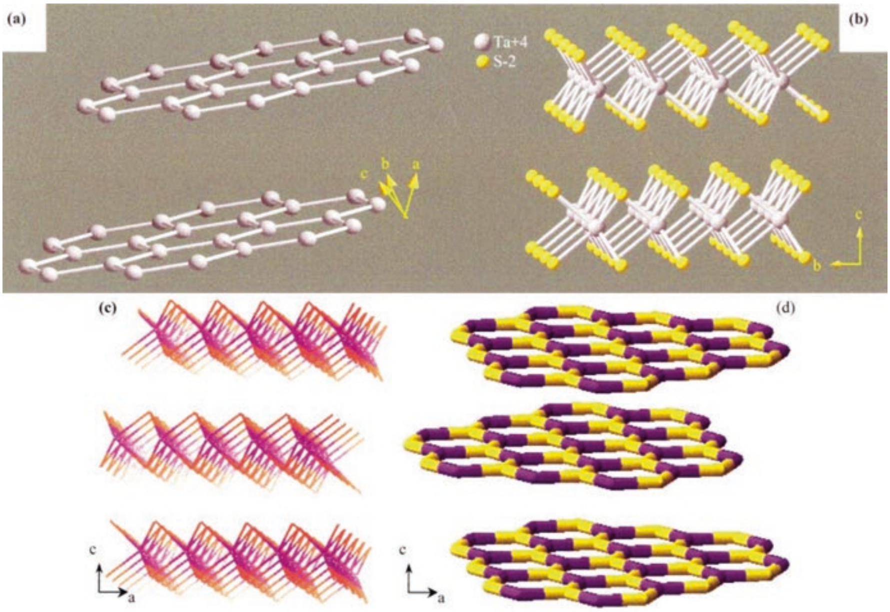

Fig. 2.4 Comparison of the structures of (**a**) graphite and inorganic layered compounds such as (**b**) NbS_2/TaS_2; (**c**) MoS_2; and (**d**) BN. In the layered dichalcogenides, the metal is in trigonal either prismatic (TaS_2) or octahedral coordination (MoS_2). (*Reproduced with permission from ref. [43]*)

Over the last two decades, the INTs have opened innovative research direction as a challenge for synthesis of new catalytic materials. The most used methods to produce INTs for catalytic applications are (1) the arc discharge and laser ablation, (2) sol–gel, (3) hydrothermal treatment, (4) assisted template method, and (5) electrochemical anodic oxidation. The main synthetic routes for INT production are summarized in Table 2.2. As it can be seen, the metal dichalcogenides (e.g., MoS_2, $MoSe_2$, and WS_2) can be easily fabricated through the arc discharge, laser ablation, as well as chemical reactions involving the stable oxides, such as MoO_3 and WO_3, upon heating [43]. The carbon nanotube template route is used to obtain INTs by adsorbing the precursors on the outer walls of CNTs and covering it with inorganic materials [51–53].

In case of the hydrothermal treatment method, it has been used for synthesizing nanotubes from several metal oxides such as SiO_2, Al_2O_3, $Na_2Ti_3O_7{\cdot}n H_2O$, V_2O_5, ZnO_2, $PbTiO_3$, and $BaTiO_3$ [54–56].

The sol–gel method provides a new approach to the preparation of INTs, as for silica, TiO_2, Ga_2O_3, and In_2O_3. Besides, the strategy based on the sol–gel route is that of the oxide gels in the presence of surfactants or suitable templates form nanotubes. The coating of the CNTs with oxide gels is performed and then burning off the carbon provides the formation of nanotubes and nanowires of a variety of metal oxides including ZrO_2, SiO_2, and MoO_3 [54]. Another method is the layer-by-layer

Table 2.2 Types of INTs produced by different routes [64–69]

Type of nanotubes	Synthetic strategy	Refs.
Al_2O_3	(1) Chips were electropolished to anodization in a solution containing ethanol and $HClO_4$ (2) H_2SO_4 was used in the first anodization step (3) After the pulses in H_2SO_4 electrolyte, the remaining aluminum substrate was removed by wet chemical etching	[64]
CeO_2	(1) $K_{1.33}Mn_8O_{16}$ nanowires and $Ce(NO_3)_3$ were transferred into Teflon-lined, during hydrothermal treatment process (2) Product was rinsed with ethanol and deionized water, and dried in air	[65]
$PdCl_2$	(1) Aqueous $PdCl_2$ was slowly added in solution containing Ag nanowires and NaCl, under vigorous stirring (2) Product was washed with ethanol and water for removing AgCl and NaCl (3) Finally, reminiscent Ag was removed with addition of H_2O_2 solution	[66]
SiO_2	(1) TEOS was added to the solution containing glycyldodecylamide (GDA) and ethanol and stirred at room temperature (2) Product was washed with ethanol to remove the surfactant (3) Aminopropyltriethoxylsilane (APTES) was added to a suspension of toluene-containing silica nanotubes (4) Solution was heated under reflux	[67]
$Na_2Ti_3O_7{\cdot}nH_2O$	(1) TiO_2 (rutile) was added in NaOH aqueous solution (2) Mixture was placed into Nalgene flask during 20 h at 110 °C (3) Product was treated with distilled water and then centrifuged to separate the powder (titanate nanotube)	[68]
MoS_2	(1) Large-surface-area MoS_2 atomic layers (2) Synthesized on SiO_2 substrates by chemical vapor deposition using MoO_3 and S powders as the reactants	[69]

(LBL) assembly of the precursors on CNT templates in combination with subsequent calcination that has been developed to prepare porous SnO_2 and In_2O_3 nanotubes [57].

Furthermore, the sol–gel chemistry can also be used to obtain oxide nanotubes in the pores of alumina membranes. Through this method, MoS_2 nanotubes are also synthesized by the decomposition of a precursor in the pores of an alumina membrane [43, 55]. Also, cobalt, iron, nickel, and copper nanotubes have been synthesized using polycarbonate membranes as templates [58].

The use of precursors via direct decomposition has been reported as a vastly applied method to obtain the disulfide nanotubes. The selenide nanotubes are obtained through H_2Se reactions whereas the sulfide nanotubes are prepared from MoS_3, WS_3, NbS_2, and HfS_2. Both molybdenum and tungsten dichalcogenides can also be obtained through the decomposition of the precursor ammonium salt, such as $(NH_4)_2MX_4$ (X = S, Se; M = Mo, W) [43]. The types of INTs produced by different routes are summarized in Table 2.2.

The metal oxide nanotubes can also be prepared by the surfactant-assisted synthesis combined with sulfidizing/selenidizing agent, with CdSe and CdS nanotubes being good examples of the use of such method [59]. Nanotubes of other oxides such as Er, Tm, Yb, and Lu have been prepared by the aforesaid template-mediated reactions using dodecyl sulfate assemblies [60].

Importantly, the transition metal halides, oxides, and nitrides in layered structures as well as GeO_2 and GaN nanotubes are reported to be prepared by heating of their salt precursors in air to vanish the water of crystallization, with the heating under nitrogen flow being the final step to prepare the solids [59]. Moreover, nanotubes of both $PbTiO_3$ and $BaTiO_3$ can be better discussed elsewhere [61]. Boron nitride nanotubes have also been prepared by coprecipitation and annealing routes and striking an electric arc between HfB_2 electrodes in nitrogen atmosphere as well [62, 63]. The polysiloxane nanotubes were synthesized via trifunctional organosilanes, as reported elsewhere [63].

Similar morphologies of the INTs including nanowires, nanorings, nanowhiskers, nanofilaments, nanorods, and nanobelts have begun to emerge through the use of the abovementioned methods [43, 63].

Among the discussed methods of synthesis, hydrothermal treatment is attractive, since it allows the preparation by a simple route and is of low cost to design catalysts.

Numerous investigations have been reported to ascertain how the INT synthesis conditions affect their properties and thereby affect their catalytic performance. Therefore, suitable characterizations of the crystal and/or textural structure features of the INTs are essential in understanding their physicochemical properties. The conventional measurements by TEM, SEM, Raman and FTIR spectroscopy, XRD, TGA/DSC/DTA, and nitrogen physisorption isotherms give deep insight into the structure, texture, and surface morphologies of the synthesized INTs [49–51, 53–63]. Other techniques such as temperature-programmed desorption of CO, CO_2, or O_2 (TPD); temperature-programmed reduction of hydrogen (H_2-TPR); extended X-ray absorption fine structure (EXAFS); and X-ray photoelectron spectroscopy (XPS) give information on the reducibility, defects, and oxidation state of metal and oxygen elements of the INTs, which are indispensable properties to justify the efficiency (inefficiency) of the catalysts in the reactions.

Despite the fact that INTs have not yet been applied in industry up to now and there is still a long way to walk on before their commercialization, the easy availability, their potential for extensive applications, and tuneable physicochemical properties make them bouncy materials for catalytic studies.

2.2.2.1 Titanate Nanotubes: Preparation, Characterization, and Applications

Titanate nanotubes blossomed since the turn of the twentieth century led by pioneers such as Kasuga and coworkers [70, 71]. TNTs are 1D nanostructures consisting of a layered structure with a hollow cavity (Fig. 2.5). The scrolling of an

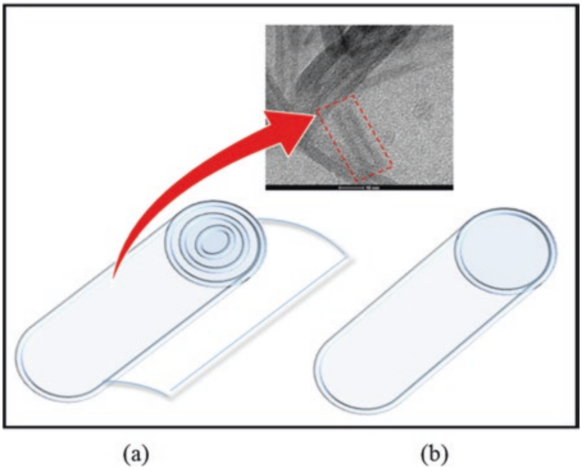

Fig. 2.5 Types of TNTs: (**a**) single-layer nanosheets and multilayer nanosheets (**b**)

exfoliated layered titanate nanosheet is formed in the nanotube structure through hydrothermal treatment by folding nanosheets [71]. According to the figure, there are two types of nanosheets that is to say, single-layer nanosheets, which are isolated (100) planes of titanates (Fig. 2.5a), or multilayer nanosheets (Fig. 2.5b), which are several conjugated (100) planes of titanates [71]. Additionally, both types of nanosheets are very thin and could be found in both planar and curved shapes. The TNTs can be prepared by the sol–gel, hydrothermal treatment synthesis, anodization, atomic layer deposition, template assisted, and supercritical media, providing access to the fabrication of morphologically diverse TiO_2 nanomaterials [72–75].

The hydrothermal treatment of TiO_2 is the simplest synthetic tool to obtain the TNTs with low cost and harnesses and requiring neither expensive apparatus nor special chemicals. The advantages of this technique are indeed enormous, since the TNT's unusual morphology and unique physicochemical properties can be easily and flexibly controlled. The nanosheets are usually observed in the early stage of preparation of TNTs or as a small impurity in the final product obtained via the alkaline hydrothermal treatment [71]. Moreover, dimensions and morphology can be controlled by adjusting the temperature and pressure parameters as well as the alkaline concentration and synthesis time [76–78].

Many applications of the TNTs have burgeoned since then in photocatalysts, gas sensors, photoluminescence, dye-sensitized solar cells, electrochemical capacitors, water treatment, proton conduction, lithium inserting, hydrogen storage, catalysts or catalyst carriers, medicine, proton transport, and adsorbents. The TNTs have charted progress in these areas that have indeed become prosperous fields in the discovery of new TiO_2-nanotube materials [49, 70–76, 79].

This likely pursues from the certain degree of porosity associated with the high surface areas of the solids in relation to the more straightforward understanding of the superior adsorption capacities and thereby catalytic properties of the TNT nanomaterials.

2.2.2.2 Heterogeneous Catalysis Using Titanate Nanotubes

Titanium functionalities give redox and acid-base properties making the interactions between the solid surface and hydrocarbons molecules easy. The structures derived from titanium functionalities are TiO_2 in rutile or anatase phases and titanate nanotubes. The catalytic applications of TNTs date back over 15 years and the evolution of the chemistry of the TNTs, until very recently, has been more gradual. Most of the studies on application of the titanate nanotubes in catalysis field are devoted towards their uses as catalysts or catalyst carriers.

As catalysts, the moderate acid-base property can be considered as one of the earlier attempts to use protonated titanate nanotubes in Friedel-Crafts alkylation of toluene with benzyl chloride, photocatalysis, hydroxyalkylation/alkylation of 2-methylfuran and *n*-butanal from lignocelluloses, esterification, dye oxidation, and hydrolysis of 2-chloroethyl ethyl sulfide [71, 80–83]. Despite that highly active Lewis acid catalyst with active Brønsted acid sites is often found, the TNTs provide the drawback of being not reusable for several times. Also, they have a much lower catalytic activity than the traditional catalyst applied in title reactions.

The use of TNTs as catalyst carriers has been investigated for water gas shift reaction, reduction of methyl orange, Knoevenagel reaction, isomerization of allylbenzene polymerization of methyl methacrylate, Cannizzaro reaction, CO oxidation, hydroformylation of vinyl acetate and phenol oxidation, NO_x storage/reduction, and hydrotreating for ring opening of tetralin, among others [48, 64, 71–80, 84]. Some of them are depicted in Fig. 2.6. Another interesting feature is that the as-synthesized titanate nanotubes can be *in situ* transformed into active centers for supported catalysts.

Thus, the unique physicochemical properties of TNTs seem to be imperative to attend these reactions. In this sense, TNT materials with remarkable catalytic performance have been obtained by virtue of the intercalation of metal cations in TNTs and/or decoration of metal oxide nanoparticle procedures [71]. Thereby, the majority of the studies reported on these reactions have demonstrated that the TNTs decorated with CuO, La_2O_3, RuO_2, NiO, ZnO, CeO_2, NiO, MoO_x, MnO_x, Cs_2O, and SnO_2, doped with boron or nitrogen nanoparticles, have outstanding performance as acid-base catalysts. Indeed, insights into the redox ability of TNTs is displayed, when the nanotubes contain Fe_2O_3, ZnO, Au, Cr, As, Cd, Pd, Cu, Ce, Ru, Ni, and Pt [42, 80–83, 85–93].

It is quite necessary to study the physicochemical features of the TNTs and their effect on the reaction mechanisms. Though not addressed here, the disadvantages associated to deactivation of TNTs in the reaction media due to diverse aspects as pore blocking and/or coke formation are still in debate.

Of the applications available in catalysis, photocatalysis degradation of contaminants by TNTs has been widely investigated [71, 73, 94]. One remarkable advantage of the TNTs is the elevated photocatalytic activity over counterparts of TiO_2 nanoparticles. This is due to the shape-dependent structure of the TNTs associated with their high surface-to-volume ratio and superior physicochemical properties [95]. However, the usage of TNTs in photocatalytic applications suffers from intrin-

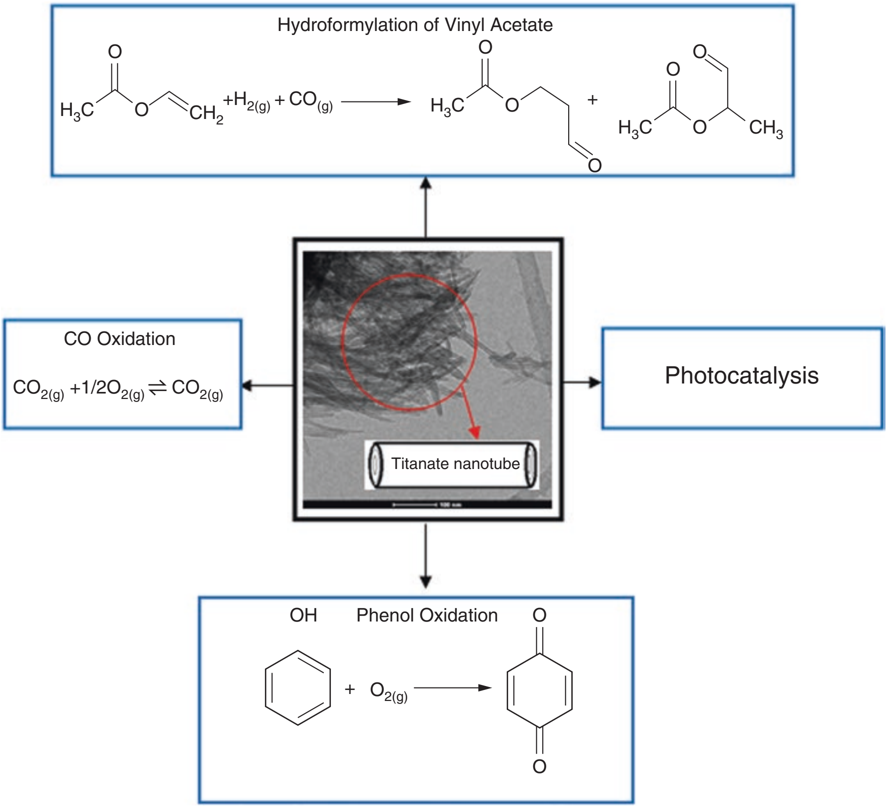

Fig. 2.6 Some reported catalytic reactions using TNTs

sic disadvantages of photocorrosion, which greatly decreases their photoactivity and photostability.

Clearly, the methods for synthesizing TNTs need to be optimized to develop the technology for an active, selective, and stable catalyst and lastly a long-standing challenge for their commercialization successfully. It should be kept in mind that the capital cost savings can be gained through the preparation of large amounts of TNT catalysts. The environmental friendly aspect is another factor that limits the discarding needs of the industrial plants and also enhances the economic feasibility of these materials as heterogeneous catalysts.

2.2.3 Transition Metal Carbides and Nitrides: General Aspects

TMC and TMN are known to be interstitial compounds where nonmetal atoms are located at big interstitial sites of the cubic and octahedral prismatic structure of metals. These materials follow Hägg's rule which establishes that the formed structure depends on the atomic ratios of metal and nonmetal elements [96].

Moreover, regarding structure and composition, it is important to mention that carbon and nitrogen form compounds with all transition metals except late metals of the second and third rows of the periodic table. TMC and TMN exhibit a variety of structures depending on metals involved, varying from *fcc* to *hex* and *hcp*. These structures are mainly determined by their electronic properties and their trends have been found to be similar to those found for metals by the Engel-Brewer theory [97, 98]. Group 6 metals form structures similar to M_2X (X = C, N), while groups 3–5 form structures like MX. It is also notable that compounds formed with early transition metals show structures such as MX and M_2X, but in the late transition metals the M_3X and M_4X stoichiometry prevailed (see Fig. 2.7). This increase in M/X ratio when moving to the right of the periodic table represents a C and N rejection of the metal and reflects a decrease in carbides and nitride stability in comparison to their parent metals [99].

The discovery of new phases with unique properties has permitted to use TMC and TMN in diverse areas, such as that reported by Yu et al. [99] in which an oxynitride of V-Mo has more activity in the HDN of quinoline under industrial conditions than the pure V or Mo nitrides, or a conventional NiMoS catalyst.

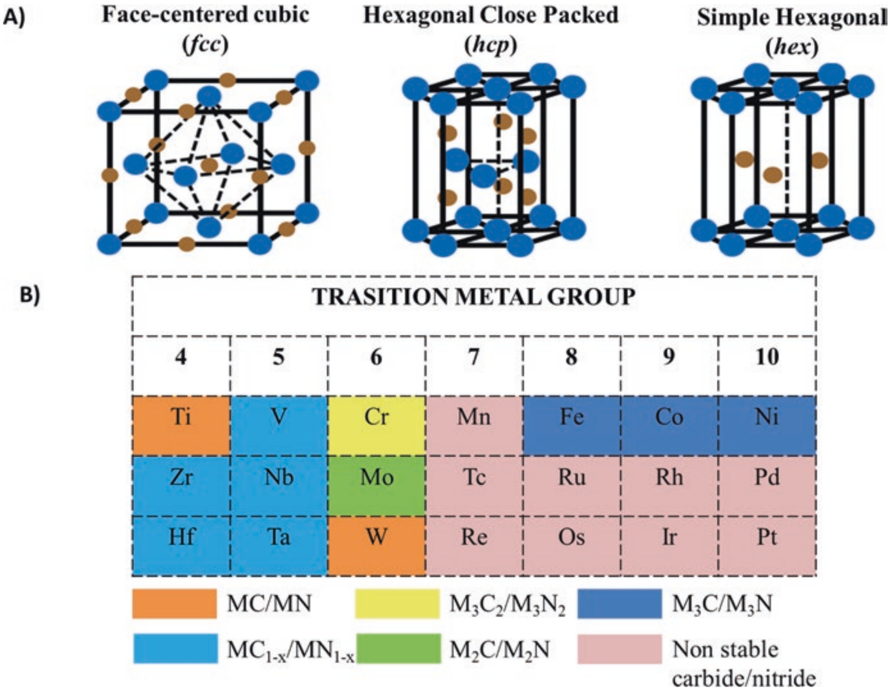

TRASITION METAL GROUP						
4	5	6	7	8	9	10
Ti	V	Cr	Mn	Fe	Co	Ni
Zr	Nb	Mo	Tc	Ru	Rh	Pd
Hf	Ta	W	Re	Os	Ir	Pt

Fig. 2.7 (**a**) Crystalline structures of TMC and TMN compounds. ● (Blue) = Metal; ● (Brown) = C o N. (**b**) TMC and TMN compound stoichiometry. Reproduced with permission of refs. [100–102]

2.2.3.1 Synthesis, Characterization, and Applications

Many methods have been developed for the synthesis of TMCs and TMNs, which can be used to obtain materials with different physical properties, such as high or low surface area. Also, bulk or supported materials can be prepared. For catalytic applications, usually high-surface-area materials are desirable, being prepared at moderate temperatures (see Table 2.3). Temperature-programmed reaction is a method that consists of the treatment of a precursor compound with a stream of reactive gas while increasing temperature uniformly (until around 700–800 °C). Oxides, sulfides, nitrides, or other compounds can be used as precursors in this method, while the reactive gas can be a mixture of a hydrocarbon (e.g., methane) and hydrogen in order to obtain carbides, and ammonia for obtaining nitrides. This reaction is usually carried out in a packed bed flow reactor with the precursor in the form of powder or pellets, using a program for temperature which enables to balance synthesis and sintering, giving products with high specific surface areas [25, 103–106]. A better control of textural properties (surface area and pore size distribution) and use of the active phase can be achieved by means of a support. Well-dispersed phases of carbides and nitrides have successfully been prepared by impregnation method to obtain oxidic precursors (as it was described earlier in Sect. 2.2.2) and then applying the temperature-programmed reaction method [15, 25, 103–107].

Table 2.3 Synthesis methods for obtaining TMCs and TMNs with low surface areas (adapted from ref. [108])

Reaction of metals or metallic compounds with reactive gases	Carbides	$M + 2C \rightarrow MC + CO_2$	Cr_3C_2, Mo_2C, TcC, Fe_3C, Fe_5C_2, Co_2C, Ni_3C
	Nitrides	$MO + NH_3 \rightarrow MN + H_2O + 1/2H_2$	Mo_2N, TiN, ZrN, HfN, VN, NbN, W_2N
Decomposition of metal halide vapors	Carbides	$MCl + H_xC_y \rightarrow MC + HCl + \ldots$	TiC, TaC, HfC
	Nitrides	$MCl + N_2/H_2 \rightarrow MN + HCl + \ldots$	TiN, VN, Re_2N, Fe_2N, Fe_4N, Cu_3N
Decomposition of metal compounds	Carbides	$W(CO)_n + H_xC_y \rightarrow WC + H_2O + CO$	HfC, VC, WC
	Nitrides	$Ti(NR_2)_4 + NH_3 \rightarrow TiN + \ldots$	TiN, Zr_3N_4
Temperature-programmed methods	Carbides	$MoO_3 + CH_4 + H_2 \rightarrow Mo_2C + \ldots$	Mo_2C, MoC_{1-x}, WC, WC_{1-x}, NbC
	Nitrides	$WO_3 + NH_3 \rightarrow W_2N + \ldots$	Mo_2N, MoN, VN
Utilization of high-surface-area supports	Carbides	$Mo(CO)_6/Al_2O_3 \rightarrow Mo_2C/Al_2O_3$	Mo_2C/Al_2O_3
	Nitrides	$TiO_2/SiO_2 \rightarrow TiN/SiO_2$	TiN/SiO_2
Reaction between metal oxide vapor and solid carbon	Carbides	$M + C \rightarrow MC$	Mo_2C, W_2C
	Nitrides	$M + 1/2N_2 \rightarrow MN$	CoN, Ni_3N_2, TiN, LaN

Furthermore, Volpe and Boudart [104] used the temperature-programmed reaction method to transform MoO_3 and WO_3 with NH_3 as a new path for the preparation of bulk Mo_2N and W_2N with high surface areas (220 and 91 m^2/g, respectively). They revealed that this transformation is topotactic, since the (1 0 0) planes of Mo_2N are parallel to (0 1 0) planes of the MoO_3, resulting in platelets of a highly porous nitride that is pseudomorph of the MoO_3. Later Boudart with Lee et al. [106] synthesized Mo carbide with a mixture or CH_4/H_2, starting from bulk MoO_3 and Mo_2N, obtaining β-Mo_2C (*hcp*; 50–100 m^2/g) and α-MoC_{1-X} (*fcc*; 200 m^2/g). These materials also exhibited pseudomorphism with precursors and topotactic changes. Later, Ramanathan and Oyama [109] prepared a series of Mo, W, V, Nb, and Ti carbides and nitrides by this method starting from metallic oxides and using CH_4/H_2 (20% v/v mixture) and NH_3 (100%).

Extensive studies regarding synthesis condition effect over active sites of these materials were carried out by Nagai and coworkers [110–114]. Nitriding temperature variations conduct to a distribution of species γ-Mo_2N, β-$Mo_2N_{0.78}$, metallic Mo and unreacted MoO_2. Low temperatures lead to high amounts of γ-Mo_2N. Increasing temperature promotes γ-Mo_2N transformation to β-$Mo_2N_{0.78}$ and metallic Mo. Also, it was noticed that the gaseous environment used during cooling to room temperature may affect product properties, since catalysts cooled in NH_3 resulted in a more active catalyst than that obtained when cooling with He. Surface properties of these materials are influenced by synthesis conditions [115], and it has to be taken into account that these materials are pyrophoric; thus, after their preparation, they must be passivated in a mixture that contains 1% or less of O_2 with a noble gas [116].

TMC and TMN have many technological applications due to their great strength and stability; they have been used as tools and they can handle severe conditions of temperature and pressure (for example in rocket nozzles). Also, they can perform optical, electronic, and magnetic functions [117–120]. These materials have also been proven to be good catalysts for ammonia synthesis, hydrogenation, Fischer-Tropsch, and reactions involving hydrogen adsorption, activation, and transfer, such as hydrotreatment reactions (HDN, HDS, and others) [104]. They have also been described to have similarities with noble metals and in some cases have resulted to be more active, selective, stable, and resistant to deactivation and poisoning [104].

Due to earlier described properties, they have been attracting attention in research and development for interesting applications in catalysis, electronics, and optics. In this chapter, specific applications as catalysts for hydrotreatment of model molecules and crude oil are discussed.

2.2.3.2 Applications as Catalysts for Hydrotreatment of Model Molecules and Crude Oil

Hydrotreatment is a process that involves different reactions and carries out the removal of S, N, and more, in the presence of hydrogen and an active catalyst. This process is widely used in the oil industry and other chemical processes. Recently, TMCs and TMNs have been considered as alternative catalysts for hydrotreatment since they are highly active and also resistant to high contents of S and N in feedstocks [16, 121–126]. Some efforts have been made to understand the active sites responsible for this behavior, most of them based on hydrogen adsorption ability [127, 128]. Also, particle size and temperatures have been considered for several authors to be determining for the adsorption-activation-transfer of hydrogen and catalytic performance of Mo and W carbides and nitrides. Noteworthy, in contrast to conventional sulfide-based catalysts, researchers have found that TMCs and TMNs with lower surface areas (large particle sizes) could lead to more active catalysts [122, 128]. Furimsky [116] discussed a mechanism proposed by Li and coworkers [129] for the adsorption activation and transfer of hydrogen over a surface of Mo nitride (due to an extensive availability of data for nitrides in contrast to carbides). This mechanism is summarized in Fig. 2.8.

First, heterolytic dissociation occurs over sites with Mo-N pairs, where blue box represents N deficiency in a surface Mo atom. It should be noticed that these deficiencies could be eliminated during passivation step and also be regenerated during reduction (or activation) with H_2. According to Nagai and coworkers [112, 113] Mo_2N prepared at high temperatures has low surface area and a high amount or N-deficient Mo atoms on the surface. In addition, Guerrero-Ruiz and colleagues [131] reported that hydrogen adsorption increases when particle size increases (and surface area decreases) in the same Mo nitride. On the other hand, high amount of surface Mo could lead to homolytic dissociation, obtaining Mo–H species, where hydrogen can be easily transferred to reactant molecules due to the low strength of the Mo–H bond. In this point, a migration of H into the subsurface and/or interstices can occur, motivated by the force of the N–H bond [122]. Similarly, this behavior could occur in the surface of Mo carbide since the bonding strengths of N–H and C–H are in the same range [132].

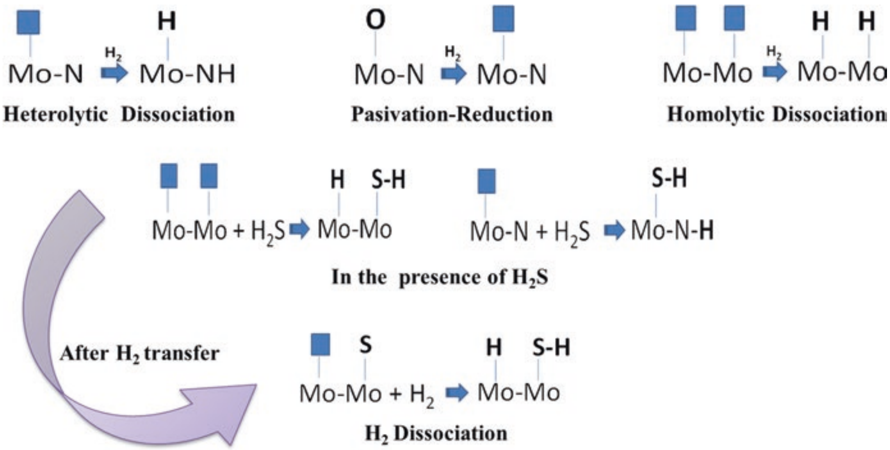

Fig. 2.8 Hydrogen activation and transfer over Mo nitride surface (adapted from refs. [116, 129, 130])

Moreover, TMC and TMN have shown interesting surface properties during hydrotreatment reactions, due to the presence (or formation) of H_2S, which have led to a surface modification obtaining a so-called sulfo-carbided or sulfo-nitrided species, showing good performances, as it was reported by several research groups [16, 133–135]. Additionally, MoS_2 slabs have been found in samples of passivated, presulfided and promoted carbides and nitrides as it was reported by Villasana et al. (see Figs. 2.9 and 2.10).

Scarcer information is available regarding the role of promoting metals in hydrogen adsorption, activation, and transfer over these materials. However, some studies have shown that promoted carbide and nitride catalysts have shown better performances than un-promoted compounds [136–139].

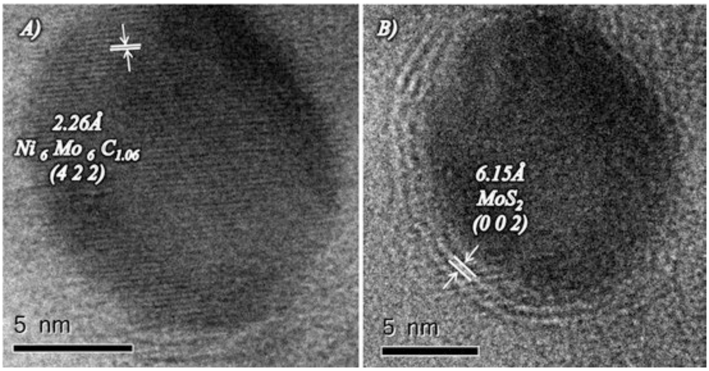

Fig. 2.9 HRTEM images of NiMo carbide (Ni/(Ni + Mo) = 0.33) after presulfiding: (**a**) NiMo carbide particle and (**b**) MoS_2 slabs coverage over NiMo carbide particle (reproduced from ref. [16])

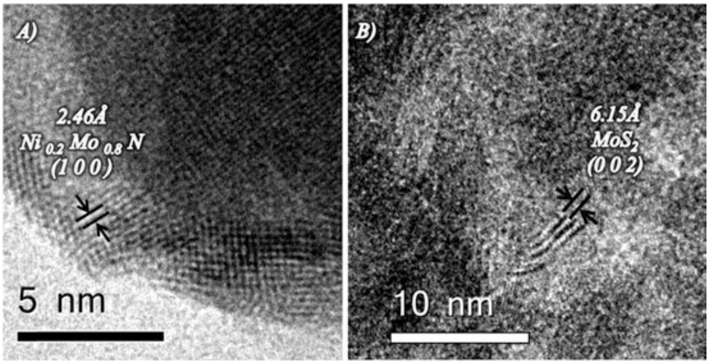

Fig. 2.10 HRTEM images of NiMo nitride (Ni/(Ni + Mo) = 0.33) after presulfiding: (**a**) NiMo nitride particle, (**b**) MoS_2 slabs in a particle agglomerate of particles in the NiMo nitride catalyst (reproduced from ref. [16])

Support role in the catalytic activity of these materials has yet to be investigated and it could be compared to earlier reports of transition metal sulfides, in terms of hydrogen migration, as it has been compared as a hydrogen reservoir [140, 141].

In these sense, Villasana [142] sustained earlier proposals of Furimsky [116], by also suggesting that during passivation process a surface monolayer of transition metal carbides and nitrides could be oxidized, and later, being sulfided (during a presulfiding step), thus being converted into MoS_2 and WS_2, based on results of XRD, ECA, SEM, and HRTEM analysis, and also thiophene HDS and crude oil hydrotreatment tests [15, 16, 143, 144]. Hence, it could have a key role in the activation and transfer of hydrogen to reactant molecules such as thiophene (model molecule) or asphaltenes (real feed), considering that both C and N attract hydrogen to the inside of particles, due to earlier mentioned C–H and N–H bond strengths, which could serve as hydrogen reservoir and promote catalytic performance. This was corroborated by the results almost simultaneously reported by Oliveira et al. [145] in which experimental and theoretical methods revealed the occlusion of hydrogen inside the bulk of Mo carbide during synthesis and reactivity tests.

TMC and TMN have been proven during hydrotreatment of diesel, light and heavy gas oil, and medium and extra-heavy crude oil, also with Carabobo crude oil (Venezuelan extra-heavy crude oil) and Maya crude oil (medium crude oil) showing good performances. Earlier reports revealed interesting results related to residue conversion, change in asphaltene and resin content and nature, sulfur and metal content, viscosity, API gravity, apparently due to cracking, HDS, and hydrogenation over these materials [16, 107, 142–144, 146–148].

Finally, due to their easy and low-cost synthesis method, transition from conventional catalysts to TMC and TMN catalysts could be done relatively quick, since they can be easily obtained by using common streams in the petrochemical industry (i.e., CH_4, H_2, and NH_3) and will also be suitable in an already installed industrial structure, since they have shown to be stable during severe conditions as industrial processes demand [109].

2.3 Summary and Conclusions

This chapter provides a summary of the synthesis of novel catalytic materials focused on titanate nanotubes and transition metal carbides and nitrides. Throughout the discussion, the primary objective has been to describe the forecasts and the method of synthesis to obtain innovative catalytic materials such as INTs, MOF, picnides, graphene, hierarchically porous materials, spinel oxides, hexaaluminates, composite oxides, and zeolites. The aims also included the aspects concerning the fundamental chemistry of precipitation, sol–gel, impregnation, and ion exchange, among other methods, for designing new catalytic materials. Among the INTs, special attention was given to the titanate nanotubes, whose unique properties allow them to be applied in a variety of catalytic processes, e.g., polymerization, photocatalytic activity, anodization, Knoevenagel reaction, oxidations, reduction of methyl orange, and acid-base and Cannizzaro reactions, and as as-synthesized catalysts or carriers. Also, the technical challenges of the synthesis that need to be overcome to enable the commercial deployment of future novel catalytic materials have been emphasized. Also, transition metal carbide and nitride synthesis, properties, and applications are discussed mainly focusing on their application in hydrotreatment reactions.

In conclusion, the consolidated methods of synthesis of catalytic materials are mature assessments, despite some remaining questions about the best method to develop the exact solid properties to attend the mechanism of a specific reaction. Interest in the use of inorganic "nanotubes," TMC and TMN appears to be increasing since these compounds are versatile as catalysts. Among the wide range of methods discussed for the TNTs, the hydrothermal treatment one is largely applied. Moreover, the TNTs are active selectives to the desired products and seem to have stability for some reactions due to their high specific surface area, redox and acid-base properties, and ion-exchange capacities. Nevertheless, there are still limitations in the industrial use of TNTs in catalytic process at severe conditions such as low recyclability, coking, and phase transformations. In order to overcome these drawbacks, efforts have been made in synthetic strategies based on the need to reduce total capital costs by developing processes with high product yields and conversions.

On the other hand, TMC and TMN are promising materials in the petroleum industry since they can accomplish several reactions over their non-fully understood active sites, and also some recent modifications of surface species (Mo and W sulfide slabs) and the incorporation of promoters (such as Fe, Ni, and Co) could enhance their performance in hydrotreating. This could lead to savings in operation and handling of heavy feedstocks in terms of time manageability, solvent consumption, catalyst poisoning, deactivation avoiding, and more, but there is still much work to do in the understanding of reaction mechanism and their physical and chemical surface behavior during hydrotreatment.

Acknowledgements The support by CNPq (473568/2012-8, 470793/2013-9) and CAPES/Funcap (23038.008860/2013-92) is greatly acknowledged. Also, Villasana wants to thank the technical support offered by Joaquín L. Brito, Franklin J. Méndez, and Yelisbeth Escalante from the Venezuelan Institute for Scientific Research and Edgar Cañizalez from PDVSA Intevep.

References

1. J. Wang, G. Cao, J. Domínguez, Advances in new catalytic materials, in *Advanced Materials Research*, ed. by J. Wang, G. Cao, J. Domínguez, (Trans Tech Publications, Stafa-Zurich, 2009), pp. 1–300
2. A. Corma, Preparation and catalytic properties of new mesoporous materials. Top. Catal. **4**, 249–260 (1997)
3. K. Wilson, A. Lee, M. Ecormier, D. Macquarrie, J. Clark, New catalytic materials for clean technology: structure-reactivity relationships in mesoporous solid acid catalysts, in

Nanotechnology in Catalysis, ed. by B. Zhou, S. Hermans, G. Somorjai, vol. 1, (Springer, New York, 2004), pp. 293–312

4. C. Pham-Huu, M.-J. Ledoux, Carbon nanomaterials with controlled macroscopic shapes as new catalytic materials. Top. Catal. **40**, 49–63 (2006)
5. K. Wilson, A.F. Lee, M.A. Ecormier, D.J. Macquarrie, J.H. Clark, *New Catalytic Materials for Clean Technology Structure-Reactivity Relationships in Mesoporous Solid Acid Catalysts*, vol 1 (Kluwer Academic/Plenum, New York, 2004), pp. 293–312
6. G. Busca, Heterogeneous catalytic materials: solid state chemistry, surface chemistry and catalytic behaviour, in *Heterogeneous Catalytic Materials: Solid State Chemistry, Surface Chemistry and Catalytic Behaviour*, (Newnes, Oxford, 2014)
7. G.L. Haller, New catalytic concepts from new materials: understanding catalysis from a fundamental perspective, past, present, and future. J. Catal. **216**, 12–22 (2003)
8. G.A. Gonzalez, M. Alvarado, M.A. Ramos, G. Berhault, R.R. Chianelli, Transition states energies for catalytic hydrodesulfurization reaction in Co9S8/MoS_2 theoretical interface using computer-assisted simulations. Comput. Mater. Sci. **121**, 240–247 (2016)
9. M. Ramos, G. Berhault, D.A. Ferrer, B. Torres, R.R. Chianelli, HRTEM and molecular modeling of the MoS2-Co9S8 interface: understanding the promotion effect in bulk HDS catalysts. Cat. Sci. Technol. **2**, 164–178 (2012)
10. M. Ramos et al., In-situ HRTEM study of the reactive carbide phase of Co/MoS_2 catalyst. Ultramicroscopy **127**, 64–69 (2013)
11. I.V. Parvulescu, E. Kemnitz, in New Materials for Catalytic Applications, vol 1 (Elsevier Amsterdam 2016) pp. 1–386
12. A. Tiwari, S. Titinchi, in Advanced Catalytic Materials, (Wiley & Sons, Inc. Hoboken, New Jersey, and Scrivener Publishing LLC, Salem, Massachusett 2015) pp. 1–446
13. ACS Publications. http://pubs.acs.org/action/doSearch?AllField=new+materials&target=default&targetTab=std&startPage=&dateRange=%3E. Accessed 20 May 2015
14. W. Moser *in* Advanced Catalysts and Nanostructured Materials (Elsevier, Amsterdam 1996) pp. 1–596
15. Y. Villasana et al., Atomic ratio effect on catalytic performance of FeW-based carbides and nitrides on thiophene hydrodesulfurization. Fuel **110**, 259–267 (2013)
16. Y. Villasana et al., Maya crude oil hydrotreating reaction in a batch reactor using alumina-supported NiMo carbide and nitride as catalysts. Catal. Today **220–222**, 318–326 (2014)
17. B. Dhandapani, T. St. Clair, S.T. Oyama, Simultaneous hydrodesulfurization, hydrodeoxygenation, and hydrogenation with molybdenum carbide. Appl. Catal. A Gen. **168**, 219–228 (1998)
18. J.M. Cameron, R.W. Hughes, Y. Zhao, D.H. Gregory, Ternary and higher pnictides; prospects for new materials and applications. Chem. Soc. Rev. **40**, 4099–4118 (2011)
19. L. Kőrösi, S. Papp, I. Dékány, Synthesis, structure, and photocatalytic activity of titanium dioxide and some of its surface-modified derivatives. L.Guczi, A. Erdôhely (eds). Catal. Altern. Energy Gener, 459–489 (2012). https://doi.org/10.1007/978-1-4614-0344-9
20. J.A. Schwarz, C. Contescu, A. Contescu, Methods for preparation of catalytic materials. Chem. Rev. **95**, 477–510 (1995)
21. J. Allouche, Synthesis of Organic and Bioorganic Nanoparticles: An Overview of the Preparation Methods, in *Nanomaterials*, (Springer, London, 2013). https://doi.org/10.1007/978-1-4471-4213-3
22. B. Grzybowska-Swierkosz, J. Haber, Chapter 11. Catalysis. Annu. Rep. Sect. C **91**, 395–439 (1994)
23. F.F. de Sousa et al., Nanostructured Ni-containing spinel oxides for the dry reforming of methane: effect of the presence of cobalt and nickel on the deactivation behaviour of catalysts. Int. J. Hydrog. Energy **37**, 3201–3212 (2012)
24. R.B. Levy, M. Boudart, Platinum-like behavior of tungsten carbide in surface catalysis. Science **181**, 547–549 (1973)
25. S.T. Oyama, Preparation and catalytic properties of transition metal carbides and nitrides. Catal. Today **15**, 179–200 (1992)

26. J. Ancheyta, M.S. Rana, E. Furimsky, Hydroprocessing of heavy petroleum feeds: Tutorial. Catal. Today **109**, 3–15 (2005)
27. J.K. Norskov, T. Bligaard, J. Rossmeisl, C.H. Christensen, Towards the computational design of solid catalysts. Nat. Chem. **1**, 37–46 (2009)
28. A. Kafizas, C.J. Carmalt, I.P. Parkin, CVD and precursor chemistry of transition metal nitrides. Coord. Chem. Rev. **257**, 2073–2119 (2013)
29. M.S. Rana, J. Ancheyta, S.K. Maity, P. Rayo, Heavy crude oil hydroprocessing: a zeolite-based CoMo catalyst and its spent catalyst characterization. Catal. Today **130**, 411–420 (2008)
30. X. Song, E. Yang, R. Ma, H. Chen, Y. Zhao, Sodium dodecyl sulfate-assisted synthesis of CoWO4 nanorods. J. Nanopart. Res. **10**, 709–713 (2008)
31. D. Astruc, Transition-metal nanoparticles in catalysis: from historical background to the state-of-the art, in *Nanoparticles and Catalysis*, (Wiley-VCH Verlag GmbH & Co. KGaA, Weinheim, 2008), pp. 1–48. https://doi.org/10.1002/9783527621323.ch1
32. R.D. Gonzalez, T. Lopez, R. Gomez, Sol–gel preparation of supported metal catalysts. Catal. Today **35**, 293–317 (1997)
33. D. Barkhuizen et al., Experimental approaches to the preparation of supported metal nanoparticles. Pure Appl. Chem. **78**, 1759–1769 (2006)
34. D.A. Ward, E.I. Ko, Preparing catalytic materials by the sol-gel method. Ind. Eng. Chem. Res. **34**, 421–433 (1995)
35. S. Li, J. Gong, Strategies for improving the performance and stability of Ni-based catalysts for reforming reactions. Chem. Soc. Rev. **43**, 7245–7256 (2014)
36. K. Omata, H. Mazaki, H. Yagita, K. Fujimoto, Preparation of nickel-on-active carbon catalyst by CVD method for methanol carbonylation. Catal. Lett. **4**, 123–127 (1990)
37. A. Magrez, J.W. Seo, R. Smajda, M. Mionić, L. Forró, Catalytic CVD synthesis of carbon nanotubes: towards high yield and low temperature growth. Materials (Basel) **3**, 4871–4891 (2010)
38. A.C. Oliveira, N. Essayem, A. Tuel, J.-M. Clacens, Y.B. Taarit, Studies on MeAPSO-5: an investigation of physicochemical and acidic properties. Catal. Today **133**, 56–62 (2008)
39. J. Livage, Sol–gel synthesis of heterogeneous catalysts from aqueous solutions. Catal. Today **41**, 3–19 (1998)
40. S. Tait, J. Tamis, B. Edgerton, D.J. Batstone, Anaerobic digestion of spent bedding from deep litter piggery housing. Bioresour. Technol. **100**, 2210–2218 (2009)
41. J. Geus, Production of supported catalysts by impregnation and (Viscous) drying, in *Catalyst Preparation*, (CRC Press, Boca Raton, 2006), pp. 341–372. https://doi.org/10.1201/9781420006506.ch15
42. Z. Guo et al., Recent advances in heterogeneous selective oxidation catalysis for sustainable chemistry. Chem. Soc. Rev. **43**, 3480–3524 (2014)
43. C.N.R. Rao, M. Nath, Inorganic nanotubes. Dalton Trans. **1–24**, (2003). https://doi.org/10.1039/B208990B
44. J. Haber, J.H. Block, B. Delmon, Manual of methods and procedures for catalyst characterization (Technical Report). Pure Appl. Chem. **67**, 1257–1306 (1995)
45. S.-Y. Lee, R. Aris, The distribution of active ingredients in supported catalysts prepared by impregnation. Catal. Rev. **27**, 207–340 (1985)
46. M. Behrens, Coprecipitation: an excellent tool for the synthesis of supported metal catalysts—from the understanding of the well-known recipes to new materials. Catal. Today **246**, 46–54 (2015)
47. M. Sunkara, M. Meyyappan, *Inorganic nanowires: applications, properties, and characterization* (CRC Press, Boca Raton, 2009). https://doi.org/10.1201/b13579-2
48. R. Tenne, Recent advances in the research of inorganic nanotubes and fullerene-like nanoparticles. Front. Physiol. **9**, 370–377 (2014)
49. N.M. dos Santos et al., Metal cations intercalated titanate nanotubes as catalysts for α,β unsaturated esters production. Appl. Catal. A Gen. **454**, 74–80 (2013)

50. A.R. Adini, M. Redlich, R. Tenne, Medical applications of inorganic fullerene-like nanoparticles. J. Mater. Chem. **21**, 15121–15131 (2011)
51. D.V. Bavykin, J.M. Friedrich, F.C. Walsh, Protonated titanates and TiO_2 nanostructured materials: synthesis, properties, and applications. Adv. Mater. **18**, 2807–2824 (2006)
52. R. Tenne, Inorganic nanotubes and fullerene-like nanoparticles. Nat. Nanotechnol. **1**, 103–111 (2006)
53. P. Nguyen, H.T. Ng, M. Meyyappan, Catalyst metal selection for synthesis of inorganic nanowires. Adv. Mater. **17**, 1773–1777 (2005)
54. I. Kiricsi et al., Synthesis, characterization and catalytic application of inorganic nanotubes. Stud. Surf. Sci. Catal. **130**, 1115–1120 (2000)
55. H. Nefzi, F. Sediri, Vanadium oxide nanotubes VOx-NTs: hydrothermal synthesis, characterization, electrical study and dielectric properties. J. Solid State Chem. **201**, 237–243 (2013)
56. S. Kim, M. Kim, S.-H. Hwang, S.K. Lim, Enhancement of photocatalytic activity of titania–titanate nanotubes by surface modification. Appl. Catal. B Environ. **123**, 391–397 (2012)
57. H. Chu, L. Wei, R. Cui, J. Wang, Y. Li, Carbon nanotubes combined with inorganic nanomaterials: preparations and applications. Coord. Chem. Rev. **254**, 1117–1134 (2010)
58. C.N.R. Rao, A. Govindaraj, F.L. Deepak, N.A. Gunari, M. Nath, Surfactant-assisted synthesis of semiconductor nanotubes and nanowires. Appl. Phys. Lett. **78**, 1853 (2001)
59. G. Tourillon, L. Pontonnier, J.P. Levy, V.L. Electrochemically, Synthesized Co and Fe nanowires and nanotubes. Electrochem. Solid-State Lett. **3**, 20 (1999)
60. M. Yada, M. Mihara, S. Mouri, M. Kuroki, T. Kijima, Rare earth (Er, Tm, Yb, Lu) oxide nanotubes templated by dodecylsulfate assemblies. Adv. Mater. **14**, 309–313 (2002)
61. B.A. Hernandez, K.-S. Chang, E.R. Fisher, P.K. Dorhout, Sol−gel template synthesis and characterization of BaTiO3 and $PbTiO_3$ nanotubes. Chem. Mater. **14**, 480–482 (2002)
62. A. Loiseau, F. Willaime, N. Demoncy, G. Hug, H. Pascard, Boron nitride nanotubes with reduced numbers of layers synthesized by arc discharge. Phys. Rev. Lett. **76**, 4737–4740 (1996)
63. A. Stojanovic, S. Olveira, M. Fischer, S. Seeger, Polysiloxane nanotubes. Chem. Mater. **25**, 2787–2792 (2013)
64. Y. Wang, A. Santos, A. Evdokiou, D. Losic, Rational design of ultra-short anodic alumina nanotubes by short-time pulse anodization. Electrochim. Acta **154**, 379–386 (2015)
65. J. Wu et al., Chemically controlled growth of porous CeO_2 nanotubes for Cr(VI) photoreduction. Appl. Catal. B Environ. **174**, 435–444 (2015)
66. H. Hu, Z. Jiao, J. Ye, G. Lu, Y. Bi, Highly efficient hydrogen production from alkaline aldehyde solutions facilitated by palladium nanotubes. Nano Energy **8**, 103–109 (2014)
67. Y.-H. Seo, S.-C. Han, S.-E. Park, Amino functionalized silica nanotube for base catalyzed reaction. Stud. Surf. Sci. Catal. **174**, 1081–1086 (2008)
68. T. Kasuga, M. Hiramatsu, A. Hoson, T. Sekino, K. Niihara, Titania nanotubes prepared by chemical processing. Adv. Mater. **11**, 1307–1311 (1999)
69. Y.-H. Lee et al., Synthesis of large-area MoS_2 atomic layers with chemical vapor deposition. Adv. Mater. **24**, 2320–2325 (2012)
70. T. Kasuga, M. Hiramatsu, A. Hoson, T. Sekino, K. Niihara, Formation of titanium oxide nanotube. Langmuir **14**(123), 160–3163 (1998). https://doi.org/10.1021/LA9713816
71. D.V. Bavykin, F.C. Walsh, P. O'Brien, H. Craighead, H. Kroto, *Titanate and Titania Nanotubes* (The Royal Society of Chemistry, London, 2009). https://doi.org/10.1039/9781849730778
72. A. Nakahira, T. Kubo, C. Numako, TiO_2-derived titanate nanotubes by hydrothermal process with acid treatments and their microstructural evaluation. ACS Appl. Mater. Interfaces **2**, 2611–2616 (2010)
73. P. Akhter, M. Hussain, G. Saracco, N. Russo, Novel nanostructured-TiO_2 materials for the photocatalytic reduction of CO_2 greenhouse gas to hydrocarbons and syngas. Fuel **149**, 55–65 (2015)
74. M. Myahkostupov, M. Zamkov, F.N. Castellano, Dye-sensitized photovoltaic properties of hydrothermally prepared TiO_2 nanotubes. Energy Environ. Sci. **4**, 998–1010 (2011)

75. H. Wang, S. Cao, C. Cen, X. Chen, Z. Wu, Structure–activity relationship of titanate nanotube-confined ceria catalysts in selective catalytic reduction of NO with ammonia. Catal. Lett. **143**, 1312–1318 (2013)
76. A. Elsanousi et al., Hydrothermal treatment duration effect on the transformation of titanate nanotubes into nanoribbons. J. Phys. Chem. C **111**, 14353–14357 (2007)
77. J. Edisson Morgado et al., Characterization of nanostructured titanates obtained by alkali treatment of TiO_2-anatases with distinct crystal sizes. Chem. Mater. **194**, 665–676 (2007). https://doi.org/10.1021/CM061294B
78. Y. Lan et al., Titanate nanotubes and nanorods prepared from rutile powder. Adv. Funct. Mater. **15**, 1310–1318 (2005)
79. B.C. Viana et al., Alkali metal intercalated titanate nanotubes: a vibrational spectroscopy study. Vib. Spectrosc. **55**, 183–187 (2011)
80. H. Li et al., Templated synthesis of TiO2 nanotube macrostructures and their photocatalytic properties. Nano Res. **8**, 900–906 (2015)
81. M. Kitano, K. Nakajima, J.N. Kondo, S. Hayashi, M. Hara, Protonated titanate nanotubes as solid acid catalyst. J. Am. Chem. Soc. **132**, 6622–6623 (2010)
82. A. Kleinhammes et al., Decontamination of 2-chloroethyl ethylsulfide using titanate nanoscrolls. Chem. Phys. Lett. **411**, 81–85 (2005)
83. S. Li et al., Protonated titanate nanotubes as a highly active catalyst for the synthesis of renewable diesel and jet fuel range alkanes. Appl. Catal. B Environ. **170**, 124–134 (2015)
84. K. Zhu, H. Gao, G. Hu, Z. Shi, A rapid transformation of titanate nanotubes into single-crystalline anatase TiO_2 nanocrystals in supercritical water. J. Supercrit. Fluids **83**, 28–34 (2013)
85. Y. Shi et al., Synthesis and characterization of TiO_2 nanotube supported Rh-nanoparticle catalysts for regioselective hydroformylation of vinyl acetate. RSC Adv. **4**, 62215–62222 (2014)
86. D.J.M. de Vlieger, L. Lefferts, K. Seshan, Ru decorated carbon nanotubes - a promising catalyst for reforming bio-based acetic acid in the aqueous phase. Green Chem. **16**, 864–874 (2014)
87. S.Y. Lee et al., Kinetics of styrene polymerization to syndiotactic polystyrene over metallocene catalyst on flat surface, silica nanotube reactors and porous silica particles. Macromolecules **44**, 1385–1392 (2011)
88. B. Zhu et al., Synthesis of metal-doped TIO_2 nanotubes and their catalytic performance for low-temperature co oxidation. React. Kinet. Catal. Lett. **88**, 301–308 (2006)
89. S.K. Parayil et al., Photocatalytic conversion of CO_2 to hydrocarbon fuel using carbon and nitrogen co-doped sodium titanate nanotubes. Appl. Catal. A Gen. **498**, 205–213 (2015)
90. P. Hernández-Hipólito et al., Novel heterogeneous basic catalysts for biodiesel production: sodium titanate nanotubes doped with potassium. Catal. Today **250**, 187–196 (2015)
91. D. Nepak, S. Darbha, Selective aerobic oxidation of alcohols over Au–Pd/sodium titanate nanotubes. Cat. Com. **58**, 149–153 (2015)
92. C.H. Campos et al., Immobilised chiral inducer on Pt-based mesoporous titanate nanotubes as heterogeneous catalysts for enantioselective hydrogenation. J. Mol. Catal. A Chem. **398**, 190–202 (2015)
93. Y. Wang, W. Liu, T. Wang, J. Ni, Arsenate adsorption onto Fe-TNTs prepared by a novel water–ethanol hydrothermal method: Mechanism and synergistic effect. J. Colloid Interface Sci. **440**, 253–262 (2015)
94. X. Sun, J. Zhang, G. Zhang, X. Pan, T. Huang, Preparation and characteristics of TiO_2 nanotube catalysts used in hybrid photocatalysis/membrane process. Cat. Com. **18**, 76–80 (2012)
95. F.-X. Xiao, Construction of highly ordered ZnO–TiO_2 nanotube arrays (ZnO/TNTs) heterostructure for photocatalytic application. ACS Appl. Mater. Interfaces **4**, 7055–7063 (2012)
96. G. Hägg, Gezetsmassigkeiten im Kristallbau bei Hydriden, Boriden, Karbiden und Nitriden der Ubergangselemente. Z. Phys. Chem. **12**, 33–56 (1931)
97. L. Brewer, A most striking confirmation of the Engel metallic correlation. Acta Metall. **15**, 553–556 (1967)

98. N. Engel, Copper, copper alloys and the electron concentration concept. Acta Metall. **15**, 557–563 (1967)
99. C.C. Yu, S. Ramanathan, F. Sherif, S.T. Oyama, Structural, surface, and catalytic properties of a new bimetallic V-Mo oxynitride catalyst for hydrodenitrogenation. J. Phys. Chem. **98**, 13038–13041 (1994)
100. Y. Zhong et al., Transition metal carbides and nitrides in energy storage and conversion. Adv. Sci. **3**, 1500286 (2016)
101. Y. Liu, T.G. Kelly, J.G. Chen, W.E. Mustain, Metal carbides as alternative electrocatalyst supports. ACS Catal. **3**, 1184–1194 (2013)
102. D.J. Ham, J.S. Lee, Transition metal carbides and nitrides as electrode materials for low temperature fuel cells. Energies **2**, 873–899 (2009)
103. J.S. Lee, S.T. Oyama, M. Boudart, Molybdenum carbide catalysts: I. Synthesis of unsupported powders. J. Catal. **106**, 125–133 (1987)
104. L. Volpe, M. Boudart, Compounds of molybdenum and tungsten with high specific surface area: I. Nitrides. J. Solid State Chem. **59**, 332–347 (1985)
105. L. Volpe, M. Boudart, Compounds of molybdenum and tungsten with high specific surface area: II. Carbides. J. Solid State Chem. **59**, 348–356 (1985)
106. J.S. Lee, L. Volpe, F.H. Ribeiro, M. Boudart, Molybdenum carbide catalysts: II. Topotactic synthesis of unsupported powders. J. Catal. **112**, 44–53 (1988)
107. Y. Villasana et al., Maya crude oil hydrotreating reaction in a batch reactor using alumina-supported NiMo carbide and nitride as catalysts. Catal. Today **220**, 318–326 (2014)
108. S.T. Oyama, Introduction to the chemistry of transition metal carbides and nitrides, in *The Chemistry of Transition Metal Carbides and Nitrides*, ed. by S. T. Oyama, (Springer, Netherlands, 1996), pp. 1–27. https://doi.org/10.1007/978-94-009-1565-7_1
109. S. Ramanathan, S.T. Oyama, New catalysts for hydroprocessing: transition metal carbides and nitrides. J. Phys. Chem. **99**, 16365–16372 (1995)
110. M. Nagai, Transition-metal nitrides for hydrotreating catalyst—synthesis, surface properties, and reactivities. Appl. Catal. A Gen. **322**, 178–190 (2007)
111. H. Tominaga, M. Nagai, Mechanism of thiophene hydrodesulfurization on clean/sulfided β-Mo_2C(0 0 1) based on density functional theory—cis- and trans-2-Butene formation at the initial stage. Appl. Catal. A Gen. **343**, 95–103 (2008)
112. M. Nagai, Y. Goto, O. Uchino, S. Omi, TPD study and carbazole hydrodenitrogenation activity of nitrided molybdena–alumina. Catal. Today **45**, 335–340 (1998)
113. M. Nagai, Y. Goto, O. Uchino, S. Omi, TPD and XRD studies of molybdenum nitride and its activity for hydrodenitrogenation of carbazole. Catal. Today **43**, 249–259 (1998)
114. M. Nagai et al., Temperature-programmed reduction and XRD studies of ammonia-treated molybdenum oxide and its activity for carbazole hydrodenitrogenation. J. Catal. **182**, 292–301 (1999)
115. Y.-J. Zhang, Q. Xin, I. Rodriguez-Ramos, A. Guerrero-Ruiz, Simultaneous hydrodesulfurization of thiophene and hydrogenation of cyclohexene over dimolybdenum nitride catalysts. Appl. Catal. A Gen. **180**, 237–245 (1999)
116. E. Furimsky, Metal carbides and nitrides as potential catalysts for hydroprocessing. Appl. Catal. A Gen. **240**, 1–28 (2003)
117. M. Erola, J. Keinonen, A. Anttila, J. Koskinen, TiN films prepared by nitrogen implantation on Ti-coated fused SiO_2. Sol. Energy Mater. **12**, 353–359 (1985)
118. C. Ernsberger, J. Nickerson, A. Miller, D. Banks, Contact resistance behavior of titanium nitride. J. Vac. Sci. Technol. A **3**, 2303–2307 (1985)
119. I. Suni, M. Maenpaa, M.A. Nicolet, M. Luomajarvi, Thermal stability of hafnium and titanium nitride diffusion barriers in multilayer contacts to silicon. J. Electrochem. Soc. **130**, 1215–1218 (1983)
120. M. Wittmer, Properties and microelectronic applications of thin films of refractory metal nitrides. J. Vac. Sci. Technol. A **3**, 1797–1803 (1985)
121. C.W. Colling, J.-G. Choi, L.T. Thompson, Molybdenum nitride catalysts: II. H2 temperature programmed reduction and NH3 temperature programmed desorption. J. Catal. **160**, 35–42 (1996)

122. J.-S. Choi, G. Bugli, G. Djéga-Mariadassou, Influence of the degree of carburization on the density of sites and hydrogenating activity of molybdenum carbides. J. Catal. **193**, 238–247 (2000)
123. J.-G. Choi, H.J. Lee, L.T. Thompson, Temperature-programmed desorption of H_2 from molybdenum nitride thin films. Appl. Surf. Sci. **78**, 299–307 (1994)
124. J.-G. Choi et al., Synthesis and characterization of molybdenum nitride hydrodenitrogenation catalysts. Catal. Today **15**, 201–222 (1992)
125. J. Ancheyta, Properties of catalysts for heavy oil hydroprocessing, in *Deactivation of heavy oil hydroprocessing catalysts*, (John Wiley & Sons, Inc., New Jersey, 2016), pp. 31–87. https://doi.org/10.1002/9781118769638.ch2
126. S.M. Hunter, *Molybdenum Nitrides: Structural and Reactivity Studies.* Ph.D. thesis (College of Science and Engineering, School of Chemistry, 2012)
127. K. Miga, K. Stanczyk, C. Sayag, D. Brodzki, G. Djéga-Mariadassou, Bifunctional behavior of bulk mooxny and nitrided supported nimo catalyst in hydrodenitrogenation of indole. J. Catal. **183**, 63–68 (1999)
128. S.T. Oyama, G.L. Haller, *Catalysis, Specialist Periodical Review*, vol 5 (Royal Society of Chemistry, London, 1982), p. 333
129. X. Li, Y. Chen, Y. Zhang, C. Ji, Q. Xin, Temperature-programmed desorption and adsorption of hydrogen on Mo_2N. React. Kinet. Catal. Lett. **58**, 391–396 (1996)
130. X.S. Li et al., Irreversible hydrogen uptake on Mo_2N catalyst. React. Kinet. Catal. Lett. **57**, 177–182 (1996)
131. A. Guerrero-Ruiz, Q. Xin, Y.J. Zhang, A. Maroto-Valiente, I. Rodriguez-Ramos, Microcalorimetric study of H2 adsorption on molybdenum nitride catalysts. Langmuir **15**, 4927–4929 (1999)
132. Z. Wei, Q. Xin, P. Grange, B. Delmon, TPD and TPR studies of molybdenum nitride. J. Catal. **168**, 176–182 (1997)
133. J.C. Schlatter, S.T. Oyama, J.E. Metcalfe, J.M. Lambert, Catalytic behavior of selected transition metal carbides, nitrides, and borides in the hydrodenitrogenation of quinoline. Ind. Eng. Chem. Res. **27**, 1648–1653 (1988)
134. E. Puello-Polo, J.L. Brito, Effect of the activation process on thiophene hydrodesulfurization activity of activated carbon-supported bimetallic carbides. Catal. Today **149**, 316–320 (2010)
135. E. Puello-Polo, J.L. Brito, Effect of the type of precursor and the synthesis method on thiophene hydrodesulfurization activity of activated carbon supported Fe-Mo, Co-Mo and Ni-Mo carbides. J. Mol. Catal. A Chem. **281**, 85–92 (2008)
136. Y. Li et al., The modification of molybdenum nitrides: the effect of the second metal component. Catal. Lett. **48**, 239–245 (1997)
137. E.J. Markel, J.W. Van Zee, Catalytic hydrodesulfurization by molybdenum nitride. J. Catal. **126**, 643–657 (1990)
138. J. Trawczyński, Comparison of HDS of dibenzothiophene and HDN of quinoline over supported Mo and CoMo nitrided and sulfided catalysts. React. Kinet. Catal. Lett. **69**, 293–298 (2000)
139. W. Yuhong, L. Wei, Z. Minghui, G. Naijia, T. Keyi, Characterization and catalytic properties of supported nickel molybdenum nitrides for hydrodenitrogenation. Appl. Catal. A Gen. **215**, 39–45 (2001)
140. M. Breysse, P. Afanasiev, C. Geantet, M. Vrinat, Overview of support effects in hydrotreating catalysts. Appl. Catal. **86**, 5–16 (2003)
141. M. Breysse, E. Furimsky, S. Kasztelan, M. Lacroix, G. Perot, Hydrogen activation by transition metal sulfides. Catal. Rev. Eng. **44**, 651–735 (2002)
142. Y. Villasana, *Carburos, Nitruros Y Sulfuros De Mo Y W Promovidos Con Fe, Co Y Ni, Y Su Aplicación Como Catalizadores En Hidrotratamiento De Crudos Pesados* (Venezuelan Institute for Scientific Research, Mérida and Zulia, 2014)
143. Y. Villasana et al., *Nanometric CoMo carbide and nitride as heavy oil hydroprocessing catalysts: application to an Orinoco Oil Belt crude* (NANOSUR, Miami, 2014)

144. Y. Villasana et al., Quality improvement of Carabobo heavy crude oil with Al_2O_3-supported CoW carbide and nitride nanoparticles, in International Material Research Congress (2016)
145. R.R. Oliveira Jr., A.S. Rocha, V. Teixeira da Silva, A.B. Rocha, Investigation of hydrogen occlusion by molybdenum carbide. Appl. Catal. A Gen. **469**, 139–145 (2014)
146. P. Da Costa, C. Potvin, J.-M. Manoli, B. Genin, G. Djéga-Mariadassou, Deep hydrodesulphurization and hydrogenation of diesel fuels on alumina-supported and bulk molybdenum carbide catalysts. Fuel **83**, 1717–1726 (2004)
147. V. Sundaramurthy, A.K. Dalai, J. Adjaye, Comparison of P-containing γ-Al_2O_3 supported Ni-Mo bimetallic carbide, nitride and sulfide catalysts for HDN and HDS of gas oils derived from Athabasca bitumen. Appl. Catal. A Gen. **311**, 155–163 (2006)
148. Y. Villasana, S. Ramírez, J. Ancheyta, J.L. Brito, Effect of hydrotreating reaction conditions on viscosity, API gravity and specific gravity of Maya Crude Oil, in *Computational and Experimental Fluid Mechanics with Applications to Physics, Engineering and the Environment*, ed. by L. D. G. Sigalotti, J. Klapp, E. Sira, (Springer International, New York, 2014), pp. 423–430. https://doi.org/10.1007/978-3-319-00191-3_28

Chapter 3
Theoretical Insights into the Electronic Structure and Catalytic Activity on MoS_2-Based Catalyst

Xiaodong Wen, Tao Yang, Manuel Ramos, Gabriel A. Gonzalez, and Russell R. Chianelli

3.1 Introduction

Hydrodesulfurization first came into practice during World War II in the production of petroleum. One of the biggest movements in recent legislation for reduction of sulfur in gasoline products was started by a speech at that time by the President of the United States Mr. William Jefferson “Bill” Clinton on May 1, 1999, at White House in Washington D.C. His announcement was to achieve 90% reduction of sulfur content in automobile gasoline in the United States by the year 2004 as suggested by Environmental Protection Agency (EPA), wherein parallel efforts were underway around the world by other nations like France, Germany, and the United Kingdom [1]. One can find more details about EPA document and environmental justification around this important environmental legislation decision. Additionally,

---

X. Wen (✉)
State Key Laboratory of Coal Conversion, Institute of Coal Chemistry Chinese Academy of Sciences, Taiyuan, China

Synfuels China Co. Ltd, Beijing, China
e-mail: wxd@sxicc.ac.cn

T. Yang
Beijing Advanced Innovation Center for Materials Genome Engineering, School of Computer Science, Beijing Information Science and Technology University, Beijing, China

M. Ramos
Department of Physics and Mathematics, Universidad Autónoma de Cd. Juárez, Juárez, Mexico
e-mail: manuel.ramos@uacj.mx

G. A. Gonzalez · R. R. Chianelli
Materials Research and Technology Institute, University of Texas at El Paso, El Paso, TX, USA
e-mail: gagonzalez3@miners.utep.edu; chianell@utep.edu

J. M. Domínguez-Esquivel, M. Ramos (eds.), *Advanced Catalytic Materials: Current Status and Future Progress*, https://doi.org/10.1007/978-3-030-25993-8_3

the document proposed for year 2004 to allow only 30 ppm of sulfur content in liquid fuels mainly gasoline and diesel, and furthermore to achieve a 10 ppm of sulfur content by year 2007. Now, as we have seen, fortunately the liquid fuel industry has reached that important environmental target; however the regulation continues to achieve even lower sulfur content mainly in liquid fuels.

For that particular reason the liquid fuel industry had used for more than three decades an alumina oxide-supported molybdenum disulfide catalyst, which is a chalcogenide transition metal sulfide used in operation conditions of 150–160 psi at hydrogen atmosphere and temperature ranges of 300–400 °C. The sulfur content in crude oil of 1–5% is reduced to 0.1% for final liquid fuel products and more likely the sulfur limits might be reduced to as low as 0.003–0.04%. Generally speaking, catalysts used in industry are derived from oxides of elements of group 6, such as Mo or W; group 9, such as Co; and group 10, such as Ni supported on different matrix high-temperature and -pressure materials and compounds, although one of most commonly used is alumina's oxides. The catalytic activity is related to the presence of sulfides of group 6 and group 9–10 elements having an important role of using some promoters, like nickel or cobalt, to enhance its catalytic activity. Along that particular direction, much effort has been devoted to research on both HDS activity and electronic structure of those MoS_2-based catalysts since 1920s, regarding which one can find many references in the scientific literature. In those mentioned reports, the main goal of understanding is the relationship of structure/function and active phases, exploring reaction mechanism and electronic structure of promoters (Co or Ni); the latter implies to apply several laboratory surface techniques and methods such as extended X-ray absorption fine structure (EXAFS), atomic force microscopy (AFM), high-resolution transmission electron microscopy (HREM), infrared spectroscopy (IRS), X-ray photoelectron spectroscopy (XPS), and temperature-programed reduction (TPR) among others. However, even with those mentioned and reliable experimental characterization techniques, still many questions had not been resolved about the chemistry and physical-chemistry of those catalytic TMS materials, because of high complexity during hydrogenation processes and in many cases a natural limitation of those characterization techniques, when compared to reaction operational conditions at liquid fuel industrial production.

In the past 22 years several computer-assisted theoretical approaches have been developed as a complement for standard experimental characterization tools, mainly applying a well-established density functional theory (DFT) approach. It is worth to mention that DFT had been highly used in condensed matter physics to determine electronic structure properties of solids, as well as in the pharmaceutical industry for design of novel health-related molecules; lastly a strong approach has been made with the aid of DFT in the material science field, causing DFT methods to be used as a computer-assisted characterization technique, to be able to achieve prediction on chemical reactions and deep understanding of electronic structure near the ground state at Fermi level. In this particular chapter, we discuss theoretical approximations completed on MoS_2-based catalyst in combination with experimental data. Specifically, geometrical stability of MoS_2, Co(Ni) promoted MoS_2, as well as carbide and oxide phase with a portion about HDS chemical mechanism description all based on DFT methods.

3.2 MoS_2 Catalyst Structure Prepared in Experiments

The preparation of hydrotreating catalysts can be done by a two-step pore volume impregnation procedure or by co-impregnation. In the sequential pore volume impregnation, γ-Al_2O_3 is impregnated with an aqueous solution of $(NH_4)_6Mo_7O_{24}$, followed by drying and calcination (heating in air). In a second step, the resulting material is impregnated with an aqueous solution of $Co(NO_3)_2$ or $Ni(NO_3)_2$ and dried and calcined. Alternatively, and preferentially used in the industry, all inorganic materials are co-impregnated, and the resulting catalyst precursor is dried and calcined. Several studies indicated that there are interactions between Mo and Ni or Co in the oxide state. Thus, it is known that the order of impregnation and calcination—first Mo and then Co or Ni or vice versa—plays an important role in the activity of the final sulfide catalyst. Catalysts in which the support is impregnated first with a solution containing Mo invariably have a higher activity. It has been suggested that the nickel or cobalt cations interact with the polymolybdate phase by forming a metal heteropolymolybdate [2]. The infrared absorption bands of NO adsorbed on Co-Mo/Al_2O_3 are shifted from those of NO on Co/Al_2O_3 [3], and Raman bands indicating polymeric molybdenum oxide species decrease in intensity with increasing the cobalt loading in an oxidic Co-Mo/Al_2O_3 catalyst [4]. These results suggest that nickel or cobalt cations interact especially with the most polymeric molybdenum oxide species to form species in which nickel or cobalt and molybdenum interact. The latter means that promoter cations stay near surface and close to the molybdenum cations and are positioned to chemically form a Ni–Mo–S bonding structure during sulfidation process. Additionally, the promoter ions interact to a lesser extent with the support and thus can be more chemically active after sulfidation.

After the impregnation, drying, and calcination steps, all oxide hydrotreating catalysts are formed; thus, hydrotreating catalysts need to be sulfide in a mixture of H_2S with one or more sulfur-containing compounds such as H_2S, CS_2, dimethyl disulfide, thiophene, and even elemental sulfur, depending on the preparation method; in some occasions oil fraction can be used for sulfidation purposes as well; this is called stabilization of the catalyst.

3.3 Electronic Structure of MoS_2-Based Catalysts

In 2000, Li et al. [5] for the first time studied geometrical structure and electronic states in MoS_2 clusters ($Mo_{27}S_{54}$) using computer-assisted ab initio approach as presented in Fig. 3.1. He was able to demonstrate that ab initio MO approaches were

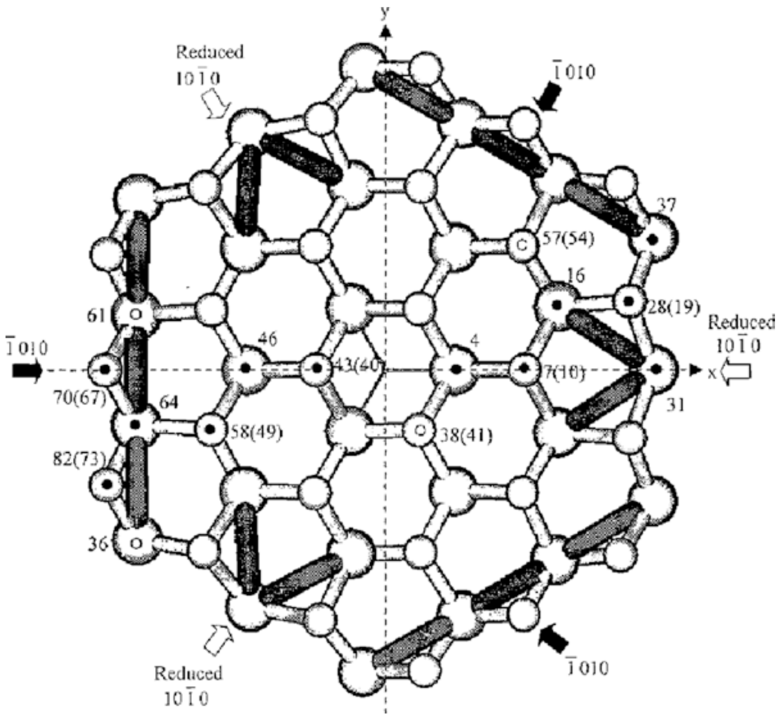

Fig. 3.1 The $Mo_{27}S_{54}$ cluster model (from ref. [6])

suitable to calculate electronic structure of the relatively large hexagonal MoS_2 clusters with average initial size (15–20 Å). The development when compared to other computer-assisted theoretical approaches is based on simplifying the molecular structural models, with different chemical bonds between Mo and S atoms along (001)-basal plane and in sulfur and molybdenum termination edges along the slab. Then the MoS_2 slab is relaxed toward the edges, having a twofold coordinately unsaturated sites (CUS) on corners with both electron-donating and -accepting properties, predicting those sites as ideal for hydrodesulfurization (HDS) (and HYD) reactions to occur. The twofold CUSs along edges (“reduced edges”) seem to allow only HYD reaction to occur or CO hydrogenation. Binding molecules along (001)-basal plane where majority of sulfur atoms are located requires high content of hydrogen species. The unreduced $\left(\bar{1}010\right)$ edges do not seem to be potentially active catalytically.

Lauritsen et al. [7] have proven combining both DFT theoretical calculations and experimentally that edges are responsible for catalytic reaction to occur, by mapping using scanning tunneling microscopy (STM) and correlating to metallic character near the edge of MoS_x nanoclusters, understanding that MoS_2 has a high band gap nature ~1.6–18 eV; thus, all clusters adopt their shapes according to the synthetic conditions, e.g., triangles under heavy sulfiding conditions or truncated

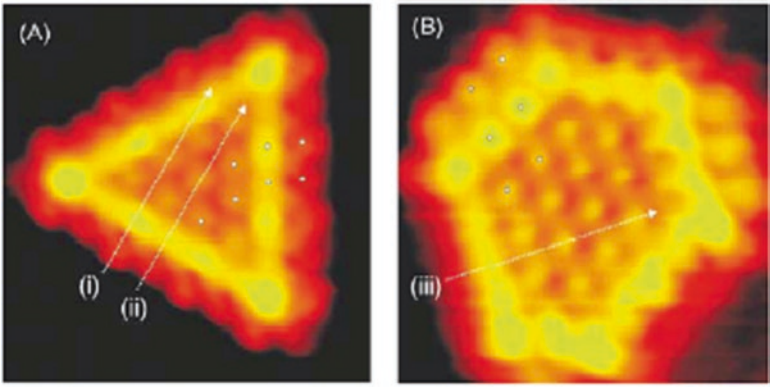

Fig. 3.2 The STM images of the triangular and hexagonal MoS_x cluster from Lauritsen et al. (taken from ref. [7])

hexagons under more sulfur-reductive conditions resembling HDS conditions as presented in Fig. 3.2.

Several theoretical models had been proposed to describe catalytic sites based on computer-assisted DFT calculations in MoS_x-based catalysts; Byskov et al. [6, 8, 9] used a chain model containing a single S–Mo–S slab constructed from two MoS_2 prisms, while Raybaud et al. [10–14], Cristol et al. [15–19], and Sun et al. [20] used larger models containing two S–Mo–S sheets exposing Mo and S edges alternatively. However, both the chain model and the two-sheet model are repeated periodically along directions perpendicular to the edge surfaces, and they represent real MoS_2 structures partially solely, when compared to HRTEM experimental observations, that can be attributed partially to its periodicity and large systems not able to hold on computer infrastructure at the time (less than 12 GB of RAM); in consequence all those models having corners and edges should be revised to make the approximation more close to real catalytic structures as observed under electron microscopy conditions. Nowadays, with the advances in hardware and computational resources available in national laboratories in the United States, Mexico, China, Canada, and Brazil, it is possible to migrate all the learned knowledge into more bigger systems as presented in the literature for Mo_2S_x [21, 22], a-Mo_3S_6 [23], b-Mo_3S_6 [24, 25], Mo_3S_9 [26], a-Mo_3S_{14} [24, 27], b-Mo_3S_{14} [24, 27], Mo_4S_{12} [28], Mo_5S_{10} [27], Mo_5S_{12} [29], Mo_6S_{14} [24], Mo_7S_{14} [28], Mo_9S_{18} [30], $Mo_{10}S_{18}$ [28, 31, 32], $Mo_{12}S_{24}$ [32–34], $Mo_{16}S_{32}$ [35, 36], $Mo_{18}S_{36}$ [32], $Mo_{19}S_{38}$ [24, 37], and $Mo_{27}S_{54}$ [5, 38], applying semiempirical methods [24–28, 31–33, 39, 40] and density functional theory methods [5, 29, 30, 34–38, 41].

In 2005, it was possible to predict systematically various MoS_x clusters that might have occurred under real hydroprocessing reaction conditions using computer-assisted thermodynamic approach and DFT as presented in Fig. 3.3 [39]. Our results indicate that when adding sulfur to Mo edges an exothermic reaction occurs; meantime, when removing sulfur S near the edge an exothermic reaction occurs for 67 and 50% sulfur coverages. On the free energy basis set along a wide range of H_2S/

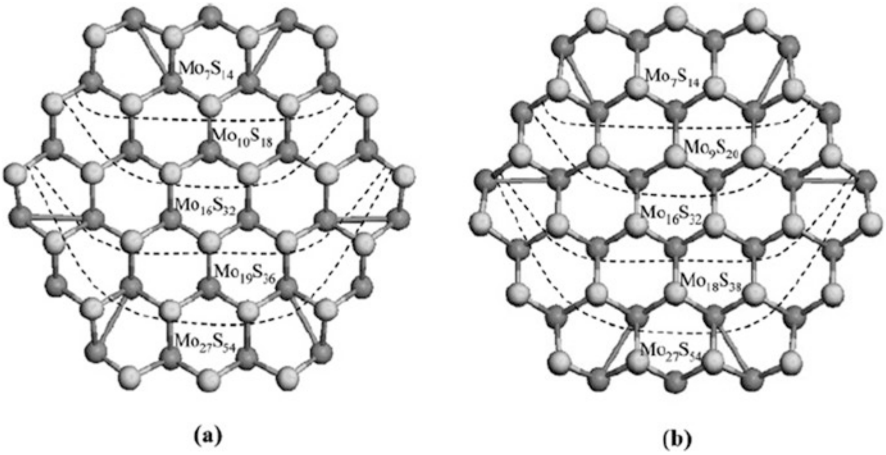

Fig. 3.3 MoS_x cluster models: (**a**) clusters with 0% sulfur coverage on the Mo edge (Mo_7S_{14}, $Mo_{10}S_{18}$, $Mo_{16}S_{32}$, $Mo_{19}S_{36}$, and $Mo_{27}S_{54}$); (**b**) clusters with 100% sulfur coverage on the S edge (Mo_7S_{14}, Mo_9S_{20}, $Mo_{16}S_{32}$, $Mo_{18}S_{38}$, and $Mo_{27}S_{54}$); image taken from ref. [39]

H_2 ratios, it was found that there are two stable structures with 33 and 50% sulfur coverages on the Mo edge by having 100% sulfur coverage on the S edge and one stable structure with 67% sulfur coverage on the S edge by having 0% sulfur coverage on the Mo edge. Under fully sulfiding atmosphere or at a very high H_2S/H_2 concentration ratio a triangular shape MoS_x structure exists with 100% sulfur coverage on Mo edge which is more stable than that with 100% sulfur coverage on S edge; this was confirmed in agreement with scanning tunneling microscopy experimental techniques.

Moreover, cluster models are based on periodic crystals as shown in Figs. 3.2, 3.3, and 3.4. Raybaud et al. [10, 11] and Cristol et al. [16] investigated the equilibrium sulfur coverage on MoS_x edge surfaces, and found that sulfur atoms bind more strongly to molybdenum atoms at S edge than at Mo edge; this indicates that those sites are energetically unfavorable to obtain a sulfur coverage lower than 50% in MoS_x edge surfaces. Although it is possible to determine the energy and electronic structure of Mo edge and S edge using chemical potentials of sulfur, these models are not possible for the energy calculation of Mo edge or S edge independently, because one calculation for periodic systems always yields an average surface energy for both types of edges; in order to overcome that Schweiger et al. [40] calculated surface energies of the individual edges of MoS_2 single-layer sheets using large cluster models, and demonstrated that Mo edge is energetically the most stable surface under realistic HDS conditions. His numerical computer-assisted calculations simulate Mo edge or S edge independently, but were not possible to show any interaction between Mo and S edges in those cluster models, and results exhibit only one type of edge in triangular shaped clusters with 0%, 50%, and 100% sulfur coverage.

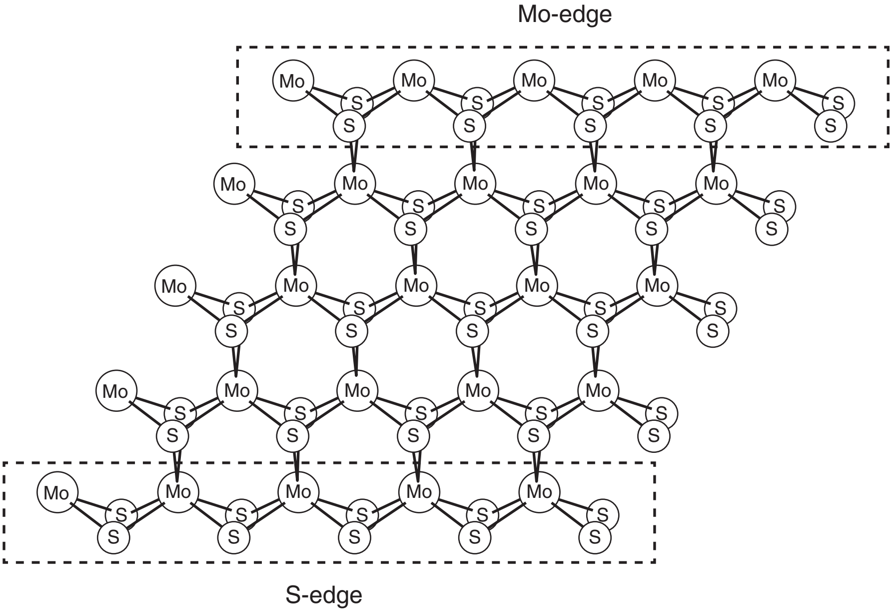

Fig. 3.4 The single layer of S–Mo–S slab models; image taken from ref. [40]

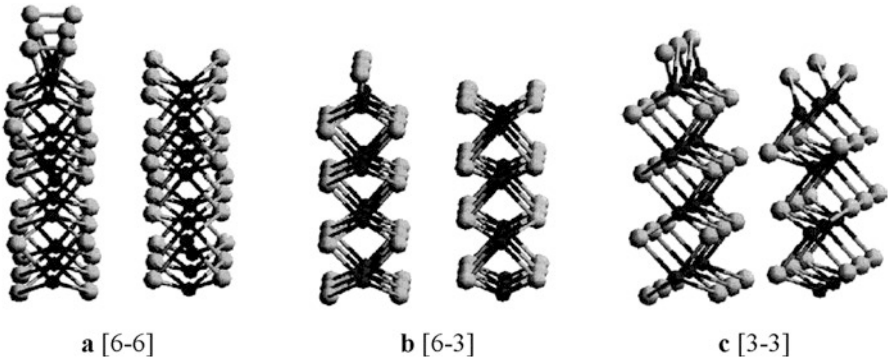
a [6-6] **b** [6-3] **c** [3-3]

Fig. 3.5 The two-layer S–Mo–S slab models; image adapted from ref. [39]

A significant advantage when using periodic cluster models as shown in Fig. 3.5 to study MoS_2 surface is low computation cost when making those computations for large MoS_x periodic systems; in other words, this can be attributed to study one portion considering as a seed for the complete system. Nonetheless, one need to stay that highly dispersed supported MoS_x catalysts can have a predominant sizes close to 10–30 Å [39, 41, 42], indicating that there should be two, three, or four Mo atoms (or S pairs) on a corresponding edge plane, and the electronic properties of each Mo atom (or S pairs) at different positions of the edge planes should be different [33].

3.4 Electronic Structure of Cobalt and Nickel MoS_2 Catalysts

The so-called promoted catalytic MoS_2- or WS_2-based materials are used to be distributed on a high-surface-area alumina supports in nanoscaled particle form. It has been established that MoS_2 crystallites present an average size in the order of ~2–3 nm. Besides, theoretical and experimental evidence has shown that when Co or Ni is added into MoS_2 preparation a new electronic structure phase is formed coined by others as "NiMoS" or "CoMoS" causing then an increase of catalytic reactivity; however, just a small fraction of Co or Ni relative to Mo can be added in terms of *Goldilocks* as stated in Chap. 1 (Fig. 1.10), meaning too much promoter can lower catalytic HDS activity and poor quantities of promoters can enhance the catalytic activity to a great extent, when compared with pure MoS_2 crystallites.

One can find in the literature few studies about the location of promoters into the MoS_2 molecular structure with active phases in catalysts to its reactivity [43, 44] and experimental evidence indicates that Co is located along sulfur or molybdenum edge causing a brim site effect (more metallic edges) as described by Lauritsen et al. and presented in Fig. 3.6 [45].

In terms of electronic structure and catalytic reactivity the so-called Co–Mo–S phase is one of the most interesting to study due to its high application in real industrial catalyst and competes highly with other commercial formulas such as NEBULA and STARS developed by Exxon research laboratories during 1990s. The Co–Mo–S phase is nonstoichiometric with respect to the Co/Mo ratio, and no unit cell can be defined in the crystallographic meaning. For instance in un-promoted MoS_2 systems, it is well known that just sulfur termination edges are responsible for catalytic HDS to occur; thus achieving a homogeneous cobalt promotion is important during chemical synthesis. However, the precise origin of electronic structure remains certainly unclear for other types of morphological configuration, meaning, nanotubes, spheres, or aggregate Co-MoS_2 clusters. On the other hand, one can find just a few structural studies to describe nickel-promoted systems; some authors indicate that Ni–Mo–S phase has a similar structural molecular composition as Co–Mo–S, but there is low experimental information available confirming that.

With the aid of density functional theory methods it was possible to depict the interaction between cobalt sulfide (Co_9S_8) and molybdenum disulfide (MoS_2) as observed experimentally with the usage of HRTEM instrument [46]. Ramos et al. were able to address an old question about this mixed Co_9S_8/MoS_2 phase as formed during hydrothermal synthesis from thiomolybdate salts; their findings were to determine a epitaxial contact between MoS_2 edge and (111)-Co_9S_8 creating what they have referred to as catalytical interface presented in Fig. 3.7. The following question to answer once the model was proven and accepted in the scientific community is to understand the possible catalytic sites proposing three different

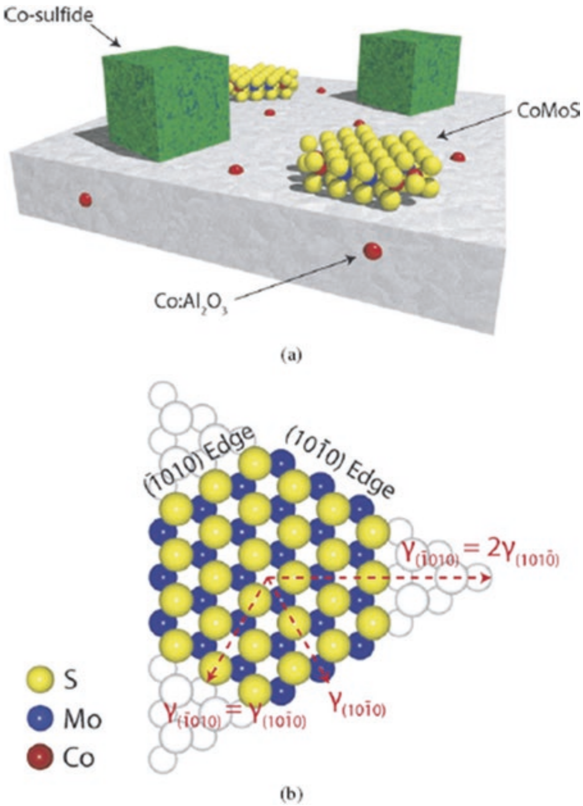

Fig. 3.6 Schematic drawing to depict the location of cobalt and nickel promoters. *Top*: MoS_2 crystallites dispersed over alumina oxide support. *Bottom*: MoS_2 single slab indicating sulfur and molybdenum termination edges (image adapted from ref. [45])

locations: sulfur–sulfur (S, S) sites, molybdenum–sulfur (Mo, S), and molybdenum–molybdenum (Mo, Mo) to made a theoretical DFT-based study about transitional states for one complete HDS reaction of dibenzothiophene model molecule; in their findings it was possible to reveal that (S, S) edge site was the most active adsorption of DBT molecule in consequence of removal of sulfur content. The most important characteristic about Gonzalez et al.'s study is to use Halgren-Lipscomb DFT-based algorithm to determine theoretically new ways to understand the Co_9S_8/MoS_2 bulk phase [45] as presented in Fig. 3.8 and later another study also by Gonzalez et al. reflected the effect of stacking height of MoS_2 slabs over (111)-Co_9S_8 [47], also presented in Fig. 3.9. Those numerical transitional state computations mainly to understand hydrogen activation and stacking height effect (layers (n), $1 < n < 4$) in Co_9S_8/MoS_2 interface model were carried out to determine overall hydrogenation energies, a one-step process that occurs during HDS reaction, and passivation or activation of the catalytic material under testing, in our case study, focused solely on molybdenum-based catalyst.

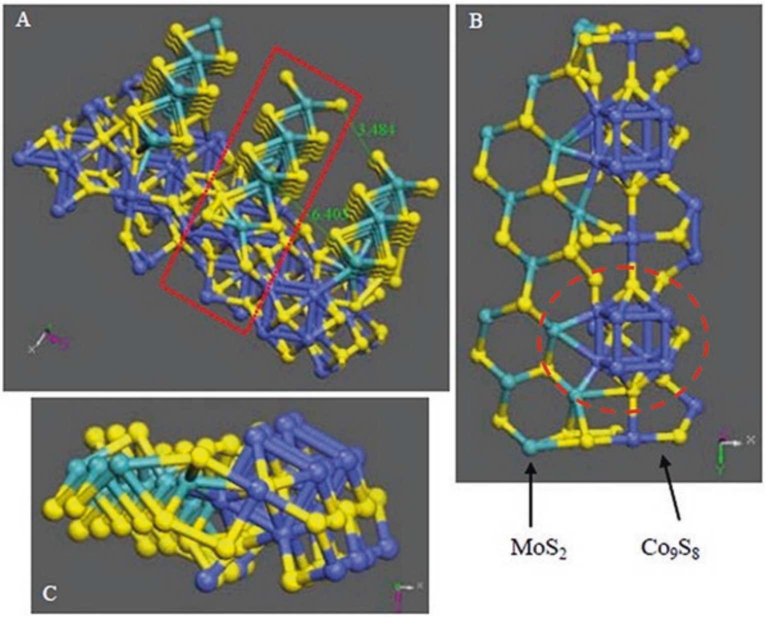

Fig. 3.7 (**a**) The resulting model interface between the layered MoS_2 (010) plane and the Co_9S_8 (111) plane. The atoms are colored as follows: cobalt (blue), sulfur (yellow), and molybdenum (green); (**b**) portion of the interface called “seed” from red dashed line used for DFT calculations; (**c**) the side view for the model; one can observe a direct bonding between cobalt and molybdenum atoms, causing an electronic donation as indicated from band structure plots as described in detail in ref. [46] (image adapted from ref. [46])

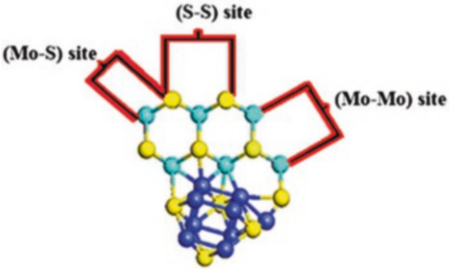

Fig. 3.8 Portion used from MoS_2/Co_9S_8 considered as a “seed model” to perform all Halgren-Lipscomb transitional state numerical DFT computations. Sulfur atoms (yellow color), molybdenum atoms (turquoise color), and cobalt atoms (blue color) (image adapted from ref. [45])

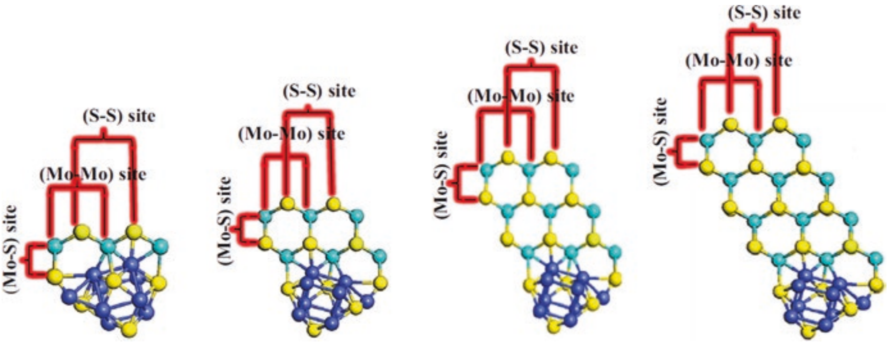

Fig. 3.9 Molecular representation of stacking height effect from MoS_2/Co_9S_8 bulk interface used for hydrogen activation transitional state energy calculations, as described in detail in ref. [47] by Gonzalez et al. (image adapted from ref. [47])

3.5 Electronic Structure of Carbide and Oxide MoS_2 Catalysts

When MoS_2-based catalysts undergo real hydroprocessing working conditions its electronic structure becomes more complex, due to its direct exposition to high temperature, pressure, and organic compounds, as contained in crude oil. One of the problems found in fresh catalyst is its stability after first 10 h of operation conditions, which is caused by carbonaceous species that “clog” the active sites during hydrotreating. In 1982, Hallie et al. found an enhanced activity in HDS and HDN conversion of a vacuum gas oil by using CS_2 instead of H_2/H_2S as the sulfiding agent and early evidences for the structural carbon were proposed by Chianelli and Pecoraro [48, 49]; ruthenium disulfide (RuS_2) catalyst stabilized at 1000 h of operation conditions in pilot plant; their conclusions exhibited a carbide-phase $RuS_{2-x}C_x$ having carbon atoms attached or replacing sulfur atoms near edge or surface, as depicted in Fig. 3.10. Moreover, Seiver and Chianelli [50] showed that layered transition metal sulfides such as MoS_2 and WS_2 catalysts can be carburized phase during stabilization at operation conditions, in occasions indicating activation of hydrotreating catalysts can occur in presence of crude oil more efficient than in gas-phase procedure. Hallie [51] has shown a strong dependency of the HDS activity on the nature of the sulfiding agent (RSH, $CH_3–S–S–CH_3$, and CS_2), which is in agreement also with Chianelli and Pecoraro [48, 49] who found that the catalyst activity by using $(NR_4)_2MoS_4$ (R = alkyl group) as the precursor for catalyst preparation was higher than that by using ammonium heptamolybdate $(NH_4)_6Mo_7O_{24}$. Later, Kasztelan [52] suggested that replacing sulfur atoms at MoS_2 crystallite edges by carbon can be confirmed using EXAFS techniques by crystallographic determination, which allowed Chianelli and Berhault [53] to propose a molybdenum carbide phase as an important factor for the stability of active catalysts.

Fig. 3.10 Schematic representation of carbide phase in MoS_2, presented by Chianelli and Pecoraro (image adapted from ref. [48])

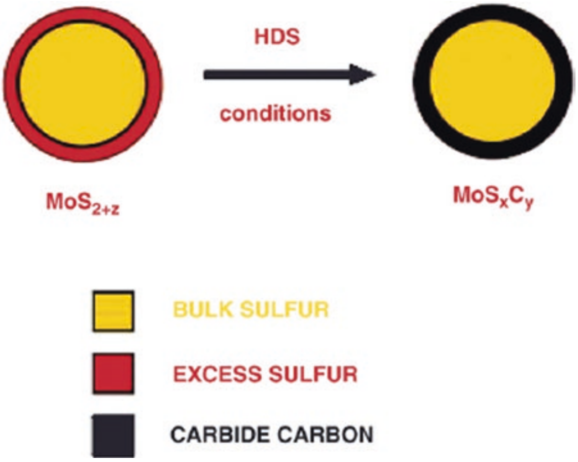

Furthermore, based on the existence of carbide phase in MoS_x catalyst it was possible to carry out DFT numerical calculations by replacing carbon atoms over sulfur surface in Mo edge and S edge as well as in bulk phase as presented in Fig. 3.11 [54]; proposed models were subjected to geometrical optimization and binding energy computations, leading to the determination that carburization process is more favorable than sulfidation in fresh catalysts. In sulfur surface having different coverage, carbon replacement was found to be easier, over sulfur atoms, and formation of CS and C_2 bridging units. In contrast, the replacement of carbon at Mo edge containing sulfur-binding atoms was least energetically favorable; this concludes an endothermic sulfidation of transition metal sulfides [55].

Furthermore, we have carried out systematic, similar approach to determine any oxidation process over sulfur surface at molybdenum edges and sulfur edges using MoS_x molecular slab; a complete description is shown in Fig. 3.12 [56], where it was possible to determine its thermodynamic stability; when comparing these oxidation processes on surfaces, our results indicated that oxidation over a 100% sulfur edge and 50% coverage is more favorable to happen than at molybdenum edges, due to sulfur electronic affinity to accept-donor electronic charge to oxygen species. The latter proves there are no evidence on the effects of coverage in oxidation over sulfur edges, also our study indicate that oxidation over corner sites is more likeable to occur than over line made of sulfur edges. Furthermore, when comparing this oxidation process with carburization processes on similar surfaces, it was found that oxidation is energetically feasible to happen than carburization defined by binding energy results, as described in Fig. 3.12.

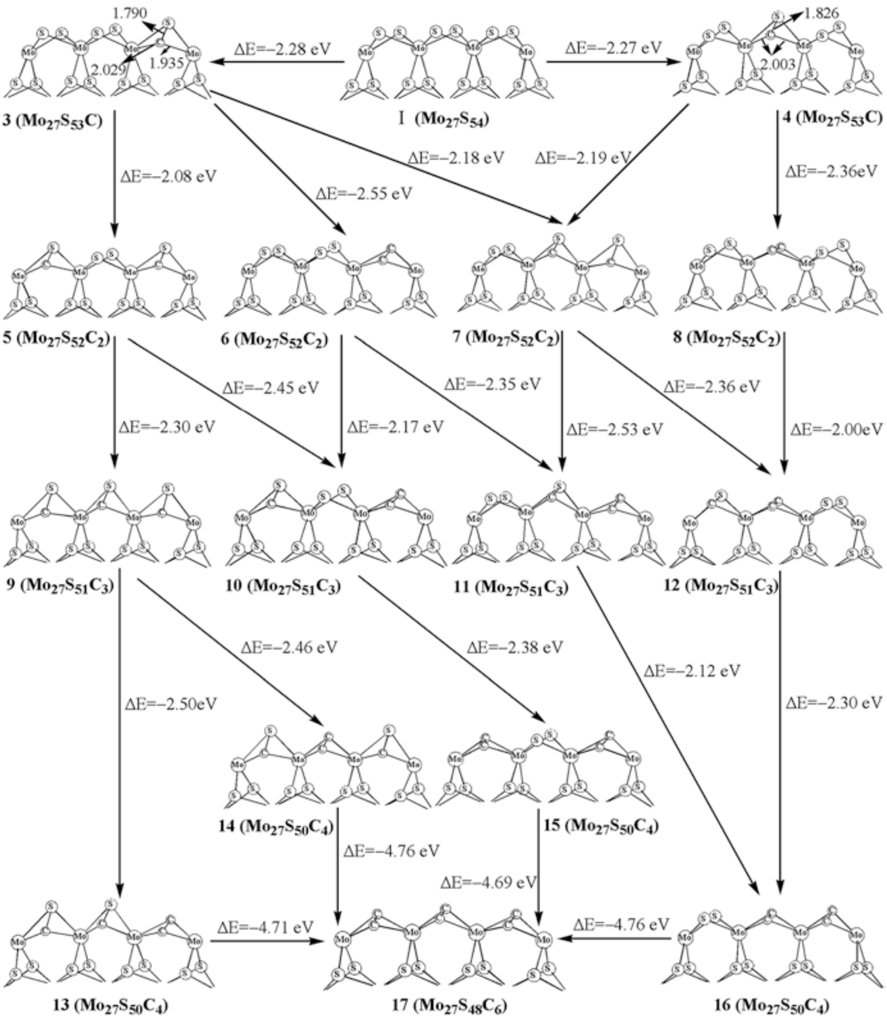

Fig. 3.11 Schematic representation of carbon replacement over S edge in MoS_2 molecular model (image adapted from ref. [54])

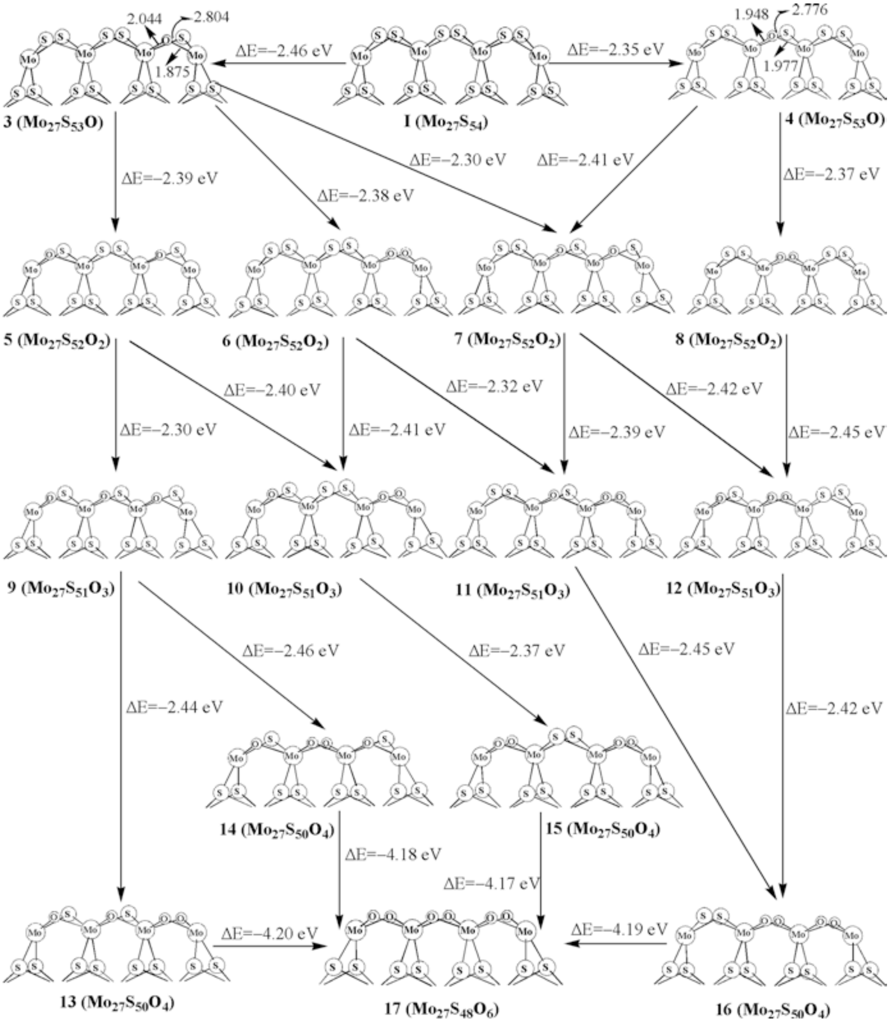

Fig. 3.12 Complete computer-assisted DFT calculations for oxidation steps over sulfur edge with 100% sulfur coverage in MoS_2 slab molecular model (image adapted from ref. [56])

3.6 Computer-Assisted Reaction Coordination of Organic Molecules at MoS_2 Catalyst

3.6.1 DFT Calculations for Hydrogen Adsorption in MoS_2 Catalyst

There is experimental evidence indicating that MoS_2 consumes large quantities of hydrogen H_2 [57–59] during the operation HDS conditions, causing in many cases the complete operation of liquid fuel production to exceed budgeting limitations. The dissociation process of H_2 and the states of the adsorbed hydrogen on MoS_2 until now are certainly unclear; it is possible to find in the literature two fundamental H_2 dissociation schemes: (1) heterolytic dissociation over sulfur vacancies to yield Mo–H and Mo–SH species and (2) homolytic dissociation over disulfide groups to form Mo–SH groups [60]. In both cases, one computer assisted is found in the literature for molecular coordinated complexes over (100)-MoS_2 and compared with experimental evidence from EXAFS and TPR techniques presented by Cristol et al. [16].

Other studies made an effort to determine the heterolytic character dissociation of H_2 in surfaces of metal sulfides (MoS_2, NiS_x, and RuS_2) with the formation of metal hydrides and –SH groups [62, 63]. In Cristol et al. findings indicate that most stable surface does not contain any coordinated unsaturated sites (CUS), and that all heterolytic dissociation of H_2 forming Mo–H and –SH is always endothermic without formation of new CUS over sulfur or molybdenum surface edges [16]. Travert et al. determined an ability to dissociate H_2 over surface which depends on the metallic nature of Mo atom and coordination environment [17]; also Byskov et al. studied hydrogen dissociation over edges composed by Co promoted on MoS_2 slab, and found that sulfur atoms at those edges can move up to extract one hydrogen atom from the dissociating H_2 and transport it to the other side of the slab where it diffuses on, in agreement with similar model reaction as proposed by Bollinger et al. [64, 65], who also studied electronic states, in their particular cluster model stating that dissociation and transfer as well formation of CUS, as it was also computer by us on $Mo_{27}S_{54}$ cluster using similar density functional theory methods as shown in Fig. 3.13, our model two different sites constituted by sulfur and molybdenum edges for hydrogen adsorption are consider, in adsorption and relative energies we have revealed that homolytic dissociation over sulfur edge having a S–H group and heterolytic dissociation occurs with intersection of Mo and S edges forming –SH and/or Mo–H bonds are more thermodynamically stable, our computation for vibrational frequencies of S–H are in full agreement with experimental data [66].

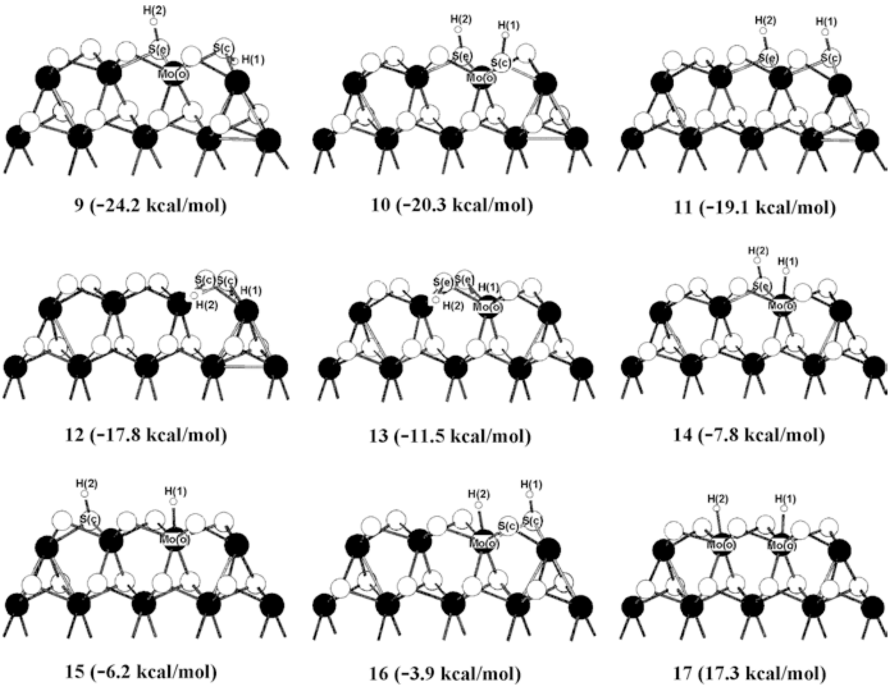

9 (−24.2 kcal/mol) **10 (−20.3 kcal/mol)** **11 (−19.1 kcal/mol)**

12 (−17.8 kcal/mol) **13 (−11.5 kcal/mol)** **14 (−7.8 kcal/mol)**

15 (−6.2 kcal/mol) **16 (−3.9 kcal/mol)** **17 (17.3 kcal/mol)**

Fig. 3.13 Theoretical description used for DFT computations of hydrogen H_2 adsorption over S edge in MoS_2 slab molecular model (image adapted from ref. [66])

3.6.2 DFT Computations for Organic Molecules with Sulfur Content Over MoS_2 Catalyst

The organic chemical composition of crude oil contains large amounts of complex organic molecules containing sulfur and other heterogeneous atoms (oxygen, nickel, vanadium, iron, among others). For that particular reason, it is important to apply computer-assisted DFT numerical simulations to the adsorption of most sulfur compounds such as R–SH, R–S–R, thiophene, and DBT. Experimental efforts have been dedicated to target the complex understanding of adsorption/desorption during HDS process. Usually an agreement was stated to name those sulfur content molecules as non-heterocycles and heterocycles. Heterocycles are mainly composed of thiophenes with one to several aromatic rings and their alkyl or aryl substituents like thiophene, BT, DBT, and 4,6-DMDBT. And it is found in the literature poor information and studies about non-heterocycle sulfur molecules over MoS_2-based catalysts. To achieve theoretical understanding of heterocycles in sulfur content molecules, thiophene has been widely used as a molecular model for HDS due to its electronic structure stability during DFT computations and direct comparison with laboratory HDS experimental batch reactions [12, 28, 30, 67–72]. One typical catalyst used during HDS test is Al_2O_3-supported molybdenum catalysts promoted either with cobalt or nickel; however, when attempting to compare computer-assisted DFT calculations in that particular system it becomes highly complicated due to alumina support matrix, along with location of adsorbed molecules over MoS_2 slab catalyst model. However, some studies about adsorption of BT and DBT molecules are using computer-assisted DFT theoretical framework presented in the literature, as it is done by Yang et al. [31, 32] who studied adsorption of various methylated DBT derivatives over molybdenum edge in $Mo_{10}S_{18}$ and Gonzalez et al. [47] who studied the Co_9S_8/MoS_2 interface model; in both cases the differences among substituted, non-substituted, and hydrogenated derivatives only rely on molybdenum edges in agreement with Cristol et al. [19] who applied similar approach.

3.7 Conclusion

In conclusion, from the studies made as well as information and data as found in the literature it was possible to determine that by applying computer-assisted numerical simulations which are based on density functional theory mathematical framework it is possible to determine electronic structure and other catalytic properties near the equilibrium conditions at Femi level using molecular models for MoS_2- and cobalt/nickel-promoted and oxide and carbide catalytic systems. Results indicate that those numerical simulations in many occasions can be directly correlated to experimental data as found by extended X-ray absorption fine structure (EXAFS), atomic force microscopy (AFM), High-resolution transmission electron microscopy (HREM), infrared spectroscopy (IRS), X-ray photoelectron spectroscopy (XPS), and temperature-programed reduction (TPR) techniques. Lastly, one can recognize that the future of DFT computer-assisted simulations is to use large systems (more than 40 atoms), mainly with the aid of high-performance computing (HPC) as currently available in national laboratories worldwide, and also that commercial code and open access code have been improved to make those calculations more reliable, applying norm-conserving and ultrasoft pseudopotentials (local density approximation plus Hubbard LDA+U) and general gradient approximation (GGA) in plane-wave basis sets to treat the systems as periodic boundary conditions or localized isolated cluster species, when computing crystal geometrical structure, vibrational frequencies, and magnetic moments in orbital coupled electronic configurations. For more discussion about basis set and numerical approximations, we recommend the reader a comprehensive textbook by Richard M. Martin entitled: "Electronic Structure: Basic Theory and Practical Methods" (ISBN-13: 978-0521534406) [73].

References

1. http://www.epa.gov/region04/oeapages/intergov/sg060499.htm
2. A. Stanislaus, B.H. Cooper, Catal. Rev. Sci. Eng. **36**, 75 (1994)
3. N. Topsøe, H. Topsøe, J. Catal. **75**, 354 (1982)
4. X. Gao, Q. Xin, Catal. Lett. **18**, 409 (1993)
5. Y.W. Li, X.Y. Pang, B. Delmon, J. Phys. Chem. A **104**, 11375 (2000)
6. L.S. Byskov, J.K. Nørskov, B.S. Clausen, H. Topsøe, Catal. Lett. **64**, 95 (2000)
7. J.V. Lauritsen, M.V. Bollinger, E. Lægsgaard, K.W. Jacobsen, J.K. Nøskov, B.S. Clausen, H. Topsøe, F. Besenbacher, J. Catal. **221**, 510 (2004)
8. L.S. Byskov, B. Hammer, J.K. Nørskov, B.S. Clausen, H. Topsøe, Catal. Lett. **47**, 177 (1997)
9. L.S. Byskov, J.K. Nørskov, B.S. Clausen, H. Topsøe, J. Catal. **187**, 109 (1999)
10. P. Raybaud, J. Hafner, G. Kresse, H. Toulhoat, Phys. Rev. Lett. **80**, 1481 (1998)
11. P. Raybaud, J. Hafner, G. Kresse, H. Toulhoat, Surf. Sci. **407**, 237 (1998)
12. H. Toulhoat, P. Raybaud, S. Kasztelan, G. Kresse, J. Hafner, Catal. Today **50**, 629 (1999)
13. P. Raybaud, J. Hafner, G. Kresse, S. Kasztelan, H. Toulhoat, J. Catal. **189**, 129 (2000)
14. P. Raybaud, J. Hafner, G. Kresse, S. Kasztelan, H. Toulhoat, J. Catal. **190**, 128 (2000)
15. S. Cristol, J.F. Paul, E. Payen, D. Bougeard, J. Hafner, F. Hutschka, Stud. Surf. Sci. Catal. **127**, 327 (1999)
16. S. Cristol, J.F. Paul, E. Payen, D. Bougeard, S. Clémendot, F. Hutschka, J. Phys. Chem. B **104**, 11220 (2000)
17. A. Travert, H. Nakamura, R.A. van Santen, S. Cristol, J.F. Paul, E. Payen, J. Am. Chem. Soc. **124**, 7084 (2002)
18. J.F. Paul, E. Payen, J. Phys. Chem. B **107**, 4057 (2003)
19. S. Cristol, J.F. Paul, E. Payen, D. Bougeard, F. Hutschka, S. Clémendot, J. Catal. **224**, 138 (2004)
20. M. Sun, A.E. Nelson, J. Adjaye, J. Catal. **226**, 32 (2004)
21. A. Sierraalta, A. Herize, R. Añez, J. Phys. Chem. A **105**, 6519 (2001)
22. R. Pis Diez, A.H. Jubert, J. Mol. Catal. **73**, 65 (1992)
23. A.E. Gainza, E.N. Rodríguez-Arias, F. Ruette, J. Mol. Catal. **85**, 345 (1993)
24. R. Chen, Q. Xin, J. Mol. Catal. **64**, 321 (1991)
25. K. Teraishi, J. Mol. Catal. A **126**, 73 (1997)
26. H. Jiao, Y.W. Li, B. Delmon, J.F. Halet, J. Am. Chem. Soc. **123**, 7334 (2001)
27. R. Pis Diez, A.H. Jubert, J. Mol. Catal. **83**, 219 (1993)
28. X. Ma, H.H. Schobert, J. Mol. Catal. A **160**, 409 (2000)
29. R. Chen, Q. Xin, C. Wang, J. Mol. Catal. **89**, 345 (1994)
30. J.A. Rodriguez, J. Phys. Chem. B **101**, 7524 (1997)
31. H. Yang, C. Fairbridge, Z. Ring, Energy Fuel **17**, 387 (2003)
32. H. Yang, C. Fairbridge, J. Chen, Z. Ring, Catal. Lett. **97**, 217 (2004)
33. P. Faye, E. Payen, D. Bougeard, J. Catal. **179**, 560 (1998)
34. P. Faye, E. Payen, D. Bougeard, J. Mol. Model. **5**, 63 (1999)
35. H. Orita, K. Uchida, N. Itoh, Appl. Catal. A: Gen. **258**, 115 (2004)
36. T. Zeng, X.-D. Wen, G.-S. Wu, Y.-W. Li, H. Jiao, J. Phys. Chem. B **109**, 2846 (2005)
37. R. Pis Diez, A.H. Jubert, J. Mol. Struct. **210**, 329 (1990)
38. H. Orita, K. Uchida, N. Itoh, J. Mol. Catal. A **195**, 173 (2003)
39. X.-D. Wen, T. Zeng, Y.-W. Li, J. Wang, H. Jiao, J. Phys. Chem. B **109**, 18491–18499 (2005)
40. H. Schweiger, P. Raybaud, G. Kresse, H. Toulhoat, J. Catal. **207**, 76 (2002)
41. F. Delannay, Appl. Catal. **161**, 135 (1985)
42. A.N. Startsev, V.I. Zaikovskii, Kinet. Katal. **35**, 288 (1994)
43. B. Delmon, in *Catalysts in Petroleum Refining*, ed. by D. L. Trimm, S. Akashah, M. Absi-Halabi, A. Bishara, (Elsevier, Amsterdam, 1989), p. 1990
44. H. Topsøe, B.S. Clausen, R. Candia, C. Wivel, S. Morup, J. Catal. **68**, 433 (1984)

45. G.A. Gonzalez, M. Alvarado, M.A. Ramos, G. Berhault, R.R. Chianelli, Comput. Mater. Sci. **121**, 240–247 (2016)
46. M. Ramos, G. Berhault, D.A. Ferrer, B. Torres, R.R. Chianelli, Cat. Sci. Technol. **2**, 164 (2012)
47. G.A. Gonzalez, M. Alvarado, M.A. Ramos, G. Berhault, R.R. Chianelli, Comput. Mater. Sci. **123**, 93–105 (2016)
48. R.R. Chianelli, T.A. Pecoraro, U.S. Patent 4,288,422, 1981
49. T.A. Pecoraro, R.R. Chianelli, J. Catal. **67**, 430 (1981)
50. R.L. Seiver, R.R. Chianelli, U.S. Patent 4430,443, 1984
51. H. Hallie, *Ketjen Catalysts Symposium* (Elsevier, Amsterdam, 1982), p. 58
52. S. Kasztelan, C. R. Acad. Sci. Paris Ser. II **307**, 727 (1988)
53. R.R. Chianelli, G. Berhault, Catal. Today **53**, 357 (1999)
54. X.-D. Wen, Z. Cao, Y.-W. Li, J. Wang, H. Jiao, J. Phys. Chem. B **110**(47), 23860–23869 (2006)
55. H. Ge, X.-D. Wen, M.A. Ramos, R.R. Chianelli, S. Wang, J. Wang, Z. Qin, Z. Lyu, X. Li, ACS Catal. **4**, 2556–2565 (2014)
56. X. Liu, D. Cao, T. Yang, H. Li, H. Ge, M. Ramos, Q. Peng, A.K. Dearden, Z. Cao, Y. Yang, Y.-W. Li, X.-D. Wen, RSC Adv. **7**, 9513–9520 (2017)
57. C.J. Wright, C. Sampson, D. Fraser, R.B. Moyes, P.B. Wells, C. Riekel, J. Chem. Soc. Faraday Trans. **176**, 1585 (1980)
58. J. Polz, H. Zeilinger, B. Müller, H. Knözinger, J. Catal. **120**, 22 (1989)
59. W.P. Dianis, Appl. Catal. **30**, 99 (1987)
60. A.B. Anderson, Z.Y. Al-Saigh, W.K. Hall, J. Phys. Chem. **92**, 803 (1988)
61. M.R. Dubois, M.C. van Der Veer, D.L. Dubois, R.C. Haltiwanger, N.K. Miller, J. Am. Chem. Soc. **102**, 7456 (1980)
62. M. Neurock, R.A. van Santen, J. Am. Chem. Soc. **116**, 4427 (1994)
63. F. Frechard, P. Sautet, Surf. Sci. **389**, 131 (1997)
64. L.S. Byskov, M. Bollinger, J.K. Nørskov, B.S. Clausen, H. Topsøe, J. Mol. Catal. A **163**, 117 (2000)
65. M.V. Bollinger, K.W. Jaconben, J.K. Nørskov, Phys. Rev. B **67**, 085410 (2003)
66. X.-D. Wen, T. Zeng, B.-T. Teng, F.-Q. Zhang, Y.-W. Li, J. Wang, H. Jiao, J. Mol. Catal. A **249**, 191–200 (2006)
67. P. Mills, S. Korlann, M.E. Bussell, J. Phys. Chem. A **105**, 4418 (2001)
68. P.C.H. Mitchell, D.A. Green, E. Payen, J. Tomkinson, S.F. Parker, Phys. Chem. Chem. Phys. **1**, 3357 (1999)
69. S. Harris, R.R. Chianelli, J. Catal. **98**, 17 (1986)
70. D.L. Sullivan, J.G. Ekerdt, J. Catal. **178**, 226 (1998)
71. G.D. Atter, D.M. Chapman, R.E. Hester, D.A. Green, P.C.H. Mitchell, J. Tomkinson, J. Chem. Soc. Faraday Trans. **93**, 2977 (1997)
72. P. Raybaud, G. Kresse, J. Hafner, H. Toulhoat, Phys. Rev. Lett. **80**, 1481 (1998)
73. R.M. Martin, *Electronic Structure: Basic Theory and Practical Methods* (Cambridge University Press, Cambridge, 2004). ISBN-13: 978-0521534406

Chapter 4
Catalytic Materials for Hydrodesulfurization Processes, Experimental Strategies to Improve Their Performance

Jorge Ramírez, Perla Castillo-Villalón, Aída Gutiérrez-Alejandre, Rogelio Cuevas, and Aline Villarreal

4.1 Introduction

The production of clean liquid transport fuels requires highly active hydrodesulfurization catalytic materials to achieve the set goals of low sulfur content in accordance with worldwide environmental regulations that are pushing the limits for nearly zero ppm of sulfur content in liquid fuels. The increasing use of feedstocks with low quality, which contain higher concentrations of sulfur, nitrogen, metals, and other contaminants, creates heavier demands on the catalytic materials used for hydrodesulfurization, which must eliminate larger amounts of organic sulfur compounds of low reactivity and other nitrogen compounds that inhibit hydrodesulfurization and hydrogenation reactions.

The removal of sulfur from molecules of low reactivity takes place by two main reaction routes: the direct desulfurization (DDS) and hydrogenation (HY). In that sense, it is necessary to achieve a good understanding of the nature and chemical behavior of the different active sites in the catalytic material, and of the factors that influence activity and selectivity, concerning both direct desulfurization and hydrogenation catalyst functionalities.

Most hydrodesulfurization catalytic materials are composed of MoS_2 crystallites with addition of cobalt or nickel (Co, Ni) atoms to comprise a sulfide phase. For commercial applications, due to high pressure and temperature reaction conditions, the Co(Ni)Mo sulfide phase is usually supported on alumina oxide (Al_2O_3), as well described by Topsøe et al. [1].

J. Ramírez (✉) · P. Castillo-Villalón · A. Gutiérrez-Alejandre · R. Cuevas · A. Villarreal
UNICAT, Departamento de Ingeniería Química, Facultad de Química, UNAM,
CDMX, Mexico
e-mail: jrs@unam.mx

J. M. Domínguez-Esquivel, M. Ramos (eds.), *Advanced Catalytic Materials: Current Status and Future Progress*, https://doi.org/10.1007/978-3-030-25993-8_4

Experimental and theoretical evidence points out that active sites for sulfur removal are located at sulfur vacancies at MoS_2 crystallite edges. Therefore, the overall HDS reaction is structure sensitive in principle and the activity of the catalytic material will be dependent on the crystallite size and edge termination as presented using theoretical density functional theory-based studies by different research groups [2–9]. Moreover, Lauritsen et al. presented a study using scanning tunneling microscopy (STM) contrasted with computer-assisted DFT simulations to determine the location of the Co promoter on MoS_2 low-size slabs, allowing the understanding of "brim sites," providing better knowledge of the catalytic material [10, 11].

Furthermore, the same group lead by H. Topsøe achieved one STM study to determine any chemical interaction of sterically hindered dibenzothiophenes using same triangular cobalt-promoted MoS_2 model particles under ultrahigh-vacuum operational conditions. Dibenzothiophene (DBT), which is mainly used to test at laboratory scale HDS catalytic materials, was adsorbed at edge sites located near corners of the MoS_2 triangular nanostructure whereas the adsorption of 4,6-dimethyldibenzothiophene, which is a sterically hindered molecule, and is mainly transformed through the hydrogenation route, took place on the so-called brim sites located near the edge at MoS_2 crystallites [12]. These results suggested a two-site reaction model for HDS of 4,6-DMDBT to occur, composed of hydrogenation of the first aromatic ring taking place at brim sites and subsequent sulfur removal of the hydrogenated intermediate at sulfur vacancies at the edge of the MoS_2 particle. The optimization of a catalyst depends then on the rate-controlling step in the sequence of reactions.

Now, sulfur molecules present in the different liquid fuels obtained from crude oil can display different reactivity and complex chemical structures, making important a high-quality design of HDS catalytic materials. For example, to obtain ultralow sulfur diesel one must eliminate sulfur from refractory molecules like 4,6-DMDBT and therefore the hydrogenating functionality of the catalytic material should be enhanced because those molecules react mainly through the hydrogenation reaction routes; in other words, a catalyst with a high hydrogenation/desulfurization selectivity is necessary to achieve good catalytic performance. On the contrary, for the hydrodesulfurization of fluid catalytic cracking (FCC) liquid gasoline, which contains sulfur aromatic compounds such as thiophenes and benzothiophenes, a low hydrogenation/desulfurization selectivity is required in the catalytic material to enhance the direct desulfurization route and inhibit deep hydrogenation, avoiding in this way olefin saturation, which is the main cause of hydrogen consumption and octane loss, with economic benefits.

When the feed is mixed with low-value fractions, as occurs for diesel production where sometimes light cycle oil is added to the feed, the catalyst must eliminate sulfur in the presence of high concentrations of nitrogen and aromatic compounds, which are poisons to both the hydrogenating and direct desulfurization sites of the catalyst. From theoretical studies made using DFT methods, it was possible to determine that basic heterocyclic nitrogen compounds strongly inhibit the hydrogenation route for HDS, which is the key step for achieving ultralow sulfur diesel, because the elimination of the most refractory sulfur-containing molecules like 4,6-DMDBT is necessary, which mainly occurs through the hydrogenation routes [13].

The nature of the support matrix, mainly composed in commercial catalysts by alumina oxides (Al_2O_3), can have great influence in the performance of the hydrotreating catalyst. A support matrix with high chemical interaction allows uniform dispersion of the cobalt, nickel, and molybdenum precursor phases; however, it can be detrimental to the degree of sulfidation of the final Ni- and Co-promoted MoS_2 nanoclusters. Some experimental studies using X-ray photoelectron spectroscopy (XPS) indicate electronic binding of oxygen species from the Al_2O_3 complex matrix and molybdenum, which mainly occurs during the calcination process and remains after the sulfidation step, made with hydrogen disulfide (H_2S), giving rise to the presence of oxysulfides in the final catalytic material. These partially sulfided structures have low catalytic activity and have been named type I Co(Ni)-Mo-S whereas the well-sulfided ones displaying high HDS activity have been named type II Co(Ni)MoS structures [14]. A density functional theory study made to investigate the origin of the activity differences between type I and type II MoS_2-based structures in hydrotreating catalysts showed that indeed the presence of bridging oxygen bonds between molybdenum and support matrix modifies the electronic properties of the MoS_2-supported phase [9].

Experimental evidence shows that the adequate choice of the catalytic support is important since its chemical nature regulates the interaction between the Mo and Co (or Ni) phases with the support matrix surface, playing an important role to achieve high dispersion, sulfidation, and promotion of the MoS_2 nanoclusters and finally high HDS activity in the transformation of complex organic sulfur molecules as those present in crude oil. In our research group, some strategies used to prepare highly active HDS catalysts consist of optimizing dispersion, sulfidation, and promotion of the MoS_2 nanoclusters by using different supports, organic additives like EDTA or citric acid, Mo and Co(Ni) heteropolycompounds as precursor salts, and modification of the sulfidation methodology. In what follows some work performed using these strategies is outlined.

4.2 Choice of the Catalyst Support

Experimental studies made by us revealed that the composition of the catalyst support matrix has an important effect on the dispersion of the active phase and plays an important role in the extent of promotion and sometimes in the intrinsic activity of Mo- and Co-promoted Mo sulfide particles [15, 16] improving HDS catalyst performance.

With the aim of improving the performance of HDS catalysts, to produce ultralow sulfur fuels, support materials with different metal-support interaction strength have been tried during the past years [17–19]. Benefits in HDS activity for catalysts using many different supports such as titanium dioxide (TiO_2), zirconium dioxide (ZrO_2), magnesium oxide (MgO), pristine forms of carbon, cerium oxide (CeO_2), silicon oxide (SiO_2), zeolites, MCM-41, SBA-15, natural mineral clays, and various mixed oxides, TiO_2–Al_2O_3, among others, have been reported. For more information, we invite the reader to revise Ramirez et al. [16].

Earlier, Ramírez et al. [15] reported that the turnover frequency in thiophene HDS is about 4.4 times higher for titania-supported than for γ-alumina-supported MoS_2. To explain this important finding, electronic effects [15], orientation effects [20], and promotion by Ti [21–23] have been proposed in the past. Theoretical methods such as density functional theory (DFT) simulations have also been tried to understand the structure and behavior of HDS catalysts supported on different materials such as γ-Al_2O_3 or TiO_2 [24].

In a study that combined thiophene HDS activity and X-ray photoelectron spectroscopy on flat model systems of sulfided HDS Mo catalysts, Coulier et al. [23] found that the sulfided Ti species can act as a promoter in the same way as Co and Ni, although less effectively, confirming the original proposal of Ramírez et al. [21]. The fact that Ti in TiO_2 can act as an electronic promoter of the supported MoS_2 explains the higher thiophene HDS activity and hydrogenation selectivity of Mo/TiO_2 compared with Mo/Al_2O_3.

Another experimental study targeting at the effects of cobalt and nickel promoters for molybdenum disulfide catalysts supported either on Al_2O_3 or TiO_2 reported on the hydrodesulfurization of thiophene (T), dibenzothiophene (DBT), and 4,6-dimethyldibenzothiophene (4,6-DMDBT) [25]. The study, that comprised different catalytic supports (TiO_2 and Al_2O_3) and reacting molecules (thiophene, dibenzothiophene, and 4,6-DMSBT), showed that the greater activity displayed by Mo/TiO_2 compared to Mo/Al_2O_3 comes from a moderate increase in the direct desulfurization capability but mostly from an increase in the hydrogenating character of the catalyst due to the enhanced MoS_2 metallic character induced by TiO_2, showing that not only the overall HDS activity but also the HYD/DDS selectivity can be significantly influenced by the nature of the catalytic support matrix. The hydrodesulfurization rate constants for thiophene (T), dibenzothiophene (DBT), and 4,6-dimethyldibenzothiophene (4,6-DMDBT) over Mo, CoMo, and NiMo catalysts supported on TiO_2 and Al_2O_3 are displayed in Fig. 4.1 that shows that for the unpromoted catalysts there is a clear advantage in using titania instead of alumina as matrix support, MoS_2 supported on titania being 4, 4.4, and 2.7 times more active in the hydrodesulfurization of thiophene (T), dibenzothiophene (DBT), and 4,6-dimethyldibenzothiophene (4,6-DMDBT), respectively. However, promoted systems display a different behavior. The magnitude of the promotional effect varies with the reacting molecule and seems to be more effective when the reacting molecule is transformed through the direct desulfurization route, as in the case of thiophene and DBT. In contrast, for the hydrodesulfurization of 4,6-DMDBT, that takes place mainly via the hydrogenation route, the promotional effect for Co(Ni)Mo/TiO_2 is not observed, in spite of the fact that Mo/TiO_2 is 2.75 times more active than Mo/Al_2O_3, suggesting that the promotion effect expected from Co or Ni was already achieved by the use of titania as support matrix.

For thiophene and DBT that undergo HDS mainly by the direct desulfurization route, the promotional effect of Co or Ni for the TiO_2-supported catalysts is clearly

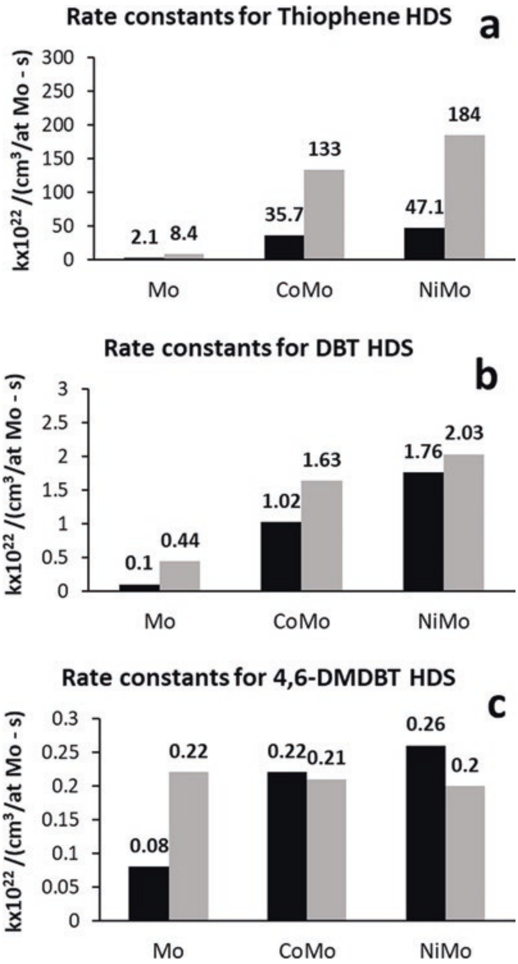

Fig. 4.1 Overall rate constant for the HDS of (**a**) thiophene, (**b**) dibenzothiophene, and (**c**) 4,6-dimethyldibenzothiophene over Mo, CoMo, and NiMo catalysts supported on Al_2O_3 and TiO_2. Extracted from [25] with permission from Elsevier

observed: ≈16 times for thiophene and ≈3.7 times for DBT. Therefore, enhancement of catalytic activity when using TiO_2 support matrix seems to be more effective for direct desulfurization reactions.

In the case of Al_2O_3-supported MoS_2, the promotional effects of Co or Ni are clearly observed during HDS laboratory test runs for the three different reactant molecules, and are much higher than those observed for TiO_2-supported catalysts.

In the past we postulated that under HDS reaction conditions (high H_2 pressure and temperature) TiO_2 could act as an electronic promoter [22], as found in an experimental temperature-programmed reduction study of the sulfided materials (TPR-S) made by Ramírez et al. [21]. The study showed that the number of coordinatively unsaturated sites (CUS), or sulfur vacancies, per Mo atom increased with the Ti content. It was proposed that the increased number of sulfur vacancies in the catalyst would be the result of an electronic promotion of Mo by Ti causing the weakening of the Mo–S bond due to injection of electrons, coming from Ti^{3+} centers, to the HOMO of Mo, occupying antibonding orbitals.

The fact that the promotion either with Ni or Co is smaller for Mo/TiO_2 than for Mo/Al_2O_3 systems [25] suggests that either the Mo species supported on TiO_2 are more difficult to promote than those supported over alumina matrix or the optimum value of the Mo–S bond energy was not reached with the electronic promotion of Ti, and that some additional promotion coming from Ni or Co is required to achieve the value of the metal–sulfur bond energy that optimizes the interaction between the sulfur organic compound and the CUS active site. The electronic promotion must have a limit, or a maximum according to the Sabatier principle, as explained by Chianelli et al. for transition metal sulfides [26], because excessive weakening of the metal sulfur bonds in MoS_2 would lead to an excessively weak interaction between the sulfur compounds and the active phase. The results reported by Ramírez et al. [27], showing that the reduction of Mo or W oxide phases supported on pure TiO_2 or TiO_2–Al_2O_3 materials takes place at lower temperatures than for pure alumina-supported systems, are in agreement with the above explanation.

DFT investigations comparing the thermodynamic stability of MoS_2 particles anchored by S edge and Mo edge on alumina and titania under HDS conditions were presented by Costa et al. [28]. It was proposed that an edge-wetting effect present in Mo/TiO_2 and not in Mo/Al_2O_3 is at the origin of the smaller MoS_2 particles found for supported Mo on TiO_2. Their results indicated that at HDS conditions MoS_2 particles supported on anatase are edge-on with a trapezoidal shape exposing only one sulfur edge and two Mo edges. However, the higher dispersion achieved by the smaller particles is partly compensated by the number of Mo atoms buried in the MoS_2-anatase interphase (two sulfur edges and one Mo edge). Therefore, the number of exposed sulfur edge Mo atoms does not increase sufficiently to explain the fourfold increase in thiophene HDS activity observed experimentally. Since the variation in edge dispersion did not account for the observed results, an explanation related to the intrinsic nature of the catalytic site was proposed.

Recently, Castillo-Villalón et al. [25] found experimentally, by CO adsorption analyzed by FTIR spectroscopy, that the promotion of Mo by Co is more difficult when Mo is supported on TiO_2 than when supported on Al_2O_3. Thus, the number of promoted sites in CoMo supported on alumina is much higher than when supported on TiO_2. Additionally, UV-vis-NIR DRS electronic spectroscopy results indicated that in the oxide precursors, more defective Mo oxidic particles in stronger interaction with the support are formed on alumina than on titania. Since the alumina-supported catalyst is better promoted, as the IR-CO results indicated, it was postulated that the lower promotion of CoMo supported on titania compared to CoMo/Al_2O_3 has a structural origin and that the highly defective Mo oxide-phase structure supported on alumina facilitates the incorporation of the promoter into the crystalline lattice of MoS_2. This finding is in line with the differences in MoS_2 structure predicted by DFT theory when the support changes from alumina to titania [28] since an edge-on MoS_2 structure found on TiO_2 would be more difficult to promote than a flat defective structure on the alumina surface.

It is clear that the value of the specific hydrodesulfurization rate constant (per gram of catalyst) for MoS_2 catalysts supported on different oxides is the result of several contributions that affect not only the edge dispersion of the MoS_2 particles but also the intrinsic activity of the different catalytic sites. The choice of the support matrix is therefore a key parameter in the preparation of highly active HDS catalytic materials since its nature can affect the performance of the different active sites in the catalyst. Moreover, it can affect the dispersion, the sulfidation, and the redox process of the supported phases during catalyst preparation and under HDS reaction conditions.

4.2.1 Catalyst Support Materials for Hydrodesulfurization of FCC Gasoline

Gasoline, one of the most widely used transport fuels, is a complex mix and in this way the gasoline pool receives contributions from a variety of refinery streams, including light straight run naphtha, isomerate, alkylate, FCC naphtha, and hydrocracker gasoline. Of these cuts, FCC naphtha is typically the largest volume component of the gasoline pool (30–40% v/v); moreover, FCC naphtha is responsible for about 80–95% of the total sulfur because it contains up to 2.5 wt% sulfur [29]. In contrast, the straight run naphtha, isomerate, and alkylate streams are very low in sulfur (<1 ppm S). Sulfur content is important because of environmental issues. Consequently, to achieve low sulfur content in the final fuel and meet environmental regulations like Tier 3 [30], the sulfur in the FCC naphtha incorporated to the gasoline pool must be reduced to 20–30 ppm. On the other hand, FCC naphtha contributes significantly to octane number due to its high content of olefins, up to 20 wt% [31], and aromatic compounds.

There are various process alternatives to decrease the sulfur content in FCC naphtha; among them one can either (a) pretreat the feed to the FCC unit, which is an expensive solution because of the high volume to pretreat, or (b) post-treat only the FCC product fraction that will be added to the gasoline pool (the so-called FCC naphtha).

The FCC naphtha fraction contains mainly thiophenic sulfur compounds of high reactivity and therefore, it is possible to attain during hydrotreatment sulfur levels below 10 ppm without great difficulty. In fact, it would be sufficient to operate at higher pressure and/or temperature to achieve low sulfur levels. However, under these more severe operating conditions, if allowed by thermodynamics, the hydrogenation reactions are enhanced and an important decrease in the olefin content, from 20 to 60 vol% to approximately 2 vol%, can take place, leading to a decrease of up to 10 octane numbers in the final gasoline [31]. Therefore, the key of this technology lies in the possibility to achieve high hydrodesulfurization (HDS) minimizing the hydrogenation (HYD) reactions. There are two possibilities to solve this challenge: one is to understand the effect of the process variables, pressure (*P*), temperature (*T*), and liquid hourly space velocity (LHSV[1]). The other is the development of catalytic materials able to perform high hydrodesulfurization with minimum hydrogenation.

To analyze the possibility of obtaining low sulfur and high RON in the hydrodesulfurization of FCC naphtha, a laboratory study was conducted on the effects of changing the operating HDS conditions (*T*, *P*, LHSV) on the RON and sulfur content of the product, using a commercial $CoMoAl_2O_3$ catalyst, and a feed of stabilized FCC naphtha (original RON = 69) added with the proper amount of thiophene to reach 1000 ppm S. Both the experimental design and statistical analysis were performed using Statgraphics software.

A multiple response surface methodology and a Box-Behnken-type experimental design [32] were used to analyze two responses, the remaining sulfur content $\left(\bar{y}\mathrm{s}\right)$ and the RON, as a function of three operating variables (factors in statistical nomenclature): LHSV = 3, 6, and 9 h^{-1}; temperature = 270, 300, and 330 °C; and pressure = 440, 480, and 520 psia leading to a total of 27 experiments. However, using the methodology Box-Behnken only 16 experiments were necessary to analyze the system.

In an attempt to illustrate the effect of three variables (LHSV, *T*, *P*) in a two-dimensional field, Fig. 4.2 shows an example of the effects obtained for each variable when the other two remain constant.

To help understand the effect of *T*, *P*, and LHSV, on the process, a surface response analysis was made by building a piecewise desirability function (δ) that expresses the desirable response for a combination of the process variables as a value of one if the response achieves some fixed desirable value. In this case, $\delta = 1$ if less than 30 ppm of sulfur is achieved in the processed naphtha: an intermediate value between 0 and 1 if the response factor is in the interval 1000–30 S ppm, and a value of zero if the response is equal or greater than the initial value. A maximization was used for the RON whereas a minimization was established for the remaining sulfur content in the product.

(a) For RON maximization, a loss of four RON units was considered acceptable with a RON lower limit of 65. In this case, the desirability function (δ) was defined as

$$\delta = \begin{cases} 0 & \text{if } \bar{y} \text{ does not reach } \mathrm{RON_{LL}} \\ \left[\dfrac{\bar{y} - \mathrm{RON_{LL}}}{\mathrm{RON^0} - \mathrm{RON_{LL}}}\right] & \text{if } \mathrm{RON_{LL}} \le \bar{y} \le \mathrm{RON^0} \\ 1 & \text{if } \bar{y} \ge \mathrm{RON^0} \end{cases}$$

---

[1] LHSV is the ratio of the hourly volume of oil processed to the volume of catalyst.

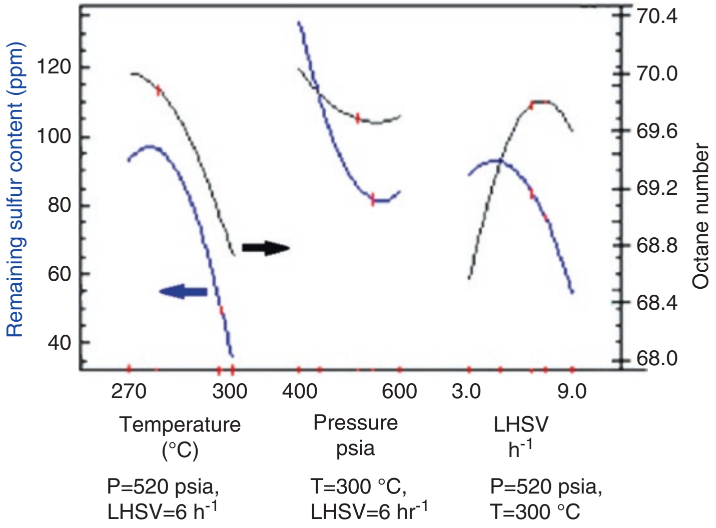

Fig. 4.2 Effect of temperature, pressure, and LHSV on the sulfur content (blue) and RON (black) after the hydrotreating of stabilized FCC naphtha with 1000 ppm S

where $\bar{y}$ is the RON after HDS processing, $\mathrm{RON_{LL}}$ is the lower acceptable RON limit, and $\mathrm{RON^0}$ is the initial RON (in this case RON = 69).

(b) For the minimization of the remaining sulfur content ($\bar{y}$ s), considering 1000 ppm of S in the feed and setting the desirable lower limit of sulfur ($\mathrm{S_{LL}}$) at 30 ppm. In consequence, the desirability function (δ) was defined as

$$\delta = \begin{cases} 1 & \text{if } \bar{y}\mathrm{s} \text{ is lower than } \mathrm{S_{LL}} \\ \left[\dfrac{\bar{y}\mathrm{s} - \mathrm{S}^0}{\mathrm{S_{LL}} - \mathrm{S}^0}\right] & \text{if } \mathrm{S_{LL}} \le \bar{y}\mathrm{s} \le \mathrm{S}^0 \\ 0 & \text{if } \bar{y}\mathrm{s} \ge \mathrm{S}^0 \end{cases}$$

where ($\bar{y}$ s) is the product sulfur content after HDS processing and S^0 is the initial sulfur concentration in ppm.

An optimization for the responses under the operating variables was made with the restrictions that the process must reach at least: RON >65, and S content <30 ppm. The best performance was obtained at LHSV = 6.75 $\mathrm{h^{-1}}$. Using this fixed LHSV, the surface response for RON and remaining product sulfur was obtained for the different values of *T* and *P* (see Fig. 4.3).

The results of this example show that with a conventional CoMo HDS catalyst it is not possible, through the optimization of the operating conditions, to comply with the sulfur specification of 30 ppm S, maintaining simultaneously a desirable high octane number.

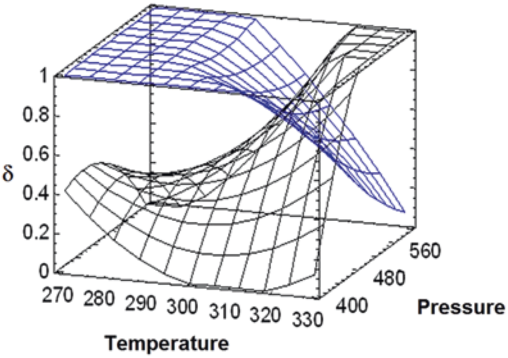

Fig. 4.3 Surface responses for the desirability function (δ) with respect to RON (blue) and remaining sulfur content (black), at LHSV of 6.75 h^{-1}, on the HDS of stabilized naphtha with 1000 ppm of sulfur

Therefore, a complete solution to the issue of obtaining clean FCC gasoline with high RON needs both the optimization of the process variables and the developing of hydrodesulfurization catalytic materials with high HDS/HYD selectivity ratio. To this end, several studies have been made in the past using catalysts with basic support matrixes to inhibit the transport of hydrogen and achieve HDS/HYD selectivity ratios higher than those obtained with active phases supported on alumina.

In an early study, Shimada et al. [33] analyzed the effect of using CoMo catalysts supported on MgO on the activity for hydrocracking (HYC) diphenylmethane. With MgO being a basic support the observed decrease in hydrocracking activity was an expected result. Nonetheless, an interesting result was that the MgO-supported catalyst showed a significant decrease in the hydrogenation activity. In another work, the same group confirmed this result using 1-methyl-naphthalene as reactant [17].

However, MgO in dry conditions has a surface area of around 200 m^2/g but is a highly hygroscopic material and in the presence of water it is easily transformed into $Mg(OH)_2$, which has a low surface area of about 2 m^2/g, and is therefore not a good matrix support for the HDS catalyst. Several approaches have been used in the preparation of HDS catalytic materials to compensate this problem: (i) producing MgO with high surface area [34], or (ii) using nonaqueous preparation methods to avoid the hydration of MgO [35]. However, such preparations are more expensive. A third approach has been to use a catalyst support matrix different from MgO, over which magnesia can be grafted or dispersed.

Supports of magnesia grafted on the surface of alumina were also investigated with the hypothesis that the hygroscopic behavior of pure magnesia could be avoided once magnesia is bonded to alumina through Mg-O-Al bridges. This approach hopes to preserve the high surface area provided by alumina.

Figure 4.4a shows the behavior of NiMo catalysts supported on alumina modified with different amounts of magnesia ($NiMo/MgO(x)/Al_2O_3$), where x = monolayers of MgO. It should be noted that the NiMo active phase chosen for this study presents a stronger hydrogenating function than the most suitable CoMo formulation. Catalysts were tested on two different reactions at atmospheric pressure: thiophene hydrodesulfurization and cyclohexene hydrogenation. The results showed that addition of magnesia to alumina produced a strong decrement in cyclohexene

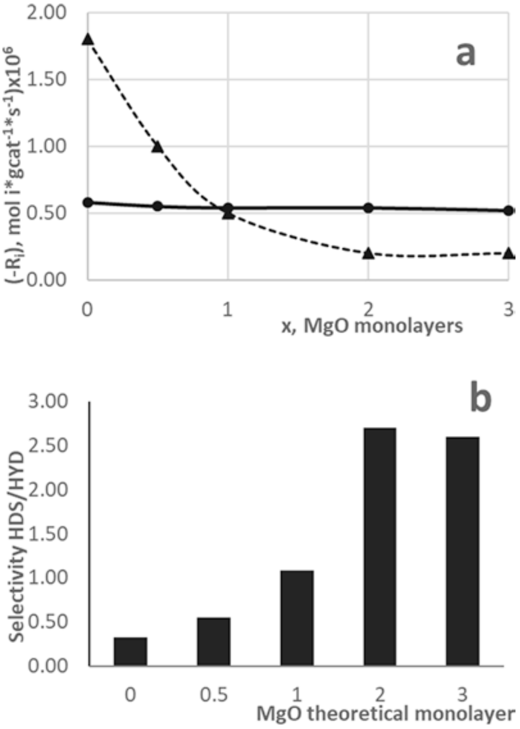

Fig. 4.4 NiMo/Mg(X)-Al_2O_3: (**a**) activity for thiophene HDS (•) and cyclohexene HYD (▲); (**b**) selectivity ratio HDS of thiophene/HYD cyclohexene. Atmospheric pressure, differential continuous reactor. Theoretical MgO monolayer estimated as 2 OHs per Mg^{2+}

hydrogenation while the HDS of thiophene presented only a slight decrement. The decrement in the hydrogenation reaction was five times higher than the decrement of the desulfurization reaction, leading to an improved HDS/HYD ratio (Fig. 4.4b).

For NiMo catalysts supported on Al_2O_3–MgO mixed oxides with different x = MgO/MgO + Al_2O_3 molar ratios (0.0, 0.05, 0.25, 0.5, 0.75, and 1.0) [36], textural stability to the presence of water and high HDS/HYD ratio were found by Solis et al. [37] for low MgO contents (<0.25% mol). The catalysts however displayed a tendency to form nickel molybdate and NiO–MgO solid solution, taking away a significant amount of the Ni necessary to promote the MoS_2 phase.

Magnesium is not the only additive that confers basic properties. The possibility of modifying the alumina support with alkaline oxides has also been investigated. The addition of Li or K oxides to the alumina support of commercial catalysts caused a decrease in the hydrogenation and hydrodesulfurization activities. However, as in the case of magnesia, the decrease in HDS was less pronounced, leading to an improved HDS/HYD selectivity [38]. The addition of barium to the alumina support also caused the same behavior, a decrease in both rates of HDS and HYD but with an increase in the HDS/HYD selectivity [39]. In contrast, Miller et al. [40] reported no effect on the activity or HDS/HYD selectivity with addition of Ce to MoS_2/Al_2O_3 or K to $CoMo/Al_2O_3$. Likewise, supports of different kinds as hydrotalcites have been used with success to improve the HDS/HYD selectivity ratio during the hydrodesulfurization of cracked naphtha [41].

Although the addition of alkaline earth oxides like MgO to alumina improves the HDS/HYD selectivity ratio, a decrease in the HDS activity is also caused to some extent because the Ni or Co promoters can form a stable phase with the support matrix. To overcome this problem, the combined use of alkaline-earth oxides as basic additives, heteropolycompounds as active-phase precursors containing Mo and Ni or Co promoter, and chelating agents to avoid the interaction of the Ni or Co promoter with the support matrix has been analyzed. Trejo et al. [42] used an aqueous impregnation with a chelating agent (CyDTA) to preserve or improve the HDS activity in CoMo catalysts supported on alumina modified with different amounts of MgO. The combination of potassium, citric acid, and a heteropolyacid, $H_3PMo_{12}O_{40}$, was also used in the preparation of selective $KCoMoP/Al_2O_3$ catalysts for the hydrotreating of FCC gasoline [43, 44].

Although several industrial processes based on catalysts with high HDS/HYD selectivity are offered (ScanFinning by Exxon-Mobil or Prime G by Axens), the research in this field continues since more restrictive environmental regulations are expected in the near future.

4.3 Improving HDS Catalytic Materials with the Use of Chelating Organic Additives

Alumina is widely used as a support for industrial hydrodesulfurization (HDS) catalysts of Co(Ni)-promoted molybdenum sulfide. The current challenge is to improve the alumina-supported catalysts in order to fulfill the requirements of production of clean transportation fuels [1, 19, 45]. The use of organic additives such as chelating agents during the preparation of Co(Ni)Mo HDS catalysts helps to improve their catalytic performance; according to literature, the use of a chelating agent during the catalyst preparation can lead to an increase in the number of Co(Ni)MoS promoted sites in the final catalyst [46–48]. It has been explained that the interaction of the chelating agent with the promoter produces a stable complex that sulfides at temperatures similar or higher than those required to sulfide oxidic Mo, facilitating the formation of the mixed Co(Ni)MoS phase and minimizing the formation of isolated phases of Ni or Co sulfide [49–52]. According to these results, the use of a chelating agent results in an enhanced promotion. However, a more detailed explanation of the effect of a chelating agent is convenient to better understand the characteristics of the active sites and to enable further improvements of the catalytic systems. It is not the purpose of this section to make a review of all chelating agents used in the preparation of HDS catalyst, but to make instead a detailed analysis of the effect of two chelating agents (ethylenediaminetetraacetic acid -EDTA- and citric acid -CA-) in Mo and CoMo HDS catalysts, with the aim of thoroughly understanding which of the changes induced by the use of the chelating agent has a real influence on the HDS behavior.

The CoMoS phase model, extensively used to analyze and explain the catalytic properties of hydrodesulfurization catalysts, is very useful to achieve this goal. This model is supported by experimental results that revealed the presence of Co atoms in MoS_2 crystallites, that is, the CoMoS phase, and is now accepted that such structures govern the catalytic activity of promoted catalysts [53–55]. Recently, scanning tunneling microscopy (STM) experiments and density functional theory (DFT) were used to demonstrate that in the most stable CoMoS phase, Co substitutes Mo at the edges of MoS_2 particles [2, 4, 11, 56, 57]. Some important characteristics of the active phase are still a subject of debate, for example, the local structure of the cobalt atoms on the edges of the MoS_2 crystallites. Based on nuclear magnetic resonance (NMR) and X-ray absorption near edge structure (XANES) analysis of promoted catalysts supported on different materials, several local structures where the Co atoms are bonded to five and/or six sulfur atoms in the CoMoS phase have been proposed [58–64].

Controversially, the combination of experimental and theoretical techniques revealed that the coordination number of Co in the CoMoS phase can be four instead of five or six. In particular, based on experimental results using STM or FT-IR of CO combined with DFT calculations, it was proposed that the Co atoms that substitute Mo on the edges of MoS_2 crystallites are fourfold coordinated with either tetrahedral, pseudo-tetrahedral, or square planar structure depending on the sulfur coverage, type of substituted edge (S or Mo), and promotion degree [11, 57, 65, 66].

It is not surprising that the FT-IR of CO can provide experimental evidence to achieve such type of information of the catalytic materials. The IR analysis of adsorbed NO or CO probe molecules is a technique widely used to study unpromoted and promoted binding sites in HDS catalysts [67–70], including those prepared with organic additives such as the chelating agents, because the absorbance and features of the IR spectrum of the adsorbed molecule provide information on the amount and electronic characteristics of the binding sites. Several important issues in sulfided catalysts have been discussed with the IR analysis of probe molecules, sometimes in combination with other techniques. For example, IR studies of adsorbed NO with EXAFS showed that the adsorption sites are located in the MoS_2 edges instead of on the basal planes [71]. Better results were obtained with CO adsorption because it can distinguish Mo–S unpromoted sites from CoMoS promoted ones. On sulfided Mo/Al_2O_3 catalysts, Mo–S binding sites are associated with a strong band at 2110 cm^{-1} (Mo in Mo edge) with a weak, broad component at 2070 cm^{-1} (Mo in S edge). The intensity of the bands correlates well with the HDS activity of the unpromoted catalysts [72–74]. For sulfided $CoMo/Al_2O_3$ catalysts, a new strong band at 2070 cm^{-1}, which intensity is in line with the catalytic activity [75], corresponds to CO adsorbed on promoted sites.

The nature of the promoted sites (Mo or Co) and its local structure (tetrahedral, pseudo-tetrahedral, or square planar) is not clearly established by the features of the experimental IR spectrum alone. The information available from the spectrum is that the corresponding CO band on promoted sites appears at a different frequency, shifted from the bands corresponding to the adsorption on unpromoted Mo–S sites

(2110 cm^{-1}) and Co sites in cobalt sulfide (2094 cm^{-1}). DFT calculations were needed to propose the structures of the promoted sites mentioned above [65].

To improve the current supported catalysts it is important to know the local geometry of Co on the edges of the MoS_2 crystallites, to better understand and explain how the catalysts behave in reaction conditions. Even more important is to establish if the structure of Co has or not a significant impact on the catalyst activity. This is the subject of the following sections.

4.3.1 Effect of EDTA in the Electronic and Structural Characteristics of the CoMoS Site and Catalytic Performance of Co-promoted Mo/Al_2O_3 Catalysts

A detailed analysis of the FT-IR spectra of CO adsorbed on a series of catalysts (Mo/Al_2O_3, $CoMo/Al_2O_3$ (without EDTA) and CoMo-E/Al_2O_3 (using EDTA during preparation)) was useful to study the effect of the chelating agent EDTA in the promotion of CoMo catalysts [76].

It was observed that the absorbance of the peak of CO adsorbed on CoMoS sites (at ~2072 cm^{-1}) [76] in the IR spectra is bigger in CoMo-E/Al_2O_3, compared to the $CoMo/Al_2O_3$ catalyst (see Fig. 4.5). The evaluation of the number of sites and the absorption coefficient indicated that the more intense absorbance is not related to a greater amount of adsorbing sites, but instead to a bigger absorption coefficient in CoMo-E/Al_2O_3: $\varepsilon_{\mathrm{CoMoS}}$ (CoMo-E/Al_2O_3)/$\varepsilon_{\mathrm{CoMoS}}$ ($CoMo/Al_2O_3$) = 1.9 [76]. This result needed an interpretation of the CO spectra different to the traditional one, because

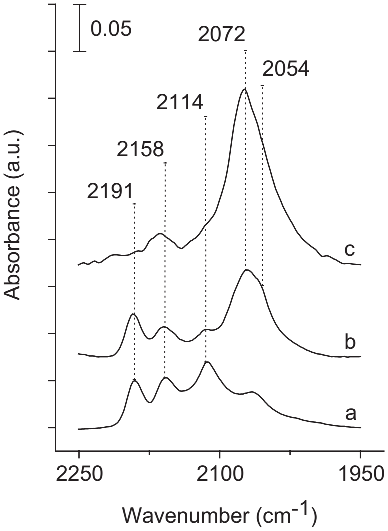

Fig. 4.5 IR spectra of CO adsorbed on sulfided catalysts at ~100 K and 1 Torr. (**a**) Mo/Al_2O_3, (**b**) $CoMo/Al_2O_3$, (**c**) CoMo-E/Al_2O_3. Reprinted from [76] with permission from Elsevier

it was regularly assumed that at each CO vibration frequency on sulfided catalysts (at 2072 cm^{-1} in this case) corresponds to the same value of CO absorption coefficient.

The observed change in the magnitude of the absorption coefficients must arise from differences in the electronic interaction between the probe and the CoMoS adsorbing site. It was proposed in [76] that the CO absorption coefficient changes with the local structure of the surface atoms to which the probe is adsorbed.

The experimental fact that the absorption coefficient of CO adsorbed on CoMoS sites in CoMo/Al_2O_3 is different to that of CO adsorbed on CoMo-E/Al_2O_3 indicates that at least part of the surface where CO is adsorbed on the catalysts has metallic character or that sites with metallic character are in the vicinity of the CO-adsorbing sites [77]. Otherwise, no changes in absorbance could be detected. This inference of metallic character in MoS_2 crystallites can be well supported by repeated reports of the metallic character of cobalt-substituted edges and at the S layer at the top of MoS_2 crystallites, observed with STM experiments and explained by DFT calculations [57].

In the case of adsorption on metallic surfaces, the IR selection rule states that a vibrational mode will be IR active only if there is a nonzero projection of the dynamic dipole moment along the surface normal [78]. In other words, the magnitude of the absorption coefficient will depend on the inclination of the adsorbed molecule with respect to the surface normal. The effect is considered to apply to particles down to a few nanometers in size [79, 80], or even to metal carbonyl clusters [81], and has been observed in experiments performed in transmission IR spectroscopy [82, 83].

DFT calculations of different possible local structures of Co or Mo in Co-promoted MoS_2 crystallites showed that the fully promoted MoS_2 crystallite exposes cobalt atoms in fourfold coordination with tetrahedral structure in the S edge and square planar structure in the Mo edge [65]. For the non-fully promoted MoS_2 crystallite, where both Mo and Co are exposed on the edges, it was found that in the S edge Mo and Co are fourfold coordinated in tetrahedral structure and that in the Mo edge Mo is fourfold and fivefold coordinated, while Co is fourfold coordinated and presents pseudo-tetrahedral structure. That is, Mo and Co have a tetrahedral or pseudo-tetrahedral structure, except in the fully promoted Mo edges, where Co has a square planar structure.

The use of the chelating agent leads to higher promotion and presumably to higher proportion of CoMoS sites with Co in square planar structure in fully promoted Mo edges of the MoS_2 crystallite in CoMo-E/Al_2O_3 [76]. In this type of Co local structure the adsorption of CO can be perpendicular to the surface, resulting in an increased absorption coefficient, compared to a hindered adsorption in Co or Mo with tetrahedral or pseudo-tetrahedral local structure that projects a smaller part of the dynamic dipole into the surface normal. Then, the increased absorption coefficient in CoMo-E/Al_2O_3 can be related to a bigger proportion of Co in a square planar local structure in the better promoted catalyst [76].

In this interpretation of an experimental fact (the increased absorption coefficient with the use of EDTA as chelating agent) an important issue of the IR analysis of CO adsorbed on Co-promoted molybdenum catalysts is revealed: the correct quantification of adsorption sites requires the proper assignation of the absorption coefficient for each catalyst.

It is important to highlight that the analysis of CO adsorbed on the several possible structures of the CoMoS sites provided by DFT calculations allowed to understand that the Co atom is the adsorption site, and that as the promotion is enhanced with the use of EDTA as chelating agent more Co in square planar local structure is found in the surface of the MoS_2 crystallites.

The effect of this change in local structure, consequence of the addition of EDTA, in the catalytic activity was analyzed with the HDS of thiophene, dibenzothiophene, and 4,6-dimethyl dibenzothiophene [76]. TOF values are presented in Table 4.1.

The ratio (TOF of CoMoS)/(TOF of MoS) indicated that the addition of EDTA does not have a significant effect on the HDS of thiophene or DBT, meaning that the change in local structure to square planar in the catalysts prepared with EDTA does not have an impact on the HDS of thiophene or DBT: these molecules are transformed independently of the local structure of the promoted site. In the case of 4,6-DMDBT, the TOF's ratio changes with the use of EDTA, from 5.2 in CoMo-E/Al_2O_3 to 4.4 in CoMo/Al_2O_3. Apparently, with this sterically hindered molecule, the change from tetrahedral and/or pseudo-tetrahedral to the open square planar structure induced by the use of a chelating agent as EDTA has a positive effect on the hydrodesulfurization of 4,6-DMDBT.

In summary, the IR analysis of adsorbed CO indicates that the use of EDTA as chelating agent during preparation induces changes in the structure of the CoMoS sites in supported catalysts. These changes have no effect on the TOF of thiophene or DBT, while a positive one is observed in the case of 4,6-DMDBT.

Table 4.1 Turnover frequency for the HDS reaction of S-containing molecules

		TOF × 10^2 (Mo–S site, s^{-1})	TOF × 10^2 (Co–Mo–S site, s^{-1})	$\frac{TOF_{Co-Mo-S}}{TOF_{Mo-S}}$
4,6-DMDBT	Mo	0.11	–	–
	CoMo	–	0.49	4.4
	CoMo-E	–	0.58	5.2
DBT	Mo	0.23	–	–
	CoMo	–	4.02	17.1
	CoMo-E	–	4.18	17.7
T	Mo	3.26	–	–
	CoMo	–	91.7	28.1
	CoMo-E	–	91.3	28.0

Taken from [76] with permission from Elsevier

4.3.2 *Effect of Citric Acid in the Characteristics and Catalytic Performance of Non-promoted and Co-promoted Molybdenum HDS Catalyst*

The use of chelating agents in the preparation of Mo-based catalysts can lead to other modifications in the characteristics of the active phase (besides that in the structure of the CoMoS sites with the use of EDTA explained above), such as the sulfidation extent, edge dispersion, amount of adsorbing sites, level of promotion, and stacking of MoS_2 crystallites [84, 85]. It is important to understand if the changes in the active phase have a significant impact on the HDS catalytic activity. The study of the effect of citric acid (CA) in alumina-supported unpromoted and Co-promoted Mo catalysts was used to analyze which of the changes induced by the presence of the chelating agent have more influence on the HDS catalytic activity. To this end, two series of catalysts with increasing amounts of CA (CA/metal = 0, 1, and 2) were prepared, one of unpromoted Mo catalysts (Mo–CA(0)/Al_2O_3, Mo–CA(1)/Al_2O_3, and Mo–CA(2)/Al_2O_3), and a second one of catalyst promoted with Co (CoMo–CA(0)/Al_2O_3, CoMo–CA(1)/Al_2O_3, and CoMo–CA(2)/Al_2O_3). The calcination step during preparation was avoided to preserve the effect of the organic agent until sulfidation. For comparison, two calcined catalysts were prepared (Mo/Al_2O_3 and CoMo/Al_2O_3) [86].

The effect of CA on the amount and nature (MoS or CoMoS) of adsorbing sites was studied with infrared spectroscopy of adsorbed CO. The results in Table 4.2 show that CA causes a slight decrease in number of adsorbing sites in the case of unpromoted catalysts. In contrast, in the case of Co-promoted catalysts the use of CA has two important consequences: (a) the amount of total adsorbing sites (MoS and CoMoS) is strongly increased, mainly due to an approximately fourfold enlargement of CoMoS sites; (b) in the catalysts prepared with CA, the proportion of CoMoS site is increased: in CoMo–CA(1)/Al_2O_3 and CoMo–CA(2)/Al_2O_3 almost all adsorbing sites are promoted ones.

It is observed in Table 4.3 that the absorption coefficients of catalysts prepared without citric acid are small (21.7 ± 3.7 cm $\mu mole^{-1}$) compared with those of cata-

Table 4.2 Amount ($\mu mole/g_{cat}$) and percentage of active sites in sulfided catalysts evaluated with FT-IR of adsorbed CO

	Mo–S sites	Co–Mo–S sites	Total sites
Mo/Al_2O_3	155	–	155
Mo–CA(0)/Al_2O_3	170	–	170
Mo–CA(1)/Al_2O_3	110	–	110
Mo–CA(2)/Al_2O_3	118	–	118
CoMo/Al_2O_3	62 (47.7%)	68 (52.3%)	130
CoMo–CA(0)/Al_2O_3	37 (26.4%)	103 (73.6%)	140
CoMo–CA(1)/Al_2O_3	10 (5.4%)	175 (94.6%)	185
CoMo–CA(2)/Al_2O_3	11 (4.2%)	253 (95.8%)	264

Taken from [86] with permission from Elsevier

Table 4.3 Absorption coefficients (cm µmole^{-1}) of CO adsorbed on sulfided catalysts

	ε of Co–Mo–S sites
CoMo/Al$_2$O$_3$—(2067 cm^{-1})	24.3
CoMo–CA(0)/Al$_2$O$_3$—(2067 cm^{-1})	19.1
CoMo–CA(1)/Al$_2$O$_3$—(2067 cm^{-1})	32.8
CoMo–CA(2)/Al$_2$O$_3$—(2067 cm^{-1})	27.9

Extracted from [86] with permission from Elsevier

lysts prepared with CA (30.4 ± 3.5 cm µmole^{-1}). As in the case of catalysts prepared with EDTA, the absorption coefficient of CO for CoMoS sites increases in the catalysts prepared with CA even though the vibration frequency of CO remains at 2067 cm^{-1}, suggesting differences in the local structure of Co in the CoMoS site. The increase in the absorption coefficient of adsorbed CO can be explained through a greater proportion of fully promoted Mo edges in the MoS$_2$ crystallites with Co in square planar structure. In contrast, the lower absorption coefficient of CO in catalysts prepared without CA indicates that CO is adsorbed on Co with tetrahedral or pseudo-tetrahedral structures, present in partially promoted Mo edges and also in S edges.

The sulfidation extent is also affected by the presence of CA in the catalyst preparation. From temperature-programmed sulfidation experiments (TPS) of catalysts sulfided at 10 K/min, it was found that the total S/Mo ratio increases from 1.3 and 1.0 in Mo/Al$_2$O$_3$ and Mo–CA(0)/Al$_2$O$_3$ to S/Mo ratios of 2.1 and 2.2 for Mo–CA(1)/Al$_2$O$_3$ and Mo–CA(2)/Al$_2$O$_3$, respectively. Also in Co-promoted catalysts, the S/(Mo + Co) ratio increases from 1.0 and 0.7 in CoMo/Al$_2$O$_3$ and CoMo–CA(0)/Al$_2$O$_3$ to 1.7 and 2.0 for CoMo–CA(1)/Al$_2$O$_3$ and CoMo–CA(2)/Al$_2$O$_3$. Temperature-programmed reduction of sulfide experiments (TPR-S) also pointed to a better sulfidation of unpromoted and Co-promoted catalysts with CA. In the reduction patterns of unpromoted and Co-promoted molybdenum sulfide (see Fig. 4.6 for TPR-S patterns of promoted catalysts), the reduction of stoichiometric MoS$_2$ begins at 452 K and continues until 1233 K. At the final temperature of the experiment the reduction is still in progress, but the S/Mo ratio in the case of unpromoted catalysts and the S/(Mo + Co) ratio in the case of promoted ones increase with the CA content (Table 4.4). These results evidence that the introduction of CA during the preparation of the catalysts induces a better sulfidation.

Using the TPR-S experiments, the value of $\Delta H°$ of reduction of MoS$_2$ in the catalysts can be calculated from a plot of $1/T$ versus ln[H$_2$S], like the one presented in Fig. 4.7 [87]. The results, reported in Table 4.4, showed that the introduction of Co renders the MoS$_2$ crystallite more defective and therefore more reducible in surface and bulk in catalysts with and without CA.

As explained above, several characteristics of the Mo-based catalysts change with the addition of an organic agent as CA. Their catalytic performance was evaluated in the HDS of DBT and 4,6-DMDBT to identify which of the changes is important to the activity. DBT is a good choice to probe the level of promotion of MoS$_2$

Fig. 4.6 TPR-S patterns of promoted sulfided catalysts. (**a**) CoMo/Al_2O_3, (**b**) CoMo–CA(0)/Al_2O_3, (**c**) CoMo–CA(1)/Al_2O_3, (**d**) CoMo–CA(2)/Al_2O_3. Reprinted from [86] with permission from Elsevier

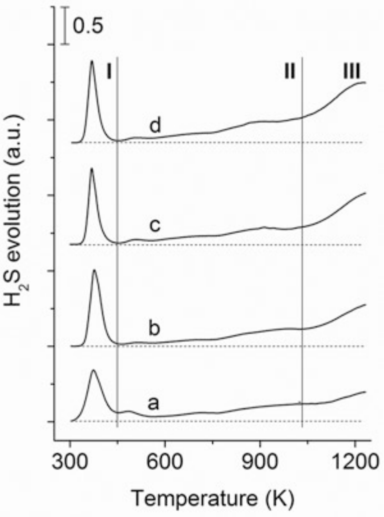

Table 4.4 S/Mo, S/(Mo + Co) ratios, and $\Delta H°_{red}$ from TPR-S experiments

	S/Mo, S/(Mo + Co) (II + III)	$\Delta H°_{red}$ (kJ/g at S)
Mo/Al_2O_3	0.5	79
Mo–CA(0)/Al_2O_3	0.4	70
Mo–CA(1)/Al_2O_3	0.9	71.5
Mo–CA(2)/Al_2O_3	1.4	70
CoMo/Al_2O_3	0.7	46
CoMo–CA(0)/Al_2O_3	0.8	64
CoMo–CA(1)/Al_2O_3	1.0	68
CoMo–CA(2)/Al_2O_3	1.3	60

The enthalpy of reduction was calculated from the H_2S evolution in region III. Extracted from [86] with permission from Elsevier

crystallites, since it is transformed through the hydrogenation route as well as the direct desulfurization one over unpromoted MoS_2, while in the promoted catalysts the former is predominant. The measurement of activity in the 4,6-DMDBT molecule helps to evaluate if the changes induced by the use of CA have an influence on the HDS of refractory molecules that occur mainly through the hydrogenating path [88].

Table 4.5 reports the results of rate constants in both HDS reactions. In the case of unpromoted catalysts, no significant increase is observed in the rate constants with the presence of CA in the HDS of DBT. The TOF values (obtained from the measurement of the number of adsorption sites in the IR analysis of CO) are small

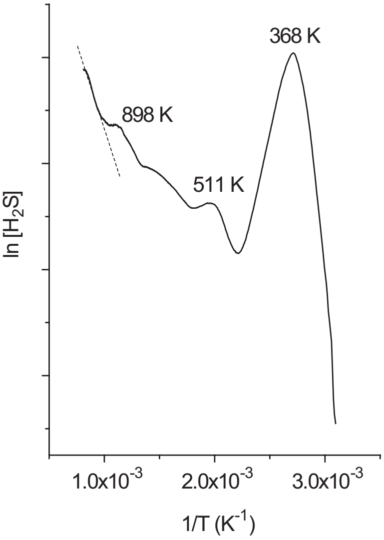

Fig. 4.7 Plot of ln[H_2S] versus 1/*T* of the TPR-S pattern of CoMo–CA(2)/Al_2O_3. The linearization in 1034–1206 K is pointed out by the dotted straight line. Reprinted from [86] with permission from Elsevier

Table 4.5 Turnover frequency (TOF) and rate constant for the HDS of dibenzothiophene

	Rate constant × 10^1 ($cm^3\ g_{Mo+Co}^{-1}\ s^{-1}$)	TOF × 10^2 (Mo–S sites, s^{-1})	TOF × 10^2 (Co–Mo–S sites, s^{-1})
Mo/Al_2O_3	0.81	0.14	–
Mo–CA(0)/Al_2O_3	1.2	0.18	–
Mo–CA(1)/Al_2O_3	1.0	0.26	–
Mo–CA(2)/Al_2O_3	1.2	0.29	–
CoMo/Al_2O_3	5.9	–	2.7
CoMo–CA(0)/Al_2O_3	8.1	–	2.2
CoMo–CA(1)/Al_2O_3	11.6	–	2.3
CoMo–CA(2)/Al_2O_3	15.3	–	2.1

Taken from [86] with permission from Elsevier

for the unpromoted catalysts and do not considerably change with the use of citric acid. This means that the modifications induced by citric acid, as the increase of the sulfidation extent, have little or no effect on the catalytic activity of the MoS site. On the contrary, the incorporation of CA in promoted catalysts leads to an approximately threefold increase in the rate constant. However, the change in the TOF value is not significant. The result indicates that the change in the local structure from mainly tetrahedral (catalysts with no CA) to mainly square planar (catalysts with CA)

Table 4.6 Turnover frequency (TOF) and rate constant (*k*) for the HDS of 4,6-dimethyldibenzothiophene

	$k \times 10^1$ (cm^3 g$_{\mathrm{Mo+Co}}^{-1}$ s^{-1})	TOF × 10^2 (Mo–S sites, s^{-1})	TOF × 10^2 (Co–Mo–S sites, s^{-1})
Mo/Al_2O_3	0.96	0.17	–
CoMo/Al_2O_3	1.1	–	0.38
CoMo–CA(1)/Al_2O_3	2.1	–	0.41
CoMo–CA(2)/Al_2O_3	2.5	–	0.33

Taken from [86] with permission from Elsevier

and the greater sulfidation extent induced by CA have little influence on the intrinsic activity of the catalytic site. Therefore, the increase in the rate constant with CA is related to an increase in the number of promoted active sites.

The incorporation of Co to the MoS_2 phase does not significantly change the HDS activity in 4,6-DMDBT. However, the use of CA duplicates the rate constant (Table 4.6). The fact that the TOF does not change considerably with the incorporation of the promoter or with the addition of CA indicates that the higher sulfidation level of the catalysts prepared with CA, which favors the formation of the more hydrogenating type II and brim active sites, does not affect substantially the intrinsic activity of the catalytic site.

In conclusion, these two examples show that both EDTA and CA induce changes in the sulfided catalysts. The IR analysis of adsorbed CO in catalysts prepared with and without EDTA showed that the absorption coefficient is not the same in both cases, revealing that the electronic structure is different. It was proposed that the local structure of Co in the edges of the MoS_2 crystallite changes with the use of EDTA. The same was observed in catalysts prepared with CA, but this is not the only characteristic that may be modified with the use of a chelating agent. The study of promoted and unpromoted catalysts prepared with CA was useful to understand that the increase in the rate constant with CA is related to an increase in the number of promoted active sites, and that the other characteristics that change with the use of the chelating agent, as the Co local structure and sulfidation extent, have less influence on the catalytic behavior of sulfided catalysts.

4.4 Co(Ni)-Mo(W)-Based Heteropolycompounds as Catalyst Precursors

The synthesis of highly active hydrodesulfurization catalysts depends significantly on the level of promotion reached during catalyst preparation. To achieve a higher number of promoted Co(Ni)-Mo(W)-S sites, it is desirable for the Co(Ni) and Mo(W) atoms to be as close as possible during the activation step of the catalyst. An interesting alternative to achieve this is the use of a single precursor salt that already contains in its structure both atoms, Mo(W) and Co(Ni), in the desired ratio, instead of using two different salt precursors, one for Mo(W) and one for Co(Ni), as in the conventional HDS catalyst preparation procedure. Several experimental works concerning the use of Mo(W) heteropolycompounds (HPC) with different structures as precursor salts for the preparation of HDS catalysts are reported in the scientific literature.

In a recent review, Nikulshin et al. [89] and references therein reported the use of several polyoxometalate structures to prepare hydrotreatment catalysts: Lindqvist $[M_xM'_{6-x}O_{19}]^{(2+x)-}$, Keggin $[XM_{12}O_{40}]^{n-}$, Anderson $[XM_6O_{24}H_6]^{n-}$, Dawson $[X_2M_{18}O_{62}]^{n-}$, Strandberg $[X_2M_5O_{23}]^{n-}$, or Waugh $[Ni_9MoO_{32}]^{6-}$, where M(M′) is a metallic cation and X is a nonmetallic one. However, the most frequently used heteropolymolybdates (heteropolytungstates) for the preparation of catalysts for deep HDS are heteropolyacids with Keggin, Dawson, or Anderson structures, and their Co(Ni) salts [90, 91].

Alumina-supported catalysts synthesized using polyoxometalate structures have mainly been evaluated in the HDS of thiophene and dibenzothiophene [92, 93], and some catalysts supported on mesoporous silica (HMS) have been tested in the HDS of dibenzothiophene [94] and only a few in the HDS of a refractory compound like 4,6-DMDBT or real mixtures such as straight run gas oil (SRGO) or a mixture of SRGO with LCGO [95]. In all cases whatever the polyoxometalate structure used to prepare the catalyst, the performance was better than for similar catalysts prepared from conventional precursors such as ammonium heptamolybdate and nickel or cobalt nitrate.

One of the drawbacks of the use of heteropolycompounds as impregnating salts for the preparation of HDS catalysts is the low stoichiometric Co(Ni)/Mo atomic ratio, which is below the optimal value (0.49) reported for catalysts synthesized using conventional precursors. Some authors have used reduced Keggin-type HPCs to increase the stoichiometric Co(Ni)/Mo ratio from 0.125 to 0.29. In laboratory tests of the hydrodesulfurization of thiophene and 4,6-DMDBT HDS, catalysts prepared with heteropolycompounds showed conversions 10 and 29% higher than their counterparts prepared using conventional precursors, respectively. The higher HDS activity of the catalysts prepared with HPCs was related to an increment in the number of Co-promoted molybdenum sites produced by the close interaction between cobalt and molybdenum in the Keggin structure during the catalyst activation (sulfidation) process [92, 96].

Recently, the optimal Co/Mo ratio has been achieved using a cobalt salt of the dimer $Co_2Mo_{10}O_{39}H_4^{6-}$ with Anderson structure as impregnating precursor for CoMo catalysts supported on alumina, titania, and zirconia and tested in the HDS of thiophene. For all the CoMo catalysts, whatever the support, the best performance was obtained for those prepared with the cobalt salt of the $Co_2Mo_{10}O_{39}H_4^{6-}$ dimer [97]. The superior performance of the catalyst prepared with the dimer was related to the higher dispersion achieved with this preparation method, and to the better cobalt promotion associated to the preservation of the Anderson structure during the catalyst preparation.

4.4.1 *Stability of the Supported Polyoxometalate Structure*

4.4.1.1 Stability During Support Impregnation

An important aspect to be considered, during the catalyst synthesis, is the stability of the heteropolyacid (HPA) or heteropolycompound (HPC) during the impregnation of the support. Several materials have been used to support both types of precursors (HPA and HPC), and their thermal stability depends on the surface characteristics of the support matrix and on the metallic load. Greater stability is achieved when the HPC is impregnated on a support matrix with an isoelectric point (IEP) ≤ 7, for example, on titania [98], silica [97], or silica-containing mesoporous materials like MCM-41 [99] and SBA-15 [100]. For alumina- and zirconia-supported catalysts where the support IEP is >7, the HPA structure is not preserved after impregnation due to the stronger interaction between the electronegative molybdophosphate anions and the electropositive Zr and Al cations, which contribute first to its distortion and then to its breakdown during the impregnation process [94]. To overcome this problem, Griboval et al. [101] proposed the use of a cobalt salt of the reduced Keggin HPA for the preparation of cobalt-promoted alumina-supported HDS catalysts. The preservation of the HPA molecular structure after impregnation was corroborated by Raman and NMR analysis. The higher stability of the reduced salt at a pH value near the isoelectric point of the alumina support (IEP = 8) avoids the interaction of cobalt atoms with the support, preventing the formation of the inactive $CoAl_2O_4$ spinel, allowing for a higher number of cobalt atoms to be available for the formation of the active CoMoS mixed phase, as demonstrated in [70].

In another work, Ramírez et al. [96] used a less interacting support like SBA-15 with 0–15 wt% of titanium oxide grafted on the surface to prepare NiMoP HDS catalysts, using phosphomolybdic acid and nickel citrate as precursors for the active phase. The use of the heteropolyacid led to catalysts with higher HDS activity in the HDS of 4,6-DMDBT than those prepared conventionally with ammonium heptamolybdate, nickel nitrate, and phosphoric acid. The observed changes in catalytic activity were related to a twofold increase in the activity of the catalytic sites. Additionally, it was found that grafting TiO_2 to the surface of the SBA matrix stabilizes and preserves the ordered structure of the latter during the calcination process, and the structure of the heteropoly anion in the impregnation step [92].

4.4.1.2 Stability Under Thermal Treatment

The preparation of HDS catalysts with MoS_2 structures well promoted by Co or Ni requires to maintain the Ni(Co) and Mo elements close to each other. Therefore, the structure of the heteropolycompound must be preserved up until the catalyst is activated by sulfidation. The calcination of the active-phase precursor salts, which is normally applied before activating the catalyst by sulfidation, must be avoided when using heteropolycompounds as active-phase precursors since this step is detrimental to the structure of the HPC and therefore to the promotion and final performance of the catalyst, as reported by Romero-Galarza et al. [70] for alumina-supported CoMoP catalysts. For the case of CoMoP HDS catalysts prepared by impregnating alumina with an aqueous solution of a reduced heteropolycompound with Keggin structure, $Co_{7/2}PMo_{12}O_{40}$, Fig. 4.8 reveals that the catalytic activity of the uncalcined catalyst was 1.33 times higher than the calcined one. This effect was related to a higher number of Co-promoted molybdenum sites that were quantified by CO adsorption experiments (Table 4.7).

In summary, the improvement in HDS activity when using polyoxometalate structures as precursors for the synthesis of Co(Ni)Mo hydrotreatment catalysts is related to maintaining stable the structure of the heteropolyoxometalate up until the activation step in order to achieve high promotion of the molybdenum species after the sulfidation process. The good performance of the HDS catalysts prepared with polyoxometalate structures can be explained because molybdenum and cobalt(nickel)

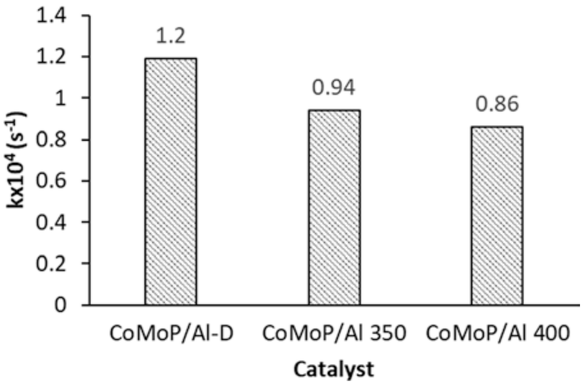

Fig. 4.8 Pseudo first-order reaction rate constants for dried (CoMoP/Al-D) and calcined CoMoP/Al catalysts. HDS of 4,6-DMDBT at $T = 320$ °C and 1200 psig of hydrogen. D = dried catalyst, 350 and 400 are the calcination temperatures in Celsius degrees. Adapted from [70] with permission of Elsevier

Table 4.7 Quantitative analysis from CO adsorption experiments and pseudo first-order rate constants for CoMoP/Al catalysts prepared at different calcination temperatures

Catalyst	$k \times 10^4$ (s^{-1})	Mo sites 2110 cm^{-1} (mol/g_{cat}) × 10^5	CoMo sites 2070 cm^{-1} (mol/g_{cat}) × 10^5	Total sites (mol/g_{cat}) × 10^5
CoMoP/Al-D	1.19	2.6	3.6	6.2
CoMoP/Al350	0.94	3.0	2.7	5.7
CoMoP/Al400	0.86	1.7	2.0	3.7
CoAHM/Al400	0.47	1.8	1.6	3.4

HDS of 4,6-DMDBT after 6 h of reaction at $T = 320$ °C and 1200 psig of hydrogen. D = dried catalyst, 350 and 400 are the calcination temperatures in Celsius degrees. *AHM* Ammonium heptamolybdate

Extracted from [70] with permission of Elsevier are part of the same compound structure, and this avoids the formation of inactive phases formed by the interaction of the promotor atoms with the support framework, and favors the formation of a greater number of promoted sites in the Co(Ni)–Mo–S nanoclusters.

4.5 Sulfidation Methodology

The final step in the preparation of supported hydrodesulfurization catalysts is the transformation of the active-phase oxide precursors into sulfides. The operating conditions at which the sulfidation process takes place have crucial importance in the active-phase morphology and catalytic performance as shown by several authors [1, 102–106].

The sulfidation of the oxide catalyst precursors can lead to two different types of promoted structures in CoMo/Al_2O_3 catalysts named “type I” and “type II.” “Type I” structure displays low HDS activity and is typical of molybdenum sulfide interacting with the alumina support through Mo-O-Al bridges. The other structure called “type II” has high HDS activity and is obtained when the sulfidation of the oxide precursor is complete, and Mo and Al are not bonded.

Most of the studies on sulfidation have been made at laboratory scale, with sulfidation usually carried out flowing a gaseous stream of H_2S/H_2 through the catalyst bed at atmospheric pressure and temperatures ranging from 573 to 723 K. In contrast, industrial sulfidation involves the use of high pressures and liquid sulfiding agents (i.e., dimethyl disulfide) [107, 108], where also temperature and H_2S concentration gradients in the catalyst bed must be accounted for in the sulfidation procedure [109].

The sulfidation-reduction of supported Mo oxide species supported on alumina to produce supported MoS_2 is well known and has been studied by several authors [102, 110–112]. The first systematic study of the sulfidation of MoO_3 supported on alumina was made by Arnoldy et al. [110] (see Fig. 4.9).

In general, the sulfidation-reduction process can follow two transformation routes: (a) oxygen-sulfur exchange in Mo^{6+} oxide species followed by reduction, or (b) reduction of Mo oxide species followed by sulfidation as Fig. 4.9 shows. The $O \rightarrow S$ exchange (I) in Mo^{6+} species is an easy process that takes place without change in the structure, and occurs at temperatures lower than 500 K. In this process, the reaction consumes H_2S and releases water. The reduction of partially or fully exchanged species consumes hydrogen and releases H_2S. The suggested route for the sulfidation of hydrodesulfurization catalyst is to achieve first full sulfidation of the Mo^{6+} species at low temperatures and then increase the temperature to reduce MoS_3 to MoS_2.

The reduction of oxide Mo^{6+} to Mo^{4+} species involves a change of structure and occurs at higher temperatures, consuming H_2 and producing water. The subsequent sulfidation of reduced Mo^{4+} oxide species is not easy and may be at the origin of the presence of partially sulfided species of low activity in the final catalyst.

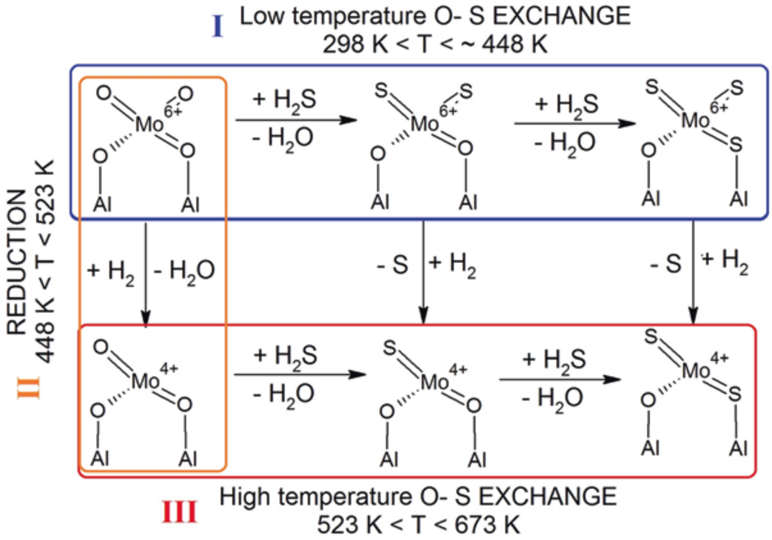

Fig. 4.9 Sulfidation paths for supported MoO_3/Al_2O_3. Adapted from [110] with permission from Elsevier

According to literature [111], better levels of sulfidation are achieved when the major part of the H_2S consumption takes place before Mo^{6+} is converted into Mo^{4+} [113]. Arnoldy et al. suggested that full exchange of oxygen by sulfur in Mo^{6+} species at low temperatures can be achieved by using a low heating rate (1 K/min) during sulfidation. This will give time to do the exchange of oxygen by sulfur at the lower temperatures and then, at the higher temperatures reached at the end of the heating ramp, perform the reduction of Mo^{6+} to Mo^{4+}. This is especially relevant since strong support interactions and small particle size could slow down the sulfidation kinetics of Mo and Ni [114, 115].

During temperature-programmed reduction or sulfidation (TPR or TPRS) experiments carried out to analyze the reduction or sulfidation behavior of the supported species, it must be considered that the reduction or sulfidation peaks associated to the different species can overlap significantly due to the presence of highly defective surface species making difficult the interpretation of the thermogram traces.

With the aim of studying the role of the sulfidation process in the case of hydrodesulfurization catalysts prepared with or without an organic additive (citric acid), Villarreal et al. [116] prepared and tested $NiMo/SiO_2/Al_2O_3$ hydrodesulfurization catalysts using/or not citric acid as additive and 4 wt% SiO_2 grafted on γ-Al_2O_3 as support. The use of citric acid can increase the level of promotion, reduce the metal-support interaction, and enhance the hydrogenation/desulfurization selectivity due to the better sulfidation of the catalysts [84, 86, 112, 114, 117–119]. To investigate the effect of the sulfidation heating ramp on the catalyst activity and selectivity, $NiMo/SiO_2/Al_2O_3$ catalysts prepared with or without citric acid (CA) were tested in the hydrodesulfurization of 4,6-DMDBT using different rates of heating during sulfidation (1, 3, 10 K/min), as displayed in Fig. 4.10.

As shown in Fig. 4.10, the catalysts with and without citric acid (CA/NiMo and NiMo) increase their HDS activity when the sulfidation heating ramp is slow. For the catalyst with citric acid the activity increased 100% when the heating ramp went from 10 to 1 K/min. Furthermore, the effect of the slow heating rate was higher when citric acid was used because the slower heating rate avoided the rapid decomposition of the organic and preserved the metal dispersion [86, 120, 121].

Using temperature-programed sulfidation (TPS) it was possible to evaluate the consumption of H_2S (Table 4.8). For both catalysts, with and without citric acid, the amount of H_2S consumed before the main peak of H_2S production was greater when slow heating rates were used.

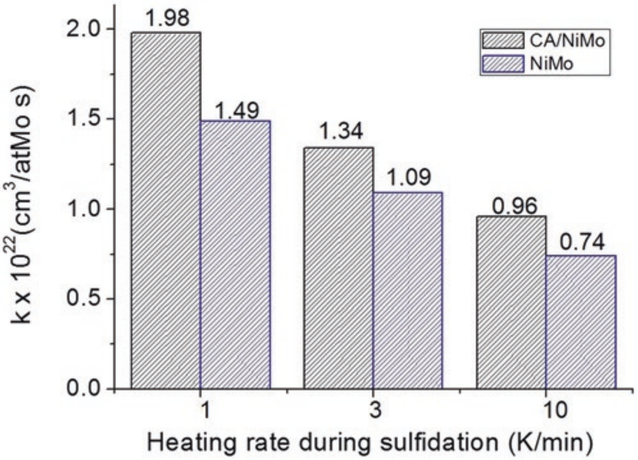

Fig. 4.10 Catalytic activity of $NiMo/SiO_2/Al_2O_3$ and $CA/NiMo/SiO_2/Al_2O_3$ in the HDS of 4,6-DMDBT (593 K and 1200 PSI) previously sulfided in a flow of H_2S/H_2 (15% vol.) at 673 K heating at 1, 3, and 10 K/min. Reprinted from [116] with permission from Elsevier

Table 4.8 H_2S consumption, and sulfidation levels (S/Mo) for $NiMo/SiO_2/Al_2O_3$ and $CA/NiMo/SiO_2/Al_2O_3$ catalyst

	Heating rate during sulfidation (K/min)	H_2S consumption (mmols)[a]	S/Mo atomic ratio[a]
$NiMo/SiO_2/Al_2O_3$	1	0.41	1.73
	3	0.32	1.36
	10	0.15	0.64
$CA/NiMo/SiO_2/Al_2O_3$	1	0.41	1.75
	3	0.38	1.64
	10	0.33	1.43

[a] Calculated at the end of the TPS experiment

Adapted from [116] with permission from Elsevier

These results show that although the sulfidation is not complete, a slower rate of heating leads to better sulfidation levels and improved catalytic activity, probably because it favors the sulfidation of Mo^{6+} species before its reduction to Mo^{4+}. Accordingly, the catalysts sulfided with a slow heating rate consume the most part of H_2S at low temperatures. Oxysulfidic species, resulting from partial sulfidation, are difficult to sulfide and are known as type I species with low HDS activity [114, 122].

To study the effect of the sulfidation methodology in NiMo catalysts prepared from Keggin heteropolyacids supported on alumina grafted with 4 wt% TiO_2 or SiO_2 (TiO_2/Al_2O_3 or SiO_2/Al_2O_3), the catalysts were sulfided in one or two steps using in all cases a heating ramp of 1 K/min and the following temperature programs: (a) 673 K for 4 h, (b) 563 K for 4 h, and (c) a first plateau at 423 K for 2 h followed by a second plateau at 563 K for 3 h. After sulfidation, the activity of these catalysts was tested in the HDS of 4,6-DMDBT.

The pseudo first-order reaction rate constants and the individual hydrogenation and direct desulfurization rate constants are presented in Table 4.9. Sulfiding directly from ambient to 673 K is the worst procedure leading to lower global activities and also lower hydrogenation and direct desulfurization individual rate constants. The best procedure seems to be the use of a two-temperature-step sulfidation. In this case, regardless of the support, the global activity is the highest.

Low-temperature sulfidation or sulfiding in two steps seems to increase slightly the hydrogenation rate constant. In contrast, clear increases in the direct desulfurization constant are observed when sulfiding at lower temperature or in two steps. In the analysis of these results, no account was taken of the changes in dispersion caused by the different sulfidation temperatures.

The above results indicate that to obtain more active HDS catalysts it is convenient to establish a sulfidation procedure that allows the largest exchange of S in the low-temperature region, before reducing Mo. This will enhance the sulfidation of the catalyst and the formation of more active type II catalytic sites, leading to a higher activity, particularly when the catalysts are prepared using organic additives, such as citric acid [86, 115, 118, 123–125].

Table 4.9 Rate constants (k) in the HDS of 4,6-DMDBT (593 K and 1200 PSI), catalysts were sulfided in a flow of H_2S/H_2 (15% vol.)

Catalyst	Sulfidation program	$k \times 10^{22}$ cm^3/at Mo–s	k_{HYD} cm^3/at Mo–s	k_{DDS} cm^3/at Mo–s
$NiMoP/TiO_2/Al_2O_3$	(a) 673 K, 4 h	0.83	0.65	0.18
	(b) 563 K, 4 h	1.10	0.89	0.21
	(c) 423 K, 2 h; 563 K, 3 h	1.24	0.84	0.40
$NiMoP/SiO_2/Al_2O_3$	(a) 673 K, 4 h	0.59	0.52	0.07
	(b) 563 K, 4 h	0.70	0.57	0.13
	(c) 423 K, 2 h; 563 K, 3 h	0.80	0.60	0.20

4.6 Final Comments

The performance of supported hydrodesulfurization catalysts is highly sensitive to the preparation method. Important improvements in activity and selectivity can be achieved through the selection of the catalyst support, the use of organic additives, and the use of different precursor salts, particularly heteropolycompounds that include in their structure the adequate ratio of Co(Ni) to Mo. It is also clear that the procedure used for activating hydrodesulfurization catalysts by sulfidation can substantially change the catalyst performance. The use of a slow heating ramp (1 K/min) or several ramps during the sulfidation procedure can help to achieve higher extents of sulfidation and consequently more active catalysts.

Hydrogenation and hydrodesulfurization reactions take place at different active sites located in different parts of the active-phase nanoparticle. Therefore, the particle morphology influences the activity and hydrogenation/desulfurization selectivity of the catalysts. Thus, careful attention must be paid to the consequences of changing the catalyst preparation procedure since, given the different nature of the desulfurization and hydrogenation active sites, a change that benefits one type of site can be deleterious to the other. Generally, a combination of strategies is required to achieve high-performing HDS catalysts.

Acknowledgements We acknowledge Facultad de Química-UNAM, PAIP 5000-9072, for financial support.

References

1. H. Topsøe, B.S. Clausen, F.E. Massoth, Hydrotreating catalysis, in *Catalysis*, ed. by A. J. R. Boudart, M., (Springer-Verlag, Berlin Heidelberg New York, 1996), pp. 1–269. https://doi.org/10.1007/978-3-642-61040-0_1
2. L.S. Byskov, J.K. Nørskov, B.S. Clausen, H. Topsøe, DFT calculations of unpromoted and promoted MoS_2-based hydrodesulfurization catalysts. J. Catal. **187**, 109–122 (1999). https://doi.org/10.1006/jcat.1999.2598
3. P. Raybaud, J. Hafner, G. Kresse, S. Kasztelan, H. Toulhoat, Ab Initio study of the H_2–H_2S/MoS_2 gas–solid interface: the nature of the catalytically active sites. J. Catal. **189**, 129 (2000). https://doi.org/10.1006/jcat.1999.2698
4. P. Raybaud, J. Hafner, G. Kresse, S. Kasztelan, H. Toulhoat, Structure, energetics, and electronic properties of the surface of a promoted MoS_2 catalyst: an ab initio local density functional study. J. Catal. **190**, 128–143 (2000). https://doi.org/10.1006/jcat.1999.2743
5. H. Schweiger, P. Raybaud, G. Kresse, H. Toulhoat, Shape and edge sites modifications of MoS_2 catalytic nanoparticles induced by working conditions: a theoretical study. J. Catal. **207**, 76–87 (2002). https://doi.org/10.1006/jcat.2002.3508
6. H. Schweiger, P. Raybaud, H. Toulhoat, Promoter sensitive shapes of Co(Ni)MoS nanocatalysts in sulfo-reductive conditions. J. Catal. **212**, 33–38 (2002). https://doi.org/10.1006/jcat.2002.3737
7. S. Cristol, J.F. Paul, E. Payen, D. Bougeard, S. Clémendot, F. Hutschka, Theoretical study of the MoS_2 (100) surface: a chemical potential analysis of sulfur and hydrogen coverage. 2. Effect of the total pressure on surface stability. J. Phys. Chem. B **106**, 5659–5667 (2002). https://doi.org/10.1021/jp0134603

8. M.V. Bollinger, K.W. Jacobsen, J.K. Nørskov, Atomic and electronic structure of MoS_2 nanoparticles. Phys. Rev. B **67**, 085410 (2003). https://doi.org/10.1103/PhysRevB.67.085410
9. B. Hinnemann, J.K. Nørskov, H. Topsøe, A density functional study of the chemical differences between type I and type II MoS_2-based structures in hydrotreating catalysts. J. Phys. Chem. B **109**, 2245–2253 (2005). https://doi.org/10.1021/jp048842y
10. S. Helveg, J.V. Lauritsen, E. Laegsgaard, I. Stensgaard, J.K. Nørskov, B.S. Clausen, H. Topsøe, F. Besenbacher, Atomic-scale structure of single-layer MoS_2 nanoclusters. Phys. Rev. Lett. **84**, 951–954 (2000). https://doi.org/10.1103/PhysRevLett.84.951
11. J.V. Lauritsen, S. Helveg, E. Lægsgaard, I. Stensgaard, B.S. Clausen, H. Topsøe, F. Besenbacher, Atomic-scale structure of Co-Mo-S nanoclusters in hydrotreating catalysts. J. Catal. **197**, 1–5 (2001). https://doi.org/10.1006/jcat.2000.3088
12. A.K. Tuxen, H.G. Füchtbauer, B. Temel, B. Hinnemann, H. Topsøe, K.G. Knudsen, F. Besenbacher, J.V. Lauritsen, Atomic-scale insight into adsorption of sterically hindered dibenzothiophenes on MoS_2 and Co–Mo–S hydrotreating catalysts. J. Catal. **295**, 146–154 (2012). https://doi.org/10.1016/j.jcat.2012.08.004
13. Á. Logadóttir, P.G. Moses, B. Hinnemann, N.Y. Topsøe, K.G. Knudsen, H. Topsøe, J.K. Nørskov, A density functional study of inhibition of the HDS hydrogenation pathway by pyridine, benzene, and H_2S on MoS_2-based catalysts. Catal. Today **111**, 44–51 (2006). https://doi.org/10.1016/j.cattod.2005.10.018
14. R. Candia, O. Sørensen, J. Villadsen, N.-Y. Topsøe, B.S. Clausen, H. Topsøe, Effect of sulfiding temperature on activity and structures of Co-Mo/Al_2O_3 catalysts. II. Bull. Soc. Chim. Belg. **93**, 763–773 (1984). https://doi.org/10.1002/bscb.19840930818
15. J. Ramirez, S. Fuentes, G. Díaz, M. Vrinat, M. Breysse, M. Lacroix, Hydrodesulphurization activity and characterization of sulphided molybdenum and cobalt-molybdenum catalysts. Comparison of alumina-, silica-alumina- and titania-supported catalysts. Appl. Catal. **52**, 211–224 (1989). https://doi.org/10.1016/S0166-9834(00)83385-0
16. J. Ramírez, F. Sánchez-Minero, Support effects in the hydrotreatment of model molecules. Catal. Today **130**, 267–271 (2008). https://doi.org/10.1016/j.cattod.2007.10.103
17. H. Shimada, T. Sato, Y. Yoshimura, J. Hiraishi, A. Nishijima, Support effect on the catalytic activity and properties of sulfided molybdenum catalysts. J. Catal. **110**, 275–284 (1988). https://doi.org/10.1016/0021-9517(88)90319-3
18. M. Breysse, J.L. Portefaix, M. Vrinat, Support effects on hydrotreating catalysts. Catal. Today **10**, 489–505 (1991). https://doi.org/10.1016/0920-5861(91)80035-8
19. A. Stanislaus, A. Marafi, M.S. Rana, Recent advances in the science and technology of ultra low sulfur diesel (ULSD) production. Catal. Today **153**, 1–68 (2010). https://doi.org/10.1016/j.cattod.2010.05.011
20. H. Shimada, Morphology and orientation of MoS_2 clusters on Al_2O_3 and TiO_2 supports and their effect on catalytic performance. Catal. Today **86**, 17–29 (2003). https://doi.org/10.1016/S0920-5861(03)00401-2
21. J. Ramirez, L. Cedeño, G. Busca, The role of titania support in Mo-based hydrodesulfurization catalysts. J. Catal. **184**, 59–67 (1999). https://doi.org/10.1006/jcat.1999.2451
22. J. Ramírez, G. Macías, L. Cedeño, A. Gutiérrez-Alejandre, R. Cuevas, P. Castillo, The role of titania in supported Mo, CoMo, NiMo, and NiW hydrodesulfurization catalysts: analysis of past and new evidences. Catal. Today **98**, 19–30 (2004). https://doi.org/10.1016/j.cattod.2004.07.050
23. L. Coulier, J.A.R. van Veen, J.W. Niemantsverdriet, TiO_2-supported Mo model catalysts: Ti as promoter for thiophene HDS. Catal. Lett. **79**, 149–155 (2002). https://doi.org/10.1023/A:1015312509749
24. C. Arrouvel, M. Breysse, H. Toulhoat, P. Raybaud, A density functional theory comparison of anatase (TiO_2)- and γ-Al_2O_3-supported MoS_2 catalysts. J. Catal. **232**, 161–178 (2005). https://doi.org/10.1016/j.jcat.2005.02.018
25. P. Castillo-Villalón, J. Ramírez, R. Cuevas, P. Vázquez, R. Castañeda, Influence of the support on the catalytic performance of Mo, CoMo, and NiMo catalysts supported on Al_2O_3

and TiO_2 during the HDS of thiophene, dibenzothiophene, or 4,6-dimethyldibenzothiophene. Catal. Today **259**, 140–149 (2015). https://doi.org/10.1016/j.cattod.2015.06.008

26. R.R. Chianelli, G. Berhault, P. Raybaud, S. Kasztelan, J. Hafner, H. Toulhoat, Periodic trends in hydrodesulfurization: in support of the Sabatier principle. Appl. Catal. A Gen. **227**, 83–96 (2002). https://doi.org/10.1016/S0926-860X(01)00924-3
27. J. Ramírez, A. Gutierrez-Alejandre, Characterization and hydrodesulfurization activity of W-based catalysts supported on Al_2O_3–TiO_2 mixed oxides. J. Catal. **170**, 108–122 (1997). https://doi.org/10.1006/jcat.1997.1713
28. D. Costa, C. Arrouvel, M. Breysse, H. Toulhoat, P. Raybaud, Edge wetting effects of γ-Al_2O_3 and anatase-TiO_2 supports by MoS_2 and CoMoS active phases: A DFT study. J. Catal. **246**, 325–343 (2007). https://doi.org/10.1016/j.jcat.2006.12.007
29. T.G. Kaufmann, A. Kaldor, G.F. Stuntz, M.C. Kerby, L.L. Ansell, Catalysis science and technology for cleaner transportation fuels. Catal. Today **62**, 77–90 (2000). https://doi.org/10.1016/S0920-5861(00)00410-7
30. P. Gripka, O. Bhan, W. Whitecotton, J. Esteban, Catalytic strategies to meet gasoline sulphur limits. Digit. Refining Process. Oper. Maintenance (2015). www.digitalrefining.com/article/1001120
31. C. Song, An overview of new approaches to deep desulfurization for ultra-clean gasoline, diesel fuel and jet fuel. Catal. Today **86**, 211–263 (2003). https://doi.org/10.1016/S0920-5861(03)00412-7
32. G.E.P. Box, J.S. Hunter, W.G. Hunter, *Statistics for Experimenters: Design, Innovation, and Discovery*, 2nd edn. (John Wiley & Sons, Inc., Hoboken, NJ, 2005)
33. H. Shimada, M. Kurita, T. Sato, Y. Yoshimura, T. Hirata, T. Konakahara, K. Sato, A. Nishihima, Support effect on the hydrocracking activity of molybdenum catalysts. Chem. Lett. **13**, 1861–1864 (1984). https://doi.org/10.1246/cl.1984.1861
34. T. Klicpera, M. Zdražil, High surface area MoO_3/MgO: preparation by the new slurry impregnation method and activity in sulphided state in hydrodesulphurization of benzothiophene. Catal. Lett. **58**, 47–51 (1999). https://doi.org/10.1023/A:1019036724583
35. T. Klicpera, M. Zdražil, Synthesis of a high surface area monolayer MoO_3/MgO catalyst in a $(NH_4)_6Mo_7O_{24}$/MgO/methanol slurry, and its hydrodesulfurization activity. J. Mater. Chem. **10**, 1603–1608 (2000). https://doi.org/10.1039/b001375g
36. T. Klimova, D. Solís Casados, J. Ramirez, New selective Mo and NiMo HDS catalysts supported on Al_2O_3-MgO(x) mixed oxides. Catal. Today **43**, 135–146 (1998). https://doi.org/10.1016/S0920-5861(98)00142-4
37. D. Solís, T. Klimova, J. Ramírez, T. Cortez, NiMo/Al_2O_3–MgO(x) catalysts: the effect of the prolonged exposure to ambient air on the textural and catalytic properties. Catal. Today **98**, 99–108 (2004). https://doi.org/10.1016/j.cattod.2004.07.024
38. D. Mey, S. Brunet, C. Canaff, F. Maugé, C. Bouchy, F. Diehl, HDS of a model FCC gasoline over a sulfided CoMo/Al_2O_3 catalyst: Effect of the addition of potassium. J. Catal. **227**, 436–447 (2004). https://doi.org/10.1016/j.jcat.2004.07.013
39. R. Zhao, C. Yin, H. Zhao, C. Liu, Effects of modified Co-Mo catalysts for FCC gasoline HDS on catalytic activity. Pet. Sci. Technol. **22**, 1455–1463 (2004). https://doi.org/10.1081/LPET-200027756
40. J.T. Miller, W.J. Reagan, J.A. Kaduk, C.L. Marshall, A.J. Kropf, Selective hydrodesulfurization of FCC naphtha with supported MoS_2 catalysts: the role of cobalt. J. Catal. **193**, 123–131 (2000). https://doi.org/10.1006/jcat.2000.2873
41. C. Sudhakar, Selective hydrodesulfurization of cracked naphtha using hydrotalcite-supported catalysts, Patent 5,851,382, 1998
42. F. Trejo, M. Rana, J. Ancheyta, CoMo/MgO–Al_2O_3 supported catalysts: an alternative approach to prepare HDS catalysts. Catal. Today **130**, 327–336 (2008). https://doi.org/10.1016/j.cattod.2007.10.105
43. P. Nikulshin, D. Ishutenko, Y. Anashkin, A. Mozhaev, A. Pimerzin, Selective hydrotreating of FCC gasoline over KCoMoP/Al_2O_3 catalysts prepared with $H_3PMo_{12}O_{40}$: Effect of metal loading. Fuel **182**, 632–639 (2016). https://doi.org/10.1016/j.fuel.2016.06.016

44. D. Ishutenko, P. Nikulshin, A. Pimerzin, Relation between composition and morphology of K(Co)MoS active phase species and their performances in hydrotreating of model FCC gasoline. Catal. Today **271**, 16–27 (2016). https://doi.org/10.1016/j.cattod.2015.11.025
45. D.D. Whitehurst, T. Isoda, I. Mochida, Present state of the art and future challenges in the hydrodesulfurization of polyaromatic sulfur compounds. Adv. Catal. **42**, 345–471 (1998). https://doi.org/10.1016/S0360-0564(08)60631-8
46. J.A.R. van Veen, E. Gerkema, A.M. van der Kraan, P.A.J.M. Hendriks, H. Beens, A ^{57}Co Mössbauer emission spectrometric study of some supported CoMo hydrodesulfurization catalysts. J. Catal. **133**, 112–123 (1992). https://doi.org/10.1016/0021-9517(92)90189-O
47. R. Cattaneo, F. Rota, R. Prins, An XAFS study of the different influence of chelating ligands on the HDN and HDS of γ-Al_2O_3-supported NiMo catalysts. J. Catal. **199**, 318–327 (2001). https://doi.org/10.1006/jcat.2001.3170
48. A.J. van Dillen, R.J.A.M. Terörde, D.J. Lensveld, J.W. Geus, K.P. de Jong, Synthesis of supported catalysts by impregnation and drying using aqueous chelated metal complexes. J. Catal. **216**, 257–264 (2003). https://doi.org/10.1016/S0021-9517(02)00130-6
49. M. Sun, D. Nicosia, R. Prins, The effects of fluorine, phosphate and chelating agents on hydrotreating catalysts and catalysis. Catal. Today **86**, 173–189 (2003). https://doi.org/10.1016/S0920-5861(03)00410-3
50. G. Kishan, J.A.R. van Veen, J.W. Niemantsverdriet, Realistic surface science models of hydrodesulfurization catalysts on planar thin-film supports: the role of chelating agents in the preparation of CoW/SiO_2 catalysts. Top. Catal. **29**, 103–110 (2004). https://doi.org/10.1023/B:TOCA.0000029792.45691.d4
51. M.S. Rana, J. Ramírez, A. Gutiérrez-Alejandre, J. Ancheyta, L. Cedeño, S.K. Maity, Support effects in CoMo hydrodesulfurization catalysts prepared with EDTA as a chelating agent. J. Catal. **246**, 100–108 (2007). https://doi.org/10.1016/j.jcat.2006.11.025
52. N. Frizi, P. Blanchard, E. Payen, P. Baranek, M. Reibeilleau, C. Dupuy, J.P. Dath, Genesis of new HDS catalysts through a careful control of the sulfidation of both Co and Mo atoms: Study of their activation under gas phase. Catal. Today **130**, 272–282 (2008). https://doi.org/10.1016/j.cattod.2007.10.109
53. C. Wivel, R. Candia, B.S. Clausen, S. Mørup, H. Topsøe, On the catalytic significance of a Co-Mo-S phase in Co-Mo/Al_2O_3 hydrodesulfurization catalysts: combined in situ Mössbauer emission spectroscopy and activity studies. J. Catal. **68**, 453–463 (1981). https://doi.org/10.1016/0021-9517(81)90115-9
54. H. Topsøe, B.S. Clausen, R. Candia, C. Wivel, S. Mørup, In situ Mössbauer emission spectroscopy studies of unsupported and supported sulfided Co-Mo hydrodesulfurization catalysts: evidence for and nature of a Co-Mo-S phase. J. Catal. **68**, 433–452 (1981). https://doi.org/10.1016/0021-9517(81)90114-7
55. N.-Y. Topsøe, H. Topsøe, Characterization of the structures and active sites in sulfided Co-Mo/Al_2O_3 and Ni-Mo/Al_2O_3 catalysts by NO chemisorption. J. Catal. **84**, 386–401 (1983). https://doi.org/10.1016/0021-9517(83)90010-6
56. P. Raybaud, Understanding and predicting improved sulfide catalysts: Insights from first principles modeling. Appl. Catal. A Gen. **322**, 76–91 (2007). https://doi.org/10.1016/j.apcata.2007.01.005
57. J.V. Lauritsen, J. Kibsgaard, G.H. Olesen, P.G. Moses, B. Hinnemann, S. Helveg, J.K. Nørskov, B.S. Clausen, H. Topsøe, E. Lægsgaard, F. Besenbacher, Location and coordination of promoter atoms in Co- and Ni-promoted MoS_2-based hydrotreating catalysts. J. Catal. **249**, 220–233 (2007). https://doi.org/10.1016/j.jcat.2007.04.013
58. M.J. Ledoux, O. Michaux, G. Agostini, P. Panissod, CoMo sulfide catalysts studies by metal solid NMR: the question of the existence of the chemical synergy. J. Catal. **96**, 189–201 (1985). https://doi.org/10.1016/0021-9517(85)90372-0
59. M.J. Ledoux, On the structure of cobalt sulfide catalysts. Catal. Lett. **1**, 429–431 (1988). https://doi.org/10.1007/BF00766202
60. S.M.A.M. Bouwens, J.A.R. van Veen, D.C. Koningsberger, V.H.J. de Beer, R. Prins, Extended X-ray absorption fine structure determination of the structure of cobalt in carbon-supported

Co and Co-Mo sulfide hydrodesulfurization catalysts. J. Phys. Chem. **95**, 123–134 (1991). https://doi.org/10.1021/j100154a028

61. S.M.A.M. Bouwens, F.B.M. van Zon, M.P. van dijk, A.M. van der Kraan, V.H.J. de Beer, J.A.R. van Veen, D.C. Koningsberger, On the structural differences between alumina-supported CoMoS type I and alumina-, silica-, and carbon-supported CoMoS type ii phases studied by XAFS, MES, and XPS. J. Catal. **146**, 375–393 (1994). https://doi.org/10.1006/jcat.1994.1076
62. J.T. Miller, C.L. Marshall, A.J. Kropf, (Co)MoS2/alumina hydrotreating catalysts: an EXAFS study of the chemisorption and partial oxidation with O_2. J. Catal. **202**, 89–99 (2001). https://doi.org/10.1006/jcat.2001.3273
63. M.W.J. Crajé, S.P.A. Louwers, V.H.J. de Beer, R. Prins, A.M. van der Kraan, E.X.A.F.S. An, Study on the So-Called "Co-Mo-S" phase in Co/C and Co-Mo/C, compared with a Mössbauer emission spectroscopy study. J. Phys. Chem. **96**, 5445–5452 (1992). https://doi.org/10.1021/j100192a048
64. L. van Haandel, G.M. Bremmer, E.J.M. Hensen, T. Weber, The effect of organic additives and phosphoric acid on sulfidation and activity of (Co)Mo/Al_2O_3 hydrodesulfurization catalysts. J. Catal. **351**, 95–106 (2017). https://doi.org/10.1016/j.jcat.2017.04.012
65. A. Travert, C. Dujardin, F. Maugé, E. Veilly, S. Cristol, J.F. Paul, E. Payen, CO adsorption on CoMo and NiMo sulfide catalysts: a combined IR and DFT study. J. Phys. Chem. B **110**, 1261–1270 (2006). https://doi.org/10.1021/jp0536549
66. Y. Zhu, Q.M. Ramasse, M. Brorson, P.G. Moses, L.P. Hansen, C.F. Kisielowski, S. Helveg, Visualizing the stoichiometry of industrial-style Co-Mo-S catalysts with single-atom sensitivity. Angew. Chem. Int. Ed. Engl. **53**, 10723–10727 (2014). https://doi.org/10.1002/anie.201405690
67. F. Maugé, J.C. Lavalley, FT-IR study of CO adsorption on sulfided Mo/Al_2O_3 unpromoted or promoted by metal carbonyls: titration of sites. J. Catal. **137**, 69–76 (1992). https://doi.org/10.1016/0021-9517(92)90139-9
68. N.-Y. Topsøe, A. Tuxen, B. Hinnemann, J.V. Lauritsen, K.G. Knudsen, F. Besenbacher, H. Topsøe, Spectroscopy, microscopy and theoretical study of NO adsorption on MoS_2 and Co–Mo–S hydrotreating catalysts. J. Catal. **279**, 337–351 (2011). https://doi.org/10.1016/j.jcat.2011.02.002
69. J. Ramirez, P. Castillo, L. Cedeño, R. Cuevas, M. Castillo, J.M. Palacios, A. López-Agudo, Effect of boron addition on the activity and selectivity of hydrotreating CoMo/Al_2O_3 catalysts. Appl. Catal. A Gen. **132**, 317–334 (1995). https://doi.org/10.1016/0926-860X(95)00166-2
70. A. Romero-Galarza, A. Gutiérrez-Alejandre, J. Ramírez, Analysis of the promotion of CoMoP/Al_2O_3 HDS catalysts prepared from a reduced H–P–Mo heteropolyacid Co salt. J. Catal. **280**, 230–238 (2011). https://doi.org/10.1016/j.jcat.2011.03.021
71. H. Topsøe, R. Candia, N.-Y. Topsøe, B.S. Clausen, On the state of the Co-Mo-S Model. Bull. Des Sociétés Chim. Belges. **93**, 783–806 (1984). https://doi.org/10.1002/bscb.19840930820
72. J.B. Peri, Computerized infrared studies of Mo/Al_2O_3 and Mo/SiO_2 catalysts. J. Phys. Chem. **86**, 1615–1622 (1982). https://doi.org/10.1021/j100206a028
73. J. Bachelier, M. Tilliette, M. Cornac, J.C. Duchet, J.C. Lavalley, D. Cornet, Sulfided Co-Mo/Al_2O_3 catalysts: carbon monoxide chemisorption and surface structures. Bull. Soc. Chim. Belg. **93**, 743–750 (1984). https://doi.org/10.1002/bscb.19840930816
74. B. Müller, A.D. van Langeveld, J.A. Moulijn, H. Knözinger, Characterization of sulfided Mo/Al_2O_3 catalysts by temperature-programmed reduction and low-temperature Fourier transform infrared spectroscopy of adsorbed carbon monoxide. J. Phys. Chem. **97**, 9028–9033 (1993). https://doi.org/10.1021/j100137a031
75. F. Maugé, A. Vallet, J. Bachelier, J.C. Duchet, J.C. Lavalley, Preparation, characterization, and activity of sulfided catalysts promoted by $Co(CO)_3NO$ thermodecomposition. J. Catal. **162**, 88–95 (1996). https://doi.org/10.1006/jcat.1996.0262
76. P. Castillo-Villalón, J. Ramirez, R. Castañeda, Relationship between the hydrodesulfurization of thiophene, dibenzothiophene, and 4,6-dimethyl dibenzothiophene and the local structure

of Co in Co-Mo-S sites: Infrared study of adsorbed CO. J. Catal. **294**, 54–62 (2012). https://doi.org/10.1016/j.jcat.2012.07.002

77. M. Osawa, K.-I. Ataka, K. Yoshii, Y. Nishikawa, Surface-enhanced infrared spectroscopy: the origin of the absorption enhancement and band selection rule in the infrared spectra of molecules adsorbed on fine metal particles. Appl. Spectrosc. **47**, 1497–1502 (1993). https://doi.org/10.1366/0003702934067478
78. J. Fan, M. Trenary, Symmetry and the surface infrared selection rule for the determination of the structure of molecules on metal surfaces. Langmuir **10**, 3649–3657 (1994). https://doi.org/10.1021/la00022a044
79. N. Sheppard, J. Erkelens, Vibrational spectra of species adsorbed on surfaces: forms of vibrations and selection rules for regular arrays of adsorbed species. Appl. Spectrosc. **38**, 471–485 (1984). https://doi.org/10.1366/0003702844555133
80. R.G. Greenler, D.R. Snider, D. Witt, R.S. Sorbello, The metal-surface selection rule for infrared spectra of molecules adsorbed on small metal particles. Surf. Sci. **118**, 415–428 (1982). https://doi.org/10.1016/0039-6028(82)90197-2
81. S.F.A. Kettle, The metal surface selection rule: its extension to transition metal carbonyl clusters. Spectrochim. Acta A Mol. Biomol. Spectrosc. **54**, 1639–1643 (1998). https://doi.org/10.1016/S1386-1425(98)00091-2
82. Y. Nishikawa, K. Fujiwara, T. Shima, A study of the qualitative and quantitative analysis of nanogram samples by transmission infrared spectroscopy with the use of Silver Island films. Appl. Spectrosc. **45**, 747–751 (1991)
83. M. Osawa, M. Ikeda, Surface-enhanced infrared absorption of p-nitrobenzoic acid deposited on Silver Island films: contributions of electromagnetic and chemical mechanisms. J. Phys. Chem. **95**, 9914–9919 (1991). https://doi.org/10.1021/j100177a056
84. N. Rinaldi, T. Kubota, Y. Okamoto, Effect of citric acid addition on the hydrodesulfurization activity of MoO_3/Al_2O_3 catalysts. Appl. Catal. A Gen. **374**, 228–236 (2010). https://doi.org/10.1016/j.apcata.2009.12.015
85. N. Rinaldi, K.A.-D. Usman, T. Kubota, Y. Okamoto, Preparation of Co–Mo/B_2O_3/Al_2O_3 catalysts for hydrodesulfurization: effect of citric acid addition. Appl. Catal. A Gen. **360**, 130–136 (2009). https://doi.org/10.1016/j.apcata.2009.03.006
86. P. Castillo-Villalón, J. Ramirez, J.A. Vargas-Luciano, Analysis of the role of citric acid in the preparation of highly active HDS catalysts. J. Catal. **320**, 127–136 (2014). https://doi.org/10.1016/j.jcat.2014.09.021
87. P. Afanasiev, On the interpretation of temperature programmed reduction patterns of transition metals sulphides. Appl. Catal. A Gen. **303**, 110–115 (2006). https://doi.org/10.1016/j.apcata.2006.02.014
88. F. Bataille, J.-L. Lemberton, P. Michaud, G. Pérot, M. Vrinat, M. Lemaire, E. Schulz, M. Breysse, S. Kasztelan, Alkyldibenzothiophenes hydrodesulfurization-promoter effect, reactivity, and reaction mechanism. J. Catal. **191**, 409–422 (2000). https://doi.org/10.1006/jcat.1999.2790
89. P. Nikulshin, A. Mozhaev, C. Lancelot, P. Blanchard, E. Payen, C. Lamonier, Hydroprocessing catalysts based on transition metal sulfides prepared from Anderson and dimeric Co_2Mo_{10}-heteropolyanions. a review. C. R. Chim. **19**, 1276–1285 (2016). https://doi.org/10.1016/j.crci.2015.10.006
90. J. Liang, M. Wu, P. Wei, J. Zhao, H. Huang, C. Li, Y. Lu, Y. Liu, C. Liu, Efficient hydrodesulfurization catalysts derived from Strandberg P–Mo–Ni polyoxometalates. J. Catal. **358**, 155–167 (2018). https://doi.org/10.1016/j.jcat.2017.11.026
91. N. Al-zaqri, A. Alsalme, S.F. Adil, A. Alsaleh, S.G. Alshammari, S.I. Alresayes, R. Alotaibi, M. Al-Kinany, M.R.H. Siddiqui, Comparative catalytic evaluation of nickel and cobalt substituted phosphomolybdic acid catalyst supported on silica for hydrodesulfurization of thiophene. J. Saudi Chem. Soc. **21**, 965–973 (2017). https://doi.org/10.1016/j.jscs.2017.05.004
92. A. Griboval, P. Blanchard, E. Payen, M. Fournier, J.L. Dubois, Alumina supported HDS catalysts prepared by impregnation with new heteropolycompounds. Comparison with cata-

lysts prepared by conventional Co–Mo–P coimpregnation. Catal. Today **45**, 277–283 (1998). https://doi.org/10.1016/S0920-5861(98)00230-2

93. A. Pimerzin, A. Mozhaev, A. Varakin, K. Maslakov, P. Nikulshin, Comparison of citric acid and glycol effects on the state of active phase species and catalytic properties of CoPMo/Al_2O_3 hydrotreating catalysts. Appl. Catal. B Environ. **205**, 93–103 (2017). https://doi.org/10.1016/j.apcatb.2016.12.022
94. B. Pawelec, S. Damyanova, R. Mariscal, J.L.G. Fierro, I. Sobrados, J. Sanz, L. Petrov, HDS of dibenzothiophene over polyphosphates supported on mesoporous silica. J. Catal. **223**, 86–97 (2004). https://doi.org/10.1016/j.jcat.2004.01.018
95. P.A. Nikulshin, A.V. Mozhaev, A.A. Pimerzin, V.V. Konovalov, A.A. Pimerzin, CoMo/Al_2O_3 catalysts prepared on the basis of Co_2Mo_{10}-heteropolyacid and cobalt citrate: effect of Co/Mo ratio. Fuel **100**, 24–33 (2012). https://doi.org/10.1016/j.fuel.2011.11.028
96. J. Ramírez, A. Gutiérrez-Alejandre, F. Sánchez-Minero, V. MacÍas-Alcántara, P. Castillo-Villalón, L. Oliviero, F. Maugé, HDS of 4,6-DMDBT over NiMoP/(x)Ti-SBA-15 catalysts prepared with $H_3PMo_{12}O_{40}$. Energy Fuel **26**, 773–782 (2012). https://doi.org/10.1021/ef201590g
97. C.I. Cabello, F.M. Cabrerizo, A. Alvarez, H.J. Thomas, Decamolybdodicobaltate(III) heteropolyanion: structural, spectroscopical, thermal and hydrotreating catalytic properties. J. Mol. Catal. A Chem. **186**, 89–100 (2002). https://doi.org/10.1016/S1381-1169(02)00043-2
98. S. Damyanova, J.L.G. Fierro, Structural features and thermal stability of titania-supported 12-molybdophosphoric heteropoly compounds. Chem. Mater. **10**, 871–879 (1998). https://doi.org/10.1021/cm970639a
99. L.R. Pizzio, P.G. Vázquez, C.V. Cáceres, M.N. Blanco, Supported Keggin type heteropolycompounds for ecofriendly reactions. Appl. Catal. A Gen. **256**, 125–139 (2003). https://doi.org/10.1016/S0926-860X(03)00394-6
100. L. Lizama, T. Klimova, Highly active deep HDS catalysts prepared using Mo and W heteropolyacids supported on SBA-15. Appl. Catal. B Environ. **82**, 139–150 (2008). https://doi.org/10.1016/j.apcatb.2008.01.018
101. A. Griboval, P. Blanchard, L. Gengembre, E. Payen, M. Fournier, J.L. Dubois, J.R. Bernard, Hydrotreatment catalysts prepared with heteropolycompound: characterisation of the oxidic precursors. J. Catal. **188**, 102–110 (1999). https://doi.org/10.1006/jcat.1999.2633
102. Y. Okamoto, A. Kato, N.R. Usman, T. Fujikawa, H. Koshika, I. Hiromitsu, T. Kubota, Effect of sulfidation temperature on the intrinsic activity of Co–MoS_2 and Co–WS_2 hydrodesulfurization catalysts. J. Catal. **265**, 216–228 (2009). https://doi.org/10.1016/j.jcat.2009.05.003
103. Y. Gochi, C. Ornelas, F. Paraguay, S. Fuentes, L. Alvarez, J.L. Rico, G. Alonso-Núñez, Effect of sulfidation on Mo-W-Ni trimetallic catalysts in the HDS of DBT. Catal. Today **107–108**, 531–536 (2005). https://doi.org/10.1016/j.cattod.2005.07.068
104. B.M. Vogelaar, N. Kagami, T.F. van der Zijden, A.D. van Langeveld, S. Eijsbouts, J.A. Moulijn, Relation between sulfur coordination of active sites and HDS activity for Mo and NiMo catalysts. J. Mol. Catal. A Chem. **309**, 79–88 (2009). https://doi.org/10.1016/j.molcata.2009.04.018
105. V.P. Fedin, J. Czyzniewska, R. Prins, T. Weber, Supported molybdenum–sulfur cluster compounds as precursors for HDS catalysts. Appl. Catal. A Gen. **213**, 123–132 (2001). https://doi.org/10.1016/S0926-860X(00)00894-2
106. W. Qian, A. Ishihara, Y. Aoyama, T. Kabe, Sulfidation of nickel- and cobalt-promoted molybdenum–alumina catalysts using a radioisotope ^{35}S-labeled H_2S pulse tracer method. Appl. Catal. A Gen. **196**, 103–110 (2000). https://doi.org/10.1016/S0926-860X(99)00454-8
107. C. Geantet, J.-M.M. Millet, *Design of Heterogeneous Catalysts*, 1st edn. (Wiley-VCH Verlag GmbH & Co. KGaA, Weinheim, 2009). https://doi.org/10.1002/9783527625321
108. M. Tang, H. Ge, W. Fan, G. Wang, Z. Lyu, X. Li, Presulfidation and activation mechanism of Mo/Al_2O_3 catalyst sulfided by ammonium thiosulfate. Korean J. Chem. Eng. **31**, 1368–1376 (2014). https://doi.org/10.1007/s11814-014-0053-z
109. T.C. Ho, S.C. Reyes, Design of catalyst sulfiding procedures. Chem. Eng. Sci. **45**, 2633–2638 (1990). https://doi.org/10.1016/0009-2509(90)80152-5

110. P. Arnoldy, J.A.M. van den Heijkant, G.D. de Bok, J.A. Moulijn, Temperature-programmed sulfiding of MoO_3/Al_2O_3 catalysts. J. Catal. **92**, 35–55 (1985). https://doi.org/10.1016/0021-9517(85)90235-0
111. T. Weber, J.C. Muijsers, J.H.M.C. van Wolput, C.P.J. Verhagen, J.W. Niemantsverdriet, Basic reaction steps in the sulfidation of crystalline MoO_3 to MoS_2 , as studied by X-ray photoelectron and infrared emission spectroscopy. J. Phys. Chem. **100**, 14144–14150 (1996). https://doi.org/10.1021/jp961204y
112. C. Bara, A.-F. Lamic-Humblot, E. Fonda, A.-S. Gay, A.-L. Taleb, E. Devers, M. Digne, G.D. Pirngruber, X. Carrier, Surface-dependent sulfidation and orientation of MoS_2 slabs on alumina-supported model hydrodesulfurization catalysts. J. Catal. **344**, 591–605 (2016). https://doi.org/10.1016/j.jcat.2016.10.001
113. H. Farag, Effect of sulfidation temperatures on the bulk structures of various molybdenum precursors. Energy Fuel **16**, 944–950 (2002). https://doi.org/10.1021/ef0102972
114. L. van Haandel, G.M. Bremmer, E.J.M. Hensen, T. Weber, Influence of sulfiding agent and pressure on structure and performance of $CoMo/Al_2O_3$ hydrodesulfurization catalysts. J. Catal. **342**, 27–39 (2016). https://doi.org/10.1016/j.jcat.2016.07.009
115. L. van Haandel, M. Bremmer, P.J. Kooyman, J.A.R. van Veen, T. Weber, E.J.M. Hensen, Structure-activity correlations in hydrodesulfurization reactions over Ni-promoted $Mo_xW_{(1-x)}S_2/Al_2O_3$ Catalysts. ACS Catal. **5**, 7276–7287 (2015). https://doi.org/10.1021/acscatal.5b01806
116. A. Villarreal, J. Ramírez, L. Cedeño-Caero, P. Castillo-Villalón, A. Gutiérrez-Alejandre, Importance of the sulfidation step in the preparation of highly active $NiMo/SiO_2/Al_2O_3$ hydrodesulfurization catalysts. Catal. Today **250**, 60–65 (2015). https://doi.org/10.1016/j.cattod.2014.03.035
117. T. Kubota, N. Rinaldi, K. Okumura, T. Honma, S. Hirayama, Y. Okamoto, In situ XAFS study of the sulfidation of $Co–Mo/B_2O_3/Al_2O_3$ hydrodesulfurization catalysts prepared by using citric acid as a chelating agent. Appl. Catal. A Gen. **373**, 214–221 (2010). https://doi.org/10.1016/j.apcata.2009.11.023
118. J. Escobar, M.C. Barrera, A.W. Gutiérrez, J.E. Terrazas, Benzothiophene hydrodesulfurization over NiMo/alumina catalysts modified by citric acid. Effect of addition stage of organic modifier. Fuel Process. Technol. **156**, 33–42 (2017). https://doi.org/10.1016/j.fuproc.2016.09.028
119. L. van Haandel, E.J.M. Hensen, T. Weber, FT-IR study of NO adsorption on MoS_2/Al_2O_3 hydrodesulfurization catalysts: effect of catalyst preparation. Catal. Today **292**, 67–73 (2017). https://doi.org/10.1016/j.cattod.2016.07.028
120. A.V. Pashigreva, G.A. Bukhtiyarova, O.V. Klimov, G.S. Litvak, A.S. Noskov, Influence of the heat treatment conditions on the activity of the $CoMo/Al_2O_3$ catalyst for deep hydrodesulfurization of diesel fractions. Kinet. Catal. **49**, 812–820 (2008). https://doi.org/10.1134/S0023158408060062
121. H. Li, M. Li, Y. Chu, F. Liu, H. Nie, Essential role of citric acid in preparation of efficient NiW/Al_2O_3 HDS catalysts. Appl. Catal. A Gen. **403**, 75–82 (2011). https://doi.org/10.1016/j.apcata.2011.06.015
122. E.J.M. Hensen, V.H.J. de Beer, J.A.R. van Veen, R.A. van Santen, A refinement on the notion of type I and II (Co)MoS phases in hydrotreating catalysts. Catal. Lett. **84**, 59–67 (2002). https://doi.org/10.1023/A:1021024617582
123. P. Blanchard, C. Lamonier, A. Griboval, E. Payen, New insight in the preparation of alumina supported hydrotreatment oxidic precursors: a molecular approach. Appl. Catal. A Gen. **322**, 33–45 (2007). https://doi.org/10.1016/j.apcata.2007.01.018
124. L. Bing, A. Tian, J. Li, K. Yi, F. Wang, C. Wu, G. Wang, The effects of chelating agents on $CoMo/TiO_2–Al_2O_3$ hydrodesulfurization catalysts. Catal. Lett. **148**, 1309–1314 (2018). https://doi.org/10.1007/s10562-018-2331-6
125. Y. Zhang, W. Han, X. Long, H. Nie, Redispersion effects of citric acid on $CoMo/\gamma\text{-}Al_2O_3$ hydrodesulfurization catalysts. Catal. Commun. **82**, 20–23 (2016). https://doi.org/10.1016/j.catcom.2016.04.012

Chapter 5
Electron Microscopy Techniques to Study Structure/Function Relationships in Catalytic Materials

Álvaro Mayoral, Paz del Angel, and Manuel Ramos

5.1 Introduction

Electron microscopy instruments have become standard tools for the understanding of structure/function relationships at atomic level in matter, mainly when studying complex crystallographic structures in both fresh and spent catalytic materials. Scanning electron microscope (SEM) is mostly used for understanding surface characteristics with high magnification varying from 20× to about 300,000× and spatial resolution of 10 to 100 nm; however, modern versions of SEM claim spatial resolution of ~1 nm at 30 kV of operational voltages [1]. And scanning and transmission electron microscopes (STEM/TEM) are mainly used to obtain crystallographic information on matter [2], including Z-atomic contrast, interlayer distances, dislocations, morphology, turbostracity (curvatures), and inclusive temperature dependence reactivity under nanometric scale bar resolution [3, 4]. One important feature when using STEM/TEM units is the capacity of achieving spectroscopy studies to determine chemical surface's compositions by applying energy-disperse or energy electron-loss spectroscopies [5, 6]. However, many other interesting

---

Á. Mayoral
Center for High-resolution Electron Microscopy (ChEM), School of Physical Science and Technology (SPST), ShanghaiTech University, 393 Middle Huaxia Road, Pudong, Shanghai 201210, China
e-mail: amayoral@shanghaitech.edu.cn

P. del Angel (✉)
Laboratorio de Microscopía Electrónica, Instituto Mexicano del Petróleo, Ciudad de México, Mexico
e-mail: pangel@imp.mx

M. Ramos
Departamento de Física y Matemáticas, Instituto de Ingeniería y Tecnología, Universidad Autónoma de Cd. Juárez, Chihuahua, Mexico
e-mail: manuel.ramos@uacj.mx

J. M. Domínguez-Esquivel, M. Ramos (eds.), *Advanced Catalytic Materials: Current Status and Future Progress*, https://doi.org/10.1007/978-3-030-25993-8_5

phenomena can be observed to be studied related to inelastic scattering [7], electron radiation damage [8], in situ phase formation [9, 10], and optical design which goes more along the lines of developing modern techniques and applications in STEM/TEM; here we focus solely on the usage of this powerful tool to understand structure/function relationships on catalytic materials, with special emphasis on layered chalcogenides for hydrodesulfurization, zeolitic support, bimetallic tungsten-zirconia oxides, and "in situ *operando*" carburization effects on cobalt-promoted molybdenum disulfide (Co/MoS_2) and electron holography. In this particular chapter we present three different cases of study on **the heterogeneous catalytic zeolites**: This material is to be encountered among the most important heterogeneous catalysts, especially for petroleum refining [11]. They were discovered in the year 1756 and are described as crystalline aluminosilicates, having a three-dimensional porous network composed by SiO_4 and AlO_4 tetrahedral, as shown in Fig. 5.1a [12]. These tetrahedrals are linked to each other through oxygen bridges (Fig. 5.1b, c)

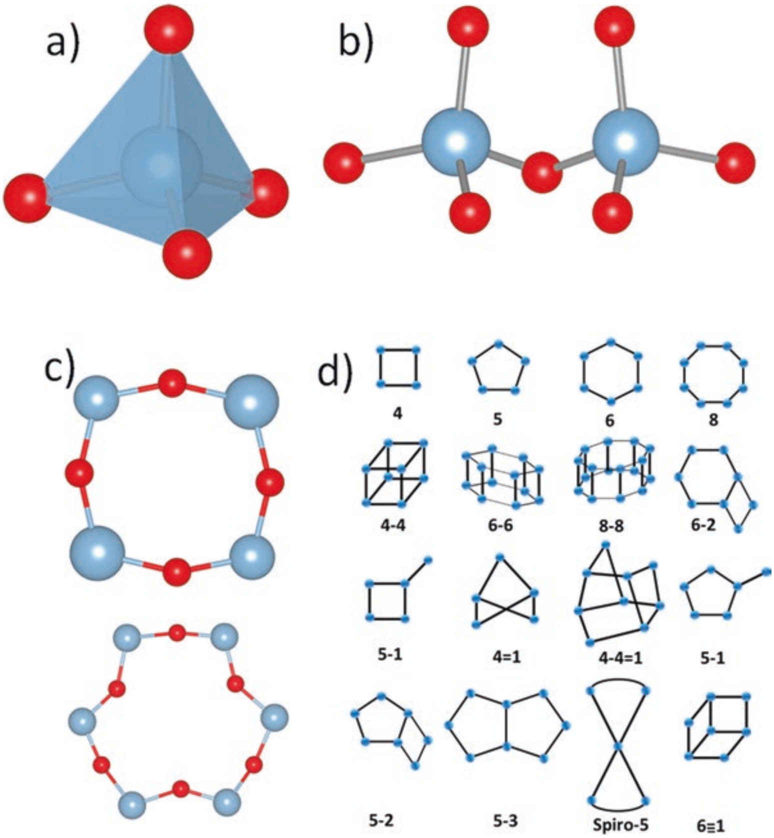

Fig. 5.1 (**a**) Basic unit, the tetrahedron with the "T" atom in the center, in blue, surrounded by four oxygens. (**b**) Two tetrahedra linked by O bridges. (**c**) Four-member ring (top) and six-member ring bottom. (**d**) Schematic representation of the secondary building units (SBUs)

leading to the formation of the secondary building units (SBUs), Fig. 5.1d, that finally are interconnected into the three-dimensional space forming the final material composed by channels and/or cages. The structural parameters of these solids confer them exceptional properties for different catalytical processes.

Probably, the most direct one can be extracted from the chemical formula of zeolites, in which due to the different charges of Al (3+) compared to Si (4+) each Al unit introduces a negative charge into the framework that needs to be compensated by cations in order to achieve an electroneutral framework. These cations can be partially or totally exchanged, giving as a result that one of the major applications of zeolites is the ability to soften the water by removing Ca^{2+} [13]. Another important characteristic of zeolites of interest in catalysis refining is the case of the acidity that they exhibit when the cation that compensates the charge is a proton that can act as Brönsted centers [14]. On the other hand, the relative lattice instability that is associated to the presence of Al^{3+} favors migration of Al outside the lattice framework generally denoted as extra framework aluminum especially when the materials are rich in Al content and are subjected to thermal treatments in the presence of steam or other chemicals. The species generated are believed to be responsible to give zeolites Lewis acidity, conferring zeolites Brønsted and Lewis acid sites ascribed to the OH groups between Al and Si tetrahedra and extra framework aluminum, respectively. One of the first examples of industrial application of zeolites dates to 1953 when Union Carbide commercialized synthetic zeolites for industrial separation and purification purposes, starting for the drying of natural gas [13]. Few years later, the same company marketed the process for normal isoparaffin separation, being the first time where molecular sieves were used in a bulk separation reaction. In 1962, zeolite X was introduced by Mobil Oil as a cracking catalyst. Fluid catalytic cracking (FCC) is the most important process in refineries to improve the yields of gasoline resulting in the treatment of liquefied petroleum gas (LPG) distillate and C3 olefin in the presence of zeolite Y and ZSM-5. Rare earth metals containing zeolite Y are employed for octane making, as the metal incorporation enhances the hydrothermal stability retaining the activity within the FCC regenerator [14]. Meanwhile, ZSM-5-based material is employed to enhance the octane number of paraffin and aromatic rich gasoline which is produced through a control of the Si/Al ratio of the porous matrix. **Tungstate Zirconia (WO_3–ZrO_2)**: The chemical solid acids such as sulfated zirconia (SO_4–ZrO_2) or tungstate zirconia (WO_3–ZrO_2) have received significant attention in the last decade due to their catalytic properties, which come mainly from their chemical acidic features. These solid catalysts offer several advantages over liquid acids; for instance, these materials are not corrosive like sulfuric or hydrofluoric acids and require no extra separation processes [15]; mainly as described in the literature, tungstate zirconia has been used in reactions that will require an acid function as catalyst according to Hino and Arata [16]. Tungstate zirconia has been assessed in several reactions such as isomerization of alkanes [17], esterification and transesterification [18, 19], acetylation of alcohols and phenols [20], dehydration of alcohols [21], and alkylation reactions [22]. From these studies, it is clear that the modification of zirconia by tungsten oxide produces dispersed WO_x clusters that are responsible for creation/formation of

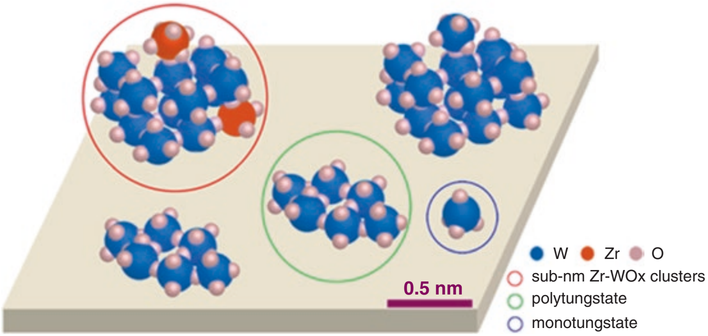

Fig. 5.2 Schematic drawing representation of mono-tungstates (blue circle), poly-tungstates (green circle), Zr–WO_3 clusters (red circle), and WO_3 crystallites (without circle) supported on ZrO_2 surfaces (image taken from ref. [14])

active acid sites [23–25]. Different WO_x species have been proposed to coexist on the surface, from mono- and poly-tungstate species up to the formation of WO_x clusters and WO_3 crystallites as it is presented in Fig. 5.2 [26]. The morphology features on those structures have been studied by different characterization techniques, including electron microscopy and spectroscopic techniques, allowing to determine important information regarding the dispersion, nanostructure, and domain size of the WO_x species on zirconia supports.

The size and structure of the WO_x species are as shown in Fig. 5.3; different acid sites of WO_x species can nucleate growth over zirconia matrix, ranging from mono- to poly-tungstate species. Lewis and Brønsted sites can interplay a role with the matrix support causing one solid-state acidic catalytic material [27].

Layered Transition Metal Sulfides: These are used commercially to produce low-contaminant liquid fuels at oil refineries, due to its natural capacity to perform hydrotreatment catalytic reactions leading to removal of sulfur content molecules during fluid catalytic cracking (FCC) process [28]. The removal of those sulfur chemical compounds is desired to achieve a less atmospheric pollution due to combustion, also known as a reduction on emissions [29]. The layered solid-state structure of molybdenum disulfide (MoS_2) catalytic material has been studied with high success by X-ray crystallography, scanning, tunneling, and transmission electron microscopy [30, 31]; its structure consists of S–Mo–S chemical bonds forming hexagonal arrays with space group hexagonal R3m maintained stacked along c-crystallographic direction with van der Waals weak bonding; experimentally and theoretically an interlayer distance of ~6.2 Å was found as it is presented in Fig. 5.4. Having a weak van der Waals chemical bonding between layers has made this material also attractive for its usage as low- and high-temperature material for mechanical lubrication [32]. MoS_2 has a semiconducting electronic structure with theoretical band gap of ~1.9 eV and experimental value of ~1.6 eV; however as it has been demonstrated when it is combined with cobalt or nickel atoms the semiconducting nature changes into metallic as confirmed by many authors [33, 34]; this change on

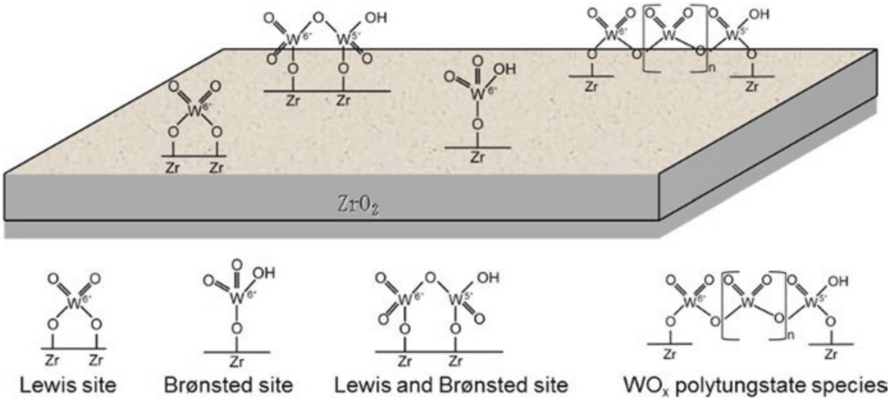

Fig. 5.3 Representation of Lewis and Brønsted sites, from mono-tungstate to poly-tungstate species (image taken from ref. [27])

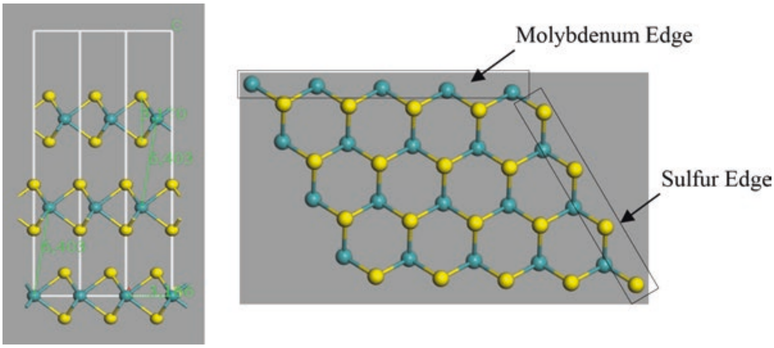

Fig. 5.4 Molecular models for molybdenum disulfide catalytic material. Left: *R*3*m* space group lattice with $a = b = 3.16$ Å and $c = 18.4$ Å parameters and angles of $\alpha = \beta = 90°$ and $\gamma = 120°$. Right: Side view of large-array lattice showing (001) basal plane and indicating sulfur and molybdenum edge terminations

electronic structure is caused due to direct bonding between metal and metal (Co–Mo, Ni–Mo), as described by Topsøe et al. [35], leading to electron donation as described in detail by Ramos et al. [36], having cobalt atoms occupying 1/8th at octahedral sites and 1/2 at tetrahedral sites; however, when it comes to chemical catalytic activity, theoretical and experimental evidence dictates that just at the presence of dangling bonds in (1010) and (1010) edge planes are the responsible for accommodate Co or Ni atoms as well for breaking of sulfur compounds to occur [28], having basal (0001) plane as insert for adsorption/reaction of chemical components during FCC process.

On the other hand, the structure/function relationships as observed by electron microscopy techniques determine that with a variation of chemical precursors and synthesis method MoS_2 can be packed in spheres, triangular prism, and nanorods

[37] and flowerlike [38]. Moreover, by using ultra-resolution TEM instruments it has been possible to determine atomistic observations of (0001) basal plane, edges, dislocations, and (1010) plane surfaces with high accuracy [31], and with the aid of special sample holders that enable to perform "in situ *operando*" experimentation it has been possible to make direct observation of carbonization in fresh Co/MoS_2 catalytic material at 350–450 °C which are operational temperatures during hydroprocessing reactions [39]. As well, electron beam radiation damage during observations made at 80, 120, and 200 kV in single MoS_2 layers, as described by García et al. [9] and Casillas et al., was able to estimate "in situ" experimental evidence of mechanical resilience even at 120 nN of external applied force during TEM observations [40].

5.2 Characterization Methods for Catalytic Materials

Considering the great importance of zeolites in both industrial and academic fields several characterization methods have been developed to gain knowledge of the structural features. X-ray diffraction (XRD) is one of the most extended methods for understanding crystallographic structure of those materials as it is sensitive to long-range order of the periodic framework. However, there are many aspects that can influence the XRD patterns such as structural defects, crystallite size, purity of the phase, or cationic site occupation. Thus, the ideal requirement to apply this technique would be a clean crystalline material that would lead into sharp high-resolution patterns. Initially, X-ray diffraction was used as a first test to check if the material had been done or if the crystallization process had gone up to completion. Nowadays, it also encompasses lots of information regarding the structure of the material. Many of the advances in the structural information derived from zeolitic science are the direct result of the improvement of the powered X-ray equipment, and of course the combination with other characterization techniques such as nuclear magnetic resonance (NMR), neutron diffraction, or electron microscopy. The typical steps that one can follow in order to determine the crystal structure can be described as follows: (i) obtain a suitable sample, (ii) collect the data, (iii) determine a trial structure using ab initio methods, and (iv) refine the data. Neutron scattering (NS) is a unique method that allows to study the structure and the dynamics of a great variety of materials at molecular and at atomic level. For the case of zeolites [41], NS is being used to obtain structural information using powder diffraction to complementary X-ray diffraction data [42]. Information on crystal growth [43] can also be extracted by small-angle neutron scattering (SANS) or the dynamical studies on the adsorption of molecules can be followed with inelastic scattering (INS) and/or quasi-elastic NS (QENS). As already mentioned, zeolites can be synthesized or modified to obtain their protonic form which are used in acid catalysis and a good example of their Brønsted acidity was the possibility of protonating water [44].

By INS, the experimental data of the vibrational spectra can be compared with simulated ab initio and to determine the location of the acid sites of even high-silica zeolites at the atomic level [45]. On the other hand, QENS can be employed to study the molecular diffusion of zeolites; this parameter is of particular importance as catalytical applications as shape-selective catalysis or separations are governed by the molecular diffusion along the pores of the reactants [46, 47]. Solid-state nuclear magnetic resonance (NMR) is a powerful characterization method as it provides information of the local environment of specific atoms and their surroundings, which are directly involved in active catalytic sites by observing a variety of the magnetically active nuclei of the framework and extra framework species [48, 49]. In addition, this technique of analysis can be used to assist X-ray diffraction methods for structural elucidation. In zeolites the Si atoms are coordinated to four oxygens forming the tetrahedra giving a series of peaks which can be attributed to SiO_4 in five different environments depending on the number of AlO_4 units to which they are coordinated allowing the determination of the Si/Al ratio [47].

5.2.1 Transmission Electron Microscopy for Sensitive Materials

One of the most advanced methods in order to gain zeolitic information is based on transmission electron microscopy (TEM), which can provide unique information on several organic and especially inorganic solids as it is the only method that offers direct images of the material, combined with diffraction information and spectroscopic analyses. The major limiting factor that one can encounter when trying to apply this technique is related to the high energetic flux of electrons that is irradiated onto the materials. There are two main beam damage factors that limit the lifetime of matter under the electron beam: (i) knock-on damage [41] and (ii) radiolysis [41]. Knock-on damage consists of the disruption of the framework due to the displacement of the atoms conforming the structure; there is usually a threshold value and below that the material remains fairly stable. However, zeolites and their derivate suffer from radiolytic damage [48–53] which consists of the ionization of chemical bonds of elements and cannot be overcome by reducing the accelerating voltage. This difficulty has limited the studies on zeolitic catalysts in comparison with other inorganic solids. Despite the difficulties related to the low stability, transmission electron microscopy (TEM) can provide very useful information [54–59] as follows: (1) it provides direct images of the framework, (2) it allows structural solution, (3) it is the best method for studying defects or intergrowths, (4) it provides information of elements incorporated into the frameworks, or (5) it combines diffraction and imaging studies together with spectroscopic chemical analyses.

5.2.2 *Ultrastable ZY, FAU, with Iridium Incorporated*

With the implementation of the spherical aberration correctors (Cs correctors) in the early year 2000 [60–62], sub-angstrom could be readily available in commercial equipment and since then matter has been observed and analyzed at an atomic level in a good range of solids. Unfortunately, for beam-sensitive materials, this crucial technological innovation was not correlated with an improvement on the quality of the data that could be extracted due to their low lifetime under the electron beam. Consequently, a great effort was concentrated on a careful control of the electron beam in order to preserve the framework intact with the intention of obtaining images with the maximum resolution possible. In fact, it was in 2010 when the first report on high-resolution aberration corrected electron microscopy applied to a zeolite was reported [63]. In this work, the determination and location of individual metal atoms and clusters within the pores of ultrastable delaminated HY were presented by aberration-corrected STEM. This imaging method, which is sensitive to the atomic number Z, allowed, combined with a deep image processing, the observation of Ir atoms. Figure 5.5a shows the experimental Cs-corrected STEM-HAADF image where the anchored Ir atoms are located over the zeolitic framework, which includes, inset, the Fourier-space band-pass filtered data to make the Ir atoms more clearly visible along the [011] direction with respect to the zeolitic framework. Due to the low signal-to-noise ratio of the images, they were treated under real-space averaging after Fourier filter, a method that has been used for biological materials; the data extracted is depicted in Fig. 5.5b, which was obtained by using the unit cell extracted with real-space averaging. This method is useful for periodic features and therefore it reveals the zeolite crystal structure, but unfortunately it omits the

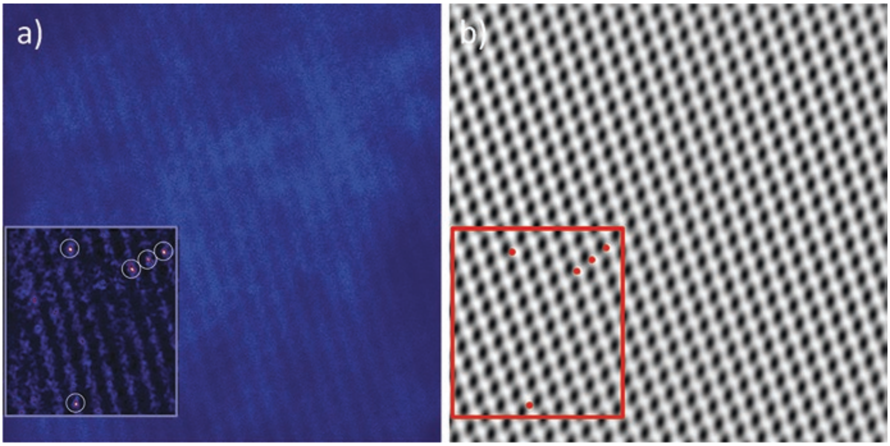

Fig. 5.5 High-resolution images of zeolite-supported metal species; (**a**) Cs-corrected STEM-HAADF image showing (white rectangle) the Ir^+ atoms denoted by white circles. (**b**) Image obtained after using the average unit cell obtained with real-space averaging. The same region where the Ir^+ was present is marked by a red rectangle with the Ir positions marked by red circles

iridium atoms. For that reason the Ir species shown in Fig. 5.5a were superimposed onto the image obtained by real-space averaging (Fig. 5.5b, marked by a square). These experimental data were correlated with STEM-HAADF simulations along the same orientation in order to associate the single Ir^+ positions with the active zeolitic framework.

5.2.3 Silver-Loaded LTA Zeolite

Silver-loaded zeolites (LTA) have been under study using electron microscopy tools as well, and even when it is possible to determine observations at atomic level to depict incorporation of heavy metals into the framework we can find in the literature that a clear image of neither zeolitic member rings nor framework has not been completed with high accuracy. During 2011, a report concerning high-resolution imaging of different zeolite materials was completed on aluminum-rich zeolite LTA Si/Al = 1 [53, 59]. The mentioned study focused on most beam-sensitive frameworks to be imaged; the results obtained from bare zeolite A, with sodium as counterion and after ion exchange with $AgNO_3$, led into the formation of silver species within the pores; Fig. 5.6a depicts the atomic resolution image of the initial Na-LTA orientated along the [001] direction, where the alpha cages appear as empty cages, in black, while the "T" atoms, Si and Al, appear in white; the study allowed to determine for the first time an extremely beam-sensitive material with a resolution allowing to identify T atoms which compose framework and to clearly identify its location

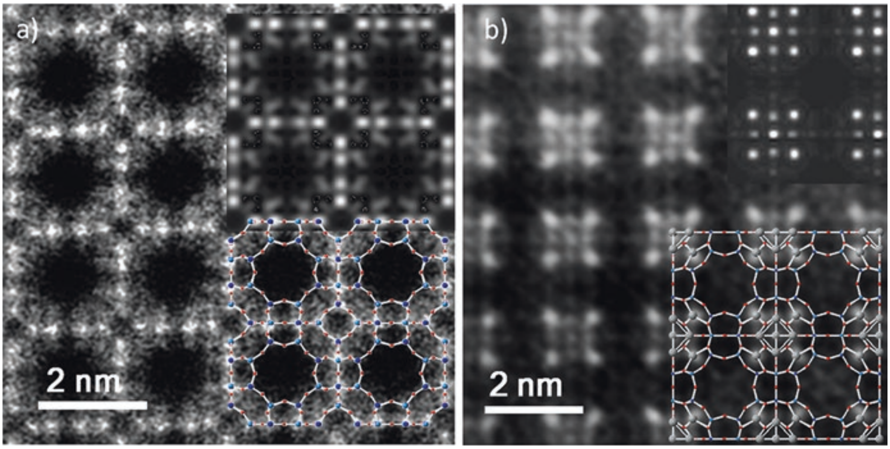

Fig. 5.6 (**a**) Cs-corrected STEM-HAADF image of Na-LTA zeolite, where the "T" atoms can be identified, the simulated data top right and the structural model superimposed perfectly matched with the experimental data obtained. (**b**) Silver ion-exchanged LTA zeolite, where the Ag^+ atoms appear brighter and do not allow the clear visualization of the zeolitic framework. The simulated data, top right, and the model constructed matches with the experimental data acquired

and coordination precision. Moreover, to correlate experimental results images corresponding to framework were subjected to molecular and TEM simulation as shown on the inset; the molecular model of those framework channels has silicon (Si) atoms in dark blue color, aluminum (Al) in light blue, and oxygen (O) in red. Now, having an excellent ion exchange capability in silver-loaded zeolites, the silver atoms were introduced by chemically replacing sodium through a liquid-phase wet chemistry reaction, followed by a dehydration of the material; by doing that there is a coloring change from white to orange as observed due to dehydration; the latter is attributed to formation of silver clusters within zeolite pores. Using high-resolution transmission electron microscopy, it was possible to find atomic resolution to confirm octahedral silver clusters (~6 atoms) located inside sodalite (SOD) cages of the zeolite and that they were encapsulated within a cube formed by 8 silver cations as described in Fig. 5.6b. As completed in starting material, all images were compared to molecular modeling along with TEM simulations, as shown in the inset of Fig. 5.6b, with high success to determine the correlation between experiment and theoretical models.

5.2.4 Cluster Formation Inside SSZ-23 Zeolite

As mentioned in the work completed by Mayoral et al. [56, 59], it was found in the literature more emphasis on performing advanced electron microscopy techniques in zeolites and zeotypes [57, 59, 64–66]; this can be attributed to influence of the high energetic electronic flux, which is considered to be the first step of metal nucleation and can be monitored using *Cs*-corrected STEM fast-throughput units. And by using this proven technique it was possible to achieve a study of Ir complexes which were introduced into one-dimensional porous system of SSZ-23 zeolites [67]; this material has a one-dimensional channel system with 14-ring pores (0.87 × 0.64 nm); such large pores facilitated their observation in comparison with the structures imaged previously; however, rather than using low-dose techniques, it was decided to make high-dose approach method with very short exposure times to prove that electron dosage in TEM instrument can provide information about localization and to track any dynamic motion of individual metallic ions as encountered within the pores of a zeolites. It was possible to determine that iridium (Ir) was incorporated on the channels of SSZ-23 in the form of monoatomic atomic species; images were recorded over the same region with no interval time in between by employing a total acquisition time of 5 s on each, allowing us to make observations of three different phenomena as remarked in colors blue, orange, and green circles in Fig. 5.4. Left side of Fig. 5.7a corresponds to the initial image while on right side the image corresponds to the same region 25 s later. The crystallographic simulations of three observed scenarios are shown in Fig. 5.7b–d along (100) and (010) crystallographic projections; a closer look of experimental images is presented in Figs. 5.7e–j. All observations made suggest that in all cases as represented in blue and orange a clear channel confinement is observed, limiting iridium atoms to move free. All

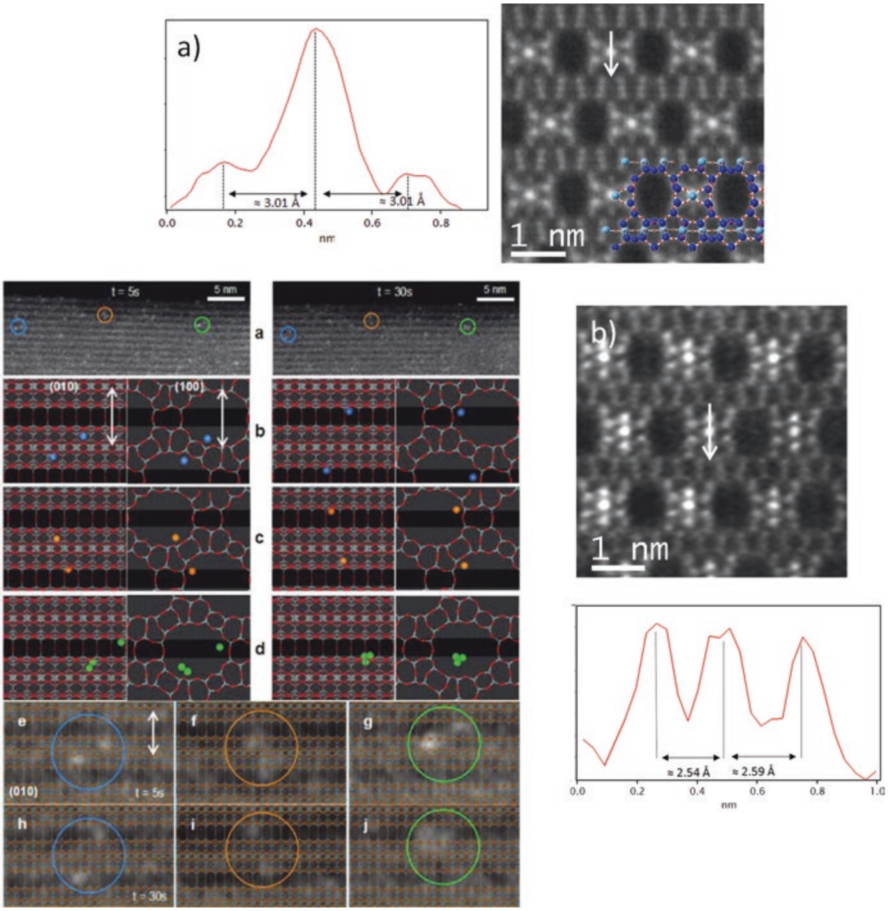

Fig. 5.7 Left: (**a**) Cs-corrected STEM-HAADF images along the (010) projection after 5 s (left) and 30 s (right). (**b**–**d**) Simulated framework with the three possibilities of metal location along the (010) and (100) projections corresponding to 5 s (left) and 30 s (right). The Ir is colored according to the circles in Fig. 5.4a. (**e**–**g**) Crystallographic simulated data along the (010) projection with the zeolitic framework superimposed for the first 5-s image. (**h**–**j**) Same simulation after 30 s of imaging. The white arrows correspond to the diameter of the SSZ-53 channels. Right: (**a**) Intensity profile obtained along the white arrow plotted over the atomic resolution Cs-corrected STEM-HAADF image of ETS-10 in its sodium form along the [110] orientation. The structural model is shown superimposed. (**b**) Eu-EST-10 material. Same intensity analysis plotted over the white arrow plotted over the Cs-corrected STEM-HAADF image along the same orientation. (**c**) Same analysis carried out over the white rectangle from the Na material. (**d**) The correspondent analysis after ion exchange

observations made are clear experimental data of initial steps for metal cluster formation, which in fact can be considered as catalytic sites for different chemical reactions, including reforming, oxidation, and Fischer-Tropsch. A proven evidence of tracking down cluster formation, using high electron beam dosage and low exposure time in combination with computer-assisted molecular simulations, provides great insights into nanotechnology revolution mainly for studying heavy metals; for example gold, an ancient metallic element, has regained immense attention in the materials community, due to its diverse catalytic properties in the nanoscale form [68, 69]. However, the location of gold atoms can be studied in complex zeolite systems such as NaY (FAU type) [66]; this observation technique can allow us to see dispersed gold nanoparticles over the crystalline matrix support allowing us to provide some chemical quest and answers of catalytic sites as isolated gold complexes. It is possible to assume that despite the difficulties associated to the low stability of zeolites, aberration-corrected STEM has been positioned as an indispensable technique to understand heavy metal-loaded zeolites and even to solve new structures [70]. Due to the intrinsic nature of STEM-HAADF of forming images where the contrast is highly sensitive to the atomic number, heavy metals can be observed using these bright contrast techniques, as described elsewhere. However, when it comes to achieving observation of lighter cations, the imaging technique can become quite difficult and on occasions tedious and complicated, as they do not "*shine*" under electron beam interaction as in the case of metallic clusters. A scientific report published in the year 2016 indicates first TEM observations of light cations inside pore channels of titanosilicate (ETS-10) zeolitic systems, through Cs-corrected STEM instrument. The chemical structure of ETS (Engelhard Corporation titanosilicate) materials consists of octahedral and tetrahedral coordinated titanium atoms, where the Ti atoms are made of Si and Ti chemicals linked by oxygen (O) bridges. Those solids had been highly attractive due to ion exchange capabilities as every Ti unit introduces two negative charges into the complete zeolite framework, causing physical and chemical properties ideal for applications in photochemistry, hydrogen membrane separation, and catalysis as presented in the literature [71–73]; also, ETS-10 has a monoclinic crystallographic structure, with space group $C2/c$ and unit cell parameters a = 21.00, b = 21.00, c = 14.51 Å; β = 111.12°, and $\alpha = \gamma$ = 90.00° and pore dimensions of 4.9 Å × 7.6 Å, formed by chains of TiO_6 and SiO_4 containing 12-membered rings (MR), 7MR, and 3MR [74]. ETS-10 was subjected to ion exchange for the introduction of rare earth metals with the intention of synthesizing a material with luminescent properties [42]. Figure 5.7a shows the intensity analysis of the aberration-corrected image of Na-ETS-10 recorded along the [110] orientation. The intensity profile recorded along the white arrow reveals a very intense maximum in the center that corresponds to the Ti column and two very weak signals that are associated to lighter elements. The structural model is superimposed allowing the visualization of all atoms forming the framework with atomic resolution, where Si appears in dark blue, Ti in light blue, and O in red. However, after ion exchange the intensity profile recorded along the same sites has significantly changed (Fig. 5.7b). For the europium-loaded ETS-10 it is clear that Eu cations can have occupied sites where an initial weak signal is detected corroborating the presence of Na^+ within the 7MR. In addition, it can also be observed that a distance is decreased revealing that Eu replaces Na only at specific sites over the matrix. When moving to a different observation region over the framework as presented in Fig. 5.7c, d, it was possible to observe how electron contrast significantly changed; Fig. 5.7c corresponds to an intensity analysis carried out over atoms denoted by a white rectangle in the initial Na-ETS-10 material.

Four different signals can be identified which corresponds to four different Si atomic columns, where intensity variations are owed to the different number of Si atoms along those columns. When ion exchange took place, Fig. 5.7d, again, the contrast suffered from severe change and the distance measured went from 1.44 Å, corresponding to the Si atoms, to 2.48 Å that is attributed to a distance between Eu and Si columns. This observation is in agreement with the possibility that the Eu replaced the Na sites which were too close to porous framework and therefore could not be distinguished due to a presence of Si; however, when ion exchange occurred the strongest scattering factor of the metal incorporated allowed the visualization of the cations at those specific sites.

5.3 TEM and STEM Survey on Tungstate Zirconia (WO_3–ZrO_2)

One important characterization tool to be used in the past two decades when it comes to determine direct observations of active catalytic species is high-resolution electron microscopes in transmission and scanning mode. Lately, it was found that active sites in tungstate zirconia catalysts have a chemical formula of Zr–WO_x mix oxide clusters with diameter size of ~0.8–1 nm [26, 75, 76], and state-of-the-art instruments having resolutions below of 1 Å allow us to achieve direct observations of WO_x active components on those complex catalytic materials. Furthermore, Cs-corrected TEM units can provide experimental evidence to describe possible catalytic mechanisms as involved during chemical processes over those materials as described by Pennycook et al. [77–79]. Though, due to fragile nature of those particular systems, on occasions it becomes very difficult to achieve good quantification of size and distribution of small metallic clusters as distributed along the support matrix, the latter occurs due to image contrast which depends mainly on particle orientation, internal structure, electron imaging conditions, and other parameters to be adjusted during observations to not cause electron radiation damage over the solid-state catalytic matrix/cluster. Thus, HRTEM can have two main matters: (1) The image is formed from interference of electrons waves, resulting the “phase-contrast” image [80]. This case does not ensure correspondence between the image contrast and the actual atomic columns. (2) The illuminating electron beam is not local, because a region of several nanometers is illuminated and is not possible to obtain individual atomic chemical analysis. However, fortunately one significant difference between HRTEM and STEM modes is usage of electron probe (STEM) as compared to spot size in TEM. The local analysis can be performed by using a focused nanometer-sized electron probe, and also be stopped at any point over the solid under observation. Moreover, high-angle annular dark field (HAADF-STEM) can be more sensitive to differentiate chemical elements, depending on their corresponding atomic number, a mode usually called as "**Z** contrast" [80, 81]. A challenge in HRTEM and STEM is the direct observation of active catalytic species. It has been recently pointed out that the active sites in tungstated zirconia catalysts are Zr–WO_x mixed oxide clusters with diameters around ~0.8–1 nm, which were only found in highly active catalyst samples [26, 75, 76]. With the introduction of aberration correctors in HRTEM and STEM with resolutions below 1 Å, now it is possible to observe directly WO_x active components in tungstated zirconia catalysts. The STEM technique, particularly by using the high-angle annular dark field (HAADF-STEM) mode, is useful in this type of samples, due to the difference in atomic number between Zr and W, which produces an adequate contrast and facilitates the observation of these clusters. Although this catalytic system remains under investigation, several groups of researchers have found important results by means of the aberration-corrected HRTEM and STEM [26, 75, 76, 82], identifying catalytic species at atomic level by direct observation of tungsten oxide structures atom by atom in this system. The aberration-corrected high-resolution transmission electron microscopy (AC-HRTEM) is one of the most useful tools for visualizing the nanostructure of heterogeneous catalysts at atomic level, allowing the understanding of the mechanisms occurring within the catalytic processes. The optimum focus conditions, also called the extended Scherzer focus, commonly used in HRTEM imaging (also known as phase-contrast imaging), provide a direct projection of the atomic structure along the beam direction [78]. The visibility of small nanoparticles or clusters generally increases with the defocus value; those variations of the image contrast are related to a dependence of the lens transfer function on the defocus value, which means that at certain special frequencies the relative contrast of the small clusters is enhanced whereas the phase-contrast imaging of the lattice fringes of the support is suppressed [77, 78, 82]. As presented in Fig. 5.8, when observation of WO_x species in Cs-TEM is the variation of image contrast and a focus change, called a serial focus, as it is presented in Fig. 5.8a corresponding to WO_x–ZrO_2 catalyst under underfocus condition, the WO_x clusters appear as black spots and are marked by arrows. By focusing over the same region as presented in Fig. 5.8b, it is possible to observe under minimum contrast that WO_x clusters almost disappeared, and in Fig. 5.8c it was obtained using overfocus condition; it was possible to see WO_x clusters appear as bright spots. The WO_x cluster circled in the three images is an example of what could happen during the observation under different defocus conditions: underfocus, focus, and overfocus.

In order to understand or to achieve image difference, a series of focuses were obtained for allowing to make identification of WO_x species, as presented in Fig. 5.9a which is an image obtained with underfocus conditions, and complete defocus was used in order to distinguish all clusters. Figure 5.9b corresponds to an image obtained under optimum focus conditions (extended Scherzer focus) near the minimum focus, but still in underfocus conditions. The inset shows the projection of the W atoms; in this case, as it was explained before, the projected atoms appear as black spots. The W and Zr atoms are at the same height, so they compete in con-

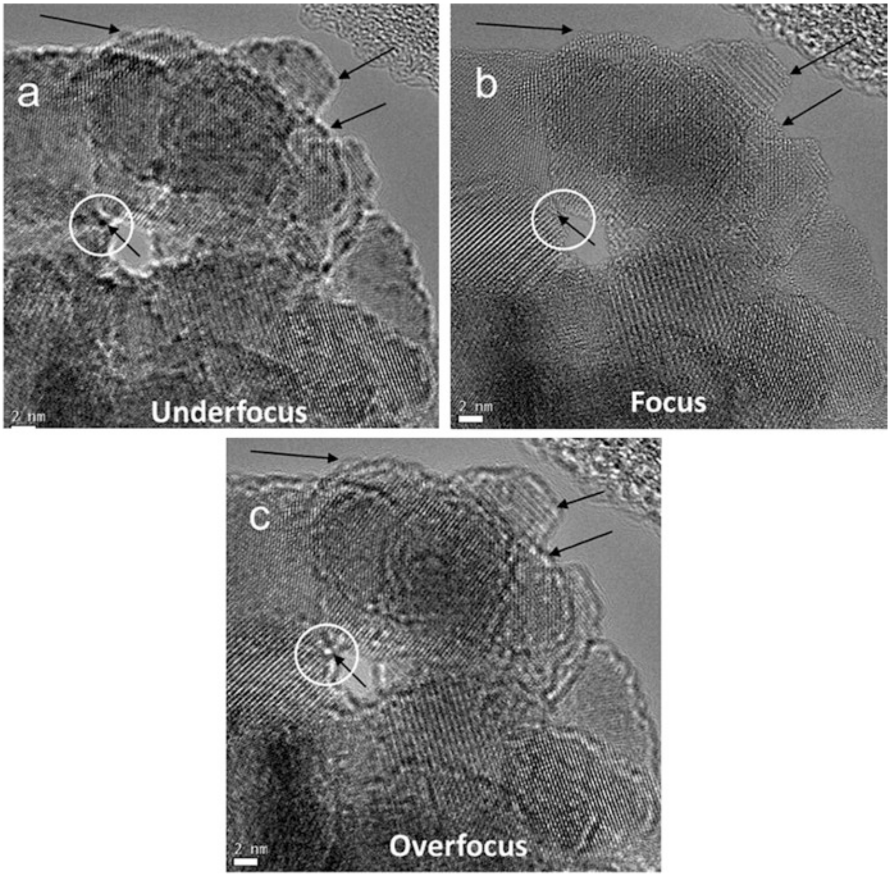

Fig. 5.8 HRTEM images of WO_x–ZrO_2 catalysts obtained under different focus conditions: (**a**) Underfocus condition WO_x clusters appear as black spots indicated by arrows; (**b**) focus condition (minimum contrast) WO_x clusters are almost not observed; and (**c**) overfocus condition WO_x clusters appear as bright spots (white ring circle)

trast. The image as presented in Fig. 5.9c was obtained under likewise region (corresponding to Fig. 5.9b), but under overfocus conditions. The inset image shows the projection of W atoms; in this case, the projected atoms appear as white spots [83]. The bottom part of the image shown in Fig. 5.9c, marked with black arrows, continues under underfocus conditions (black WO_x clusters).

Using similar electron microscopy conditions, with different focus conditions in Fig. 5.10a, an image of WO_x–ZrO_2 catalyst is obtained with underfocus conditions, showing WO_x clusters as marked with circles and arrows; WO_x species are localized over the sample; it was possible to use optimal focus condition to achieve an image as presented in Fig. 5.10b; some features are dark columns of W atoms as pointed out using white arrows. TZ was identified as tetragonal zirconia with zone axis [010] (FFT inset), where a small WO_3 crystallite (atomic planes of 2.4 Å and 2.29 Å)

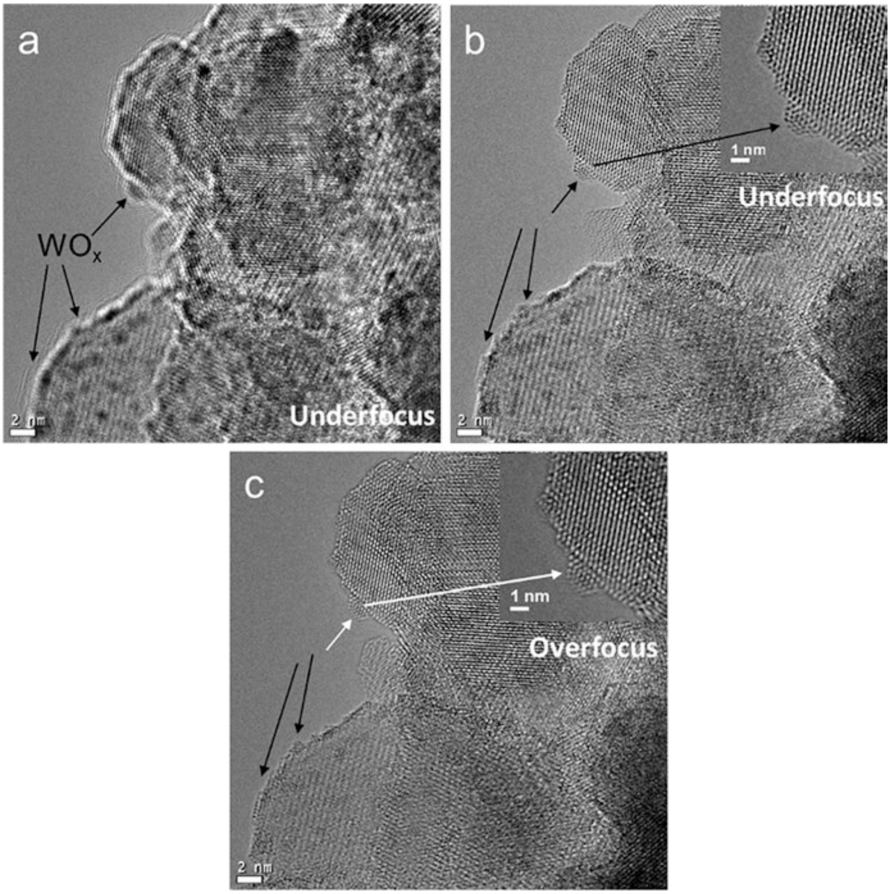

Fig. 5.9 HRTEM images of WO_x–ZrO_2 catalysts: (**a**) WO_x clusters with underfocus conditions (black spots), (**b**) with underfocus conditions, but near the minimum contrast, where the W atoms are in black; (**c**) overfocus conditions, but near the minimum contrast, where the W atoms appear as white spots. Figure 5.4c having white arrows corresponds to overfocus region and black arrows to underfocus region to differentiate the resolution in between modes (adapted from ref. [82])

is anchored over zirconia surface. Unfortunately, the high zirconia contrast does not allow the clear observation of WO_x species. In Fig. 5.10c, WO_x species conform different arrays over zirconia (TZ); with orientation (zone axis of [−120]) having a better localization of tungsten atoms, it is remarkable that all images were obtained using underfocus conditions.

Now, using Cs-STEM mode with high-angle annular dark field (HAADF) and bright-field (BF) modes and electron probe ~1 Å at resolution of ~0.8 Å, contrary to conventional TEM in STEM mode there is no wave interference between electron beam and solid sample under study due to setup of optical system on the instrument [77, 79, 80, 84]. The latter plays an important role and advantage because it allows

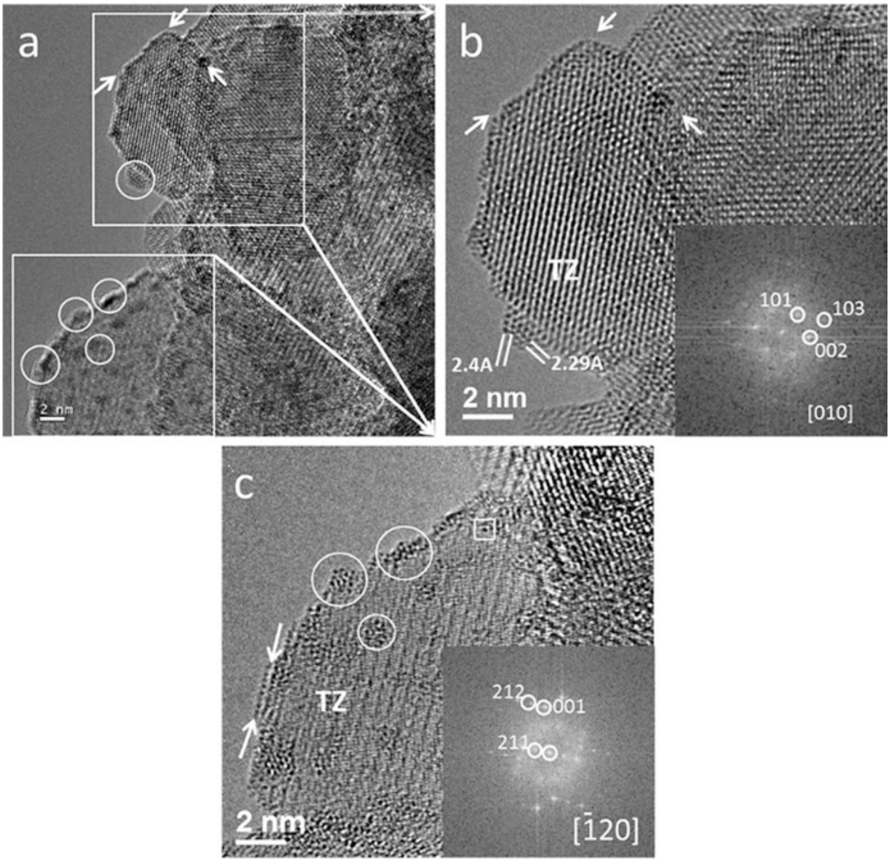

Fig. 5.10 (**a**) HRTEM image of the WO_x–ZrO_2 catalyst obtained with underfocus conditions, which shows the WO_x clusters marked with circles and arrows; (**b**) WO_x species form dark columns of W atoms (white arrows). TZ was identified as tetragonal zirconia with zone axis [010] (FFT inset), where a small crystallite of WO_3 (atomic planes of 2.4 and 2.29 Å) is anchored on the zirconia surface; and (**c**) WO_x species forming different arrays on zirconia (TZ), where the zirconia orientation (zone axis [−120]) makes possible a better localization of the W atoms. In all the cases, the images were obtained with underfocus conditions (figure adapted from ref. [82])

observers to make interpretation of results directly from acquired images, making it possible to localize atoms as distributed along amorphous and crystalline matrix of low-dimension materials [77, 79, 80, 84]. The one condition that allows to distinguish two chemical elements in terms of its Z-contrast can allow to determine chemical elements according to its particular atomic number from a list of eight positions in the periodic table [79]; knowing the Z-contrast effect, it is possible to determine chemical composition in tungstate zirconia (WO_3–ZrO_2) system, since tungsten (W) has an atomic number of 74 while zirconium (Zr) and oxygen (O) own atomic numbers of 40 and 8, respectively; therefore W is noticeable in HAADF-STEM mode as is supported over zirconia matrix. Unlike HRTEM, HAADF-STEM images give direct information about the atomic projection along the beam direction [77, 79, 80, 84]. The visibility of small nanoparticles or clusters is generally obtained at precise focus with a very short field depth. The variations in the image contrast are related to the defocus value, which means that at certain focus a region of the sample is observed, but as the focus is changed a different depth in the sample is observed, and therefore another region of the solid. These features are shown in the STEM images of WO_x–ZrO_2 catalysts as presented in Fig. 5.11; in those HAADF-STEM images WO_x is observed as white spots, homogeneously distributed over zirconia, as presented in Fig. 5.11a, c, having a great variety of WO_x species ranging from mono-tungstates to poly-tungstates. The BF-STEM images of the same regions (Fig. 5.11b, d, respectively) are just complementary information, where WO_x appears as black spots.

The white circles compare the same WO_x species in both modes; in some regions WO_x only is possible to distinguish by using HAADF-STEM mode, and then one can observe that images as obtained by HAADF-STEM have better Z-contrast. For images as presented in Fig. 5.12, along a different region in the same catalytic sample but at higher magnification, HAADF-STEM and BF-STEM can provide more information about location and coordination of WO_x species. The experience dictates that HAADF-STEM can provide more detailed information about localizing WO_x species while BF-STEM more about crystallinity of zirconia matrix, as mono-tungstated (white squares) to poly-tungstated species with different sizes (white circles) as presented in Fig. 5.12 (smaller clusters of WO_x species of sizes ~<1 nm).

We provide in Fig. 5.13 HAADF-STEM and BF-STEM images of the WO_x–ZrO_2 catalytic material; it was possible to determine several poly-tungstates at the edge of the zirconia matrix as marked using white arrows; the insets show with high resolution one of poly-tungstate clustering (white circle), as mono-tungstate species can be observed (white squares), which provides optical evidence of interaction of tungstate with the zirconia support matrix.

5.4 Cobalt-Promoted MoS_2 Catalytic Materials by TEM

The morphology aspects of this catalytic material have been studied extensively by Ramos et al. using both scanning and transmission electron microscopy techniques, as presented in Fig. 5.9 [36], and there is extensive evidence of its versatility meaning, to achieve different morphological configurations (i.e., nanotube, spherical, triangular clusters, and rag layered), which depends solely on chemical precursors and synthesis methods; usually due to its low mechanical properties, the material is mixed with high-temperature supports like alumina oxide (Al_2O_3) [85], ceria oxide (CeO_3), and zirconia oxide (ZrO_2) [86] to create pellets for catalytic evaluation during fluid catalytic cracking of crude oil. In our study, powder catalytic material was prepared from ammonium tetrathiomolybdate $(NH_4)_2MoS_4$ mixed with $CoCl_2$ in aqueous solution and then a bimetallic precursor is decomposed at 300 °C for 2 h in 50 mL of purified water to achieve 1200 psi of hydrostatic pressure in batch

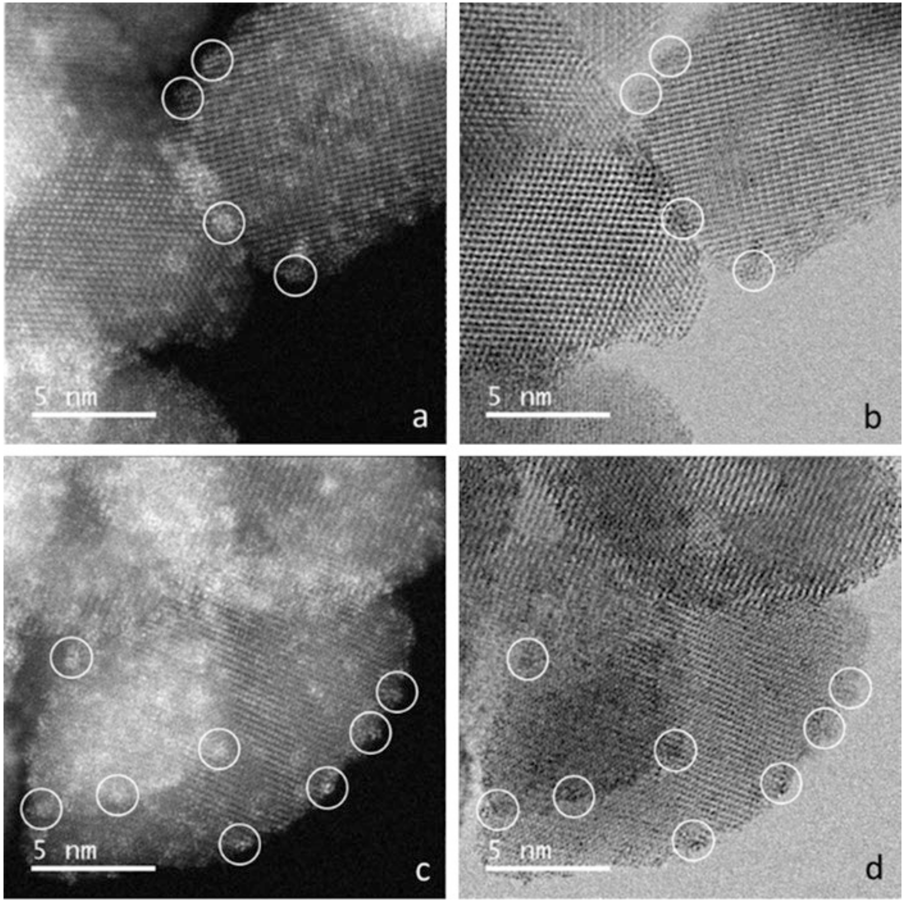

Fig. 5.11 STEM images of WO_x–ZrO_2 catalysts: (**a**, **c**) are HAADF-STEM images showing WO_x species that appear as white spots homogeneously supported on zirconia; (**b**, **d**) are BF-STEM images of the same regions, respectively. This technique gives complementary information, where the WO_x species appear as black spots

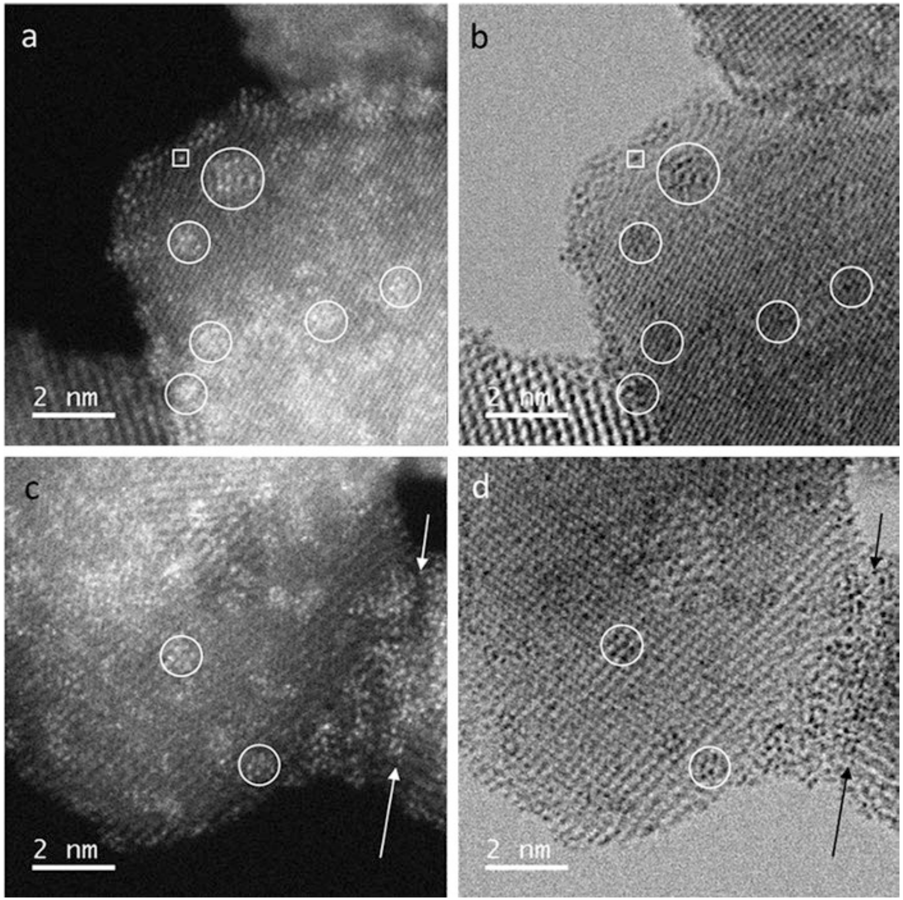

Fig. 5.12 STEM images of WO_x–ZrO_2 catalysts: (**a**, **c**) HAADF-STEM images; (**b**, **d**) BF-STEM images with WO_x species. Different sizes of tungstated species are observed, from mono-tungstate (white squares) to poly-tungstate species (white circles); smaller circles show WO_x species with sizes below 1 nm, respectively

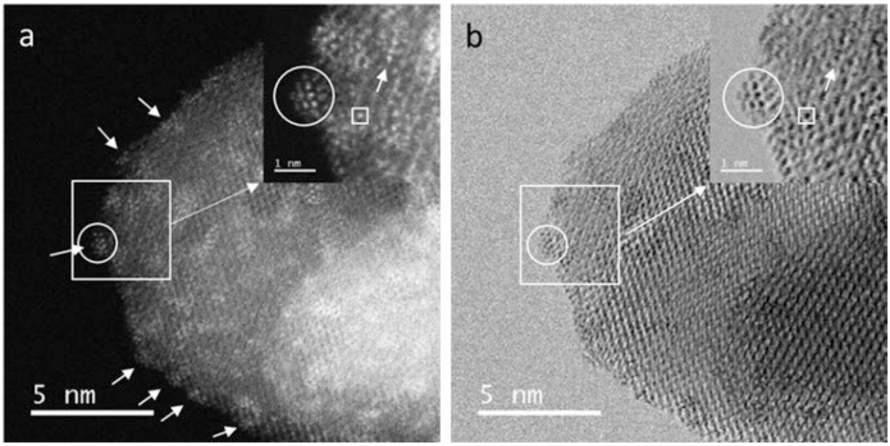

Fig. 5.13 Series of STEM images corresponding to WO_x–ZrO_2 catalytic material. (**a**) HAADF-STEM image; several WO_x species anchored on the zirconia support are observed along its edge; (**b**) BF-STEM image; in this mode WO_x species compete in contrast with the support. In the insets, for example, several species are shown: one WO_x cluster (marked with circles) with an array of atoms, a mono-tungstate (small white squares), and a poly-tungstate growing up along atomic planes of the zirconia support (marked with arrows in the insets)

hydrothermal reactor as described by Siadati et al. [87], using approximately 0.05 g of the black Co/MoS_2 powder diluted into 20 mL of isopropanol to make a homogeneous grey solution, and one drop was placed in conventional 200-mesh lacey holey carbon grid and dried at room temperature. The TEM observations were made using a FEI® Tecnai TF20 operated at 200 kV and equipped with CCD camera, STEM unit, high-angle annular dark-field (HAADF) detector, and X-Twin lenses with a resolution of ~2 nm. Images were processed using Gatan© Digital micrograph® computational package. It was possible to determine MoS_2 layered structurer "*typical fringes*" with interplanar distance of ~6.2 Å corresponding to $d_{(002)}$ basal plane as shown in Fig. 5.14; one of the features to be observed was the interaction of cobalt sulfide (Co_9S_8), corresponding to (111)-cleavage plane, as described in detail before [36]; using Gatan® digital micrograph© package it was possible to make some measurements over hexagonal lattice obtaining a 7.24 Å versus 7.37 Å found to have experimental value, confirming a preferential exposition of the (111) plane for Co_9S_8, also found using similar technique by Geantet et al. [88].

By mapping the region of interest, it was possible to observe other features like bending curvatures known as "*turbostratic*," in many cases pointed as ideal reactive sites due to its changes in electronic structure [89] as presented in Fig. 5.15.

Furthermore, using digital information from TEM observations, it was possible to build a molecular model using density functional methods of computer-assisted package. The model indicates a synergistic contact between (010)-MoS_2 plane and (111)-Co_9S_8 planes, to create a unique chemical direct bonding between Mo and Co species formed by thiocubane clusters. The proposed interface molecular model was subjected to Mulliken population analysis [90] to determine any electronic

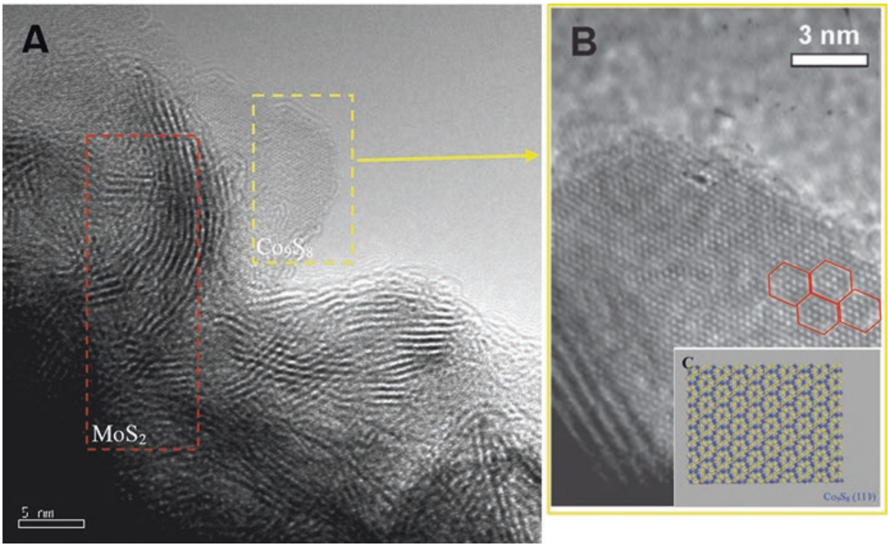

Fig. 5.14 (**a**) Transmission electron microscopy image indicating the interaction of both MoS_2 and Co_9S_8 as stacked (dotted red square). The yellow-dotted square indicates cobalt sulfide phase. (**b**) A high-resolution TEM image shows hexagon packing lattice for cobalt sulfide, which is presented in the molecular model of (111)-Co_9S_8 (blue: cobalt, yellow: sulfur) (image adapted with copyrights and permission of Ramos et al. RSC© Catal. Sci. Technol., 2012, 2, 164–178)

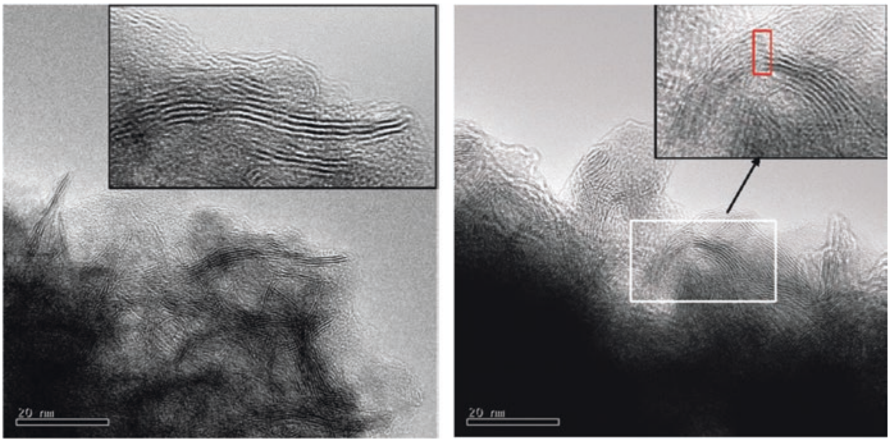

Fig. 5.15 Left: TEM image showing highly distorted MoS_2 layers as characteristic of 0.62 nm fringes. It is possible to determine elongated layers with some bending as caused due to chemical interaction with Co_9S_8 substrate forming an interface. Right: It is possible to observe some strong bending effects among MoS_2 layers with some fractures as presented in the inset (image adapted with copyrights and permission of Ramos et al. RSC© Catal. Sci. Technol., 2012, 2, 164–178)

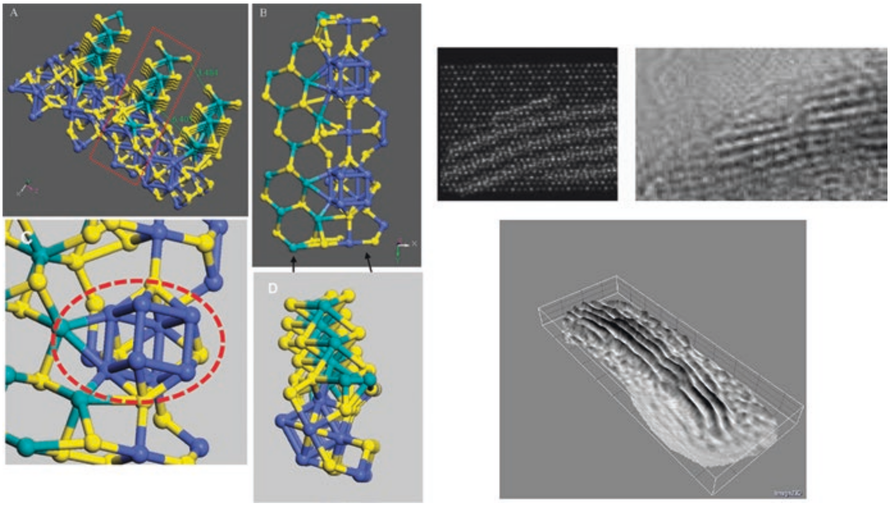

Fig. 5.16 Left: (**a**) Molecular model constructed from crystallographic information obtained by TEM; the model called "interface" is made by using (101)-plane of MoS_2 and (111)-plane of Co_9S_8 using computer-assisted density functional methods. Atoms as presented in ball-stick type with colors as sulfur (yellow), molybdenum (green), and cobalt (blue). (**b**) Only one portion of the interface was used to perform electronic structure DFT computations as indicated by red dashed line. (**c**) This image presents a close-up look at thiocubane cluster indicating direct bonding between Co and Mo atoms. (**d**) This image presents another view of interface model; here it is possible to determine stacking height effects. Right: Experimental TEM and simulated TEM images obtained from direct observations and using molecular interface model; by using ImageJ open-source package, it was possible to determine the height of slabs, indicating the epitaxial contact between planes of both crystallographic bulk molecular structures (image adapted with copyrights and permission of Ramos et al. RSC© Catal. Sci. Technol., 2012, 2, 164–178)

structure modification by synergic contact of two specific crystallographic groups, and its correlation with catalytic activity for hydrodesulfurization purposes; *DFT* Mulliken population analysis indicates electron charges of +0.49 to +0.53 in Mo atoms at the interface, as presented in Fig. 5.16. Mo charge is +0.61 for 2H-MoS_2 bulk layers, indicating that direct bonding among Co and Mo caused electron donation charge from cobalt to molybdenum. On contrary, the cobalt atoms as located in the cubic array bond to Mo have more negative (or less positive) charges (−0.07 and +0.03) in comparison with bulk Co_9S_8 values of +0.16. Moreover, as a consequence Co on first neighbors' bonding to Mo coordinated in thiocubane cluster has more positive electron charge values of +0.28 to +0.30 and second Co first neighbors have more negative values when compared to Co_9S_8 bulk −0.15 and −0.07; more details are found in Ramos et al. [90].

5.5 In Situ Carbonization Effects in Co/MoS_2 Catalytic Materials by TEM

The carbide phase in catalytic materials plays an important role due to its attribution to lower catalytic activity, by blocking active sites due to addition of carbon species [91]. For that reason, it is important to achieve a deep understanding about this carbonization process and fortunately this can be possible by using TEM by applying in situ operando techniques [92], especially with the newly designed sample holders and TEM grids [93]. Here, a representative experiment in situ operando TEM was conducted to determine the atomistic role of carbon as contained on lacey TEM grid for fresh Co/MoS_2-unsupported catalyst by heating in temperature range of 25–450 °C with a ramp rate of 150 °C/min using a Gatan-628 equipped with water-cooling system. For comparison, experiment was conducted using otherwise conditions with a lacey silicon grid. The first TEM images of the Co/MoS_2 catalyst at 25 °C show typical layered MoS_2 structure by detecting typical fringes corresponding to (1 0 1 0) and (1 0 1 0) edge planes stacking along $d_{(002)}$ spacing ~6.3 Å as shown in Fig. 5.17a, including proposed molecular model. From images, it was possible to determine bundles of intermingled MoS_2 layers stacked over *c*-axis direction; the TEM technique allowed to determine poorly crystalline MoS_2 stacks in direct contact with Co_9S_8 which was also detected and observed on this

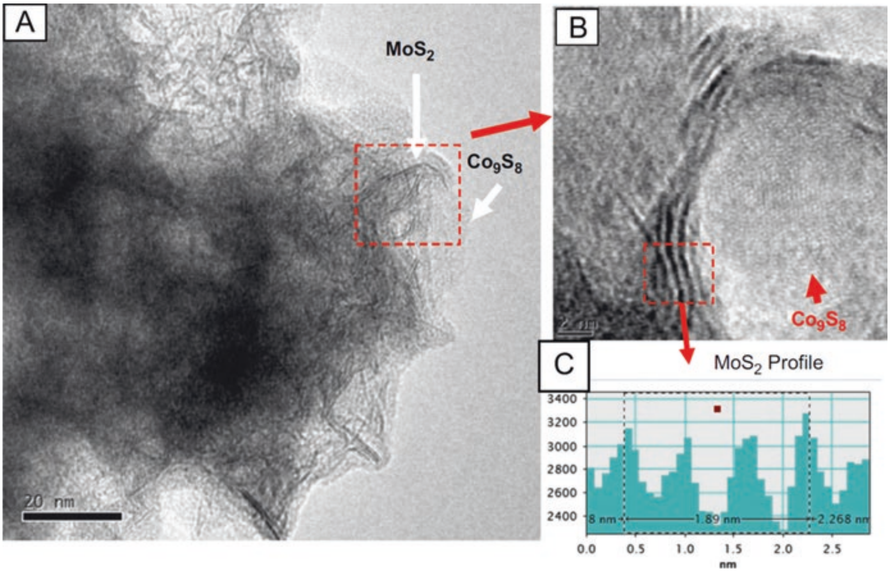

Fig. 5.17 (**a**) Typical TEM image for fresh Co/MoS_2-unsupported catalyst at 25 °C. (**b**) Zoom over MoS_2 layers as determined by black fringes; it was possible to observe a direct contact with the (111)-Co_9S_8 as observed in typical honeycomb-like structure. (**c**) Digitalized distance profile of MoS_2 interlayers 6.3 Å (image adapted with copyrights and permission of [39] Ramos et al. Elsevier© Ultramicroscopy, 127, (2013), 64–69)

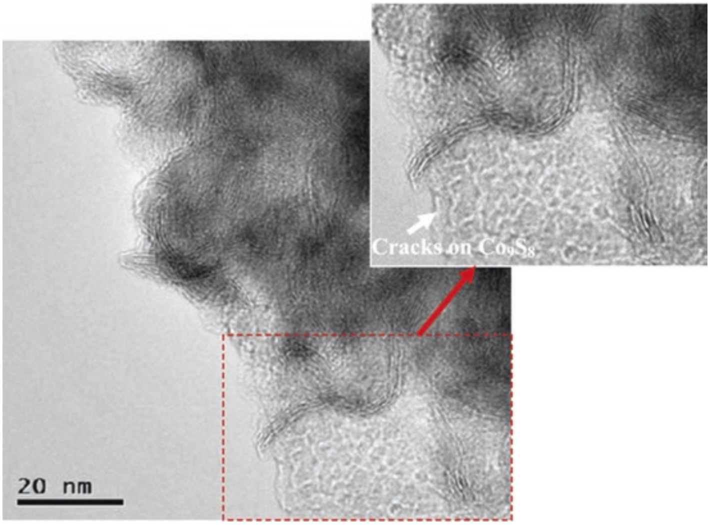

Fig. 5.18 High-resolution TEM image of the Co/MoS_2-unsupported catalyst after heating at 300 °C for 3 min; using lacey Cu/C grid and Gatan-628 holder with cooling water, partial bending effects were observed over MoS_2 layers causing cracks of (111)-plane of bulk Co_9S_8 (image adapted with copyrights and permission of [39] Ramos et al. Elsevier© Ultramicroscopy, 127, (2013), 64–69)

hydrodesulfurization catalytic low-dimension material as studied utilizing similar TEM approach and instrument operational conditions [39].

The visualization of hexagonal lattice arrangement its characteristic of (111)-planes of Co_9S_8, in a second step after temperature reached 300 °C at a rate of 150 °C/min and kept it for 3 min; allows to observed morphological changes of fringes stacked over (111)-planes to form Co/MoS_2 phase as presented in Fig. 5.18; indeed relevant cracks are clearly observed mainly over the Co_9S_8 region with typical bending effects of MoS_2 layers; this effect can be highly attributed to the presence of carbon as contained in TEM grid, which in the case of lacey silicon grid was not found ruling out other factors, such as slight pressure of residual water; this bending effect in fresh MoS_2 catalytic material by the presence of carbon was previously observed by Berhault et al. through EXAFS technique [94], leading to the formation of carbide-like MoS_2 entities (named "*structural carbon*") [94]; this carbonization effect is attributed to be the main cause of low catalytic performance under hydroprocessing reactor conditions due to high concentration of hydrocarbon species as contained naturally in crude oil; by using two main experimental techniques EELS and NEXAFS it was previously demonstrated that carbon is incorporated between edges of MoS_2 layers by replacing and/or boning to sulfur atoms [95, 96]. The carbon replacement/bonding near the edge of MoS_2 is possible due to possible low sulfur coordination of Mo sites; on the contrary a completely sulfur-coordinated Mo site located on (002)-basal planes can be more difficult to be reduced due to strong bonding and poor space to nucleate allowing poor replacement of structural carbon [96]. Now, the intrinsic tendency of molybdenum sulfide to create bending curvatures (even under absence of carbon content) is attributed to make strain effects at curved edges causing site defect very similar to the ones detected at edge planes [97]. Moreover, the presence of the cobalt promoter can induce high reducibility on MoS_2 phase through donation of electrons from Co to Mo as described by Ramos et al. [36] that can be the one main cause to accelerate edge carburization even at hydroprocessing operational conditions [95].

To confirm that bending effects as observed at 300 °C are caused by carbon reaction as contained in lacey TEM grid with fresh unsupported Co/MoS_2 catalytic material under observation the temperature was set to 450 °C and left for 10 min at that temperature; the observations showed that one clear tendency of bending is detected when looking at extremities of MoS_2 fringes as indicated in Fig. 5.19; by digitally measuring the distance between these two spots a decrease from 66 Å to 36 Å and finally to 28 Å is obtained only 1 min at 450 °C confirming a rapid tendency of MoS_2 layers to bend when temperature and carbon content are placed, making an “in situ” TEM observation for the first time of bending MoS_2 slabs. Lastly, a formation of carbon sphere fullerene-like and of copper nanoparticles was also evidenced on different TEM images after heating at 450 °C as presented in Fig. 5.20a, b; it is possible to observe a strong interaction of carbon sphere with remaining MoS_2 layers due to poor insertion with now as-formed Co/MoS_xC_y phase.

The amount of carbon to be incorporated as carbide-like entities is therefore limited and probably a high proportion of the amorphous carbon coming from the TEM grid cannot be converted into carbide moieties leading to their agglomeration into different nanostructures; moreover, lacey carbon TEM grids have copper content between box windows and formation of big copper nanoparticles (~70 nm) presenting some twinning defects, suggesting a relatively slow formation for copper

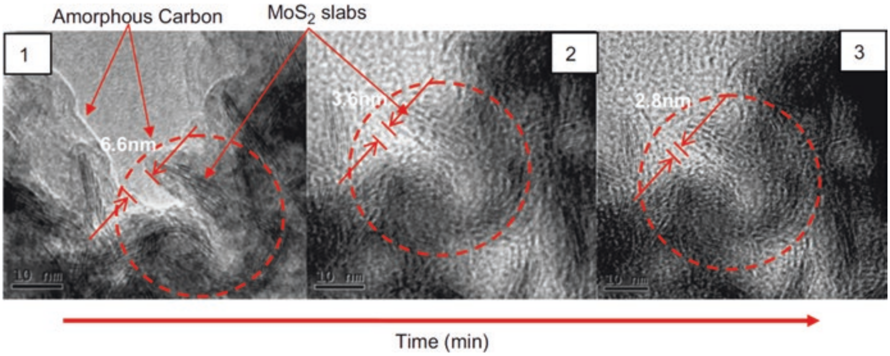

Fig. 5.19 Sequence of three in situ HRTEM images observed at 450 °C for 1 min. Here a rapid bending effect can be clearly visualized leading to a partial closing of the nanostructure under investigation and characterized by a decrease of the distance between the two slab extremities indicated by red arrows from 6.6 nm to 3.6 nm and finally 2.8 nm in less than 1 min (image and caption adapted with copyrights and permission of [39] Ramos et al. Elsevier© Ultramicroscopy, 127, (2013), 64–69)

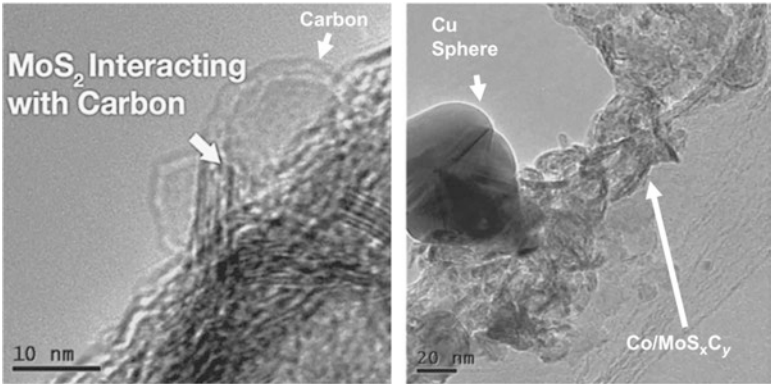

Fig. 5.20 (**a**) Formation of a large carbon sphere in close interaction with MoS_2 slabs. (**b**) Formation of a copper nanoparticle showing some twinning planes and remaining near Co/MoS_xC_y moieties (image and caption adapted with copyrights and permission of [39] Ramos et al. Elsevier© Ultramicroscopy, 127, (2013), 64–69)

nanoparticles during heating experimentation as presented in Fig. 5.20, which are produced if growth rate is sufficiently slow to allow compensation by exposition of low surface energy {1 1 1} facets as described in detail by Ajayan and Marks [98], which lacey TEM grid behavior was shown previously by "in situ" operando heating experiment by Zhang and Su [99] and using similar Gatan-628 holder and lacey 200-mesh Ted Pella® holey carbon grids which observed formation of copper-twinned nanoparticles.

For comparison the same in situ heating experiment was conducted using the same solution of fresh Co/MoS_2 catalytic unsupported material and lacey silicon copper TEM grid under otherwise conditions at 300 °C < T < 450 °C as described before; this was performed to achieve observation regarding catalytic layer evolution while heating now in the absence of a carbon source. The results indicate that contrary to preceding experimentation case for which bending effects were clearly observed due to formation of Co/MoS_xC_y phase, for a silicon TEM grid at temperatures of 300 °C all MoS_2 layers appear highly stacked along the c-axis direction and exhibit mainly flat morphologies with very limited (if any) curvature effects as shown in Fig. 5.21a. By continuing heating the system to reach 450 °C the appearance of cracks was observed for MoS_2 layers leading to a limited destacking but still without any significant bending effect, Fig. 5.21b. By making prolonged heating at 450 °C up to 5 min, it was possible to observe an increase of cracking over MoS_2 slabs in a higher frequency still leading to a limited destacking. MoS_2 layers remain still straight without any visible bending effects as compared when carbon content is present. Furthermore, some isolated Co_9S_8 nanoparticles without interaction with MoS_2 were clearly observed showing a rapid loss of the interaction between both crystallographic phases of cobalt with molybdenum sulfides. This particular physical and chemical phenomenon was not observed previously at 450 °C for fresh Co/MoS_2 sample during heating procedure using lacey carbon TEM grid confirming a

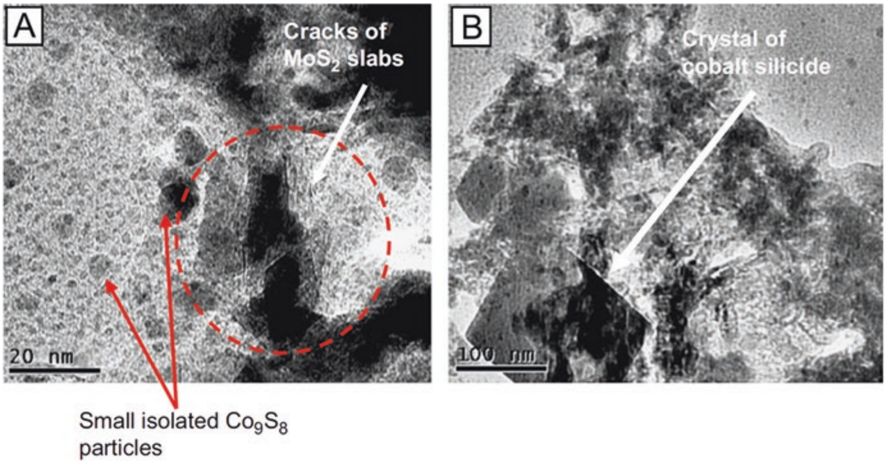

Fig. 5.21 (**a**) Results from heating using similar otherwise conditions and sample preparation for fresh Co/MoS$_2$ catalytic material over lacey silicon TEM grid from Ted Pella, Inc.©, which reveals cracks at MoS$_2$ layers in addition to formation of isolated Co$_9$S$_8$ cubic nanoparticles. (**b**) TEM image showing one large nanocrystal (~150 nm) of cobalt silicide is observed to be formed after prolonged heating at 450 °C for 5 min (image and caption adapted with copyrights and permission of [39] Ramos et al. Elsevier© Ultramicroscopy, 127, (2013), 64–69)

higher stability of the carbide Co/MoS$_x$C$_y$ phase at high temperatures. This is also in agreement with previous results showing that the stabilized active phase under HDS conditions creates a MoS$_2$ carbide phase [37, 94, 100]. Lastly, as presented in Fig. 5.21b, some cobalt silicide crystals of about 150 nm were also observed after heating the fresh Co/MoS$_2$ catalytic sample using lacey silicon TEM grid at 450 °C for 5 min. Such an effect was in situ observed previously by van Gurp et al. [101] by heating Co films in the presence of Si wafers at temperatures comprised between 400 °C and 550 °C.

5.6 Conclusions

In summary, in this chapter we present different cases of study using advanced electron microscopy methods for morphological, crystallographic, and microstructural analysis of diverse low-dimension catalytic materials. Results for *zeolites* indicate a complex chemical structure with low stability as they disintegrated within seconds of observation due to beam radiation damage; however, by controlling electron beam it was possible to subtract relevant information about heavy metals as incorporated, to which corresponds to active sites resolving with high degree of accuracy possible new structures as never reported in the literature; moreover location of light counterions was also obtained. For case study of tungsten oxide (WO$_x$) catalytic materials supported over zirconia it was possible to identify by AC-HRTEM and AC-STEM the atomistic interaction about both WO$_3$ and ZrO$_2$ bulk low-dimension species; using underfocus to overfocus techniques extraordinary imaging digitalization and acquisition were possible with minimum sample damage during TEM and STEM observations, allowing a rapid interpretation about catalytic structure/function relationships. Lastly, by using high-resolution TEM technique, it was possible to determine catalytic atomistic structure for hydroprocessing catalytic material, indicating that activity is related to synergic bulk contact between MoS_2 and Co_9S_8 crystallographic phases. By using digital information from TEM imaging, a proposed molecular model called "interface" was built and subjected to computer-assisted numerical simulations using density functional theory methods (DFT). Results indicate a direct chemical bonding between cobalt and molybdenum species to form a thiocubane cluster, and Mulliken population analysis reflects an electron donation from cobalt into molybdenum making the complete electronic structure more electro-reactive, in high agreement with results found in the literature [14]. Furthermore, a complete "in situ" TEM heating experimentation was completed for same solid hydroprocessing catalytic powder; results indicate the formation of Co/MoS_xC_y phase due to chemical reactivity of fresh catalyst with amorphous carbon contained in lacey holey 200-mesh TEM grid, causing bending effects and cracks in MoS_2 layers and (111)-Co_9S_8, respectively, at 350 °C; in contrast with formation of cobalt silicide nanoparticles when experiment was conducted using otherwise temperature, beam radiation dosage, electronic settings, and conditions for fresh Co/MoS_2 catalytic material in amorphous silicon TEM grid, observations made also indicate cracks of MoS_2 layers.

Acknowledgements Chapter author: Prof. Dr. Alvaro Mayoral thank FEDER-Construyendo Europa desde Aragón for research economical funding. Prof. Dr. Paz del Angel thank Instituto Mexicano del Petróleo, Mexico City, for usage of research facilities and equipment, and The Kleberg Advanced Microscopy Center of University of Texas at San Antonio for usage of electron microscopy facilities. Prof. Dr. Manuel Ramos thank Consejo Nacional de Ciencia y Tecnología, Mexico, for research economical support grant solicitation #207997; The Microelectronics Research Center of University of Texas at Austin for usage of electron microscope instrument; The Department of Physics and Mathematics of Universidad Autónoma de Ciudad Juárez for research economical support by solicitation PROMEP-Mexico grant #103.5/11/4377/NPTC/260-UACJ; and Materials Research and Technology of University of Texas at El Paso. The Centre for High-resolution Electron Microscopy (CħEM), supported by SPST of ShanghaiTech University under contract No. EM02161943 and the NSFC (21850410448, 21835002).

References

1. V.G. Dyukov, S.A. Nepijko, G. Schönhens, Chapter two: voltage contrast modes in a scanning electron microscope and their application. Adv. Imaging Elect. Phys. **196**, 165–246 (2016)
2. M. José-Yacamán, G. Díaz, A. Gómez, Electron microscopy of catalysts; the present, the future and the hopes. Catal. Today **23**, 161–199 (1995)
3. A.K. Datye, Electron microscopy of catalysts: recent achievements and future prospects. J. Catal. **216**, 144–154 (2003)
4. M.A. O'Keefe, Seeing atoms with aberration-corrected sub-Ångström electron microscopy. Ultramicroscopy **108**, 196–209 (2008)

5. R.R. Chianelli, A.F. Ruppert, M. José-Yacamán, A. Váquez-Zavala, HREM studies of layered transition metal sulfide catalytic materials. Catal. Today **23**, 269–281 (1995)
6. L.P. Hansen, E. Johnson, M. Brorson, S. Helveg, Growth mechanism for single- and multi-layer MoS_2 nanocrystals. J. Phys. Chem. C **118**, 22768–22773 (2014)
7. R.F. Egerton, Electron energy-loss spectroscopy in the TEM. Rep. Prog. Phys. **72**, 016502 (2009). 25pp
8. S. Khanal, A. Spitale, N. Bhattarai, D. Bahena, J.J. Velazquez-Salazar, S. Mejía-Rosales, M. M Mariscal, M. José-Yacaman, Synthesis, characterization, and growth simulations of Cu–Pt bimetallic nanoclusters. Beilstein J. Nanotechnol. **5**, 1371 (2014)
9. A. Garcia, A.M. Raya, M. Mariscal, R. Esparza, M. Herrera, S.I. Molina, G. Scavello, P.L. Galindo, M. José-Yacamán, A. Ponce, Analysis of electron [] beam damage of exfoliated MoS2 sheets and quantitative HAADF-STEM imaging. Ultramicroscopy **146**, 33–38 (2014)
10. J.E. Evans, K.L. Jungjohann, N.D. Browning, I. Arslan, Controlled growth of nanoparticles from solution with in situ liquid transmission electron microscopy. Nano Lett. **11**(7), 2809–2813 (2011)
11. A. Primo, H. Garcia, Chem. Soc. Rev. **43**, 7548–7561 (2014)
12. A.F. Crønstedt, *Kongl. Svenska Vetenskaps Acadademiens Handlingar*, vol 17 (Elsevier, Amsterdam, 1756), p. 120
13. S. Cinar, B. Beler-Baykal, Water Sci. Technol. **51**, 71–77 (2005)
14. J. Weitkamp, in *Handbook of heterogeneous catalysis*, ed. by G. Ertl et al., (Wiley, Hoboken, NJ, 2008)
15. D.G. Barton, S.L. Soled, G.D. Meitzner, G.A. Fuentes, E. Iglesia, J. Catal. **181**, 57 (1999)
16. M. Hino, K. Arata, J. Chem. Soc. Chem. Commun., 1259–1260 (1988)
17. A. Martínez, G. Prieto, M.A. Arribas, P. Concepción, J.F. Sánchez-Royo, J. Catal. **248**, 288 (2007)
18. D.G. Barton, M. Shtein, R.D. Wilson, S.L. Soled, E. Iglesia, J. Phys. Chem. B **103**, 630 (1999)
19. M.L. Hernández-Pichardo, J.A. Montoya de la Fuente, P. Del Angel, A. Vargas, J. Navarrete, I. Hernández, L. Lartundo, M. González-Brambila, Appl. Cat. A: Gen. **431-432**, 69 (2012)
20. J.M. Hidalgo, D. Kaucky, O. Bortnovsky, R. Cerny, Z. Sobalik, RSC Adv. **5**, 56625 (2015)
21. D.E. López, J.G. Goodwin, D.A. Bruce, S. Furuta, Appl. Catal. A Gen. **339**, 76 (2008)
22. A. Guldhe, B. Singh, I. Rawat, F. Bux, Chem. Eng. Res. Des. **92**, 1503 (2014)
23. B.M. Reddy, M.K. Patil, G.K. Reddy, B.T. Reddy, K.N. Rao, Appl. Catal. A Gen. **332**, 183 (2007)
24. G. Larsen, E. Lotero, L.M. Petkovic, D.S. Shobe, J. Catal. **169**, 67 (1997)
25. A. Kumar, A. Ali, K.N. Vinod, A.K. Mondal, H. Hegde, A. Menon, B.H.S. Thimmappa, J. Mol. Cat. A: Chem. **378**, 22 (2013)
26. W. Zhou, I.E. Wachs, C.J. Kiely, Curr. Opin. Solid State Mater. Sci. **16**, 10–22 (2012)
27. F. Di Gregorio, V. Keller, J. Catal. **225**, 45 (2004)
28. R.R. Chianelli, G. Berhault, B. Torres, Unsupported transition metal sulfide catalysts: 100 years of science and application. Catal. Today **147**, 275–286 (2009)
29. F.C. Menza, H.M. Seip, Environ. Sci. Pol. **7**, 253 (2004)
30. Z.M. Wang, *MoS_2 materials, physics, and devices*, vol 21 (Springer International Publishing, New York, 2014). ISSBN: 978-3-319-02849-1
31. R.R. Chianelli, A.F. Ruppert, M. José-Yacamán, A. Vázquez-Zavala, HREM Studies of layered transition metal sulfide catalytic materials. Catal. Today **23**, 269–281 (1995)
32. V. An, Y. Irtegov, Tribological properties of nanolamellar MoS_2 doped with copper nanoparticles. J. Nanomater. **2014**, 731073 (2014)
33. K.F. Mak, C. Lee, J. Hone, J. Shan, T.F. Heinz, Atomically thin MoS_2: a new direct-gap semiconductor. Phys. Rev. Lett. **105**, 136805 (2010)
34. M. Ramos, G. Berhault, R.R. Chianelli, J.L. Enríquez-Carrejo, Angular dependence of metallic states in 2H-MoS_2 slabs. Comp. Mater. Sci. **84**, 18–22 (2014)
35. H. Topsøe, B.S. Clausen, R. Candia, C. Wivel, S. Mørup, In situ Mössbauer emission spectroscopy studies of unsupported and supported sulfided Co-Mo hydrodesulfurization catalysts: evidence for and nature of a Co-Mo-S phase. J. Catal. **68**(2), 433–452 (1981)

36. M.A. Ramos, G. Berhault, D.A. Ferrer, B. Torres, R.R. Chianelli, Cat. Sci. Technol. **2**, 164–178 (2012)
37. R.R. Chianelli, G. Berhault, P. Santiago, D. Mendoza, A. Espinosa, J.A. Ascensio, M. José-Yacamán, Synthesis, fundamerital properties and applications of nanocrystals, sheets, nanotubes and cylinders based on layered transition metal chalcogenides. Mater. Technol. **15**, 54–61 (2000)
38. M.A. Ramos, V. Correa, B. Torres, S. Flores, J.R. Farías Mancilla, R.R. Chianelli, Spherical MoS_2 micro particles and their surface dispersion due to addition of cobalt promoters. Rev. Mex. Fis. **57**(3), 220–223 (2011)
39. M. Ramos, D. Ferrer, E. Martinez-Soto, H. Lopez-Lippmann, B. Torres, G. Berhault, R.R. Chianelli, In-situ HRTEM study of the reactive carbide phase of Co/MoS_2 catalyst. Ultramicroscopy **127**, 64–69 (2013)
40. G. Casillas, U. Santiago, H. Barrón, D. Alducin, A. Ponce, M. José-Yacamán, Elasticity of MoS_2 sheets by mechanical deformation observed by in situ electron microscopy. J. Phys. Chem. C **119**, 710–715 (2015)
41. H. Jobic, Curr. Opinion Solid State Mater. Sci. **6**, 415–422 (2002)
42. A.N. Fitch, H. Jobic, *Structural Information from Neutron Diffraction* (Springer-Verlag, Heidelberg, 1999)
43. E. Polak, J. Munn, P. Barnes, S.E. Tarling, C. Ritter, J. Appl. Crystallogr. **23**, 258–262 (1990)
44. T. Lemishko, S. Valencia, F. Rey, M. Jimenez-Ruiz, G. Sastre, J. Phys. Chem. C **120**, 24904–24909 (2016)
45. W. Heink, J. Karger, H. Pfeifer, K.P. Datema, A.K. Nowak, J. Chem. Soc. Faraday Trans. **88**, 3505–3509 (1992)
46. A.J. O'Malley, V. Garcia-Sakai, I.P. Silverwood, N. Dimitratos, S.F. Parker, R.A. Catlow, Phys. Chem. Chem. Phys. **18**, 17294–17302 (2016)
47. J. Klinowski, Chem. Rev. **91**, 1459–1479 (1991)
48. Y. Jiang, J. Huang, W. Dai, M. Hunger, Solid State Nucl. Mag. **39**, 116–141 (2011)
49. A. Zheng, S.J. Huang, S.B. Liu, F. Deng, Phys. Chem. Chem. Phys. **13**, 14889–14901 (2011)
50. L.A. Bursill, J.M. Thomas, K.J. Rao, Nature, 157–158 (1981)
51. M.M.J. Treacey, J.M. Newsam, Ultramicroscopy **23**, 411–420 (1987)
52. O. Terasaki, T. Ohsuna, V. Alfredson, J.-O. Bovin, D. Watanabe, K. Tsuno, Ultramicroscopy **39**, 238–246 (1991)
53. I. Díaz, A. Mayoral, Micron **42**, 512–527 (2011)
54. O. Terasaki, J. Electron. Microsc. **43**, 337–346 (1994)
55. O. Terasaki, J. Solid State Chem. **106**, 190–200 (1993)
56. A. Mayoral, T. Carey, P.A. Anderson, I. Diaz, Micropor. Mesopor. Mater. **166**, 117–122 (2013)
57. A. Mayoral, J.E. Readman, P.A. Anderson, J. Phys. Chem. C **117**, 24485–24489 (2013)
58. A. Mayoral, P.A. Anderson, I. Diaz, Micron **68**, 146–151 (2015)
59. A. Mayoral, M. Sanchez-Sanchez, A. Alfayate, J. Perez-Pariente, I. Diaz, Chem. Cat. Chem. **7**, 3719–3724 (2015)
60. M. Haider, S. Uhlemann, J. Zach, Ultramicroscopy **81**, 163 (2000)
61. P.E. Baston, N. Dellby, O.L. Krivanek, Nature **418**, 617–620 (2002)
62. P.E. Baston, Ultramicroscopy **106**, 1104 (2006)
63. V. Ortalan, A. Uzun, B.C. Gates, N.D. Browning, Nat. Nanotechnol. **5**, 506–510 (2010)
64. A. Mayoral, T. Carey, P.A. Anderson, A. Lubk, I. Diaz, Angew. Chem. Int. Ed. **50**, 11230–11233 (2011)
65. K. Yoshida, K. Toyoura, K. Matsunaga, A. Nakahira, H. Kurata, Y.H. Ikuhara, Y. Sasaki, Sci. Rep. **2**, 2457 (2013)
66. J.D. Kistler, N. Chotigkrai, P. Xu, B. Enderle, P. Praserthdam, C.Y. Chen, N.D. Browning, B.C. Gates, Angew. Chem. Int. Ed. **53**, 8904–8907 (2014)
67. C. Aydin, J. Lu, A.J. Liang, C.-Y. Chen, N.D. Browing, B. Gates, Nano Lett. **11**, 5537–5541 (2011)

68. J. Agundez, L. Martin, A. Mayoral, J. Pérez-Pariente, Catal. Today **304**, 15 (2018)
69. D. Pflästerer, A.S.K. Hashmi, Chem. Soc. Rev. **45**, 1331–1367 (2016)
70. A. Turrina, R. Garcia, A.E. Watts, H.F. Greer, J. Bradley, W. Zhou, P.A. Cox, M.D. Shannon, A. Mayoral, J.L. Casci, P.A. Wright, Chem. Mater. **29**, 2180–2190 (2017)
71. I. Tiscornia, S. Irusta, P. Pradanos, C. Tellez, J. Coronas, J. Santamaria, J. Phys. Chem. C **111**, 4702–4709 (2007)
72. S. Uma, S. Rodrigues, I.N. Martyanov, K.J. Klabunde, Micropor. Mesopor. Mater. **67**, 181–187 (2004)
73. Z. Lin, J. Rocha, A. Navajas, C. Tellez, J. Coronas, J. Santamaria, Micropor. Mesopor. Mater. **67**, 79–86 (2004)
74. A. Mayoral, R.M. Hall, R. Jackowska, J.E. Readman, Angew. Chem. Int. Ed. **55**, 16127–16131 (2016)
75. W. Zhou, E.I. Ross-Medgaarden, W.V. Knowles, M.S. Wong, I.E. Wachs, C.J. Kiely, Nat. Chem. **1**, 722 (2009)
76. W. Zhou, N. Soultanidis, H. Xu, M.S. Wong, M. Neurock, C.J. Kiely, I.E. Wachs, ACS Catal. **7**, 2181 (2017)
77. S. J. Pennycook, P. D. Nellist (eds.), *Scanning Transmission Electron Microscopy* (Springer, New York, 2011)
78. J. Liu, Microsc. Microanal. **10**, 55 (2004)
79. P. W. Hawkes (ed.), *Advances in Imaging and Electron Physics*, vol 177 (Elsevier, Amsterdam, 2013), p. 279
80. R. Erni, *Aberration-corrected imaging in transmission electron microscopy*, 2nd edn. (Imperial College Press, London, 2015)
81. N. Tanaka (ed.), *Scanning Transmission Electron Microscopy of Nanomaterials* (Imperial College Press, London, 2015)
82. P. Del Angel, M.L. Hernandez-Pichardo, J.A. Montoya de la Fuente, Catal. Today **312**, 201 (2013)
83. C.L. Jia, M. Lentzen, K. Urban, Microsc. Microanal. **10**, 174 (2004)
84. F. L. Deepak, A. Mayoral, R. Arenal (eds.), *Advanced Transmission Electron Microscopy* (Springer, New York, 2015)
85. P. Li, J. Liu, N. Nag, P.A. Crozier, Appl. Catal. A Gen. **307**, 212–221 (2006)
86. J. Ramírez, F. Sánchez-Minero, Catal. Today **130**, 267–271 (2008)
87. M.H. Siadati, G. Alonso, B. Torres, R.R. Chianelli, Appl. Catal. A Gen. **305**, 160–168 (2006)
88. C. Geantet, Y. Soldo, C. Glasson, N. Matsubayashi, M. Lacroix, O. Proux, O. Ulrich, J.L. Hazemann, In situ QEXAFS investigation at Co K-edge of the sulfidation of a CoMo/Al_2O_3 hydrotreating catalyst. Catal. Lett. **73**, 95 (2001)
89. G. Berhault, A. Mehta, A.C. Pavel, J.Z. Yang, L. Rendon, M.J. Yácaman, L.C. Araiza, A.D. Moller, R.R. Chianelli, The role of structural carbon in transition metal sulfides hydrotreating catalysts. J. Catal. **198**(1), 9–19 (2001)
90. Manuel Ramos, Gilles Berhault, Jose Rurik Farias, Jose Trinidad Elizalde, Domingo Ferrer, Brenda Torres and R. R. Chianelli, Symposium EE, Conference Proceedings MRS Fall Meeting (ID: 913573- EE06-02.R1), (2010)
91. J.A. Rodriguez, J. Hrbek, Acc. Chem. Res. **32**(9), 719–728 (1999)
92. H. Topsøe, J. Catal. **216**, 155–164 (2003)
93. https://www.protochips.com/bibliographies/?fwp_product=fusion
94. G. Berhault et al., J. Catal. **198**, 9–19 (2001)
95. Topsøe, H.; Clausen, B. S.; Massoth, F. E., Springer-Verlag: Berlin, (1996), ISBN 3-540-60380-8. A Review of Deep Hydrodesulfurization Catalysis.
96. E. Stavitskia, M. Bert, Weckhuysen. Chem. Soc. Rev. **39**, 4557–4559 (2010)
97. K. Castillo, F. Manciu, J.G. Parsons, R.R. Chianelli, J. Mater. Res. **22**(10), 2747–2757 (2007)
98. P.M. Ajayan, L.D. Marks, Phys. Rev. Lett. **80**, 585 (1998)
99. Z. Zhang, D. Su, Ultramicroscopy **109**, 766 (2009)
100. G. Berhault, L. Cota Araiza, A. Duarte Moller, A. Mehta, R.R. Chianelli, Catal. Lett. **78**, 81 (2002)
101. G.J. van Gurp, C. Langereis, J. Appl. Phys. **46**, 4301 (1975)
102. H. Jobic, A. Tuel, M. Krossner, J. Sauer, J. Phys. Chem. **100**, 19545 (1996)

Chapter 6
In Situ Upgrading via Hot Fluid and Nanocatalyst Injection

Carlos E. Scott, Lante Carbognani-Ortega, and Pedro Pereira-Almao

6.1 Introduction

The International Energy Agency has estimated that world energy demand will rise 33% by 2040 [1]. Even though there are signs that a transition to lower carbon fuels and technologies is already happening, the estimated share of these will rise to only 25% (from current 19%) in 2040 [1].

Under this scenario the exploitation of all possible energy resources will be necessary to keep pace with this ever-increasing world energy demand. Thus, hydrocarbons will continue to have an important share of the global energy mix, and heavy crude oils and bitumen, given the magnitude of their resources, are expected to have a more significant role.

Heavy, extraheavy oil and natural bitumen are originated from degradation of conventional oil, mainly by bacterial action [2]. They can be defined as petroleum or petroleum-like materials that are very viscous liquids or semisolids at reservoir conditions and are found naturally in porous and fractured media [3]. Bitumen deposits are also called tar sands, oil sands, or bituminous sands. These oils are characterized by their high viscosity, high density (low API gravity), and high concentrations of nitrogen, oxygen, sulfur, and heavy metals.

It has been reported that 70% of the world total oil reserves are in the form of heavy (H) and extraheavy (XH) oil and bitumen (see Fig. 6.1) which are usually called "unconventional oil," with the other 30% corresponding to conventional oil [4]. Worldwide trends indicate that the supply of conventional oil has been declining and will continue to diminish in the future.

C. E. Scott (✉) · L. Carbognani-Ortega · P. Pereira-Almao
Department of Chemical and Petroleum Engineering, Schulich School of Engineering,
University of Calgary, Calgary, AB, Canada
e-mail: scottc@ucalgary.ca; lcarbogn@ucalgary.ca; ppereira@ucalgary.ca

J. M. Domínguez-Esquivel, M. Ramos (eds.), *Advanced Catalytic Materials: Current Status and Future Progress*, https://doi.org/10.1007/978-3-030-25993-8_6

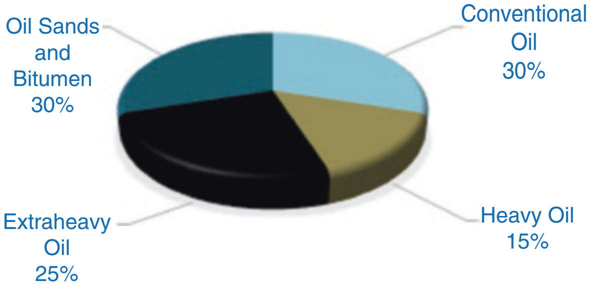

Fig. 6.1 Total world oil resources [4]

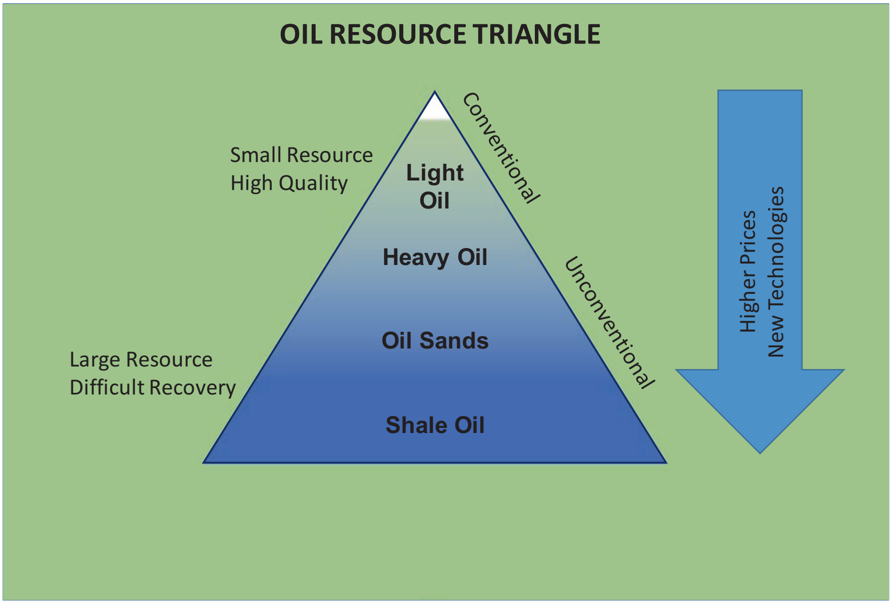

Fig. 6.2 Resource triangle for crude oil

Even though H/XH oils and bitumen represent a huge amount of total oil resources, nowadays they are only a small share of the world oil production. However, due to the huge deposits worldwide they are getting a higher proportion of the market. In recent years recovery and refining processes are being technologically modified to be able to cope with heavier crude oils.

The current low oil price scenario has brought out the need to improve heavy oil and oil sand recovery technologies. Figure 6.2 shows a resource triangle for crude oil. As indicated before, conventional oil reserves have higher quality which makes their production and processing more profitable; however, these are dwindling. In contrast, there are huge reserves of unconventional oil but the recovery is more difficult and they require higher oil prices and more sophisticated technologies in order to make their exploitation economically feasible.

Table 6.1 Heavy and extraheavy oil and bitumen [2, 3]

Type of oil	Viscosity/cp[a]	API gravity/[b]
Heavy	<10,000	10–20
Extraheavy	<10,000	<10
Bitumen	>10,000	<10

[a] Viscosities are referenced to original reservoir temperature

[b] API gravity = [(141.5/specific gravity)−131.5]. Specific gravity is referenced to 15.6 °C (60°F) and atmospheric pressure

In this scenario, in situ (or downhole) processing has been proposed as a way of producing synthetic oils from heavy oils and bitumen directly in the reservoir, thus reducing energy demands for field hydroprocessing and decreasing emissions.

Also, to be transported heavy oils require additional treatments due to their large viscosities (see Table 6.1) [2, 3]. These treatments most commonly consist of either heating or diluting with solvents to decrease the viscosity. Blending the heavy oils with a less viscous hydrocarbon, such as light crude oils, naphtha, kerosene, and condensate, is common practice; however, as much as 30% in volume of diluents is usually needed. This dilution practice is problematic because of the necessity to increase pipeline capacity and the high costs of the diluents. Even though recycling of diluents can be a solution, a large investment to install a recovery process (e.g., distillation) and additional pipeline for transporting the solvent back to the production facilities is then required. This is why nowadays in situ upgrading developments' main target is to get an important and permanent viscosity reduction, as well as a moderate increase in API gravity, instead of high-residue-fraction conversions. Thus producing a synthetic crude oil that is pipelinable (without the need of diluent addition) is a possibility that offers many advantages over thermal recovery processes (like steam-assisted gravity drainage, SAGD). In thermal recovery processes energy is applied to produce the oil by viscosity reduction but once on surface the oil recovers its viscosity and does not meet specifications to be pipelined. In contrast, in situ upgrading (ISU) produces a permanent reduction in viscosity and the oil recovered could have the viscosity required to be transported without any further treatment.

A group of researchers at the Schulich School of Engineering (University of Calgary) have developed and patented [5–7] a process called hot fluid injection or in situ upgrading technology (ISUT) via nanocatalyst that focuses on reducing the environmental footprint of heavy oil production by enhancing the upgrading of bitumen or heavy oil directly in the reservoir. In addition to the granted Canadian patents, the in situ upgrading technology (ISUT) has been filed for protection in the United States, Mexico, Colombia, China, Russia, and Brazil. In situ upgrading is a paradigm shift with the potential to transform the heavy crude oil recovery and upgrading part of the energy business.

This work is a description of the different aspects as well as the historical development of the technology.

6.2 The In Situ Upgrading Process

As described in the patents [5–7], this technology integrates the enhanced recovery and in reservoir catalytic upgrading of bitumen based upon the application of nanocatalytic technology. It consists of separating the heaviest fraction of the oil at the surface and producing catalytic nanoparticles suspended in this fraction. The heavy oil fraction, which is typically a vacuum residue (VR), is produced at temperatures between 320 and 360 °C and then catalytic nanoparticles (dispersed and in that heavy residue) are produced by a patent pending device [8] and mixed with relatively small volumes of hydrogen that solubilizes in a good proportion in the heavy hydrocarbon. This cocktail is injected into the reservoir carrying heat (due to its temperature), thus converting the heavy hydrocarbon to lighter fractions (some of which act as solvent) and gases, ultimately increasing the recovery of the oil in place. The nanocatalyst is retained in the reservoir and remains active anywhere from several months to a few years. The catalyst is only added for a period of time required to create a "catalytic bed" in the reservoir and the heavy residue is kept in a loop and converted to a lighter oil in every pass. The produced upgraded oil does not contain residue (which is continuously separated at the surface and reinjected) and can therefore be regarded as a high-quality synthetic bitumen/oil that meets pipeline specification without the need of diluent from the start of the operation. There is also no need for processing the oil at the surface, which is a required energy-intensive step for most of the current upgrading schemes.

It has also been estimated that in situ processing yields higher rate of return when comparing nanocatalytic ISUT with production by SAGD followed by surface upgrading [9]. This is expectable since in thermal recovery processes energy is applied to produce the oil (by viscosity reduction) but once on surface the oil partially recovers its viscosity and energy needs to be added again in the upgraders to produce a permanent reduction in viscosity (as well as improvement of other characteristics). Performing only one thermal treatment for both recovery and upgrading in the reservoir may lead to a substantial reduction in energy consumption that will also be beneficial from the point of view of emissions. Also, by producing a pumpable oil energy consumption used for diluent recovery and transportation is saved.

The process, with some variations, can be applied to different heavy oil reservoirs like oil sands, heavy mobile oil, and heavy oil naturally fractured reservoirs, and in different configurations like double-pair well (injector-producer) and huff and puff.

Figure 6.3 shows one of the possible configurations for an oil sand reservoir utilizing a SAGD configuration, and co-injection of steam.

For a catalytic ISU process to be feasible it is important that:

1. The catalyst has a high activity in order to speed up the upgrading reactions at lower temperatures and pressures that are usually attainable in the reservoir.
2. The catalytic particles can be injected and placed in the reservoir (along with any other needed additive) in such a way that good contact between the catalyst, co-

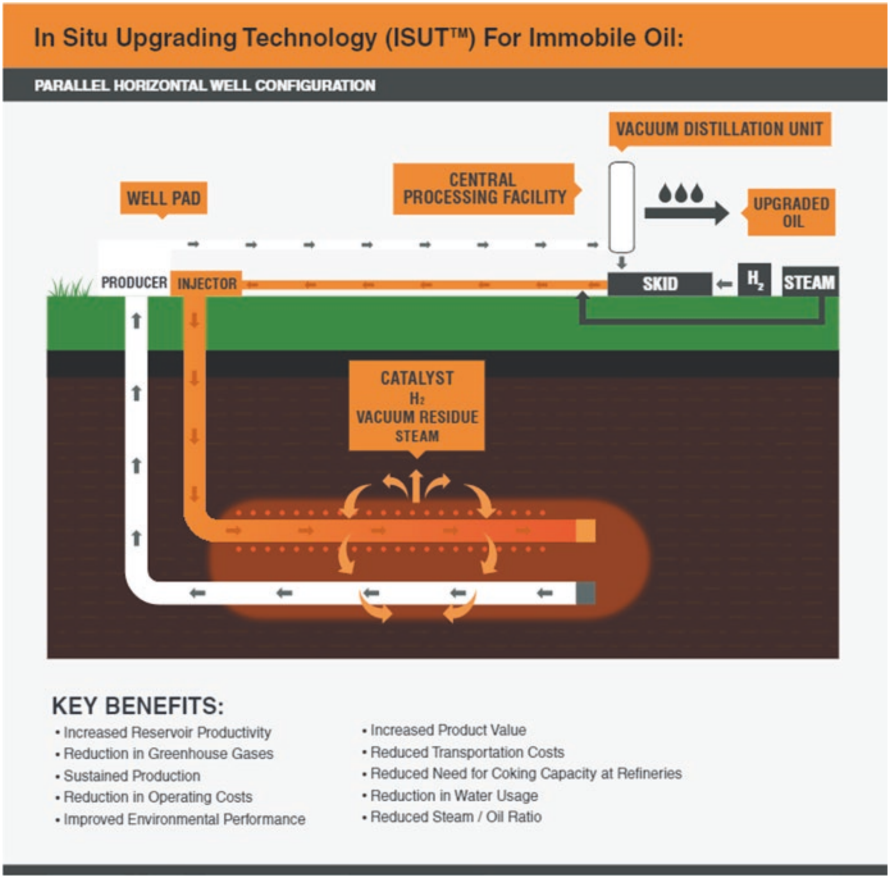

Fig. 6.3 ISUT process configuration for SAGD-type production well [10]

reactants (for example hydrogen), and oil in the heated zone of the reservoir is obtained. This means that the catalytic particles should be able to navigate through the porous media around the injector well.

In order to meet the preceding requirements, the following aspects have been thoroughly researched, and are presented in the next sections:

- Thermodynamics
- The catalysts: particular attention paid to the particle size, composition, and activity
- Transport of particles in porous media
- Hydrogen: important for the production of stable products and avoiding coke formation
- Reaction kinetics

6.3 Thermodynamics

The goal of the ISUT process is to convert the vacuum residue fraction inside the reservoir. Even though downhole upgrading can be done using longer residence times, compared to those used in refineries, temperature and pressure are generally lower. Hydrotreating of VR requires temperatures in the range of 380–450 °C and pressures of 120–160 bars, conditions which are difficult to get down hole. It is then important to know which hydrotreating reactions are thermodynamically feasible at "in-reservoir" conditions. However, heavy oils and bitumen are a complex mixture of organic compounds with a very wide variety of structures, composition, molecular sizes, and physical properties, which makes any thermodynamic determination time consuming. Then, four hypothetical molecules, that can be representative of the typical fractions considered in VR (i.e., saturates, aromatics, resins, and asphaltenes), were defined and used in thermodynamic calculations (see Fig. 6.4) [9, 11, 12]. The structures are only hypothetical and in no way they are intended to be actual molecules present in natural bitumen or heavy oil.

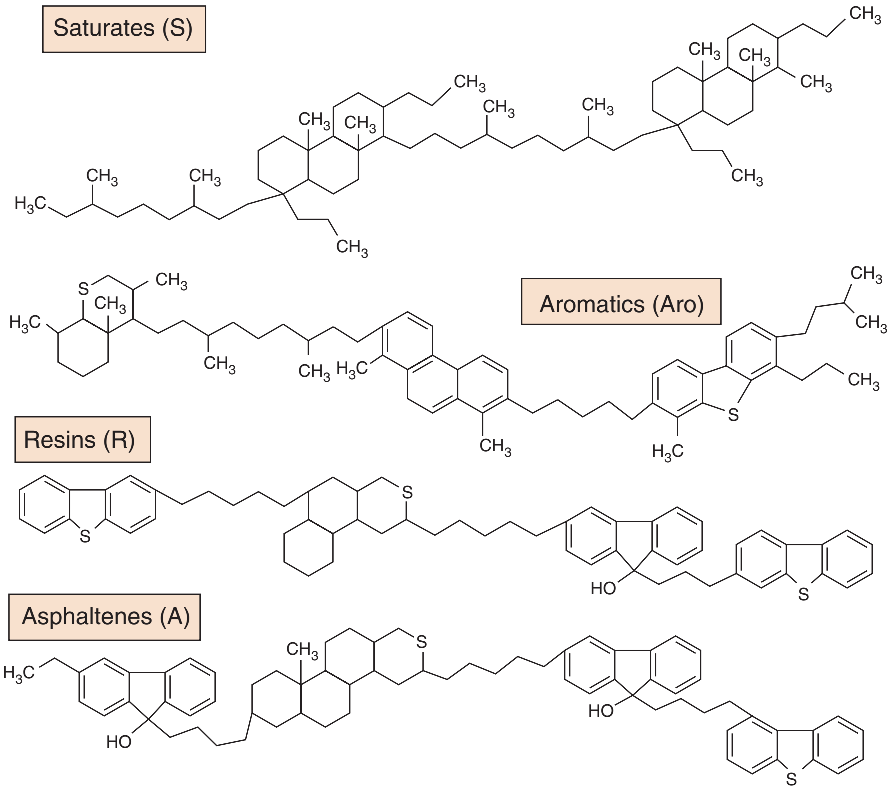

Fig. 6.4 Hypothetical model molecules representing the SARA fractions in a VR for thermodynamic evaluation [9, 11, 12]

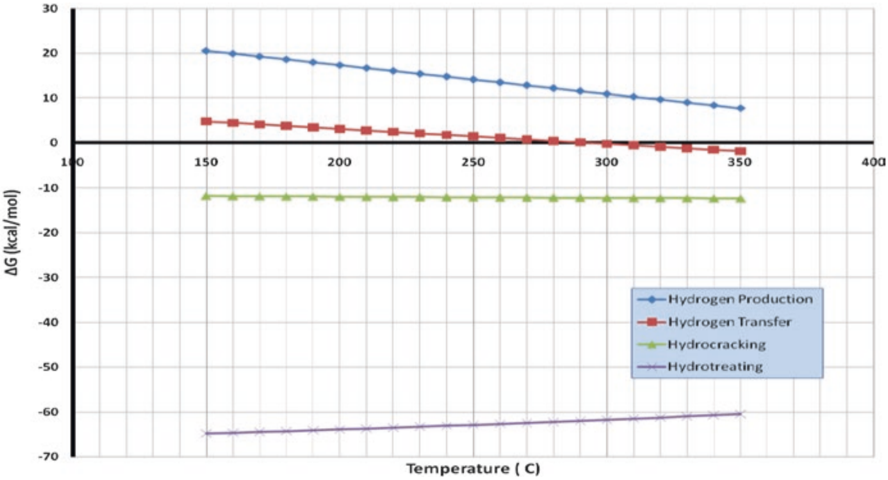

Fig. 6.5 Gibbs free energy for asphaltenes cracking under different conditions [11]

Gibbs free energies were calculated using a group contribution method, to determine which cracking reactions were spontaneous in the range of 150–350 °C. Different reaction routes were explored and it was determined that thermal cracking, in the presence of steam or hydrogen, and hydrogenation of aromatics were the most viable pathways for temperatures achievable during in situ upgrading. Similar trends to the one shown in Fig. 6.5 (for asphaltenes) were obtained for the other fractions. The implication of these results is that in situ upgrading using hydrogen is the most promising alternative since hydrocracking is feasible for all heavy fractions in the 250–350 °C range. Thermal cracking (no hydrogen) of the alkyl chains in resins and asphaltenes becomes significant at temperatures above 300 °C, but with the concomitant production of olefins [9] and coke precursors.

6.4 Nanocatalyst Preparation and Activity

From thermodynamic calculation it was determined that carbon-carbon bond cleavage in the presence of hydrogen was the most appropriate way of cracking (hydrocracking) the VR fraction under reservoir conditions. However, how fast the reactions proceed in the directions proposed is not inferred from thermodynamics; only the spontaneity is assured. It is well known that the rate of a reaction is generally increased by increasing the temperatures, but most effectively and selectively by the use of catalysts.

Nanocatalysts are particularly suited for in situ upgrading since the particles are small enough (10–100 nm) to navigate through the porosity of the reservoir without any permeability impairment of the same, and they have very large surface area and hence very high activity. From the preceding, an initial strong effort was dedicated to find the ways of producing nanoparticles and the most suitable way of injecting them into the reservoir while leading to a good contact between the particles and the oil.

Thus, Vasquez [13] carried out the preparation of Co-Mo and Ni-W catalysts in a continuous system, by mixing two water-in-oil (W/O) emulsions containing the metallic salt precursors, and thermally decomposing the mixture to produce the solid catalysts dispersed in the hydrocarbon media. A base lubricant oil was used as hydrocarbon medium, because its transparency allowed the determination of the sizes of the dispersed solids by dynamic light scattering (DLS). It also has an initial boiling point higher than catalyst preparation temperature, thus avoiding a significant fractionation of the oil during the thermal treatment of the emulsions. A portion of the solids dispersed in the oil were separated by centrifugation and washed with toluene. Solids thus obtained were characterized by temperature-programmed reduction (TPR), X-ray diffraction (XRD), and scanning electron microscopy (SEM). Solids with different Ni/(Ni + W) and Co/(Co + Mo) atomic ratios were prepared. The activity of the catalysts, for thiophene hydrodesulfurization (HDS) and toluene hydrogenation (HYD), was determined in a continuous-flow microreactor. Particles with diameter between 150 and 650 nm, as determined by DLS, were obtained. The XRD patterns showed them to be amorphous and the main components were Mo and Co sulfides (for the Co-Mo series) and Ni and W sulfides (for the Ni-W series). Typical volcano curves, usually observed in hydrotreating reactions for this type of solids, were obtained for the hydrogenation of toluene (see Fig. 6.6) using presulfided particles. The activity maxima for HYD were found at Ni/(Ni + W) and Co/(Co + W) atomic ratios of 0.5 and 0.33, respectively [9, 13].

Thompson et al. [14, 15] using a similar preparation method studied the effect of the decomposition temperature on particle size in the synthesis of molybdenum ultradispersed (UD) catalysts from water-in-oil emulsions in a continuous-flow system in two different configurations: horizontal reactor and vertical reactor.

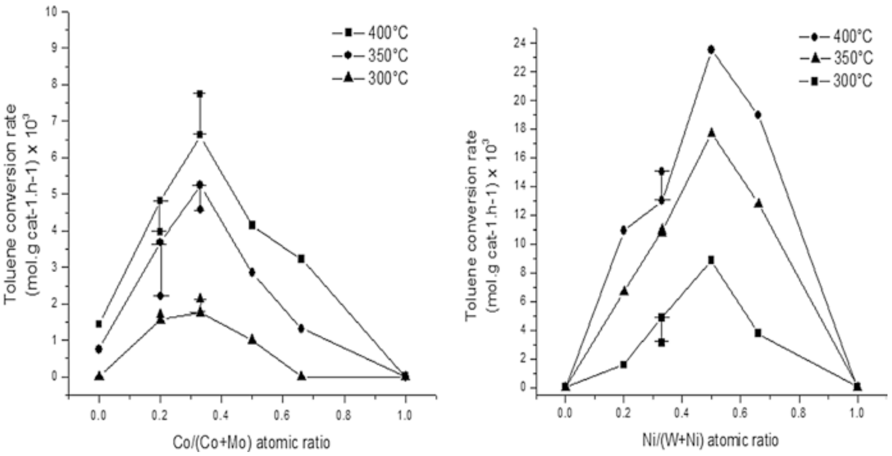

Fig. 6.6 Toluene hydrogenation using Co-Mo and Ni-W bulk catalysts [13]

The particles obtained were characterized by DLS, SEM, and XRD, and their activity in toluene hydrogenation was determined.

DLS characterization results indicated that the horizontal configuration produces particles with less dispersivity. Particle size increases from 98.5 to 658.9 nm with increasing decomposition temperature from 498 to 598 K. SEM results indicate that the particle diameter determined by DLS is in fact the result of agglomeration of smaller primary particles of 30–50 nm in diameter (see Fig. 6.7). Also, according to XRD, the original particles obtained are a mixture of MoO_2 and MoO_3 (in this preparation no sulfiding agent was added); however, after the toluene hydrogenation reactions with the as-prepared solids, the particles are converted to a new active phase, possibly molybdenum carbide. The results also suggest that the mechanism of particle size increase is most likely caused by physical agglomeration and not crystal growth [15].

Contreras et al. [16, 17] prepared nanoparticles of Ni, Mo, and NiMo using thermal decomposition of transient emulsions (emulsions that are sustained by the energy supplied to create them, but when the energy source is cut off the emulsion

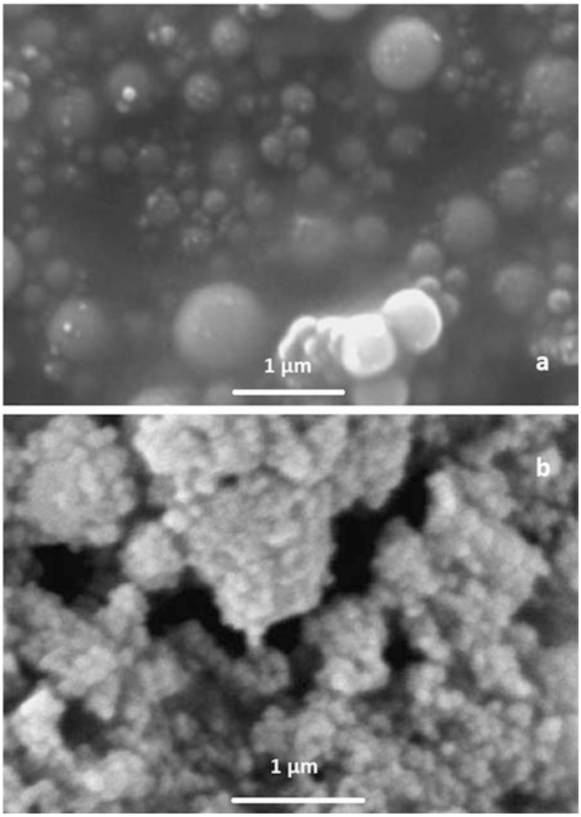

Fig. 6.7 Scanning electron microscope images of particles produced from (**a**) VR at 523 K and (**b**) 498 K [15]

tends to break in a short time frame), which were immediately decomposed after being formed in a continuous-flow system. In these preparations the dispersant used was base lubricant oil and no surfactant was added, thus producing a suspension of particles in the hydrocarbon media. This type of preparation was explored since injection of emulsions, or hydrocarbons containing surfactants, in a sand pack leads to partial plugging of the core (see Sect. 5). The study was done taking into consideration different parameters for the preparation of the transient emulsions, like the concentration of the precursor metallic salts, water percentage, use of surfactant, and intensity of mixing the various solutions. The characterization was done via DLS and transmision electron microscopy-energy dispersive spectroscopy (TEM-EDS). Also, the HDS of vacuum gas oil (VGO), with the nanoparticles produced directly in the VGO, was evaluated.

It was found that the prepared particles had average diameters, determined by DLS, in the range of 150–500 nm (depending on the conditions used for the preparation); however, the primary particle size observed by TEM was around 35 nm, indicating that the particle size obtained by DLS is the result of agglomeration of smaller particles. Freshly prepared particles contain mainly carbon, molybdenum, and oxygen, which suggests that the particles are mostly molybdenum oxide (carbon comes from the preparation matrix). A synergetic effect was observed for the hydrodesulfurization (HDS) of the VGO, which confirms the results found by Vasquez [13]. The high-resolution transmission electron microscopy (HRTEM) of the particles after reaction shows the characteristic laminar structure of MoS_2 (Fig. 6.8).

The relationship between particle size (for molybdenum sulfide) and HDS activity was also studied [18]. Particles were prepared by addition of polyvinylpyrrolidone (PVP) in different concentrations to a solution of ammonium tetrathiomolybdate and

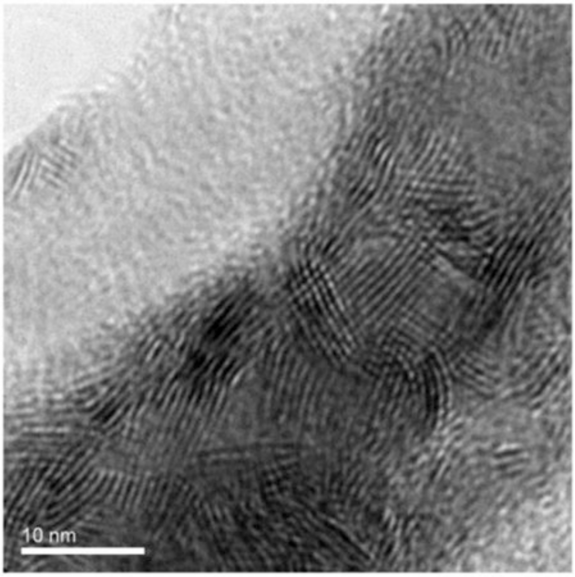

Fig. 6.8 HRTEM image of NiMo particles after reaction [16]

Table 6.2 MoSx particle diameter and HDS conversion [16, 18]

Catalyst	Particle size/ (nm)	HDS/%
MoS_x-PVP (0.5)	13 ± 1	42
MoS_x-PVP (0.02)	136 ± 32	28
MoS_x-PVP (0.01)	400 ± 130	30
MoS_x-PVP (0)	10,200 ± 2000	18

then acidifying with a sulfuric acid solution to precipitate nanoparticles of MoS_3 (which is easily converted to MoS_2 by thermal treatments). This methodology was chosen (instead of transient emulsion) in order to produce particles with a well-defined and narrow distribution of sizes. The prepared particles were characterized by DLS, TEM, XRD, and X-ray photoelectron spectroscopy (XPS), and tested in the HDS of a vacuum gas oil (VGO). A correlation between particle diameter and HDS conversion (see Table 6.2) was observed; thus for particles with sizes around 13 nm, the % of HDS was double than that of bulk molybdenum sulfide and also significantly higher when compared with particles with sizes around 100–400 nm. It was also observed that particle morphology can have an important influence in their activity.

This result shows the importance of having the smallest particle size possible to get the best activity for in situ upgrading applications.

6.5 Flow of Nanocatalyst Through Porous Media

Scientific literature on the flow of nanoparticles in porous media is scarce, in particular when the particles are suspended in hydrocarbons like the ones targeted in the ISU process.

Different ways of preparing and introducing the ultradispersed catalyst (UDC) in the processes have been proposed [19]:

1. Dispersion of fine powder in the hydrocarbon media.
2. Water-in-oil emulsion where oil-soluble salts of the precursors are dissolved in the aqueous phase. The emulsion is decomposed during the processing of the heavy feedstock, which produces the metallic precursors that are then converted to the active species during the hydroprocessing.
3. Solubilization of lipophilic metal compounds in the feed: During the processing of the feedstock these oil-soluble compounds are converted into the catalytically active species.

For downhole upgrading introduction of water-in-oil emulsion is normally proposed.

For the ISUT process it is required that the catalytic particles are placed in the formation where the upgrading reactions can be speeded up, which implies that they have to flow through the porous media without any impairment of the reservoir's permeability. The propagation of submicrometer-sized catalytic particles in the porous media was studied by Zamani et al. [20]. Initially, the propagation of molybdenum particles suspended in heavy vacuum gas oil (HVGO) at room temperature was studied. For the preparation of the dispersed catalytic particles in the oil a surfactant was added during the emulsification stage. It was found that nanodispersed particles can propagate through the sand without causing permeability damage; however, the presence of any residual surfactant (left in the catalytic suspension) produced the emulsification of the original connate water which caused a pressure drop not related to the deposited particles. It was also found that between 10 and 20% of the injected catalyst remained deposited in the sand pack and that the retained particles cannot be removed by flowing HVGO. The retention of the particles was irreversible and attributed to adsorption on the surface of the sand. In a continuation work [21] the effect of sand bed temperature, salinity of the brine, and permeability of the pack, in the propagation of the catalytic particles, was also studied. HVGO was again used for the suspension of the particles but for this study no surfactant was added during the nanodispersion preparation. No significant changes were found in relation to the previous paper [20]. In particular, increasing the sand pack temperature to 150 °C did not show any adverse effect on the behavior of the propagation of the catalyst.

Rendon [11] studied the flow and deposition of catalytic tri-metallic particles (Ni-Mo-W) using a sand pack that simulates a sandstone reservoir, under upgrading conditions (i.e., temperatures between 320 and 340 °C and in the presence of 500 psig of hydrogen). The suspension was prepared using Athabasca bitumen (ATB) and the reactivity of ATB and deasphalted oil (DAO) on the sand pack, where the catalyst had already been deposited, was also tested.

It is reported that at higher temperatures and longer residence times the percentage of particles retained in the sand pack increases and that the retention is irreversible in agreement with the work by Zamani et al. [20, 21]; however, under the conditions tested no catalyst was found in the products collected suggesting total retention of the particles injected.

Also, a model for the transient deposition and suspension of nanoparticles immersed in viscous media was developed [22–27]. This is important because during the injection of the nanocatalysts in the reservoir any particle deposition in the injector tubbing should be avoided. The time-dependent concentration of particles deposited in confined horizontal cylindrical channels or flowing through horizontal cylindrical channels was obtained with the model, the aim being to estimate the maximum size of the particles that allows them to remain suspended in the liquid hydrocarbon. Correlations between the model and experimental results, using different types of nanoparticles, showed good fittings. Also, the model predicts that for a suspension of MoO_3 particles in Athabasca bitumen flowing in pipes at temperatures between 340 and 380 °C, those with diameters below 150 nm are unlikely deposited in the channels (see Fig. 6.9, where the normalized particle concentration in the bottom of the pipe against particle diameter is presented). The importance of using nanoparticles of catalyst for ISU applications is put in evidence.

The kinetics of agglomeration of Fe_2O_3 nanoparticles suspended in oil was also investigated [27, 28]. The variation of the particle diameters with time at different

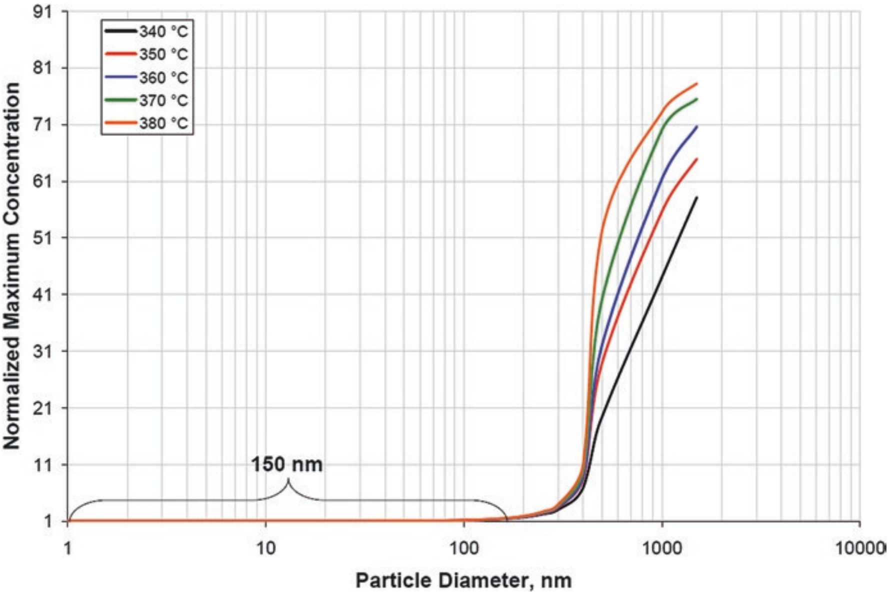

Fig. 6.9 Effect of MoO_3 particle diameter (dispersed in Athabasca bitumen) and temperature on its deposition when flowing through pipes [27]

temperatures and concentrations was studied. It was found that particles agglomerated until a critical diameter was reached which depends on the particle concentration and temperature. A kinetic model was developed which accurately reproduces the experimental results (error <5%). Finally, activation energies suggest that the agglomeration process is mainly physical, i.e., adhesion of particles resulting from collisions rather than chemical bonding through reconstruction of smaller crystals into large ones, in agreement with the previous report [15]. Rodrígues-DeVecchis et al. [29] determined the size of the catalytic particles suspended in bitumen using nanoparticle tracking analysis (NTA). The particles were also deposited in a sand pack using temperature, pressure, and residence times similar to those proposed in the ISUT process. It was found that the particles formed and suspended in the bitumen had an average diameter of 110 nm (mode) and that 80% of the particles have diameters between 57 and 176 nm. The suspension was passed through a sand pack using a vertical unit in upflow configuration in order to do the catalyst deposition on the sand. The deposition was done at 300 °C with a residence time of 24 h during 9 days. After the deposition step the unit was opened and sand samples were taken at different positions along the pack for TEM analyses. Catalytic particles were observed in all the samples and the average diameter was smaller at the entrance (85 nm) than at the exit (165 nm) with sizes similar to those determined in the bitumen suspension by NTA. EDX analysis was used to assure that the measured particles corresponded to catalyst and not to any other mineral deposited in the pack during the experiment, for example vanadium and iron originally in the oil. It was found, in agreement with previous work [11], that all the metal added as catalyst

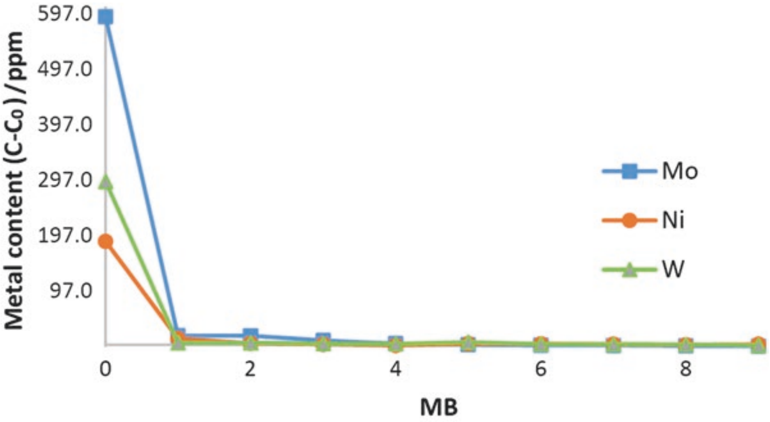

Fig. 6.10 Metal content evolution in the liquid products during catalyst deposition [29]

was retained in the sand pack. Figure 6.10 [30] shows the concentration of the added metals in the effluents collected after passing several pore volumes through the sand pack (the concentrations at 0 MB represent the amount of catalytic metal in the catalyst-bitumen suspension). The effect of the temperature and residence time on the catalyst deposition has also been investigated [30] and it was found that independent of the residence time and temperature more than 95% of the particles are retained attached to the sand.

The effect of type of mixer (static and high shear) and the sulfiding agent (ammonium sulfide and thiourea) on the particle size and composition of the catalyst, suspended in bitumen, has also been studied [31]. The particle sizes were determined using NTA and the composition by XPS. Particles with varying sizes (80–200 nm) were obtained with the smaller ones being the ones prepared using high shear mixers and ammonium sulfide. Even though in the particles obtained with both sulfiding agents (ammonium sulfide and thiourea) the metals were not completely sulfided, the use of thiourea produced a higher proportion of the metals as sulfides (the rest present as oxides).

6.6 Athabasca Bitumen Upgrading at Low-Severity Conditions

6.6.1 Batch Reactor Experiments

One important aspect of the ISUT process is the injection of hydrogen along with the heavy hydrocarbon containing the nanocatalytic particles suspended. Catalyst and hydrogen are both important since pure thermal processes inevitably lead to the formation of coke and olefins that have the tendency to polymerize and produce gums, which can have negative effects on reservoir permeability and quality of the oil produced.

The amount of hydrogen used is very low compared to what is normally used in refineries, and an important proportion is solubilized in the oil [32–34]. The combination of the hydroprocessing/hydrotreating catalyst and hydrogen, along with the relatively low temperatures used in the process, reduces the possibility of coke and coke precursor formation by saturation of the free radicals formed. It also produces the partial removal of organosulfur compounds and asphaltenes. Thus, the hydrocracking of bitumen using ultradispersed nanocatalysts at conditions of pressure, residence time, and temperature that can be obtained in reservoirs when using the ISUT process has produced very promising results.

Galarraga et al. [35, 36] carried out the hydrocracking of Athabasca bitumen at low-severity conditions, using Ni-Mo-W (1000 wppm) tri-metallic catalytic particles dispersed in the oil. The preparation of the catalytic dispersions was done using a methodology similar to previously reported [37–41]. Water-in-oil (w/o) emulsions were produced by addition of aqueous solution of the metals to a mixture of bitumen and surfactant previously homogenized. Two types of feeds were used for the upgrading experiments. The first type was charged in the batch reactor almost immediately after preparation (fresh emulsions). The amount of water determined in these emulsions was around 4.4–4.3 wt. %. The second type (dry emulsions) was obtained by letting the freshly prepared emulsions to stand for 8 h at 313 K with stirring. The amount of water in these feeds was reduced to less than 0.5 wt. %. Then the reactor (batch) was charged with the emulsion and the hydrocracking of the bitumen was performed (593–653 K, 2.5 MPa of hydrogen, 5–69 h, 500 rpm).

The products obtained from reactions using dry emulsion showed an increase in the residuum and sulfur conversions from 45 to 56% and 17.5 to 37.5%, respectively, when compared to those obtained from fresh emulsions. Also, the amount of coke is reduced from 1.3 to 0.2%, as well as the microcarbon residue (MCR) from 14.6 to 11.1%, when dry emulsions were used. It is suggested that the water present in the fresh emulsion is released during the reaction consequently reducing the hydrogen partial pressure, thus possibly having a detrimental effect on the catalysts, and on the conversion. Increasing the reaction temperatures (623–653 K) leads to a rapid increase in residue conversion and, at all temperatures tested, as the reaction time increases the conversion levels off and reaches a pseudo state of equilibrium. In summary, it was found that upgrading of Athabasca bitumen using relatively low temperature and hydrogen pressure is possible provided that long reaction times are used. Conversions up to 56% of the residuum fractions with important decrease in the viscosity and a significant reduction of the amount of coke produced (in relation to a thermal non-catalytic upgrading), as well as sulfur and MCR, in the final synthetic bitumen were observed. Also, transmission electron microscopy (TEM) of the solid collected after the reaction (380 °C and 5.8 h) evidenced the presence of two distinctive type of particles. Relatively large (500–1000 nm) and black particles were assigned to coke, while the smaller ones (<200 nm) were considered to be catalytic particles by comparison with a sample of catalyst prepared by decomposition of an emulsion but not submitted to reaction conditions (see Fig. 6.11).

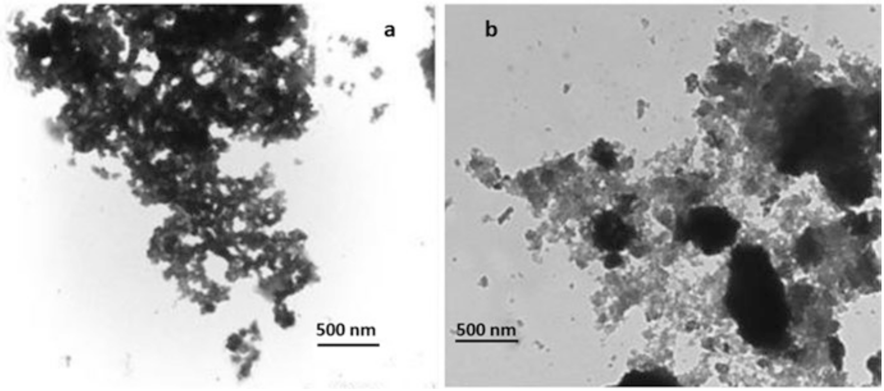

Fig. 6.11 TEM microphotographs of catalysts: (**a**) obtained by direct decomposition; (**b**) obtained after HCK reaction [35]

Reactions were also carried out, at near in-reservoir conditions, in the presence of a sand matrix ($SiO_2 > 98\%$). It was found that the incorporation of sand has a beneficial impact on the vacuum residue fraction conversion [36].

6.6.2 Continuous Flow in Sand Packs at ISUT Conditions

Several works have been carried out using vacuum gas oil (VGO) [42, 43], deasphalted oil (DAO) [11], bitumen [11, 44], and VR [44, 45]. Rendon [11] injected Athabasca bitumen (AB) containing the ultradispersed catalyst and found that using a hydrogen flow equivalent to 90 stdcm^3 per cm^3 of bitumen is enough to trigger hydrotreating reactions when long residence times are used (18–74 h) at 320–340 °C. It was also shown that once the catalyst is deposited over the sand grains the reaction continues without the need of further injection of ultradispersed catalyst. The sand with the deposited particles acts as a fixed bed of catalyst. Deasphalted oil was also used as feed and injected into the sand pack with catalytic particles already attached to it at 320 °C and residence times of 74 and 108 h. Conversion of the residue fraction of the DAO of around 25% was obtained for the most severe condition, indicating the effectiveness of the catalytic particles deposited in the sand to promote hydrotreating reactions of bitumen and DAO at ISUT conditions.

Coy [44], using similar conditions as in the previous work [11], evaluated the injection of bitumen and VR to a sand pack ($SiO_2 > 98\%$). In this case VR was used to suspend the catalytic particles which were injected to the sand (simulating a sandstone reservoir) in order to produce a sand-supported catalytic bed. The amount of catalyst deposited was 0.14–0.23 wt. % of the sand weight. After the initial catalyst deposition step, VR and hydrogen were injected continuously at residence times spanning from 133 to 377 h for several pore volumes and finally bitumen and hydrogen were injected for several additional pore volumes (always using the same catalyst/sand pack). In total around 70 pore volumes of the different feeds were injected. A thermal run (no catalyst) using VR was also carried out in order to determine whether any observed VR conversion was attributable to the presence of the catalyst. At similar conditions (24–27 h of residence time and 301–304 °C) the VR conversion was around 20 percentage points higher (21.7–23.3% vs. 4.4%) for the catalytic test. At higher residence times (around 300 h) conversions of the VR fraction of up to 32% were obtained. It was also observed that the sand pack permeability did not significantly decrease after the tests.

Carbognani et al. [45, 46] and Hovsepian et al. [47] studied the conversion of Athabasca VR working at ISUT conditions using a two-dimensional bench plant (different from previous work) designed to have a system with different vertical and horizontal permeability (see Fig. 6.12 for a schematic representation of the setup). Experiments were carried out at 500 psig, 350 °C, and hydrogen oil ratio of 300 scm^3 per cm^3 of VR injected. Residence times of 24, 72, and 288 h were used.

It was found that the VR was converted in the system (up to 60%) and that the API gravity increased substantially (from 2.4° to 16.4°) with reduction in the sulfur content (4.5–2.3%) and the viscosity (99.98% reduction). The oil left inside the system after the test was recovered and the presence of extremely light material were evidences in the lower horizontal branch (see Fig. 6.12).

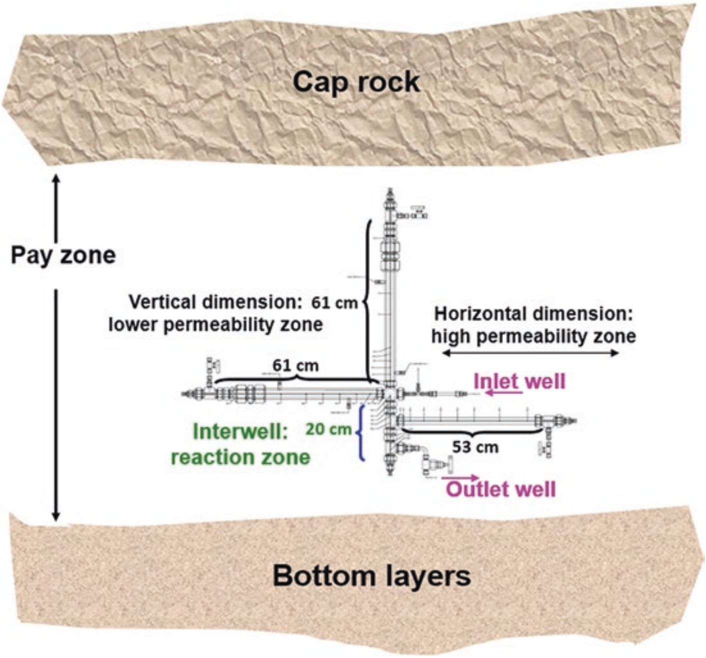

Fig. 6.12 Schematic of the two-dimensional unit representing vertical and horizontal permeability in a sandstone reservoir [46]

6.7 Kinetics for Athabasca Bitumen at Low-Severity Conditions

For ISUT it is important to know if the hydrocarbon to be injected into the reservoir is reactive at the conditions of the process (low temperatures and long residence times), then an important effort has been devoted to get the kinetic parameters (activation energies and pre-exponential factors) for the different studied feeds. Also, for reservoir's simulation purposes kinetic parameters are needed [48].

Thus, Loria et al. [49] using bitumen as a feedstock and a continuous upflow reactor (reaction conditions shown in Table 6.3) determined the kinetic parameter for the hydrocracking of the oil. The catalyst was introduced in the form of an emulsion prepared according to a previous work [35]. Also, Galarraga et al. [50] worked with a 100 cm^3 batch reactor (conditions shown in Table 6.3) using a catalyst obtained from a water-in-oil (w/o) emulsion and having 1000 ppmw of active metals. The kinetic model used in both works to get the kinetic parameters for the hydrocracking of the bitumen includes five lumps: residue, vacuum gas oil (VGO), distillates, naphtha, and gases, and ten reactions (k_1, …, k_{10}) (see Fig. 6.13) as previously proposed [51]. The values of the kinetic constants as well as those for the activation energies for each reaction are reported in Table 6.4.

Similarly, Da Silva [52] studied the hydrocracking of ABVR and ABVR's pitch (ABVR-Pitch), using a combination of catalysts and hydrogen at conditions similar to those that would be used in the ISUT process, and found that it is possible to convert the VR, reduce viscosity as well as sulfur and asphaltene content, and produce an increment of the API gravity.

Some common features of the kinetics determinations for the different feedstocks are the following:

(a) Naphtha hydrocracking is insignificant (k_4 values are negligible).
(b) Kinetic constants for the conversion of VGO into gases (k_8) are 0.
(c) Likewise, the values obtained for k_{10} (distillates to gases) are null.

From the values reported, the residence time needed to achieve 50% residue conversion fraction of AB, at 623 K (350 °C), is in the range of 40–120 h, which indicates that the use of low temperatures in the ISUT process can be compensated with the higher residence times feasible in the reservoirs which allows for similar residue conversions obtained on surface upgrading.

Table 6.3 Reaction conditions

	Loria et al. [49]	Galarraga et al. [50]	Da Silva [52]
Temperature/K	593–653	593–653	593–668
LHSV/h^{-1}	0.020–0.11		0.008–0.05
Hydrogen-to-oil ratio/stdcm^3 cm^{-3}	625	–	90
Pressure/MPa	2.76	3.45	3.45

Std = standard

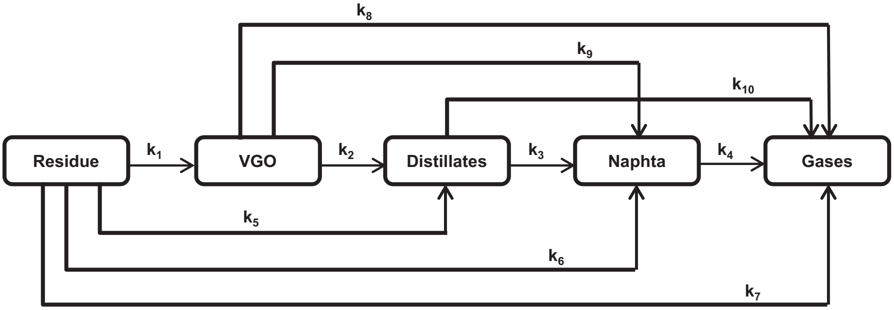

Fig. 6.13 Kinetic model for catalytic hydrocracking of Athabasca bitumen (AB), Athabasca vacuum residue (ABVR), and pitch (ABVR-Pitch)

Table 6.4 Activation energy for the hydrocracking of Athabasca bitumen (AB), its vacuum residue (ABVR), and pitch obtained from ABVR according to the model shown in Fig. 6.13

Reference	Loria et al. [49]	Galarraga et al. [50]	Da Silva [52]	Da Silva [52]
Feed	AB	AB	ABVR	ABVR-Pitch
Reaction				
1	136	172	76.6	144.4
2	145	157	70.8	168.3
3	146	242	363	487.9
4	–	–	–	–
5	167	277	43.2	173.3
6	192	272	58.1	179.8
7	261	303.1	147	276.0
8	–	–	–	–
9	190	343	–	–
10	–	–	–	–

Rodrígues-DeVecchis et al. [53] obtained the kinetics parameters for the thermal decomposition of ABVR in the presence of hydrogen and using a sand-packed reactor (no catalyst). It was found that the activation energies were generally high and that the products were unstable for conversion higher than 30%, and that a substantial amount of coke was left behind in the sand matrix.

6.8 Conclusions

One of the key outcomes of the work is that the patented ISUT process is able to produce a pipelinable oil at achievable conditions for an Athabasca-like reservoir. Nanocatalysts injected into the reservoir, suspended in a hot fluid, are almost totally retained attached to the rock and keep its activity for a long time. The addition of hydrogen and the temperature conveyed by the hot fluid allow the conversion of the heavier fraction of the heavy oil or bitumen. It was also demonstrated that the method of preparation and incorporation of the nanocatalyst is a key factor for the process to be efficient. Injection of emulsion in a sand pack produces emulsification of connate water and leads to pressure drops and reduction in permeability.

Acknowledgments The authors acknowledge the contributions of previous and current sponsors of the Catalysis for Bitumen Upgrading Group (CBUG) and the Alberta Ingenuity Center for In Situ Energy (AICISE): in particular to AICISE sponsors (Alberta Ingenuity Fund, Shell-Canada, Nexen Inc., Conoco-Phillips, Repsol-YPF, Total-Canada, and the Alberta Energy Research Institute) and to Natural Sciences and Engineering Research Council of Canada (NSERC), Alberta Innovates-Energy and Environment Solutions (AIEES), and NEXEN Inc., for the support provided through the NSERC-NEXEN-AIEES Industrial Research Chair in Catalysis for Bitumen Upgrading. In addition, the NSERC support via CRD project 499942-16 co-sponsored by Total E&P Canada Ltd. is gratefully acknowledged. Also, the contribution of facilities from the Canada Foundation for Innovation (CFI), the Institute for Sustainable Energy, Environment and Economy (ISEEE), and the Schulich School of Engineering at University of Calgary is greatly appreciated.

References

1. International Energy Agency, World-Energy-Outlook: IEA-WEO-Executive_ Summary-2015, 2015. https://www.iea.org/Textbase/npsum/WEO2015SUM.pdf
2. C.E. Scott, P. Pereira-Almao, Curr. Topic. Catal. **11**, 1 (2014)
3. E. Flores, Technology Today. Spring, 10, 2010
4. Schlumberger, E&P Defining Series. http://www.slb.com/resources/oilfield_review/~/ media/Files/resources/oilfield_review/defining_series/Defining-Heavy-Oil.ashx
5. P. Pereira-Almao, Z. Chen, B. Maini, C.E. Scott, In situ upgrading via hot fluid injection. Canadian Patent 2,810,022, 2014
6. P. Pereira-Almao, Z. Chen, B. Maini, C.E. Scott. In situ upgrading via hot fluid injection. Canadian Patent 2,864,788, May 2016
7. P. Pereira-Almao, Z. Chen, B. Maini, C.E. Scott, In situ upgrading via hot fluid injection. US Patent Application US 2015/0114636 A1, 30 Apr 2015
8. P. Pereira-Almao, A.S. Pereira Cota, A. Coy-Plazas, C.E. Scott, Catalyst preparation unit for use in processing of heavy hydrocarbons. International Patent Application WO 2016/1615142 A1, 2016
9. P. Pereira-Almao, Can. J. Chem. Eng. **90**, 320 (2012)
10. http://www.pc-cups.com
11. V. Rendon, MSc Thesis, University of Calgary, Canada, 2011
12. L. Roa, MSc Thesis, University of Calgary, Canada, 2012
13. A. Vasquez, MSc Thesis, University of Calgary, Canada, 2007
14. J. Thompson, MSc Thesis, University of Calgary, Canada, 2008
15. J. Thompson, A. Vasquez, J. Hill, P. Pereira-Almao, Catal. Lett. **123**, 16 (2008)
16. C. Contreras, MSc Thesis, University of Calgary, Canada, 2009
17. C. Contreras, C.E. Scott, P. Pereira-Almao, Prepr. Pap.-Am. Chem. Soc., Div. Petr. Chem. **54**, 56 (2009)
18. C. Contreras, F. Isquierdo, P. Pereira-Almao, C.E. Scott, J. Nanotechnol. **2016**., 9 pages (2016)
19. A. Del Bianco, N. Panariti, S. Di Carlo, J. Elmouchnino, B. Fixari, P. Le Perchec, Appl. Catal. A Gen. **94**, 1 (1993)
20. A. Zamani, B. Maini, P. Pereira-Almao, Energy Fuel **24**, 4980 (2010)
21. A. Zamani, B. Maini, P. Pereira-Almao, Can. J. Chem. Eng. **90**, 304 (2012)
22. H. Loria, P. Pereira-Almao, C.E. Scott, Ind. Eng. Chem. Res. **48**(4088) (2009)
23. H. Loria, P. Pereira-Almao, C.E. Scott, Ind. Eng. Chem. Res. **48**(4094) (2009)

24. H. Loria, P. Pereira-Almao, C.E. Scott, Ind. Eng. Chem. Res. **49**(1920) (2010)
25. H. Loria, P. Pereira-Almao, C.E. Scott, Eng. Lett. **16**, 219 (2008)
26. H. Loria, P. Pereira-Almao, C.E. Scott, Current Themes in Engineering Technologies, Eds. Sio-Long Ao, Mahyar A. Amouzegar, Su-Shing Chen. American Institute of Physics. p. 12, 2008
27. H. Loria, PhD Thesis, University of Calgary, Canada, 2009
28. H. Loria, P. Pereira-Almao, C.E. Scott, Ind. Eng. Chem. Res. **54**, 9487 (2015)
29. V. Rodriguez-DeVecchis, L. Carbognani, C.E. Scott, P. Pereira-Almao, Ind. Eng. Chem. Res. **54**, 9877 (2015)
30. V. Rodriguez-DeVecchis, L. Carbognani, C.E. Scott, P. Pereira-Almao, Ind. Eng. Chem. Res. **57**, 2835 (2018)
31. E. Scheele-Ferreira, C.E. Scott, M.J. Perez-Zurita, P. Pereira-Almao, Ind. Eng. Chem. Res. **56**, 7131 (2017)
32. H.Y. Cai, J.M. Shaw, K.H. Chung, Fuel **80**, 1055 (2001)
33. H.Y. Cai, J.M. Shaw, K.H. Chung, Fuel **80**, 1065 (2001)
34. D. Lal, F.D. Otto, A.E. Mather, Fuel **78**, 1437 (1999)
35. C.E. Galarraga, P. Pereira-Alamo, Energy Fuel **24**, 2383 (2010)
36. C.E. Galarraga, PhD Thesis, University of Calgary, Canada, 2009
37. P. Pereira-Almao, V.A. Marcano, F. Lopez-Linares, A. Vasquez, Canadian Patent, CA 2,630,365, 2010
38. P. Pereira-Almao, V.A. Marcano, F. Lopez-Linares, A. Vasquez, US Patent, US 7,897,537 B2, 2010
39. P. Pereira-Almao, V.A. Marcano, F. Lopez-Linares, A. Vasquez, US Patent, US 8,283,279 B2, 2010
40. P. Pereira-Almao, V.A. Marcano, F. Lopez-Linares, A. Vasquez, US Patent, US 8,298,982 B2, 2010
41. P. Pereira-Almao, V.A. Marcano, F. Lopez-Linares, A. Vasquez, US Patent, US 8,304,363 B2, 2010
42. R. Hashemi, N. Nassar, P. Pereira-Almao, Energy Fuel **27**, 2194 (2013)
43. R. Hashemi, N. Nassar, P. Pereira-Almao, Energy Fuel **26**, 1645 (2012)
44. A. Coy, MSc Thesis, University of Calgary. Canada, 2013
45. L. Carbognani, C. Hovsepian, C.E. Scott, P. Pereira-Almao, G. Moore, S.A. Mehta, M.G. Ursenbach, Energy Fuel **30**, 5459 (2016)
46. L. Carbognani, C. Hovsepian, C.E. Scott, P. Pereira-Almao, G. Moore, S.A. Mehta, M.G. Ursenbach, Prep. Pap.-Am.Chem.Soc., Div. Energy Fuels **61**, 680 (2016)
47. C.N. Hovsepian, L. Carbognani, P. Pereira-Almao, Energy Fuel **30**, 3652 (2016)
48. N. Nguyen, Z. Chen, P. Pereira-Almao, C.E. Scott, B. Maini, Ind. Eng. Chem. Res. **56**, 14214 (2017)
49. H. Loria, G. Trujillo-Ferrer, C. Sosa-Stull, P. Pereira-Almao, Energy Fuel **25**, 1364 (2011)
50. C.E. Galarraga, C. Scott, H. Loria, P. Pereira-Almao, Ind. Eng. Chem. Res. **51**, 140 (2012)
51. S. Sánchez, M. Rodríguez, J. Ancheyta, Ind. Eng. Chem. Res. **44**, 9409 (2005)
52. F. Da Silva, MSc Thesis, University of Calgary. Canada, 2014
53. V. Rodriguez-DeVecchis, L. Carbognani, C.E. Scott, P. Pereira-Almao, Fuel **208**, 566 (2017)

Chapter 7
Porosity and Fractality of MoS_2 and MoS_2/Co-catalytic Spheres

Félix Galindo-Hernández, Ilke Arslan, José Manuel Domínguez, and Manuel Ramos

7.1 Introduction

Layered transition metal sulfide, particularly molybdenum disulfide (MoS_2), is one of best nanoscaled materials for catalytic purposes [1, 2]. It has been extensively used for the production of low-contaminant liquid fuels from crude oil [3, 4], which is vital to supply energy demands worldwide. MoS_2 has a natural semiconducting electronic structure, as measured by experimental and theoretical techniques with a band gap in the range of 1.2–1.8 eV [5], and can be tuned into metallic when combined with either nickel or cobalt in small amounts, creating what is known as Co/MoS_2 or Ni/MoS_2 metallic phases [6–9]. Nowadays, the location of promoter atoms usually *cobalt* or *nickel* is well known and several models to explain that have been proposed in the literature throughout years; Farragher and Cossee [10] proposed a "*pseudo-intercalation*" model having Co atoms at octahedral sites of MoS_2 layers; later Delmon et al. proposed a "*synergic model*" having the mix crystallographic phase of MoS_2 and Co_9S_8 [11]; one of the most used models is the one proposed by Topsøe et al. who proposed metallic states at the edge of

---

F. Galindo-Hernández · J. M. Domínguez (✉)
Instituto Mexicano del Petróleo (IMP), 152 Eje Central Lázaro Cárdenas Norte,
Gustavo A. Madero, Ciudad de México, Estado de México, C.P. 07730, Mexico
e-mail: jmdoming@imp.mx

I. Arslan
Argonne National Laboratory, Center for Nanoscale Materials, Lemont, IL, USA

M. Ramos
Departamento de Física y Matemáticas, UACJ-Instituto de Ingeniería y Tecnología,
450 Avenida de Charro, Building G-301A, Ciudad Juárez, Chihuahua 32310, Mexico
e-mail: manuel.ramos@uacj.mx

J. M. Domínguez-Esquivel, M. Ramos (eds.), *Advanced Catalytic Materials: Current Status and Future Progress*, https://doi.org/10.1007/978-3-030-25993-8_7

MoS_2 layer, having a chemical bonding among S-Co-S-Mo by permuting cobalt atoms at molybdenum sites in typical 1H-MoS_2 layer, based on characterization using Mössbauer spectroscopy [12]. A "*rim-edge*" model was proposed by Chianelli et al. determining catalytic activity and specific edge or rim sites within stacking structure of MoS_2 and explaining both activity and selectivity [13]. Lately, Lauritsen et al. described a density functional theory (DFT) and scanning tunneling microscopy (STM) to describe metallic edge sites due to insertion of cobalt at the edges as proposed by Topsøe et al. [14, 15]. However, MoS_2 material seems to be versatile when it comes to the final morphological structure, meaning that it is possible to have triangular clusters, nanotubes, fullerenes, and spheres, as described in detail by Remškar et al. [16], Camacho-Bragado et al. [17], Blanco et al. [18], and Ramos et al. [19]. Furthermore, it has been possible to use electron microscopy techniques to determine crystallographic aspects of MoS_2 with and without promoters, as described by Ramos et al. who were able to determine interaction between mixture of (111)-Co_9S_8 and (101)-MoS_2 and confirmed with DFT models to explain the electrodonation from cobalt into molybdenum atoms due to formation of *thiocubane* clusters at the edge of interface [20], promoting the electronic band structure of MoS_2 from semiconductor into metallic [20]. TEM offers also a dynamic way to proceed with in situ operando experiments, as demonstrated by Helveg et al. who were able to synthesize MoS_2 from molybdenum oxide under hydrogen sulfide-rich atmosphere [21]; Casillas et al. were able to determine the mechanical resilient nature of 2H-MoS_2 laminates due to induced external pressure by atomic force microscope tip on TEM holder [22] and Ramos et al. were able to determine carburization effects above 350 °C due to carbon grid content using heating stage during TEM observations [23]. Scanning transmission electron microscopy and 3D electron tomography had been used also to perform extensive characterization on catalytic materials, as described by Midgley and Dunin-Borkowski [24]; Ziese et al. implemented STEM-electron tomography techniques to determine the gold nanoparticle distribution over a SBA-15-type matrix [25] and Arslan et al. used electron tomography technique to locate catalytic gold nanoparticle alumina oxide matrix support [26]. Here we present a hydrothermal synthesis to achieve MoS_2 and cobalt-promoted MoS_2 catalytic particles and a comprehensive study by surface fractal dimensions at the molecular level to determine any textural and structural aspects due to Co insertion at MoS_2 crystallographic lattice. Surface fractal dimensionality is related to the roughness, steps, and kinks at the molecular scale and it plays a key role for heterogeneous catalysts, as pointed out by several authors [27, 28]. We propose this parameter as an important one for gauging catalytic behavior of Co-promoted MoS_2 catalysts and as a complement of "electronic effects" induced by insertion of the Co promoter, because it modifies both textural and structural properties of MoS_2; this is the first time that fractal dimensionality is shown as a result of Co-promoter insertion in spherical particles of MoS_2 and the profound effects on both texture and structure as verified in the case of MoS_2/Co system.

7.2 Experimental Methods and Results

7.2.1 *Hydrothermal Synthesis of Co/MoS_2 and MoS_2*

The experimental procedure is following previous investigations found in the literature; the spherical shape was prepared using 3 mmol of sodium molybdate ($Na_2MoO_4 \cdot 2H_2O$) and 9 mmol of thioacetamide (CH_3CSNH_2), which were dissolved in 30 mL of deionized water, and then 0.5 g of sodium silicate ($Na_2SiO_3 \cdot 9H_2O$) was added into the solution under violent stirring. The pH value of the solution was adjusted to 6.0 by dropping 12 M hydrochloric acid (HCl) solution during violent stirring. 0.50 g of cobalt chloride ($CoCl_2$) was added to the solution before the hydrothermal reaction. Once cobalt is added the new solution becomes magenta color-like. The resulting magenta solution was transferred to a 50 mL Teflon-lined and placed inside the hydrothermal reactor rising temperature value to 220 °C (*inside the chamber at 1200 psi*) for 24 h and allowed to cool down naturally. The black resulting precipitates were collected and washed first with 1 M of sodium hydroxide (NaOH) solution for several times to remove possible residues specially from silicic acid and later with deionized water and absolute ethanol; finally both products were dried separately at 60 °C for 6 h in open-flow furnace. It was observed that formation of sulfide phase depends on synthesis temperature as confirmed by scanning electron microscopy techniques.

The reaction profile occurs as follows, as described by Ramos et al. [19]:

$$\begin{aligned}(1)\ & 6CoCl_2 6H_2O + 12Na_2MoO_4 + Na_2SiO_3 + 26HCl \rightarrow H_4SiCo_6Mo_{12}O_{40} \\ & \qquad + 26NaCl + 47H_2O + 6Cl_2\end{aligned}$$

$$(2)\ CH_3CSNH_2 + 2H_2O \rightarrow CH_3COOH + NH_3 + H_2S$$

$$(3)\ H_4SiCo_6Mo_{12}O_{40} + 27H_2S \rightarrow 12Co_{0.5}MoS_2 + H_2SiO_3 + 3H_2SO_4 + 25H_2O$$

7.2.2 *Morphology Aspects by Scanning Electron Microscopy*

Scanning electron microscopy is a reliable straight-way route to validate morphological and structural aspects on materials [28]. Here, samples were studied on a field-emission SEM model FEI® nova 200 at 20 kV; each individual product was placed directly onto a carbon double-sided tape. The results indicate a spherical shape morphology for MoS_2 with homogeneous distribution as presented in Fig. 7.1a. The exact mechanism of spherical shape formation is unknown until now, but possible causes could be the particle surface's energy and hydrothermal pressure conditions as described by Li et al. [27]. Figure 7.1b presents a more detailed aspect of the particles for pure MoS_2. The cobalt added can be dispersed on the spherical surface (Fig. 7.1c).

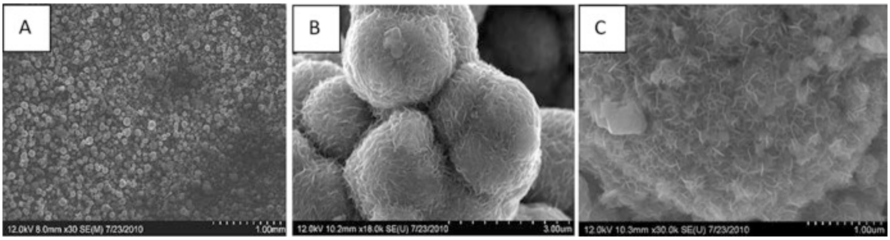

Fig. 7.1 (**a**) Scanning electron micrograph of spherical shape MoS_2 with homogeneous distribution particles. (**b**) A more detailed aspect of particle surface; it is possible to observe the edges of MoS_2 layers. (**c**) Cobalt addition on MoS_2; it is possible to observe surface dispersion [images adapted with rights and permissions from Ramos et al. Sci. Report., 7: 12322]

7.2.3 Structural Aspects by High-Resolution TEM

The structural aspects of MoS_2 spherical shape particles were investigated using a high-resolution transmission electron microscope (HRTEM) with a 2200-JEOL instrument at operational voltage of 200 kV, which was fitted with a Cs corrector (CEOS GmbH) and FEG-STEM/TEM unit; a HAADF probe size was set to 0.095 nm with a current of 23.2 pA for bright-field imaging; the condenser lens aperture size was set to 40 µm. A camera length (CL) of 8 cm/6 cm and collection angle of 68–280 mrad/90–270 mrad were set for STEM images, to eliminate contributions from un-scattered beams. The specimens were prepared for electron microscopy by isopropanol ultrasonic dispersion and one drop was dried at holey carbon grid. All images were reconstructed using Gatan Digital Micrograph® computational package. Figure 7.2a, b shows a TEM image of a MoS_2 spherical shape particle cluster and Fig. 7.2c a more detailed image at 40,000× of magnification where it is possible to observe typical needlelike structures corresponding to layers, and interlayers of S-Mo-S (see Fig. 7.2d, e), and Fig. 7.2f indicates that cobalt addition can disperse the layers creating a more pronounced needlelike structure.

7.2.4 Electron Tomography by TEM

The images taken by using ultrahigh-resolution TEM in FEI Tecnai F20 instrument operating at 200 kV in STEM mode. Images were acquired using Digital Micrograph® software for every 2°, from −70 to +70 with a total of 71 images for each tilt series. All images were aligned with respect to each other using the center of mass of the particle, as described in detail by Sanders et al. [28], which were used to achieve the 3D reconstruction using total variation (TV) regularization and visualized using TOMVIZ© software [29, 30]. Figure 7.3a shows a series of three-dimensional aspects for both pure MoS_2 and Fig. 7.3b for Co/MoS_2 particles. The computational software Novawin© 11.03 was used for all the numerical simulations for porous size distribution and textural properties.

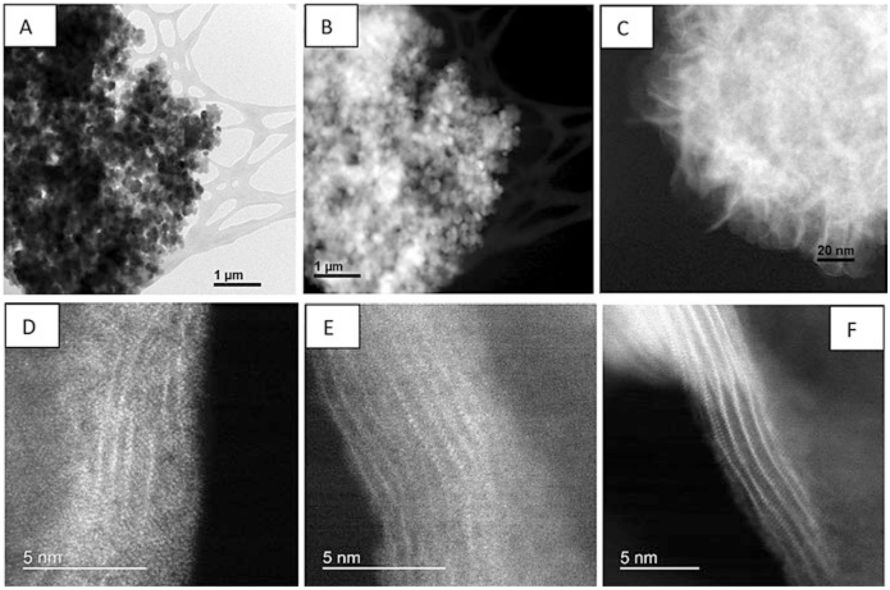

Fig. 7.2 (**a**, **b**) TEM images in dark- and bright-field modes, respectively, for spherical shape MoS_2 particles. (**c**) Image of one sphere at 40,000× of magnification is possible to observe needlelike layers. (**d**, **e**) Corresponds to columns of atoms at the interlayers of S-Mo-S for pure MoS_2 and (**f**) to needlelike column of atoms with cobalt addition [images adapted with rights and permissions from Ramos et al. Sci. Report., 7: 12322]

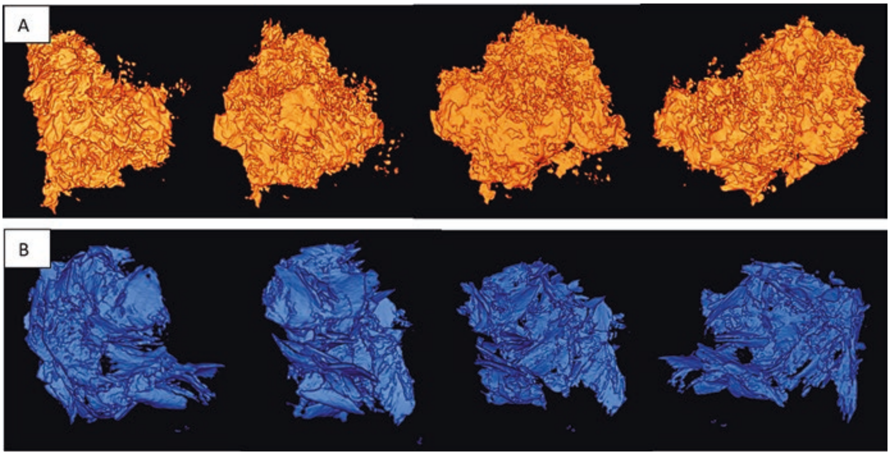

Fig. 7.3 (**a**) A series of three-dimensional electron tomography images of MoS_2 spherical particle; it is possible to observe fractal dimensions and porosity. (**b**) A series of three-dimensional electron tomography images of Co/MoS_2; it is possible to observe surface dispersion and more needlelike array of laminates (orange and blue colors are just added to differentiate one from other) [images adapted with rights and permissions from Ramos et al. Sci. Report., 7: 12322]

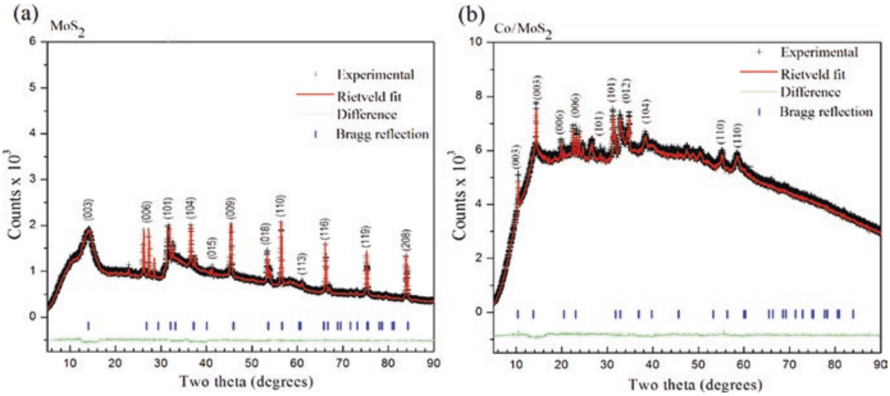

Fig. 7.4 X-ray diffraction patterns and Rietveld's refinement for (**a**) MoS_2 and (**b**) Co/MoS_2. It is possible to observe a sharp peak at (003)-basal plane when cobalt atoms are present as compared to pure MoS_2 on the sample, which could be attributed to surface dispersion [images adapted with rights and permissions from Ramos et al. Sci. Report., 7: 12322]

7.2.5 *Powder XRD and Rietveld's Refinement*

All diffraction patterns were obtained with a Bruker Advance D-8 diffractometer fitted with Bragg-Brentano geometry (Fig. 7.4), using CuKα radiation and a Lynxeye-type detector. The intensities were obtained in the 2-theta ranges between 10 and 100° with a step of 0.019447° and a measuring time of 10 s per point. The crystalline structures were refined by Rietveld's method using TOPAS-Academic software [31]. All theoretical crystal density was calculated by the following equation: ρ_{crystal} = (Z)(MM) (Avogadro's number)$^{-1}$/cell volume, where Z is the number of molecules per cell and MM is the molecular weight. Results are presented in Fig. 7.4 corresponding to MoS_2 and Co/MoS_2.

7.2.6 *Radial Distribution and Electron Distribution Functions*

The distance (r) between atoms in MoS_2 and MoS_2(Co) crystallites was obtained by radial distribution function G(r) up to 6.5 Å, in a Siemens D500 diffractometer fitted with a molybdenum anode X-ray tube. The intensities were measured in a step-by-step mode of 0.01°, from 2 to 110° (2θ), using the Radiale program [32]. Results are presented in Fig. 7.5.

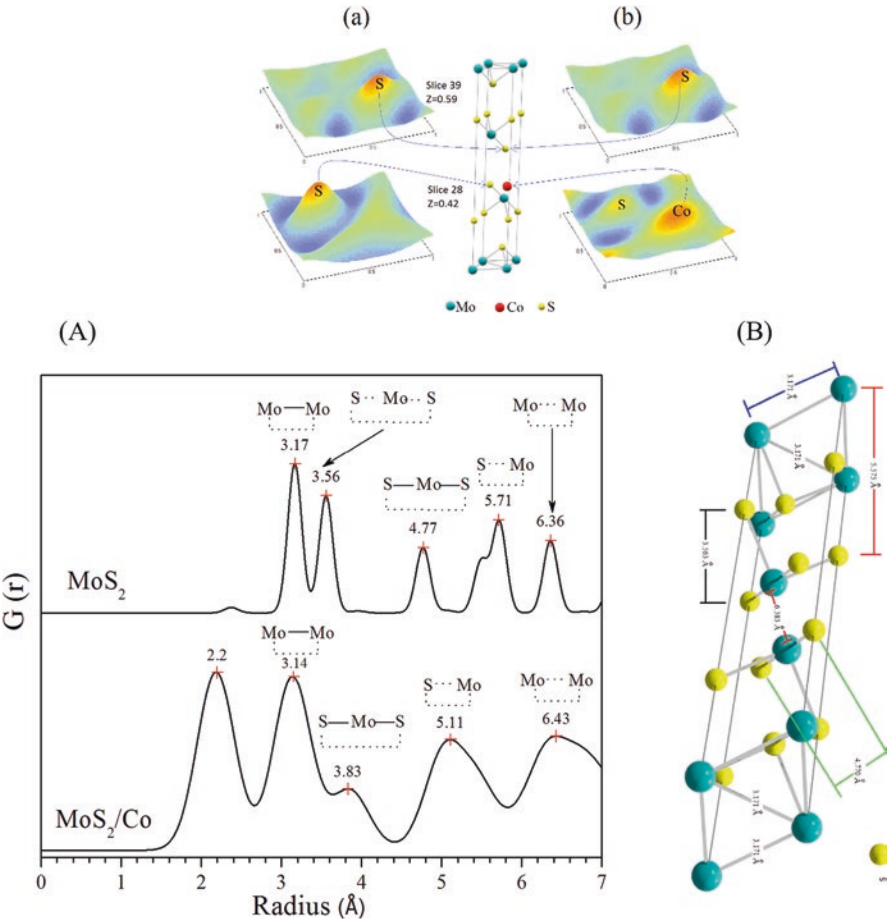

Fig. 7.5 (**A**) Radial distribution plots for Co/MoS_2. It is possible to observe a shifting of peaks at Mo-Mo and S-Mo-S peaks, as well as the appearance of new peak at 2.2 Å when cobalt atoms are present in the MoS_2 lattice. (**B**) MoS_2 crystallographic lattice ($a = b = 3.1710$ and $c = 18.3445$ Å) (SG: R3m-H). (**a**) and (**b**) correspond to electron density maps to indicate cobalt atoms at the MoS_2 crystallographic lattice, as calculated from X-ray diffraction and DFT simulations [images adapted with rights and permissions from Ramos et al. Sci. Report., 7: 12322]

7.2.7 *Adsorption/Desorption Isotherms*

All the measurements of N_2 sorption isotherms were obtained at 76 K using a Quantachrome Autosorb 3B instrument under N_2 and He gases (UHP grade) conditions. Prior to isotherm runs, all the samples were outgassed for 12 h at 473 K. The specific surface areas were calculated from desorption isotherms using BET equation, while the pore structure parameters were determined by nonlocal density functional theory approximation (Fig. 7.6).

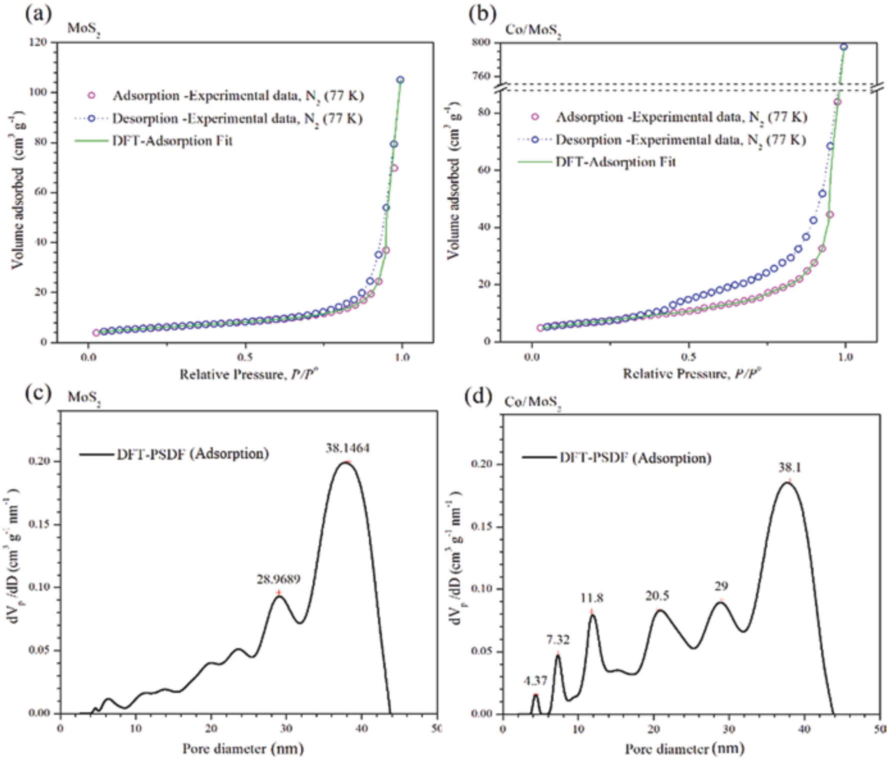

Fig. 7.6 (**a**, **b**) Nitrogen adsorption/desorption isotherms run at 77 K. (**c**, **d**) Numerical simulation of pore diameter distribution for MoS_2 samples and Co/MoS_2 samples

Using density functional theory is possible to subtract not only a microscopic model of adsorption but also a more realistic description of the thermodynamic properties related to pore fluid, which bridge the gap between molecular and macroscopic level. Using this method, it is possible to determine local fluid structure near curved solid walls and it gives us the theoretical adsorption–desorption isotherms in porous structure.

The local fluid density ρ of adsorbate confined in a pore at a given chemical potential μ and temperature T is determined by minimization of the grand thermodynamic potential Ω:

$$\Omega = \int \rho\left[f\left(r, \rho, \bar{\rho}\right) + u^{\mathrm{ext}}\left(r\right) - \mu\right] dr$$

where $\rho, \bar{\rho}$ are the local and smoothed fluid densities; $f\left(r, \rho, \bar{\rho}\right)$ is the molar Helmholtz free energy; $u^{\mathrm{ext}}(r)$ is the external potential exerted by the solid; and μ is the chemical potential. The molar Helmholtz free energy is split into the ideal term $kT[\mathrm{Ln}(\Lambda^3\rho) - 1]$, excess term $f_{\mathrm{exc}}(\bar{\rho})$ due to repulsion, and intermolecular interaction potential $u(r)$ due to attraction:

$$f(r, \rho, \bar{\rho}) = kT\left[\mathrm{Ln}\left(\Lambda^3\rho\right) - 1\right] + f_{\mathrm{exc}}(\bar{\rho}) + u(r)$$

Here k is the Boltzmann constant and Λ is the de Broglie wavelength. The smoothed density $\bar{\rho}$ is a weighted average:

$$\bar{\rho}(r) = \int \rho(r')\,\omega\left(|r - r'|, \bar{\rho}(r)\right) dr'$$

where $\omega\left(|r - r'|, \bar{\rho}(r)\right)$ is the weighting function.

Neimark-Kiselev fractal analysis: The fractal dimension is a measure to classify and quantitatively compare complex chaotic patterns such as surfaces of the porous materials. After the DFT treatment, Neimark-Kiselev method [33] can be used to obtain the fractal dimension values. Combining thermodynamic and fractal arguments:

$$S_{\mathrm{lg}} = K\left(r_k\right)^{2-D}$$

where D is the surface fractal dimension, K is a constant, and r_k is the mean radius of curvature of the adsorbate-vapor interface, given by the Kelvin equation:

$$r_k = \frac{2\gamma V_m^{\mathrm{DFT}}}{RT \ln\left(\frac{P^0}{P}\right)}$$

And S_{lg} is the adsorbate-vapor interface area, given by the Kiselev equation:

$$S_{\mathrm{lg}} = \frac{RT}{\gamma} \int_{n}^{n_{\max}} \ln\left(\frac{P^0}{P}\right) dn$$

with R being the universal gas constant, T the adsorption temperature, γ the adsorbate surface tension, V_m the adsorbate molar volume, and n and $n_{\max}$ the amounts of gas adsorbed at given P/P^0.

In our case study for low-dimension surface topology of Co/MoS_2 spheres, the fractal dimension values indicate topographic changes onto Co/MoS_2 surface's which may be related to inclusion of Co atoms at laminar sites; this approach can be used as the fundamental aspect to understand catalytic performance and selectivity, as described by references as provided in [34–38]. For a comparison results are displayed in Tables 7.5–7.9.

7.3 Results and Discussion

The crystallographic features of hydrothermally as-synthesized cobalt-promoted MoS_2 catalysts were determined by X-ray diffraction; this comprised the use of Rietveld's refinement method to verify the MoS_2 rhombohedral (R3m) symmetry, in agreement with the recent work from Wang et al. [35], from which a comparative analysis was performed as shown by Fig. 7.3, where one observes that a crystallographic variation occurs following cobalt addition during synthesis, which can be explained in terms of Frenkel's point defects [32] caused by interstitial occluded cobalt atoms into the laminar MoS_2 structure, as described by Lauritsen et al. [15]. This explains the expansion of about 12.9% (from 0.7500 to 0.8465) of *c*-axis in the primitive lattice, as demonstrated by radial distribution function results, which indicates interatomic distance variations of 11.7% for S····Mo and 24.5% for S—Mo—S, with respect to S···Mo···S distance of 3.56 Å; these are consistent with displacements of Mo atoms to interstitial sites as confirmed by electron density maps in Fig. 7.5a, b and Fig. 7.5A, B with face *ab* normalized to 1 and with $c = 0.42$ (slice 28) and $c = 0.59$ (slice 39); some specific data are reported in Tables 7.1–7.4. In fact, an increase of 10.4% (from 0.16667 to 0.18400) in occupancy position of sulfur $O_{S(2)}$ at the MoS_2/Co lattice implies a stoichiometry variation for MoS_2 to $MoS_{(2+y)}$, thus leading to a molecular increase of crystal

Table 7.1 Lattice parameters obtained by Rietveld's refinement from powder X-ray diffraction for pure spherical shape MoS_2 sample

Lattice: Rhombohedral						
MoS_2 R 3 m H (160)			Atomic fractional coordinates			
Atom	Type	Site	*x*	*y*	*z*	Occupancy
Mo (1)	Mo^{4+}	3a	0.0000	0.0000	1.0000	0.16667
S (1)	S^{2-}	3a	0.0000	0.0000	0.2500	0.16667
S (2)	S^{2-}	3a	0.0000	0.0000	0.7500	0.16667
Lattice parameters			Angles			
a	*b*	*c*	*α*	*β*	*γ*	Density (g cm^{-3})
3.1710 Å	3.1710 Å	18.3445 Å	90°	90°	120°	4.992

Table 7.2 Lattice parameters obtained by Rietveld's refinement from powder X-ray diffraction for cobalt-promoted MoS_2 sample

			Atomic fractional coordinates of S (2)			
Material	Molybdenite crystallite size (nm)	Density (g cm^{-3})	*x*	*y*	*z*	$O_{S(2)}$
MoS_2	2 (0.4)	4.989	0.0000	0.0000	0.7500	0.16667
MoS_2/Co	8 (0.8)	5.096	0.0000	0.0000	0.8465	0.18400

The number in parenthesis corresponds to the standard deviation

$O_{S(2)}$: *S* (2) occupancy (see Table 7.1)

Table 7.3 Statistical parameters after Rietveld's refinement for both cases

Material	R_p	R_{wp}	χ^2	R_{exp}
MoS_2	2.95	4.67	2.52	2.94
MoS_2/Co	1.30	1.74	2.07	1.21

Table 7.4 Radial distribution function peak values of MoS_2 and Co/MoS_2 samples

	Interatomic distances r (Å)				
Material	Mo—Mo	S····Mo····S	S—Mo—S	S····Mo	Mo····Mo
MoS_2[a]	3.171	3.563	4.770	5.575	6.383
MoS_2[b]	3.170	3.560	4.720	5.710	6.360
MoS_2/Co[b]	3.140			5.110	6.430

— Bond, --- Only distance

[a] Theoretical interatomic distances

[b] Obtained by XRD

density of about 2.14% (from 4.989 to 5.096 g/cm^3) as reported in Table 7.2; also, the mean crystallite size of MoS_2 varies from 2 to 8 nm when cobalt is inserted, as discussed before [19] and indicated in Table 7.2. The nitrogen adsorption profile of both MoS_2 and MoS_2/Co is consistent with type III isotherms, as shown in Fig. 6a, b with a pore size distribution with maxima at 29 and 38 nm for MoS_2 while these figures vary from 4 to 38 nm for MoS_2/Co as presented in Fig. 7.5c, d, thus indicating weak interactions between adsorbate and absorbent; also, a H3-type hysteresis loop (IUPAC standards) is observed in both cases, at the relative pressure ($P/P°$) interval between 0.4 and 0.45, thus leading to a model akin with slit-shaped pores, which was verified by electron tomography, as presented in Fig. 7.3a, b, thus indicating a higher N_2 uptake after comparing MoS_2 and MoS_2/Co (i.e., a variation of more than 727%); the adsorption isotherm at $P/P°$~ 0.8 suggests the formation of condensate at the pore neck for $P/P° > 0.9$; that is, liquid–vapor menisci move towards the cavity of the particles, until filling of pores with condensates occurs. With the purpose of understanding better this phenomena a series of DFT numerical simulations were completed to determine relevant pore structure parameters (i.e., S^{BET}/S^{DFT}, V_p^{DFT}, and Φ^{DFT}). We propose this parameter as an important one for gauging catalytic behavior of Co-promoted MoS_2 catalysts and as a complement of "electronic effects" induced by insertion of the Co promoter, because it modifies both textural and structural properties of MoS_2; this is the first time that fractal dimensionality is shown as a result of Co promoter insertion in spherical particles of MoS_2 and the profound effects on both texture and structure as verified in the case of MoS_2/Co system [32]. Thus, a summary of these results is presented in Table 7.5 where one observes an increase of 29% in S^{BET}/S^{DF}, with a further increase up to 110% for V_p^{DFT} as a result of the overall increase of N_2 uptake upon insertion of cobalt atoms in the MoS_2 lattice. The calculation of fractal dimension from transmission electron micrographs and the use of Neimark-Kiselev equation in $\boldsymbol{D}_{s(\text{adsorption/desorption})}$ led to determination of a decrease of 12%

Table 7.5 Specific surface area, pore volume, and mean pore size for both cases

Material	S^{BET}/S^{DFT} (m^2 g^{-1})	V_P ^{DFT} (mm^3 g^{-1})	Φ^{DFT} (nm)
MoS_2	20/21	10	29/38
MoS_2/Co	26/27	110	4/7/12/21/29/38

Values were obtained from numerical DFT simulations and experimental isotherms

Table 7.6 Fractal dimension parameters as calculated by Neimark-Kiselev from isotherm curves for MoS_2 and Co/MoS_2 samples

	Materials	
Method of analysis	MoS_2	MoS_2/Co
$D_{S\text{ (Adsorption)}}$	2.47 (6.05–40.44)[a]	2.18 (4.95–20.08)[a]
$D_{S\text{ (Desorption)}}$	2.52 (6.05–49.40)[a]	2.25 (6.05–16.44)[a]

Ds scaling interval $\in [2, 3]$
[a] Radius of curvature (nm)

after insertion of cobalt (i.e., details are shown in Table 7.6), thus implying a lower fractal dimension as exhibited in Fig. 7.6c, d for r_k values within the interval of 6.05–40.44 nm for the MoS_2 spherically shaped particles while r_k values fall within the interval of 4.95–20.08 nm for MoS_2/Co system that is spread on the surface, which is observed by STEM microscopy as presented in Fig. 7.2a, b, from which the fractal dimension is obtained using D_P, D_B, D_I, and D_M methods; that is, 1.17 and 1.05 are the fractal dimensions for MoS_2 and MoS_2/Co, while D_B decreases from 1.71 to 1.57 due to the surface topology associated with cobalt addition; D_I indicates dispersion of the surface due to the cobalt presence and finally D_M determines a dense surface on MoS_2/Co as observed a by larger array of laminates revealed by high-resolution STEM (insets of Fig. 7.2a, b). Additionally, a second run of fractal calculations was done using TEM-2D images, from which fractal values show a decreasing trend with the cobalt presence, with values of D_P (25.0%), D_B (5.3%), D_I (17.0%), and D_M (16.0%) as well as when using scanning electron images with values of D_P (34.7%), D_B (28.0%), D_I (23.4%), and D_M (1.9%) in agreement with other low-dimension systems [39, 40].

7.4 Conclusion

The abovementioned results led us to conclude that chemical state and geometric features associated might play an important role; that is, cobalt atom radius is about 20% larger than sulfur atoms while cobalt ions (Co^{2+}) are about 40% the size of sulfur ion S^{2-}; also, the specific hydrothermal synthesis method could contribute too. It was found that cobalt Co tends to occupy MoS_2 edges, as determined by Rietveld's refinement method, and thus the "CoMoS phase" should be formed. Moreover, the use of Neimark-Kiselev set of equations led us to conclude that cobalt insertion into the MoS_2 crystalline arrays induces a pore volume increase from 10 to

Table 7.7 Fractal dimension parameters and porosity as calculated by different methods from STEM images

	Method of analysis				
Material	D_p	D_B	D_I	D_M	STEM-porosity (%)
MoS_2	1.17 ± 0.01	1.71 ± 0.02	1.83 ± 0.01	1.86 ± 0.01	14.6
MoS_2/Co	1.05 ± 0.01	1.57 ± 0.01	1.64 ± 0.01	2.21 ± 0.01	23.6

D_P, D_B, D_I, and D_M are measured from STEM images; D_p scaling interval $\in [1, 2]$; D_B scaling interval $\in [1, 2]$; D_I scaling interval $\in [1, 2]$; $D_M \geq 1$

Table 7.8 Fractal dimension parameters used as calculated by different methods from high-resolution TEM images for MoS_2 and Co/MoS_2

	TEM image scale bar at 100 nm	
Method of analysis	MoS_2	MoS_2/Co
D_p	1.67 ± 0.25	1.25 ± 0.24
D_B	1.69 ± 0.08	1.60 ± 0.06
D_I	1.68 ± 0.37	1.40 ± 0.02
D_M	2.00 ± 0.09	2.32 ± 0.17

D_P, D_B, D_I, and D_M are measured from TEM images; D_p scaling interval $\in [1, 2]$; D_B scaling interval $\in [1, 2]$; D_I scaling interval $\in [1, 2]$; $D_M \geq 1$

Table 7.9 Fractal dimension parameters calculated by different methods from SEM images for both MoS_2- and cobalt-promoted MoS_2 samples

	SEM images at 1.0 μm	
Method of analysis	MoS_2	MoS_2/Co
D_p	1.64 ± 0.03	1.07 ± 0.02
D_B	1.90 ± 0.01	1.37 ± 0.01
D_I	1.92 ± 0.01	1.47 ± 0.01
D_M	1.98 ± 0.01	2.02 ± 0.02

D_P, D_B, D_I, and D_M are measured from TEM images; D_p scaling interval $\in [1, 2]$; D_B scaling interval $\in [1, 2]$; D_I scaling interval $\in [1, 2]$; $D_M \geq$ 1s

110 cm^3/g which provokes an increase of the diameter of cavities as well as formation of throats with diameters smaller than 29 nm and r_k <14.4 nm, which explains the higher N_2 consumption during the isotherm runs. Additionally, cobalt insertion promotes formation of large needlelike laminates with a stacking average of ~20 2D layers, as observed by high-resolution STEM, with D_s values falling in a region where radii of curvature are smaller (14.4 nm), which means that smoother surfaces are formed inside the cavities. Also, a decreasing trend of D_P, D_B, D_I, and D_M was found with insertion of cobalt in the MoS_2 laminates (Tables 7.6–7.9), which is interpreted as enhancing the crystallite edge smoothing and surface density. This fundamental approach allowed to understand better the behavior of “CoMoS” phase-type catalysts. Further work using a similar approach for “spent” MoS_2/Co and MoS_2 catalytic phases is underway for studying the role of carbon in the catalytic properties of those phases.

Acknowledgements This project was funded by Mexican Science Council [CONACyT-Mexico] under solicitation grant # 177077 for SENER-hydrocarbons (IMP project Y.61006). Instituto Mexicano del Petróleo is acknowledged for usage of laboratory equipment and facilities. I.A. was supported by the Laboratory Directed Research and Development Program at the Pacific Northwest National Laboratory.

Author Contribution Statement: M. Ramos was in charge of chemical synthesis and scanning electron imaging. F. Galindo-Hernández completed all computer-assisted numerical simulations. I. Arslan and T. Sanders performed electron tomography measurements and computer-assisted reconstruction. J. M. Domínguez is the principal investigator on this particular Mexican Secretary of Energy project in charge of design and supervision of all experiments. This manuscript was mainly typed by M. Ramos, F. Galindo, I. Arlsan, and J. M. Domínguez.

Competing Financial Interests: The author(s) declare no competing financial interests, nor any conflict of interest.

References

1. R.R. Chianelli, G. Berhault, B. Torres, Unsupported transition metal sulfide catalysts: 100 years of science and application. Catal. Today **147**, 275–286 (2009)
2. A. Villareal et al., Importance of the sulfidation step in the preparation of highly active NiMo/SiO_2/Al_2O_3 hydrodesulfurization catalysts. Catal. Today **250**, 60–65 (2015)
3. A. Olivas, G. Alonso, S. Fuentes, The catalytic activity of Ni/W bimetallic sulfide nanostructured catalysts in the hydrodesulfurization of dibenzothiophene. Top. Catal. **39**, 175–179 (2006)
4. M.H. Siadati, G. Alonso, B. Torres, & Chianelli R. open flow hot isostatic pressing assisted synthesis of unsupported MoS_2 catalysts. Appl. Catal. A **305**, 160–168 (2006)
5. L. Wei, C. Jun-fang, H. Qinyu, W. Teng, Electronic and elastic properties of MoS_2. Physica B **405**, 2498–2502 (2010)
6. J. Ramírez, G. Macías, L. Cedeño, A. Gutiérrez-Alejandre, R. Cuevas, P. Castillo, The role of titania in supported Mo, CoMo, NiMo, and NiW hydrodesulfurization catalysts: analysis of past and new evidences. Catal. Today **98**(1–2), 19–30 (2004)
7. A. Stanislaus, A. Marafi, M.S. Rana, Recent advances in the science and technology of ultra low sulfur diesel (ULSD) production. Catal. Today **153**, 1–68 (2010)
8. J.C. Morales-Ortuño, R.A. Ortega-Domínguez, O. Hernández-Hipólito, X. Bokhimi, T.E. Klimova, HDS performance of NiMo catalysts supported on nanostructured materials containing titania. Catal. Today **271**, 127–139 (2016)
9. B.C. Gates et al., Catalysts tor emerging energy applications. MRS Bull. **33**, 429–435 (2008)
10. A.L. Farragher, P. Cossee, Proceedings of the 5th International Congress on Catalysis, North-Holland, Amsterdam, 1301 (1973)
11. G. Hagenbach, P. Courty, B. Delmon, Physicochemical investigations and catalytic activity measurements on crystallized molydbenum sulfide-cobalt sulfide mixed catalysts. J. Catal. **31**, 264–273 (1973)
12. J.V. Lauritsen, M. Nyberg, R.T. Vang, M.V. Bollinger, B.S. Clausen, H. Topsøe, K.W. Jacobsen, E. Lægsgaard, J.K. Nørskov, F. Besenbacher, Chemistry of one-dimensional metallic edge states in MoS_2 nanoclusters. Nanotechnology **14**, 385–389 (2003)
13. M.M. Daage, R.R. Chianelli, Structure-function relations in molybdenum sulfide catalysts: the “Rim-Edge” model. J. Catal. **149**, 414–427 (1994)

14. B. Hammer, L.B. Hansen, K. Nørskov, Improved adsorption energetics within density-functional theory using revised Perdew-Burke-Ernzerhof functionals. Phys. Rev. B **59**, 7413 (1999)
15. J.V. Lauritsen et al., Location and coordination of promoter atoms in Co- and Ni-promoted MoS_2-based hydrotreating catalysts. J. Catal. **249**, 220–233 (2007)
16. M. Remškar, M. Viršek, A. Mrzel, The MoS_2 nanotube hybrids. Appl. Phys. Lett. **95**, 133122 (2009)
17. G.A. Camacho-Bragado, J.L. Elechiguerra, M. Yacaman, Characterization of low dimensional molybdenum sulfide nanostructures. J. Mat. Char. **59**, 204–212 (2008)
18. E. Blanco, P. Afanasiev, G. Berhault, D. Uzio, S. Loridant, Resonance Raman spectroscopy as a probe of the crystallite size of MoS_2 nanoparticles. Comp. Rendus Chimie **19**, 1310–1314 (2016)
19. M.A. Ramos et al., Spherical MoS_2 micro particles and their surface dispersion due to addition of cobalt promoters. Rev. Mex. Fís. **57**, 220–223 (2011)
20. M.A. Ramos, G. Berhault, D.A. Ferrer, B. Torres, R.R. Chianelli, HRTEM and molecular modeling of the MoS_2–Co_9S_8 interface: understanding the promotion effect in bulk HDS catalysts. Cat. Sci. Technol. **2**, 164–178 (2012)
21. L.P. Hansen, E. Johnson, M. Brorson, S. Helveg, Growth mechanism for single- and multi-layer MoS_2 nanocrystals. J. Phys. Chem. C **118**, 22768–22773 (2014)
22. G. Casillas et al., Elasticity of MoS_2 sheets by mechanical deformation observed by in situ electron microscopy. J. Phys. Chem. C **119**, 710–715 (2015)
23. M. Ramos et al., In-situ HRTEM study of the reactive carbide phase of Co/MoS_2 catalyst. Ultramicroscopy **127**, 64–69 (2013)
24. P.A. Midgley, R.E. Dunin-Borkowski, Electron tomography and holography in materials science. Nat. Mater. **8**, 271–280 (2009)
25. U. Ziese, K.P. de Jong, A.J. Koster, Electron tomography: A tool for 3D structural probing of heterogeneous catalysts at the nanometer scale. Appl. Catal. A Gen. **260**, 71–74 (2004)
26. I. Arslan, E.A. Marquis, M. Homer, M.A. Hekmaty, N.C. Bartelt, Towards better 3-D reconstructions by combining electron tomography and atom-probe tomography. Ultramicroscopy **108**, 1579–1585 (2008)
27. L. Ma, W.-X. Chen, L.-M. Xu, X.-P. Zhou, B. Jin, One-pot hydrothermal synthesis of MoS_2 nanosheets/C hybrid microspheres. Ceram. Int. **38**, 229–234 (2012)
28. T. Sanders, M. Prange, C. Akatay, P. Binev, Physically motivated global alignment method for electron tomography. Adv. Struct. Chem. Imaging **1**(11–11), 4 (2015)
29. T. Sanders, Discrete iterative partial segmentation technique (DIPS) for tomographic reconstruction. IEEE Trans. Comp. Imaging **2**, 71–82 (2016)
30. T. Sanders, A. Gelb, R.B. Platte, I. Arslan, K. Landskron, Recovering fine details from under-resolved electron tomography data using higher order total variation $\ell 1$ regularization. Ultramicroscopy **174**, 97–105 (2017)
31. A. Coelho, TOPAS-academic V4.1, Coelho Software, Brisbane, Australia (2007)
32. M. Magini et al., Programme en FORTRAN IV pour l'analyse des données expérimentales relatives à la diffusion des rayons X par des substances liquides, amorphes et microcristallisées. J. Appl. Crystallogr. **5**, 14 (1972)
33. A.V. Neimark, in *Multifunctional Mesoporous Inorganic Solids*, ed. by C. A. C. Sequeria, M. J. Hudson, (Kluwer, Dordrecht, 1993)
34. G. Ertl, Oscillatory catalytic reactions at single-crystal surfaces. Adv. Catal. **37**, 213–277 (1990)
35. S. Wang et al., A new molybdenum nitride catalyst with rhombohedral MoS_2 structure for hydrogenation applications. J. Am. Chem. Soc. **137**, 4815–4822 (2015)
36. F. Galindo-Hernández, J.M. Domínguez, B. Portales, Structural and textural properties of Fe_2O_3/γ-Al_2O_3 catalysts and their importance in the catalytic reforming of CH_4 with H_2S for hydrogen production. J. Power Sources **287**, 13–24 (2015)

37. J. Samuel, M. Ottolenghi, D. Avnir, Diffusion limited reactions at solid-liquid interfaces: effects of surface geometry. J. Phys. Chem. **95**, 1890–1895 (1991)
38. D. Avnir et al., Fractal analysis of size effects and surface morphology effects in catalysis and electrocatalysis. Chaos **1**, 397–410 (1991)
39. A. Seri-Levy, D. Avnir, Effects of heterogeneous surface geometry on adsorption. Langmuir **9**, 3067–3076 (1993)
40. A.V. Neimark, Calculating surface fractal dimensions of adsorbents. Ads. Sci. Tech. **7**, 210–219 (1991)

Chapter 8
Catalytic Ni/CeO_2 Nanorods and Ag/CeO_2 Nanotubes for Hydrogen Production by Methanol Reforming

Raúl Pérez-Hernández

8.1 Introduction

Low-dimension materials with morphological shape like nanorod, nanotube, and nanowire possess extraordinary properties and high potential for diverse applications in energy production, with important roles as catalytic materials, due to higher surface reactivity ideal in electrochemistry [1–5]. Nowadays, one scientific topic of interest is hydrogen production by catalytic conversion of methanol, as source of energy in fuel cells achieving reduction of emission and pollutants due to fossil fuel combustion [6]. Due to its surplus abundance from other catalytic processes, methanol is frequently considered as an attractive chemical component to produce hydrogen in proton-exchange membranes, known as fuel cells. Methanol-reforming reactions like steam reforming (SRM) [1, 7–9], partial oxidation (POM) [10], and autothermal steam reforming (ASRM) [11–15] are the most common catalytic reactions studied to produce hydrogen from methanol; in that regard the nickel-based catalysts are traditionally used reforming reactions due to their low cost and stability; furthermore, it can also be used for conversion of undesirable greenhouse gases like CH_4 and CO_2 [16]. The ceria oxide CeO_2 has been extensively used in high-temperature commercial vehicles' exhaust pipes and has become one of the most important rare oxides to achieve chemical transformation of nitrogen oxides (NO*x*) [17–19] under combustion of fossil fuel conditions in commercial units; the possible catalytic mechanism of CeO_2 is to increase dispersion of active components and its thermal stability and to enhance migration and exchange of oxygen species in the reactions to improve CO, HC oxidation, and NOx reduction [17, 18, 20–25] as well as hydrogen purification [26–29], and the water gas shift reaction [30–33].

R. Pérez-Hernández (✉)
Instituto Nacional de Investigaciones Nucleares, Carr. México-Toluca. S/N. La Marquesa, Ocoyoacac, Edo. de México, 52750, México
e-mail: raul.perez@inin.gob.mx

J. M. Domínguez-Esquivel, M. Ramos (eds.), *Advanced Catalytic Materials: Current Status and Future Progress*, https://doi.org/10.1007/978-3-030-25993-8_8

The chemical combination of species based on nickel and cerium mixtures both in oxidized and reduced states has been evidenced to be favorable for diverse oxidation and reforming catalytic reactions [13, 34–36]. Recently some groups report that one-dimensional (1D) ceria can improve CO oxidation in comparison to bulk phase [37, 38], which opens the possibility to achieve control morphology of ceria oxide nanoscaled catalytic materials; as a result, both activity and selectivity can be estimated and proportional to high surface area in low-dimension morphologies [39, 40]. Furthermore, hydrogen production by autothermal steam reforming (ASRM) catalytic reactions using nickel-loaded ceria oxide (Ni/CeO_2) nanoscaled materials has been studied in this work; the controlled synthesis indicates decorated CeO_2 nanorods supporting nickel nanoclusters as observed by TEM technique, and reported extensively in Phys. Chem. Chem. Phys., 2013, 15, 12702. Moreover, nanostructured silver clusters and nanoparticles have been extensively studied as well in diverse oxidation, reforming, and catalytic conversion of high-pressure gases [41–47]. Hydrogen can be obtained directly from methanol according to the three different processes: steam reforming (SRM) [48–50], partial oxidation (POM) [51–55], and oxidative steam reforming (OSRM) [12, 13, 56–60]. Mo et al. reported that molecular selectivity of hydrogen and carbon monoxide can vary with respect to metallic support, obtaining up to 90% when using modified CeO_2 (Ag/Ce_2OZn system) concluding that CeO_2 and ZnO oxides promote high selectivity of hydrogen from polyoxymethylene (POM) using Ag/Ce_xZn with Ag of ~5 nm nanoparticle size. In the case of bimetallic Ni-Ag catalysts it was reported that the sintering of Ni particles can be partially inhibited by using additional metals such as Ag; thus the deactivation of the catalyst by the sintering of Ni particles can be suppressed [10, 61]. This chapter presents two independent studies for usage of Ag nanowires as templates to generate Ag/CeO_2 nanotube-based catalysts and study the effects of the Ag/Ce composition for steam and oxidative steam reforming of methanol (OSRM) to produce H_2-rich gas and as mentioned before the methanol reforming using nickel-loaded ceria oxide low-dimension catalytic material. The catalytic materials were characterized by several different techniques including nitrogen adsorption–desorption, scanning electron microscopy (SEM), energy-dispersive X-ray spectroscopy (EDX), X-ray diffraction (XRD), scanning/transmission electron microscopy ((S)TEM), and temperature-programmed reduction (TPR).

8.2 Experimental Section

8.2.1 Nickel-Loading Ceria Oxide (Ni/CeO_2)

The preparation of ceria oxide nanostructured materials was completed using hydrothermal method [1, 62]. Two solutions of 32 mL of aqueous with 0.5 M $Ce(NO_3)_3$•$6H_2O$ and 48 mL of 10 M NH_4OH solution were mixed and stirred for 0.5 h; the mixture was placed into 100 mL Teflon-lined and into stainless-steel autoclave, transferred into an oven at 100 °C for 24 h, and then cooled down to room temperature. The result product was separated by centrifugation and washed with deionized water until pH was 7, with a final wash using ethanol solvent. The powder was dried at 100 °C for 24 h and calcined at 500 °C for 5 h. Later the as-synthesized CeO_2 nanorods were impregnated with an aqueous solution of $Ni(NO_3)_2$•$6H_2O$ by an incipient wetness impregnation method at an appropriate concentration to yield 3.4, 16, and 36 wt% of Ni. After impregnation the complete mixture was dried at 100 °C for 1 h and calcined at 500 °C for 2 h to remove any water or solvent residue. The as-prepared catalytic material was labeled as xNi/CeO$_2$, where $x = 3.4$, 16, and 36 wt% of Ni. The composition was analyzed using an energy-dispersive X-ray spectrometer (EDX).

8.2.2 *Silver-Loading Ceria Oxide (Ag/CeO$_2$)*

Silver nanowires were synthesized using polyvinylpyrrolidone (PVP) as the reducing agent in ethylene glycol [10, 63, 64]; then silver nitrate and PVP40 were dissolved in ethylene glycol and added to this mixture under constant stirring. After 1 h, the silver nanowires were precipitated from the reaction mixture with acetone. The Ag nanowire-CeO$_2$ catalyst was prepared by the precipitation method [40]. An aqueous solution of $Ce(NO_3)_3 \cdot 6H_2O$ and the Ag nanowires was mixed under constant stirring; the Ag concentrations were 1 and 5 wt% related to the nominal weight of CeO_2. NH_4OH (Baker) was added dropwise to complete the precipitation. The precipitated mixture was aged for 24 h and the residual liquid was removed by decanting. Then the mixture was heated at 50 °C for 24 h and at 100 °C for another 24 h. The resulting material was then calcined at 500 °C, at a rate of 5 °C/min for 5 h under an airstream, and finally cooled down slowly to room temperature (R.T.). All the samples were reduced at 450 °C using a H_2 (40 mL/min) stream for 1 h before characterization except for TPR analysis. The labeling of different catalysts will be referred to as xAg/CeO$_2$, where $x = 1$ and 5 wt% of metal on the catalysts. The actual Ag content determined by EDS technique was 0.97 and 4.93 for 1Ag-CeO$_2$ and 5Ag-CeO$_2$ nanotube catalysts, respectively.

8.3 Characterization

X-ray diffraction (XRD) powder patterns were recorded in a Siemens D-5000 diffractometer using Cu Kα ($\lambda = 0.15406$ nm). The morphology of the Ag/CeO$_2$ catalysts was analyzed by scanning electron microscopy (SEM) using a JEOL® JSM-6610LV, at an acceleration voltage of 20 kV; the images were obtained with the backscattered electron signal (BSE). HRTEM and local chemical analysis of the bimetallic nanoparticles were carried out in a microscope JEOL® model JEM 2010 with a resolution of 0.19 nm, equipped with energy-dispersive X-ray spectrometer (NORAN). For the aberration (Cs)-corrected characterization, the samples were analyzed using scanning transmission electron microscopy (STEM) with a JEOL® model ARM (200F) 200 kV FEG-STEM/TEM, equipped with a hexapole corrector (CEOS GmbH) for the electron probe. The probe size used for acquiring the HAADF as well as the BF-STEM images was 9 C (23.2 pA) and the CL aperture size was 40 μm. High-angle annular dark-field (HAADF) STEM images were acquired with a camera length of 8 cm/6 cm and the collection angle of 68–280 mrad/90–270 mrad was used. This scattering semi-angle easily fulfilled the requirement for the detector to eliminate contributions from unscattered or low-angle scattered beams. The BF-STEM images were obtained using a 3 mm/1 mm aperture and a collection angle of 17 mrad/5.6 mrad was used (camera length in this case was 8 cm). The HAADF as well as the BF images were acquired using a CCD camera [62]. For the electron microscopy analysis, the sample was dispersed in ethanol and a drop of this suspension was deposited onto a holey carbon grid. Surface area (BET) and temperature-programmed reduction (TPR) were carried out on an automatic multitask unit RIG-100 from ISR INC equipped with a thermal conductivity detector (TCD) with output to a computer [22, 31–34, 65]. For the TPR analysis, the oxidized catalyst (0.1 g) was placed in the reactor and purged with UHP Ar at room temperature and then the TPR measurement was performed using 5% H_2/Ar gas mixture (40 mL/min). The temperature was increased at a rate of 10 °C/min from room temperature to 500 °C. The effluent gas was passed through silica gel to remove water before measuring the amount of hydrogen consumed during the reduction by the TC detector. The signal was calibrated by 0.5 mL pulses of 5% H_2/Ar at the end of the experiment. After testing the catalytic activity reaction, the surface of these catalysts was cleaned by a He stream (30 mL/min) for 30 min at 450 °C and cooled at room temperature; then the sample was purged with UHP Ar flow and temperature-programmed reduction (TPR) experiments were carried out on an automatic multitask unit RIG-100 from ISR INC equipped with a thermal conductivity detector (TCD) with output to a computer. The oxidized catalyst (0.075 g) was diluted in SiC and placed in the reactor. The TPR measurement was performed using a H_2 (5%)–Ar gas mixture (40 mL min^{-1}). The temperature was increased at a rate of 10 °C min^{-1} from room temperature to 500 °C. The effluent gas was passed through silica gel to remove water before measuring the amount of hydrogen consumed during the reduction by the TCD. The activity tests for the steam reforming of methanol were conducted at 200–400 °C under atmospheric pressure in a continuous-flow reactor charged with 0.0750 g of the sample diluted in 0.125 g of SiC. Steam reforming of methanol was carried out by placing an 8 mm i.d. quartz reactor in an electric furnace consisting of two heating zones equipped with omega temperature controllers, using a commercial flow system RIG-100-ISRI. A K-type thermocouple was inserted into the catalyst bed to measure and control the bed temperature. Prior to ASRM reaction, the catalyst was reduced in situ, using a stream of H_2 (40 mL min^{-1}) increasing the temperature from room temperature to 500 °C at a heating rate of 10 1C min^{-1} and holding this temperature for 1 h. For the reaction, 30 mL of the O_2 (5%)–He mixture was passed through a stainless-steel saturator containing methanol, and 30 mL of He was passed through a stainless-steel saturator containing water and 140 mL of He as a diluent. The total flow rate was kept at 200 mL min^{-1} GHSV (reactant gas flow rate/reactor volume—gas hourly space velocity) = 76,394 h^{-1} based on the total flow). The gases were added by means of a mass flow controller (RIG-100). Reaction products were analyzed using a Gow-Mac 580 Gas chromatograph with a thermal conductivity detector equipped with a two-column system (molecular sieve 5 Å and Porapak Q columns), a double-injector controlled using Clarity software V.2.6.04.402 and a TCD. The first column was used to separate the gaseous products such as—H_2, O_2, CH_4, and CO. The second column was used to separate water, methanol, methyl formate (MF), and CO_2. All the reported data were collected for 7 h at each temperature in order to obtain the steady state of the reaction. The following equations were used to determine the methanol conversion and selectivity:

$$X(\%) = \frac{C_{\text{in}} - C_{\text{out}}}{C_{\text{in}}} \times 100; \quad H_2(\text{yield}) = \frac{\mu\text{mol } H_{2\text{produced}}}{2.5\ \mu\text{molCH}_3\text{OH}_{\text{feed}}}$$

$$S_{\text{CO}}(\%) = \frac{n\text{CO}_{-\text{out}}}{n\text{CO}_{2-\text{out}} + n\text{CO}_{-\text{out}} + n\text{CH}_4} \times 100$$

The subscripts in and out indicate the inlet and the outlet concentrations of the reactants or products.

8.4 Results and Discussion

8.4.1 Nickel-Loaded CeO$_2$ Catalyst

In Table 8.1, textural properties are presented as obtained from N_2 physisorption measurements at 77 K liquid nitrogen conditions. The surface area of the bare CeO$_2$ nanorods calcined at 500 °C was similar as reported by Guan et al. [65]; Zhou et al. [66] reported surface area values of 50 m^2 g^{-1} for CeO$_2$ nanorods. In general, it was found that the BET surface area of the catalysts decreases with Ni loading onto the CeO$_2$ nanorods. SEM images (Fig. 8.1a) with secondary and backscattered

Table 8.1 Surface area and concentration percent of reducible species in CeO$_2$ and Ni/CeO$_2$ catalyst

Catalyst	Surface area (m^2 g^{-1})	H_2 uptake (μmol H_2 per g$_{\text{cat}}$)	Reduction (%)
CeO$_2$	108	[a]	
3.4 Ni/CeO$_2$	94	78.6	164
16 Ni/CeO$_2$	71	201.0	93
36 Ni/CeO$_2$	51	413.5	81

Table obtained with copyrights of permissions of RSC®, R. Pérez-Hernández et al. Phys. Chem. Chem. Phys., 2013, 15, 12702–12708

[a] Negative peak

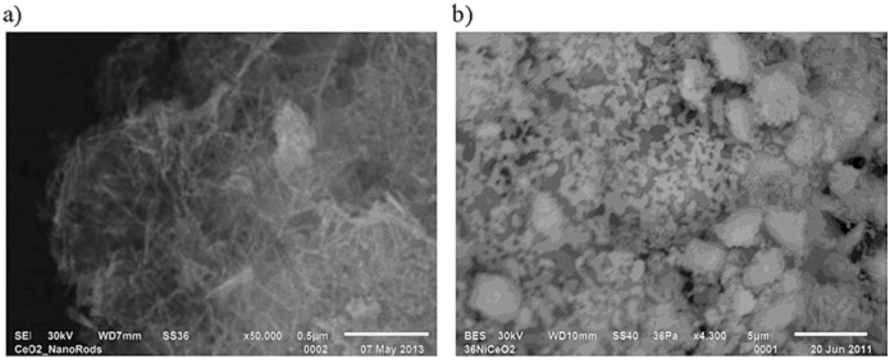

Fig. 8.1 Scanning electron microscopy images of (**a**) bare CeO_2 catalyst and (**b**) 36Ni/CeO_2 nanorod catalyst. It was possible to observe agglomerates of nickel particles over nanorod surfaces. Images taken with copyrights of permissions of RSC®, R. Pérez-Hernández et al. Phys. Chem. Chem. Phys., 2013, 15, 12702–12708, PCCP Owner Societies

electron signals showed that the CeO_2 is composed of nanorods approximately 1 mm in length.

The 36Ni/CeO_2 catalyst (Fig. 8.1b) reveals the agglomeration of Ni particles on the CeO_2 nanorod surface; this finding could explain the decrease in the surface area of the catalysts as a function of Ni addition to CeO_2, due to the dense Ni coating on the CeO_2 nanorod surface.

In Fig. 8.2, XRD patterns are presented for bare CeO_2 nanorods and Ni/CeO_2 nanorod catalysts reduced at 500 °C. The CeO_2 one-dimensional nanorods showed a highly crystalline structure with sharp diffraction peaks. The CeO_2 structure corresponds to the typical fluorite structure (cubic structure of the CeO_2 (J2CPDS 01-081-0792)); no diffraction peaks from impurities coming from the synthesis of the CeO_2 nanorods were found. In all Ni/CeO_2 catalysts, peaks corresponding to CeO_2 were clearly detected, and characteristic peaks corresponding to metallic Ni were observed. In the 3.4Ni/CeO_2 sample, the characteristic peaks of the metallic nickel were attenuated and broadened which indicates that this catalyst had better dispersion of the fine metallic Ni phase in the CeO_2 nanorod matrix or could be due to its low Ni concentration on the sample. However, a tiny diffraction peak in the (1 1 1) plane was observed at $2\theta = 44.61$ and it corresponds to metallic nickel. It's clear that intensity of the diffraction peaks of Ni increases proportionally to the Ni loading onto CeO_2 nanorods and new planes merged with (2 0 0), (2 2 0), (3 3 1), and (2 2 2) planes at 2θ = 51.91, 76.51, 93.11, and 98.61, respectively. This result is associated with the growth of Ni^0 particle size and is more evident in the 36Ni/CeO_2 sample. A similar result was reported by Rao et al. [67]. They observed that the intensity of the diffraction peaks of nickel gradually increases with the increase in Ni loading in the catalysts. The TPR profiles of the bare CeO_2 nanorods and the Ni-based catalysts are shown in Fig. 8.3. CeO_2 nanorods did not show reduction peaks until 400 °C; instead a negative peak around 300 °C was observed and it could be associated with the H_2 desorption.

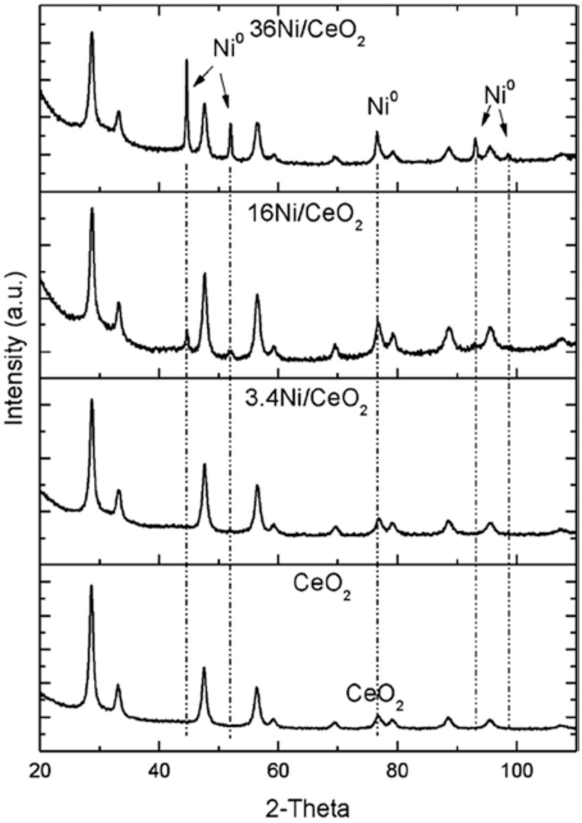

Fig. 8.2 Powder X-ray diffraction patterns of bare CeO_2 nanorods and Ni/CeO_2 catalysts. Images taken with copyrights of permissions of RSC®, R. Pérez-Hernández et al. Phys. Chem. Chem. Phys., 2013, 15, 12702–12708, PCCP Owner Societies

The TPR profiles of the bare CeO_2 nanorods and the Ni-based catalysts are shown in Fig. 8.3. CeO_2 nanorods did not show reduction peaks until 400 °C; instead a negative peak around 300 °C was observed and it could be associated with the H_2 desorption. So, during the TPR analysis, H_2 is adsorbed in a reducing environment on the surface of the CeO_2 nanorods, and then is released to the feed producing a negative peak. For the Pd/TiO_2 catalyst a negative peak was observed at 155 °C by the TPR technique due to the decomposition of PdH [7]. This result could be interesting because with an appropriate precursor these nanorods would be used for H_2 storage. A broad peak above 400 °C is observed for the CeO_2 nanorods and its intensity was very weak, indicating that only a small amount of surface ceria could be reduced from Ce^{4+} to Ce^{3+} [12, 14]; Zhou et al. [66] showed that CeO_2 nanorods exhibited a broad reduction profile centered at around 500 °C and a high-temperature reduction peak above 700 °C; however they did not observe a negative peak like in our case. This result could be associated with the difference in the surface areas reported in this work and in the literature.

The reduction profile of the 3.4Ni/CeO_2 nanorod catalyst was characterized by three reduction peaks at 220, 290, and 330 °C. The last reduction peak shifts progressively towards higher temperature as the Ni content increases on the CeO_2

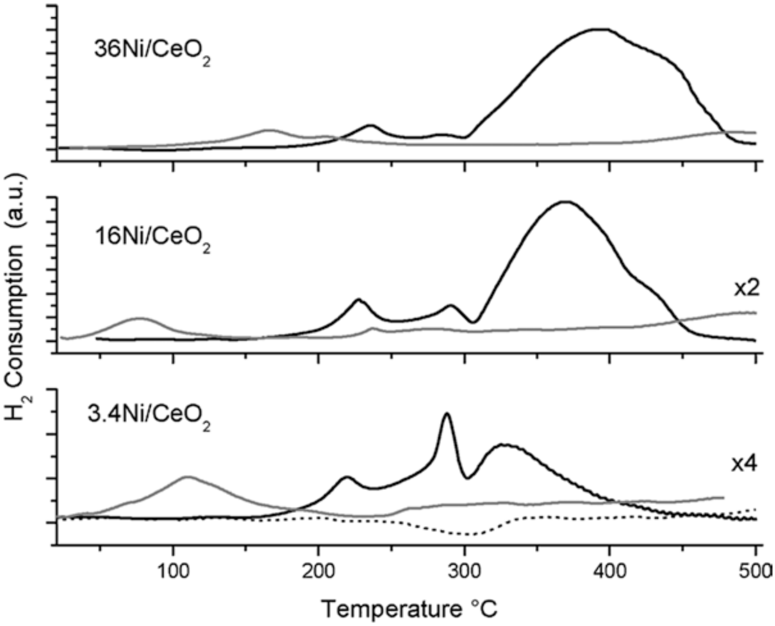

Fig. 8.3 Temperature-programmed reduction profiles of the fresh Ni/CeO$_2$ nanorod catalysts (solid line), samples after catalytic reaction (clear line) and bare CeO$_2$ nanorods (dotted line). Images taken with copyrights of permissions of RSC®, R. Pérez-Hernández et al. Phys. Chem. Chem. Phys., 2013, 15, 12702–12708, PCCP Owner Societies

nanorods. For this peak, noticeable changes were observed in the maximum in hydrogen consumption as shown by its intensity, where the main reduction took place. The wide band with maximum at 370 °C and 392 °C (with an apparent shoulder at 430 °C) was observed for the 16Ni/CeO$_2$ and 36Ni/CeO$_2$ catalysts, respectively, suggesting the reduction of different Ni species. Three reduction peaks above 2.5 wt% of Ni on CeO$_2$ were observed for the Ni/CeO$_2$ catalysts and their reduction depends on the Ni loading on the support [67]. Montoya et al. [68] reported a reduction peak at 360 °C on pure NiO and it was reduced at 420 °C on the Ni/CeO$_2$ sample. However, Ni was reduced at ca. 320–350 °C when it was supported on ZrO$_2$ [15, 56]. Generally, H$_2$ consumption at low temperature is attributed to the reduction of NiO particles with weak interaction with the support, while H$_2$ consumption at higher temperature is attributed to the reduction of NiO in intimate contact with the oxide support [69]. Thus, the reduction peaks at higher temperatures are attributed to the reduction of large Ni particles in intimate contact with the CeO$_2$ nanorods, as well as the presence of bulk NiO that delays the H$_2$ diffusion inside the particle to complete its reduction; this causes the broadening of the reduction peak at high temperature. This finding is in good agreement with XRD results, so we observed an increase in the crystallinity of the nickel with an increase in Ni loading. On the other hand, the two tiny reduction peaks observed at low temperature on the Ni/CeO$_2$ nanorod catalysts were unaffected independently of the

Ni loading on the catalysts; this indicates that these reducible species are present on the three samples, and they come from the reduction of NiO particles with weak interaction with the support. This experimental observation suggests that large crystallites tend to be reduced slower than small-size crystallites, due to their relatively low surface area exposed to H_2. Du et al. [70]; reported that the reduction of NiO takes place at ~15 °C lower when it is supported on nanoparticles than on nanorods of CeO_2. This suggested a strong interaction between NiO and the CeO_2-NR. The hydrogen consumption and reduction degree of NiO over CeO_2 nanorods are summarized in Table 8.1. It can be observed that the H_2 uptake on the fresh 3.4Ni/CeO_2 nanorod catalyst was higher than that expected for the reduction of the NiO on the catalyst. This result was associated with the fact that, in the TPR study, small Ni particles probably cause spillover (surface diffusion of activated hydrogen) of H_2 onto the support inducing a simultaneous reduction of both nickel oxide and surface of the CeO_2 nanorods. The NiO reduction degree on the catalysts decreases with the increase of nickel loading. For the samples with 16 and 36 wt% of Ni on the CeO_2 nanorods, the active phase was not reduced completely, especially in the catalyst with higher Ni loading. The TPR profiles of the samples after catalytic reaction showed only a miniscule peak at low temperature. This result indicates that most of the Ni active phase was maintained in the metallic phase; in Fig. 8.4, the catalytic activity of the ASRM reaction as a function of the temperature and Ni loading on the CeO_2 nanorods is presented. The methanol conversion of the bare CeO_2 nanorods was included for comparison, from which catalytic activity of the

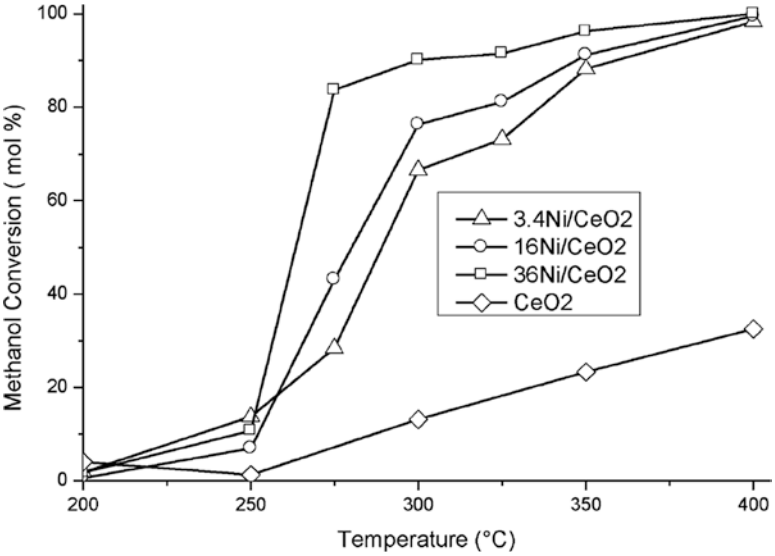

Fig. 8.4 Catalytic performance in the ASRM reaction over CeO_2 nanorods and *n*Ni/CeO_2 nanorod catalysts as a function of Ni loading and temperature. Image taken with copyrights of permissions of RSC®, R. Pérez-Hernández et al. Phys. Chem. Chem. Phys., 2013, 15, 12702–12708, PCCP Owner Societies

CeO_2 support was low, about 30% at the maximum reaction temperature. When Ni was loaded onto the CeO_2 nanorods, the methanol conversion was increased, and the methanol conversion observed on all the catalysts was higher than bare CeO_2 nanorods at the experimental range of temperature and it was completed at 400 °C. Among them 36Ni/CeO_2 nanorod catalyst displayed higher methanol conversion than that of the 16Ni/CeO_2 and 3.4Ni/CeO_2 samples. The light-off temperature for all catalysts was ca. 250 °C. At 275 °C the methanol conversion was ca. 30, 45, and 85% for the 3.4Ni/CeO_2, 16Ni/CeO_2, and 36Ni/CeO_2 catalysts, respectively. However, at the maximum reaction temperature the methanol conversion was ca. 100% on the three catalysts. Dong et al. [71] studied the oxyreforming, steam reforming, and oxy-steam reforming of methane on different Ni/CeO_2–ZrO_2 catalysts, observing that CH_4 conversion and selectivity to H_2 and CO increase with the increase of Ni loading up to 15%, and above this level the conversion of methane and selectivity to H_2 and CO decreases. Rao et al. [67] studied the selective hydrogenation of acetone to methyl isobutyl ketone and reported that the catalytic activity of the Ni/CeO_2 catalysts increases with an increase in Ni loading up to 2.5 wt% and decreases with the further increase in Ni loading onto ceria matrix. This effect was attributed to an increase in the crystallinity of the active phase on CeO_2. Similarly, Potdar et al. found that 15% Ni–Ce–ZrO_2 catalyst showed high catalytic activity and stability [72], associating nanocrystalline nature of cubic $Ce_{1-x}Zr_xO_2$ producing strong interaction with as-dispersed nanosized NiO_x particles. It has been shown that catalytic activity of Cu–CeO_2 and Au/CeO_2 catalysts in SRM and ASRM reactions is considerably affected by loading and metal addition method [12, 73–78]. In these studies, it was observed that using impregnation method it is possible to add up to 36% (w/w) on CeO_2 nanorods obtaining high catalytic activity. Thus, CeO_2 nanorods are good candidates for Ni dispersion to favor the metal–support interaction which enhances catalytic activity, in agreement with silver-loading ZnO [1]. Furthermore, the crystalline anisotropy of active phase plays an important role in methanol conversion and selectivity suggesting that ASRM reaction may be a structure-sensitive reaction [56]. This relationship between reactivity and structure depends on particle size, morphology, and crystal orientation of supported material to promote specific surface termination of adsorption/desorption of methanol molecules during reaction conditions [56, 79, 80], as described by Koga et al., who observed high methanol conversion and lower carbon monoxide concentration at similar reaction temperature on copper nanoparticles (CuNPs) supported on zinc oxide (ZnO) whiskers compared with a conventional Cu/ZnO powder catalyst [81]. Steam reforming of methanol reaction over Au supported on CeO_2 nanorods or CeO_2 nanocubes was studied by Boucher et al., who reported higher SRM rates normalized by the specific area for Au/CeO_2 nanorods than Au/CeO_2 nanocube catalysts [82]. Xiong et al. reported methanol steam reforming reaction on the mesoporous Pd/ZnO, encountering high catalytic activity due to H_2 yield and CO_2 selectivity [83], attributing to large BET surface area for mesoporous Pd/ZnO samples, in agreement with similar results for the rodlike

CuO–CeO$_2$ mixed oxides as reported by Yang et al. in the steam reforming of methanol reaction [84].

Due to morphological aspects there is higher CO oxidation activity on CeO$_2$ nanorods in comparison with CeO$_2$ nanoparticles, as reported by Zhou et al. [66]. The latter can be correlated due to crystallographic surface planes for CeO$_2$ nanorods, having reactive planes ({0 0 1} and {1 1 0}), which seem to be more active than {1 1 1} planes for ceria nanoparticles. Using TEM it was possible to achieve deep CeO$_2$ nanorod morphology observations as presented in Fig. 8.5a, having ~8 nm in width; as presented in Fig. 8.5b (high-resolution TEM) CeO$_2$ nanorods seem to have a rectangular shape. The incident electron beam is along the [0 1 1] axis and from this image we can observe that the rods grow along the [1 1 −1] axis. The d-spacing measured from the HREM image (inset in Fig. 8.5b) was 3.10 Å which corresponds to the (1 1 1) plane and 2.73 Å which corresponds to the (2 0 0) plane, associated with the cubic phase of the CeO$_2$ system (JPDF-065-5923, $a = 5.4037$ Å). FFT analysis from the HREM image of the CeO$_2$ nanorods, inset of Fig. 8.5b, shows that the crystalline structure rod was oriented along the [0 1 1] zone axis. In this orientation, the exposed planes of the CeO$_2$ nanorod structure were (%1 %1 1), (1 1 %1), (1 %1 1), (%1 1 %1), (2 0 0), and (%2 0 0).

With the [1 1 −1] growth direction of the CeO$_2$ nanorod, the exposed planes which belong to this orientation are (−2 −2 0), (−2 0 −2), (0 2 −2), (0 −2 2), (2 0 2), and (2 2 0), in accordance with the cubic crystallography. In this way, the planes in the [1 1 −1] orientation had a low contribution area for the Ni deposition than the area formed by planes from the orientation [0 1 1] zone axis. In Fig. 8.6a TEM image of 16Ni/CeO$_2$ nanorod catalyst sample corresponds to nickel nanoparticles

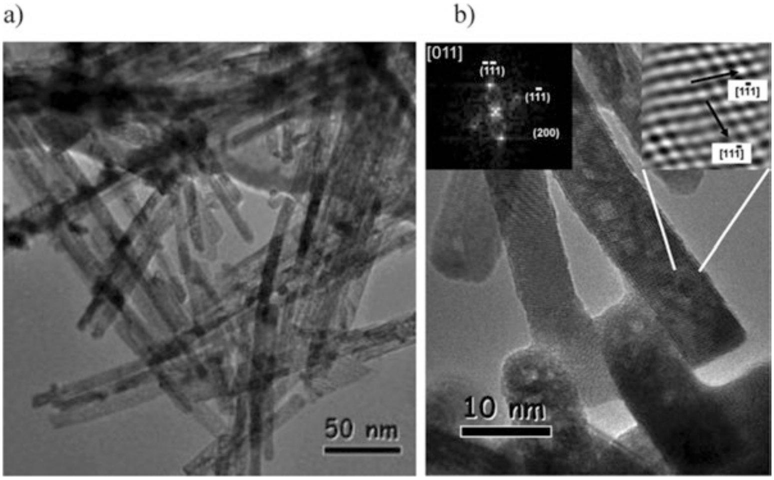

Fig. 8.5 (**a**, **b**) Transmission electron microscopy (TEM) images of bare CeO$_2$ nanorods. Image taken with copyrights of permissions of RSC®, R. Pérez-Hernández et al. Phys. Chem. Chem. Phys., 2013, 15, 12702–12708, PCCP Owner Societies

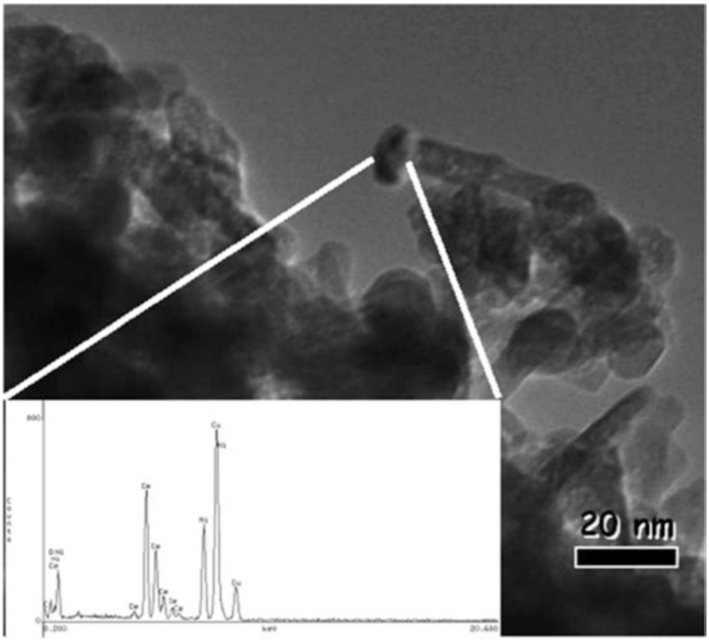

Fig. 8.6 High-resolution TEM image for 16Ni/CeO_2 nanorod catalyst sample. Inset: surface EDS spectra performed during TEM measurements over the as-observed area. Image taken with copyrights of permissions of RSC®, R. Pérez-Hernández et al. Phys. Chem. Chem. Phys., 2013, 15, 12702–12708, PCCP Owner Societies

dispersed over CeO_2 nanorods. EDS analysis spectra (inset image of Fig. 8.6) of the nanoparticles showed higher Ni concentration of around 25.49% than the theoretical composition (15%). This is because the analysis was performed on the particle rather than on the support. The Ni nanoparticle size was about 15 nm in diameter approximately. Taking into account that the catalytic activity values of bare CeO_2 nanorods were low, we suggest that the Ni was preferentially deposited on the planes of the [0 1 1] axis rather than on the planes of the [1 1 −1] axis of the CeO_2 nanorods mentioned above. So, lower contribution for catalytic activity occurred at [1 1 −1] surface, where the Ni nanoparticles were also deposited.

From data as presented in Fig. 8.7a, b, it is evident that increasing Ni loading on CeO_2 nanorods provokes increase in H_2 yield for methanol conversion. Furthermore, the increase of temperature from 250 to 300 °C led to an increase in the selectivity especially for the 36Ni/CeO_2 catalyst sample on which the H_2 yield was close to 0.80, while for 16Ni/CeO_2 catalytic sample the H_2 yield was 0.65 and for 3Ni/CeO_2 0.50. All catalysts reached a maximum H_2 yield at 400 °C. In the case of the bare CeO_2 nanorods, the selectivity towards H_2 was low, in accordance with the low catalytic activity observed on this sample. All catalysts showed high selectivity towards CO as shown in Fig. 8.7b. And the CO selectivity diminishes slightly and the CH_4 formation increases by increasing Ni loading as shown in Fig. 8.7b, which

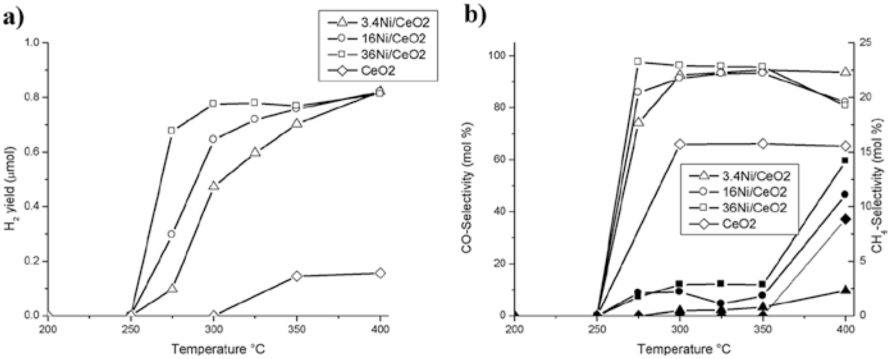

Fig. 8.7 Catalytic activity measurements for (**a**) H_2 yield and (**b**) CO and CH_4 selectivity as a function of nickel loading and temperature reaction conditions. Image taken with copyrights of permissions of RSC®, R. Pérez-Hernández et al. Phys. Chem. Chem. Phys., 2013, 15, 12702–12708, PCCP Owner Societies

is clear evidence that CeO_2 nanorods can act chemically as support nanomaterials for steam reforming catalytic reactions.

8.4.2 Silver-Loaded CeO_2 Catalyst

The samples were labeled as $1Ag/CeO_2$ and $5Ag/CeO_2$ catalysts, and specific surface area was measured by a single-point method. The value of the surface area in both samples was close to 63 m^2/g. This result was slightly higher than those as reported in the literature for similar CeO_2-based catalyst [12, 13, 59, 85]. Experimental evidence indicates that using of impregnation method diminishes surface area of the catalysts; in this case a surface area decrease was not observe, when metal was loaded; the latter can be explained due to hollow Ag-CeO_2 nanotube-like structure. Even when the silver concentration was increased, and conventionally a decrease in the surface area could be expected, the presence of hollow sections due to these Ag-CeO_2 nanotubes compensated the loss of the surface area when metal is present on the sample. In Fig. 8.8a, a scanning electron microscopy image (SEM) presents clear evidence of Ag nanowires as present on active-phase precursor of the catalysts. These nanowires, which are 80 nm in diameter average and several micrometers in length, were used for the synthesis of the final Ag-CeO_2 nanotube catalysts. In Fig. 8.8b the morphology of the $1Ag/CeO_2$ after thermal treatments (calcinations and reduction) is shown, and clearly unidirectional nanotubes with diameter ~100–300 nm had been synthesized; from images it was possible to determine also a hollow-like nanotube as shown in Fig. 8.8c. These structures could be formed during thermal treatment; where the Ag nanowires served as a template to obtain the ceria tubes, and then due to this processing, silver was disseminated outside of the ceria tubes. The mechanism to obtain this kind of structures is

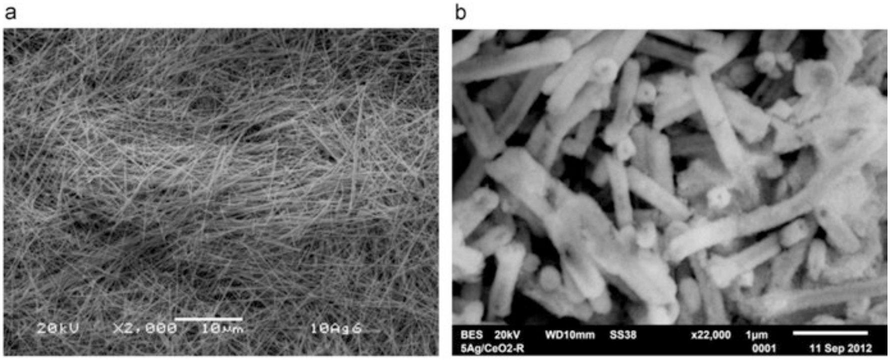

Fig. 8.8 (**a**) SEM image of the Ag nanowires used as an active-phase precursor for the Ag-CeO_2 catalysts. It reveals nanowires of 80 nm in diameter and several micrometers in length; (**b**) SEM image of the 1Ag/CeO_2 after thermal treatments (calcinations and reduction). Image taken with copyrights of permissions of R. Pérez-Hernández et al. Catalysis Today, 212, (2013) 225–231

described in detail by Mondragon-Galicia et al. [86], which can be explained through Kirkendall effect. It is important to mention that for sample labeled 1Ag/CeO_2 structures as observed seems to be less abundant in comparison with silver-rich catalyst 5Ag/CeO_2. For 1Ag/CeO_2 sample, lesser amount of Ag nanorods was used to prepare final catalysts; this can be a possible reason why Ag-CeO_2 nanotubes were less abundant in comparison with 5Ag/CeO_2. The Ag one-dimensional nanostructures worked as templates/scaffolds to achieve crystal growth Ag-CeO_2 nanotube-like structure; thus, formation of these nanotubes will depend on the concentration of silver nanostructures solely.

From X-ray powder diffraction data 1Ag/CeO_2 and 5Ag/CeO_2 samples before and after the catalytic reaction are shown in Fig. 8.9; from data it is possible to determine that all samples showed characteristic diffraction peaks of the cubic structure for fluorite CeO_2 (JCPDS 01-081-0792). In addition, it was possible to observe in the catalysts a distinctive broader peak of low intensity at $2\theta = 38.18°$, which is characteristic of the (1 1 1) diffraction planes of the metallic silver (JCPDS 65-2871). The intensity of this peak increased with the Ag loading from 1 to 5%, suggesting an increase in the particle size of the silver. In the same figure, the XRD pattern of the morphology was included . This CeO_2 nanoparticle was identified to be FCC crystallographic structure according to JPDF card # 01-081-0792 with lattice parameter of $a = 5.41$ Å.

Using high-resolution TEM technique, it was possible to determine clustering on the catalytic material as shown in Fig. 8.10a, and its corresponding surface energy-dispersive X-ray spectroscopy (EDS) in Fig. 8.10b. The particle was observed on the [−1 1 2] direction. The crystalline planes that were seen in the HRTEM image and the FFT are those of (1 −1 1) and (2 2 0), with an interplanar distance of 0.308 and 0.191 nm, respectively, as presented in Fig. 8.11 and its inset.

The reduction properties of fresh Ag nanostructures on CeO_2 catalysts before and after the catalytic reaction were investigated by H_2-TPR experiments and shown in Fig. 8.12. The TPR profile of the bare CeO_2 was included for comparison showing

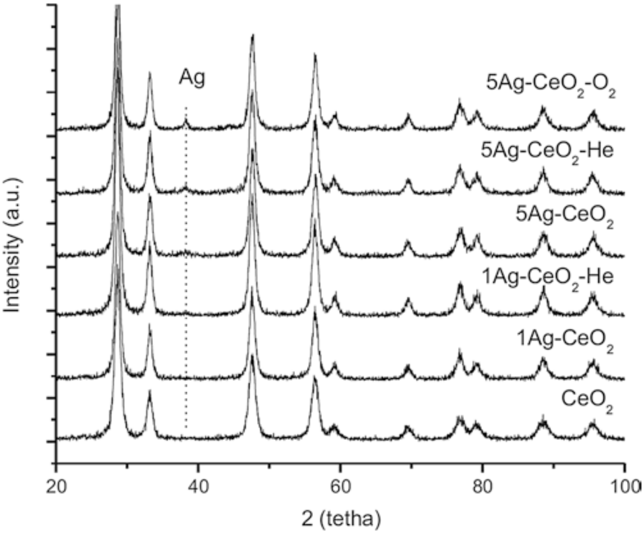

Fig. 8.9 Powder X-ray diffraction patterns of the $1Ag/CeO_2$ and $5Ag/CeO_2$ before and after the catalytic reaction. He-SRM and O_2-OSRM, respectively. Image taken with copyrights of permissions of R. Pérez-Hernández et al. Catalysis Today, 212, (2013) 225–231

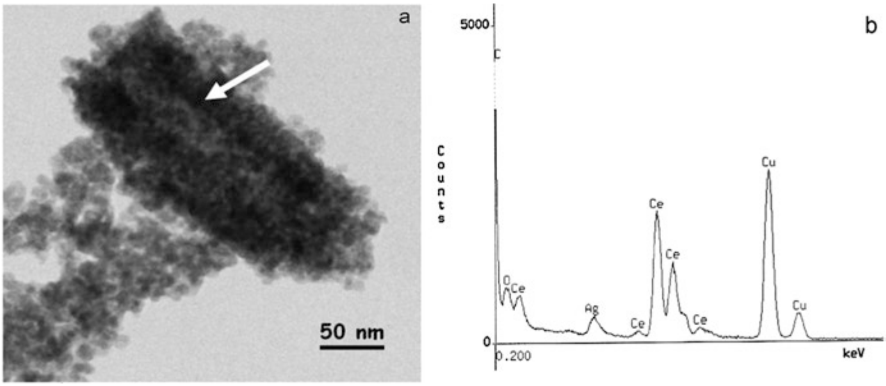

Fig. 8.10 (**a**) TEM image of the ceria nanotube with diameter of 100 nm from $5Ag/CeO_2$ catalyst. This image indicates that the nanotubes are hollow in the middle as indicated by the arrow. (**b**) EDS analysis showed the presence of the Ag. Image taken with copyrights of permissions of R. Pérez-Hernández et al. Catalysis Today, 212, (2013) 225–231

a broad peak of low intensity above 450 °C, which is assigned to reduction of ceria surface. For all the investigated catalysts, the reduction process takes place between 175 °C and 325 °C with a maximum reduction peak centered at 225–250 °C. These temperatures are considerably lower than the reduction temperature reported for pure CeO_2, spent catalysts from the SRM and OSRM reaction. It is clear that the

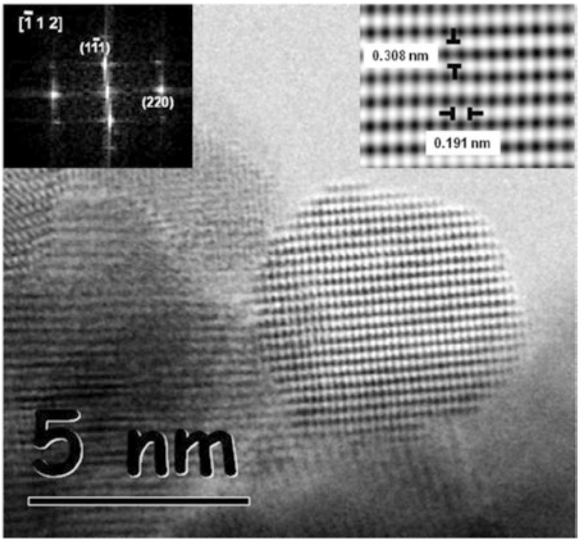

Fig. 8.11 High-resolution image of a CeO_2 nanoparticle from the nanotube. The size of the spherical nanoparticle is ~6 nm and shows a [−1 1 2] crystalline direction. (1 −1 1) and (2 2 0) crystalline planes were identified by HRTEM and FFT analysis as presented in the inset. Image taken with copyrights of permissions of R. Pérez-Hernández et al. Catalysis Today, 212, (2013) 225–231

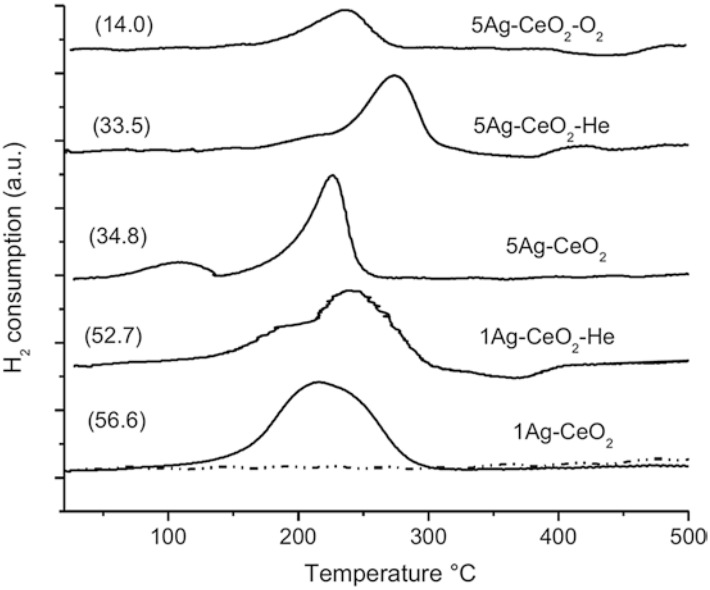

Fig. 8.12 H_2-TPR profiles of the fresh Ag-CeO_2 catalysts before and after the catalytic reaction. The He-SRM and O_2-OSRM are indicated. CeO_2 dotted line. Values in parentheses correspond to the H_2 consumption in the TPR test. Image taken with copyrights of permissions of R. Pérez-Hernández et al. Catalysis Today, 212, (2013) 225–231

intensity of the diffraction peak corresponding to the metallic silver (peak at 38.18°, 2θ) was also increased. This result could be attributed to the fact that the silver particles were sintered during the reaction. In the 5Ag/CeO_2 catalyst, the ceria nanotubes have a diameter of 100 nm, as can be observed in the representative TEM image of this catalyst in Fig. 8.10. The characteristic contrast in this image indicates that the nanotubes are hollow in the middle as indicated by the arrow in Fig. 8.10a. It also showed that the ceria nanotubes are constituted by small ceria nanoparticles. The size of these ceria nanoparticles is between 5 and 10 nm in diameter on an average, as determined by TEM/HRTEM analysis. No Ag nanowires or any other Ag nanostructures were observed by TEM on the ceria nanotubes confirming that the nanotubes were indeed hollow. However, the EDS analysis showed the presence of the Ag as shown in Fig. 8.10b. According to the EDS analysis, the chemical composition of the 5Ag/CeO$_2$ catalyst was close to theoretical value (Ag = 4.93 wt%) and as presented in Fig. 8.11 spherical shape CeO$_2$ nanoparticle from the nanotube with diameter size of ~6 nm was encountered as well.

This CeO$_2$ nanoparticle was identified to be FCC crystallographic structure according to JPDF card # 01-081-0792 having lattice parameter of $a = 5.41$ Å. The particle was observed on the [−1 1 2] direction. The crystalline planes that were seen in the HRTEM image and the FFT are those of (1 −−1 1) and (2 2 0), with an interplanar distance of 0.308 and 0.191 nm, respectively, inset of Fig. 8.11. The reduction properties of fresh Ag nanostructures on CeO$_2$ catalysts before and after the catalytic reaction were investigated by H$_2$-TPR experiments and shown in Fig. 8.12. The TPR profile of the bare CeO$_2$ was included for comparison showing a broad peak of low intensity above 450 °C, which is assigned to reduction of ceria surface. For all the investigated catalysts, the reduction process takes place between 175 and 325 ° C with a maximum reduction peak centered at 225–250 °C. These temperatures are considerably lower than the reduction temperature reported for pure CeO$_2$, which showed a single large peak at around 550 °C [13, 56, 59, 60] and higher for the reduction peak of unsupported silver oxide which was reported to be at 130 °C [10, 61]. TPR profiles of the fresh Ag/CeO$_2$ catalysts exhibited a single broad reduction peak and overlapping reduction peaks. The presence of these peaks in the samples is an indication of the existence of one or more silver species in the Ag/CeO$_2$ catalysts. A small reduction peak close to the silver oxide was observed in the 5Ag/CeO$_2$ catalyst. The H$_2$ uptake values within parenthesis in Fig. 8.12, by reduction of the fresh 1Ag/CeO$_2$ catalysts, showed that the actual hydrogen consumption was higher than the one predicted from the reduction of the Ag$_2$O on the samples. This result could be due to the fact that small Ag particles can cause spillover of hydrogen onto the support matrix inducing a concurrent reduction of both silver oxide and CeO$_2$ surfaces, as was reported extensively for CeO$_2$-based catalysts and for Ag/MnO$_2$ by others [19, 31, 32, 34, 37, 67, 68]. TPR profiles of the samples after catalytic reaction showed a slight shift in the peaks to higher temperatures. In these samples it was possible to observe a negative peak at 365 °C due to H$_2$ desorption adsorbed on the CeO$_2$; however some metal hydride cannot be ruled out. Mo et al. [10, 61] observed that the partially reduced CeO$_2$ exhibited significant capacity of hydrogen storage. The effect of the amount of Ag nanowires, in Ag-CeO$_2$ catalysts, was investigated in the steam and oxidative steam reforming of methanol as a function of the reaction temperature. In general, we observed that as population of the nanotubes was increased in the catalysts, the catalytic activity of the Ag-CeO$_2$

nanotubes was also improved. Figure 8.6 shows the catalytic activity of the Ag/CeO_2 samples on the SRM reaction. The methanol conversion at 300 °C was 3% on the sample with a low quantity of nanotubes while for the sample with nanotubes in a higher concentration was 13%. When raising the temperature up to 375 °C, the methanol conversion was 41% and 61% for the samples with low and high content of nanotubes in the catalysts, respectively. After this temperature, both samples had the same activity and reached 100% of conversion at 425 °C. Imamura et al. [87] reported that Ag accelerates the oxidation of the CH_4 in Ag/CeO_2 catalytic system, although its chemical effect due to low or large amount of Ag was not remarkable. Udani et al. [76] observed that the methanol conversion on the SRM reaction increased considerably with the addition of O_2 into the feed stream on Cu-base samples and argued that metallic copper was the active species in that particular copper ceria oxide catalytic material. In this case, it is considered that a sample with high nanotube content showed better catalytic activity in SRM reaction; the effect of the oxygen in the gas feed on the steam reforming was detailed monitored, known as OSRM. Figure 8.13 shows that addition of oxygen in the feed improved the activity of sample labeled 5Ag/CeO_2 catalyst, because the methanol conversion was shifted to lower temperatures, approximately 100 °C with respect to SRM reaction. The methanol conversion at 200 °C was 13%, raising the reaction temperature up to 250 °C; its catalytic activity approaches 50% on the OSRM, whereas for the SRM

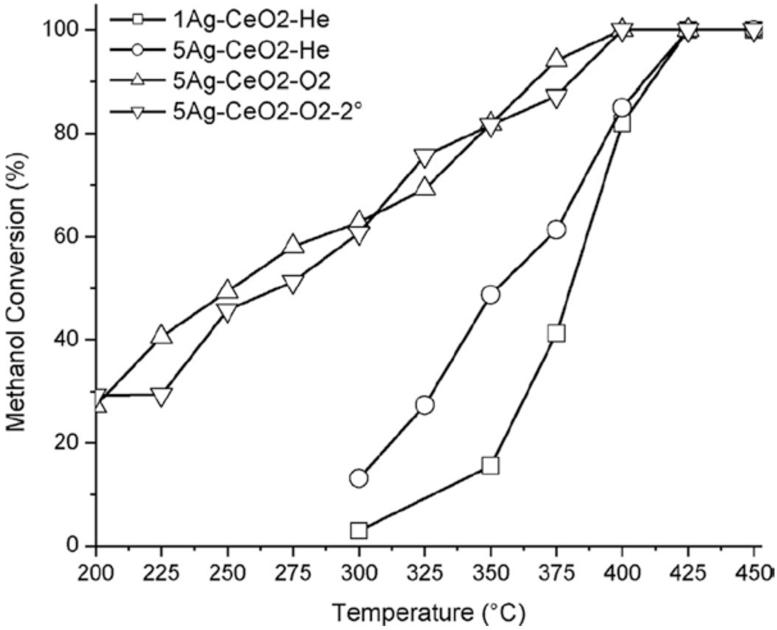

Fig. 8.13 Catalytic activity of the 5Ag/CeO_2 nanotube-based catalyst in the steam and oxidative steam reforming of methanol as a function of the reaction temperature. CH_3OH (75), H_2O (12.75), and O_2 (25.2) Torr, respectively. He-SRM and O_2-OSRM. Image taken with copyrights of permissions of R. Pérez-Hernández et al. Catalysis Today, 212, (2013) 225–231

it requires 350 °C. After 400 °C, 100% of methanol conversion was reached in the OSRM while in the SRM reaction it requires 425 °C to reach the full methanol conversion; however, a non-decrease of CH_3OH conversion was observed for both type of reactions. In order to observe 5Ag/CeO_2 catalyst activity after the first reaction cycle, a spent catalyst was tested again on the OSRM reaction (*as presented in Fig. 8.13*); spent 5Ag/CeO_2 catalyst does not suffer deactivation (second cycle of the reaction). So, the catalytic activity of the spent catalytic sample was close to the fresh catalyst, indicating that the sample was stable. In a previous study, we reported no deactivation of the silver supported on ZnO nanorod catalysts on the steam reforming of methanol reaction [50]. However, Imamura et al. [88, 89] observed that the Ag (10%)/CeO_2 sample lost its activity remarkably after the first reaction on the CH_4 oxidation. Xu et al. [90] studied the effect of the Ag particle size on the CO oxidation reaction. They observed that the best performance was presented in the sample with large Ag (5–10 nm) particles supported on β-MnO_2 nanowires. In addition, that sample showed a strong Ag–MnO_2 interaction. Luo et al. [91] suggested that the active oxygen on Ag is consumed mainly in the oxidation of CO, and Mn serves as an oxygen carrier. Scirè et al. [92] excluded that the different activity observed on the Ag/TiO_2 catalysts prepared by different methods could be related to Ag particle size. They attributed the higher catalytic activity observed on the Ag/TiO_2 sample, for the methanol combustion reaction, to the presence of spherical, multiple twinned, highly defective Ag crystallites. In our case, it was not possible to find by TEM this kind of particles in the nanotube catalyst, suggesting that probably the metallic active phase remains dispersed within the CeO_2 agglomerates. On the 1% Auceria catalyst, full methanol conversion at 300 °C was completed and no hysteresis or deactivation was observed upon cooling to lower temperatures [93]. In the same way, González-Rovira et al. [94] observed that the catalytic activity of the CeO_2 nanotubes for the CO oxidation reaction was 400 times higher than that of polycrystalline powder CeO_2 sample prepared by a conventional route. This highly improved catalytic performance must be due to the fact that the nanotubes are built by assembling a large number of randomly oriented nanocrystals, giving rise to a significant volume of very reactive boundary regions between the nanocrystals. Likewise, a greater contribution of the more reactive {1 0 0} facets to the surface structure of the material may also contribute to the observed catalytic performance enhancement. In our case, by TEM analysis it was possible to observe many CeO_2 nanoparticles along [−1 1 2] direction; therefore, their exposed planes are the {1 1 1}, {2 2 0}, and {1 3 1}. In previous work the (2 0 0) planes were also identified [86]. These crystalline planes identified in this work contribute to the catalytic activity of our experiments, as it was confirmed by González-Rovira et al. [94].

The main products identified from the SRM and OSRM reaction using the as-prepared Ag/CeO_2 catalysts were H_2, CO, CH_4, and CO_2 that can be traced. In Fig. 8.14a hydrogen selectivity of the 1Ag/CeO_2 and 5Ag/CeO_2 catalysts for SRM is presented; it was possible to observe that the loading of silver concentration in the CeO_2 support induces a reduction of the SH_2 although a high-ethanol conversion was also found during test runs; the latter can be attributed and related to surface crystallographic effect of silver particles as discussed using powder X-ray diffraction

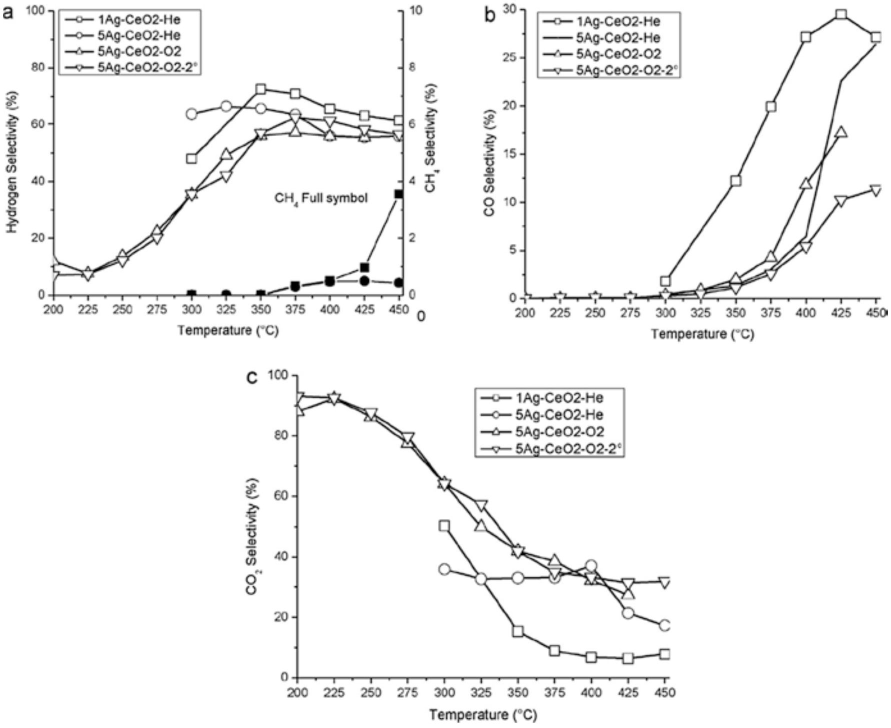

Fig. 8.14 (**a**) H_2 selectivity, (**b**) CO selectivity, and (**c**) CO_2 selectivity of the Ag-CeO_2 nanotubes in the steam and oxidative steam reforming of methanol as a function of the reaction temperature. CH_3OH (75), H_2O (12.75), and O_2 (25.2) Torr, respectively. He-SRM and O_2-OSRM. Image taken with copyrights of permissions of R. Pérez-Hernández et al. Catalysis Today, 212, (2013) 225–231

data; the hydrogen is easily oxidized to water over a catalytic sample which has large silver content. The most interesting change in selectivity is derived from silver over CeO_2 acting as support nanostructured material on CO production as indicated in Fig. 8.14b. The 5Ag/CeO_2 catalytic sample showed high CO_2 production, in accordance to data presented in Fig. 8.14c, and low selectivity towards CH_4 when compared with 1Ag/CeO_2 catalytic sample. In conclusion, increasing silver particle size leads to promotion of methanol combustion with decrease of hydrogen production and its increase of the water formation as well as CO_2 production for those catalytic systems.

8.5 Conclusions

In this chapter the chemical synthesis and catalytic activity of nickel- and silver-loaded CeO_2 nanostructures are presented. The nickel-CeO_2 catalytic material was grown by a hydrothermal method; using state-of-the-art microstructure characterization techniques it was possible to determine CeO$_2$ nanorod morphology; and according to TEM observations the width of nanorods is ~8 nm, having 3.10 Å which corresponds to the (1 1 1) planes and 2.73 Å which corresponds to the (200) planes. The exposed planes of the CeO$_2$ nanorod structure oriented along the [0 1 1] zone axis for Ni impregnation were (−1 −1 1), (1 1 −1), (1 −1 1), (−1 1 −1), (2 0 0), and (−2 0 0) and they were more reactive for methanol conversion in comparison with (−2 −2 0), (−2 0 −2), (0 2 −2), (0 −2 2), (2 0 2), and (2 2 0) planes from the [1 1 −1] axis, which corresponds to nanorod growth direction. One remarkable insight was that Ni/CeO$_2$ nanorod catalysts present high activity for autothermal steam reforming methanol (ASRM) reaction as a function of Ni loading, which is a true evidence of chemical synergistic effect between ceria oxide and nickel metallic particles. For silver ceria oxide (Ag-CeO$_2$) nanotubes are synthesized by the precipitation method and based on preformed silver nanoparticles as active-phase precursors. From transmission electron microscopy observations, it was possible to determine a nanotubular morphological structure, and the complete assembly of Ag-CeO$_2$ was used as a catalytic material for methanol-reforming reaction towards production of H$_2$ [95]. Results indicate that in the case of Ag-CeO$_2$ nanotubes, nanoparticles of CeO$_2$ are those that self-assemble to make up the tubular structures, having highly reactive surface planes of CeO$_2$ exposed creating an enhancement of catalytic activity as active phase for methanol conversion and selective for H$_2$ and CO depending on chemical concentration and composition. O$_2$ effect on the reforming reaction was clear, because the methanol conversion shifts to lower temperature and it reduces the CO production compared with selective reaction monitoring (SRM). The key of the future research is in developing these catalysts and controlling the particle size at higher Ag concentrations, in order to increase the H$_2$ production and reduce the CO selectivity, in addition for a faster way of large production and scaling of this type of catalytic systems [96].

Acknowledgements I highly thank all technical support from I. Q. Albina Gutiérrez Martínez and Carlos Salinas Molina. To research project ININ-CA-009, and financial support from CONACYT-Mexico source: CB-2008-01-104540 and CB-169682, CONACYT-SENER grant 226451. To Instituto Nacional de Investigaciones Nucleares for usage of laboratory facilities, and to Kleberg Advanced Microscopy Center of University of Texas at San Antonio for usage of electron microscopy facilities. To co-authors and colleagues G. Mondragón-Galicia, A. Allende Maravilla, J. Palacios, C. Gutiérrez-Wing, Francis Leonard Deepak, D. Mendoza-Anaya, and A. Gutiérrez-Martínez for their hard work and dedication to all research activities on this project.

References

1. R. Pérez-Hernández, A. Gutiérrez-Martínez, A. Mayoral, F.L. Deepak, M.E. Fernández-García, G. Mondragón-Galicia, M. Miki, M. José-Yacamán, Adv. Mater. Res. **132**, 205–219 (2010)
2. Y.S. Zhao, P. Zhan, J. Kim, C. Sun, J.X. Huang, ACS Nano **4**, 1630 (2010)
3. X.Y. Zhang, W. Lu, J.Y. Da, H.T. Wang, D.Y. Zhao, P.A. Webley, Chem. Commun., 195–197 (2009)

4. X.J. Feng, K. Shankar, M. Paulose, C.A. Grimes, Angew. Chem. Int. Ed. **48**, 8095 (2009)
5. Z. Wang, H. Wang, B. Liu, W. Qiu, J. Zhang, S. Ran, H. Huang, J. Xu, H. Han, D. Chen, G. Shen, ACS Nano **5**, 8412–8419 (2011)
6. A.J. Apple, F.R. Foulkes, *Fuel Cell Handbook* (Van Nostrand Reinhold, New York, 1989)
7. R. Pérez-Hernández, A.D. Avendaño, E. Rosas, V. Rodríguez, Top. Catal. **54**, 572–578 (2011)
8. F. Raimondi, J. Wambach, A. Wokaun, Phys. Chem. Chem. Phys. **5**, 4015 (2003)
9. L.D. Rogatis, T. Montini, B. Lorenzut, P. Fornasiero, Energy Environ. Sci. **1**, 501 (2008)
10. L. Mo, X. Zheng, C.-T. Yeh, Chem. Commun., 1426–1427 (2004)
11. Y.-G. Lin, Y.-K. Hsu, S.-Y. Chen, Y.-K. Lin, L.-C. Chen, K.-H. Chen, Angew. Chem. Int. Ed. **48**, 7586 (2009)
12. R. Pérez-Hernández, A. Gutiérrez-Martínez, C.E. Gutiérrez-Wing, Int. J. Hydrog. Energy **32**, 2888–2894 (2007)
13. R. Pérez-Hernández, A. Gutiérrez-Martínez, J. Palacios, M. Vega-Hernández, V. Rodríguez-Lugo, Int. J. Hydrog. Energy **36**, 6601–6608 (2011)
14. R. Pérez-Hernández, L.C. Longoria, J. Palacios, M.M. Aguila, V. Rodrı’guez, Energy Mater. Mater. Sci. Eng. Energy Syst. **3**, 152–157 (2008)
15. R. Pérez-Hernández, G. Mondragón-Galicia, D. Mendoza-Anaya, J. Palacios, C. Angeles-Chavez, J. Arenas-Alatorre, Int. J. Hydrog. Energy **33**, 4569–4576 (2008)
16. M.M. Barroso-Quiroga, A.E. Castro-Luna, Int. J. Hydrog. Energy **35**, 6052 (2010)
17. A. Trovarelli, C. De-Leitenburg, M. Boaro, G. Dolcetti, Catal. Today **50**, 353–367 (1999)
18. H.C. Yao, Y.F. Yao, J. Catal. **86**, 254 (1984)
19. R. Pérez-Hernández, F. Aguilar, A. Gomés-Cortés, G. Díaz, Catal. Today **107–108**, 175–180 (2005)
20. J.C. Fierro-Gonzales, B.C. Gates, J. Phys. Chem. B **108**, 16999 (2004)
21. M. Cargnello, C. Gentilini, T. Montini, E. Fonda, S. Mehraeen, M. Chi, M. Herrera-Collado, N.D. Browning, S. Polizzi, L. Pasquato, P. Fornasiero, Chem. Mater. **22**, 4335–4345 (2010)
22. C. Wang, H. Yin, R. Chan, S. Peng, S. Dai, S. Sun, Chem. Mater. **21**, 433–435 (2009)
23. N. Hickey, P.A. Larochette, C. Gentilini, L. Sordelli, L. Olivi, S. Polizzi, T. Montini, P. Fornasiero, L. Pasquato, M. Graziani, Chem. Mater. **19**, 650–651 (2007)
24. J. Guzman, S. Carrettin, J.C. Fierro-Gonzalez, Y. Hao, B.C. Gates, A. Corma, Angew. Chem. Int. Ed. **44**, 4778–4781 (2005)
25. J. Guzman, B.C. Gates, J. Am. Chem. Soc. **126**, 2672–2673 (2004)
26. N. Bion, F. Epron, M. Marino, D. Duprez, Top. Catal. **51**, 76 (2008)
27. W. Deng, J.D. Jesus, H. Saltsburg, M. Flytzani-Stephanopoulos, Appl. Catal. A **291**, 126 (2005)
28. A. Gómez-Cortés, Y. Márquez, J. Arenas-Alatorre, G. Díaz, Catal. Today **133–135**, 743–749 (2008)
29. R. Zhang, T. Haddadin, D.P. Rubiano, H. Nair, C.S. Polster, C.D. Baertsch, ACS Catal. **1**, 519–525 (2011)
30. A. Sandoval, A. Gómez-Cortés, R. Zanella, G. Díaz, J.M. Saniger, J. Mol. Catal. A Chem. **278**, 200 (2007)
31. P. Panagiotopoulou, J. Papavasiliou, G. Avgouropoulos, T. Ioannides, D.I. Kondarides, Chem. Eng. J. **134**, 16–22 (2007)
32. J. Kugai, J.T. Miller, N. Guo, C. Song, Appl Catal B **105**, 306–316 (2011)
33. X. Wang, J.A. Rodriguez, J.C. Hanson, J. Chem. Phys. **123**, 221101 (2005)
34. L. Filotti, A. Bensalem, F. Bozon-Verduraz, G.A. Shafeer, V.V. Voronov, Appl. Surf. Sci. **249**, 109–110 (1997)
35. W. Shan, M. Luo, P. Ying, W. Shen, C. Li, Appl. Catal. A **246**, 1 (2003)
36. T. Takeshita, W.E. Wallace, R.S. Craig, J. Catal. **44**, 236 (1976)
37. L. González-Rovira, J.M. Sánchez-Amaya, M. López-Haro, E.d. Rio, A.B. Hungría, P. Midgley, J. Calvino, S. Bernal, F.J. Botana, Nano Lett. **4**, 1395 (2009)
38. D. Zhang, C. Pan, L. Shi, L. Huang, J. Fang, H. Fu, Microporous Mesoporous Mater. **117**, 193 (2009)

39. R. Pérez-Hernández, A. Gutiérrez-Martínez, C. Gutiérrez-Wing, *Mater. Res. Soc. Symp. Proc*, vol 127 (2010), pp. 1–4
40. D. Zhang, X. Du, L. Shi, R. Gao, Dalton Trans. **41**, 14455–14475 (2012)
41. J. Perez-Juste, I. Pastoriza-Santos, L.M. Liz-Marzan, P. Mulvaney, Coord. Chem. Rev. **249**, 1870–1901 (2005)
42. S.H. Joo, S.J. Choi, I. Oh, J. Kwak, Z. Liu, O. Terasaki, R. Ryoo, Nature **412**, 169–172 (2001)
43. T. Trindade, P. O'Brien, N.L. Pickett, Chem. Mater. **13**, 3843–3858 (2001)
44. B.C. Gates, Chem. Rev. **95**, 511–522 (1995)
45. L.N. Lewis, Chem. Rev. **93**, 2693–2730 (1993)
46. I. Balint, A. Miyazaki, K.-I. Aika, Appl. Catal. B Environ. **37**, 217–229 (2002)
47. A. Miyazaki, I. Balint, K.-I. Aika, Nakano. J. Catal. **204**, 364–371 (2001)
48. J.P. Breen, J.R.H. Ross, Catal. Today **51**, 521–533 (1999)
49. S. Ito, Y. Suwa, S. Kondo, S. Kameoka, K. Tomishige, K. Kunimori, Catal. Commun. **4**, 499–503 (2003)
50. R. Pérez-Hernández, A. Gutiérrez-Martínez, A. Mayoral, F. Leonard Deepak, M.E. Fernández-García, G. Mondragón-Galicia, M. Miki, M. Jose-Yacaman, Adv. Mater. Res. **132**, 205–219 (2010)
51. T.J. Huang, S.W. Wang, Appl. Catal. **24**, 287–297 (1986)
52. Z.F. Wang, J.Y. Xi, W.P. Wang, G.X. Lu, J. Mol. Catal. A Chem. **191**, 123–134 (2003)
53. L. Alejo, R. Lago, M.A. Peňa, J.L.G. Fierro, Appl. Catal. A Gen. **162**, 281–297 (1997)
54. J. Agrell, G. Germani, S.G. Jaras, M. Boutonnet, Appl. Catal. A Gen. **242**, 233–245 (2003)
55. M.L. Cubeiro, J.L.G.J. Fierro, J. Catal. **179**, 150–162 (1998)
56. P. López, G. Mondragón-Galicia, M.E. Espinosa-Pesqueira, D. Mendoza-Anaya, M.E. Fernández, A. Gómez-Cortés, J. Bonifacio, G. Martínez-Barrera, R. Pérez-Hernández, Int. J. Hydrog. Energy **37**, 9018–9027 (2012)
57. J.P. Sheng, C. Song, Catal. Today **77**, 89–98 (2002)
58. S. Velu, S. Velu, K. Suzuki, M. Okazaki, M.P. Kapoor, T. Osaki, F. Ohashi, J. Catal. **194**, 373–384 (2000)
59. R. Pérez-Hernández, L.C. Longoria, J. Palacios, M.M. Aguila, V. Rodríguez, Energy Mater. Mater. Sci. Eng. Energy Syst. **3**, 152–157 (2008)
60. R. Pérez-Hernández, G. Mondragón Galicia, D. Mendoza Anaya, J. Palacios, C. Angeles-Chavez, J. Arenas-Alatorre, Int. J. Hydrog. Energy **33**, 4569–4576 (2008)
61. L. Mo, A.H. Wan, X. Zheng, C.-T. Yeh, Catal. Today **148**, 124–129 (2009)
62. R. Pérez-Hernández, J.J.V. Salazar, M. José-Yacamán, J. Nano Res. **14**, 69–82 (2011)
63. C. Gutiérrez-Wing, M. Pérez-Alvarez, G. Mondragón-Galicia, J. Arenas-Alatorre, M.T. Gutiérrez-Wing, M.C. Henk, I.I. Negulescu, K.A. Rusch, J. Phys. Condens. Matter **21**, 295301 (2009)
64. Y. Sun, B. Gates, B. Mayers, Y. Xia, Nano Lett. **3**, 165–168 (2002)
65. Y. Guan, D.A.J.M. Ligthart, Ö. Pirgon-Galin, J.A.Z. Pieterse, R.A.v. Santen, E.J.M. Hensen, Top. Catal. **54**, 424 (2011)
66. K. Zhou, X. Wang, X. Sun, Q. Peng, Y. Li, J. Catal. **229**, 206–212 (2005)
67. P.V.R. Rao, V.P. Kumar, G.S. Rao, K.V.R. Chary, Cat. Sci. Technol. **2**, 1665–1673 (2012)
68. J.A. Montoya, E. Romero-Pascual, C. Gimon, P.D. Angel, A. Monzon, Catal. Today **63**, 71–85 (2000)
69. A.M. Diskin, R.H. Cunningham, R.M. Ormerod, Catal. Today **46**, 147 (1998)
70. X. Du, D. Zhang, L. Shi, R. Gao, J. Zhang, J. Phys. Chem. C **116**, 10009–10016 (2012)
71. W.-S. Dong, H.-S. Roh, K.-W. Jun, S.-E. Park, Y.-S. Oh, Appl. Catal. A **226**, 63–72 (2002)
72. H.S. Potdar, H.-S. Roh, K.-W. Jun, M. Ji, Z.-W. Liu, Catal. Lett. **84**, 95–100 (2002)
73. Y. Liu, T. Hayakawa, K. Suzuki, et al., Appl. Catal. A **223**, 137–145 (2002)
74. H. Oguchi, T. Nishiguchi, T. Matsumoto, H. Kanai, K. Utani, Y. Matsumura, S. Imamura, Appl. Catal. A **281**, 69–73 (2005)
75. T.L. Reitz, S. Ahmed, M. Krumpelt, R. Kumar, H.H. Kung, J. Mol. Catal. A Chem. **162**, 275 (2000)

76. P.P.C. Udani, P.V.D.S. Gunawardana, H.C. Lee, D.H. Kim, Int. J. Hydrog. Energy **34**, 7648–7655 (2009)
77. J. Papavasiliou, G. Avgouropoulos, T. Loannides, Catal. Commun. **5**, 231–235 (2004)
78. R. Pérez-Hernández, D. Mendoza-Anaya, A.G. Martínez, A. Gómez-Cortés, Cat-alytic steam reforming of methanol to produce hydrogen on supported metalcatalysts, in: D. Minic (Ed.), Hydrogen Energy-Challenges and Perspectives,InTech, 2012, pp. 149–174 https://doi.org/10.5772/49965
79. P.L.J. Gunter, J.W. Niemantsverdriet, F.H. Ribeiro, G.A. Somorjai, Catal. Rev. Sci. Eng. **39**, 77 (1997)
80. M. Boudart, Adv. Catal. Relat. Subj. **20**, 153 (1969)
81. H. Koga, T. Kitaoka, H. Wariishi, Chem. Commun. **43**, 5616–5618 (2008)
82. M.B. Boucher, N. Yi, F. Gittleson, B. Zugic, H. Saltsburg, M. Flytzani-Stephanopoulos, J. Phys. Chem. C **115**, 1261–1268 (2011)
83. G. Xiong, L. Luo, C. Li, X. Yang, Energy Fuel **23**, 1342–1346 (2009)
84. S.C. Yang, W.-N. Su, S.D. Lin, J. Rick, B.-J. Hwang, Cat. Sci. Technol. **2**, 807–812 (2012)
85. R. Pérez-Hernández, C. Gutiérrez-Wing, *Design of New Ag-Au(1-D)-CeO2 Catalysts for Hydrogen Production by Steam Reforming of Methanol* (EuropaCat IX, Salamanca, 2009), pp. 1–3
86. G. Mondragón-Galicia, R. Pérez-Hernández, C.E. Gutiérrez-Wing, D. Mendoza-Anaya, Phys. Chem. Chem. Phys. **13**, 16756–16761 (2011)
87. S. Imamura, S. Imamura, T. Hagashihara, Y. Saito, H. Aritani, H. Kanai, Y. Matsumura, N. Tsuda, Catal. Today **50**, 369–380 (1999)
88. S. Imamura, H. Sawada, K. Uemura, S. Ishida, J. Catal. **109**, 198–205 (1988)
89. S. Imamura, H. Yamada, K. Utani, Appl. Catal. A Gen. **192**, 221–226 (2000)
90. R. Xu, X. Wang, D. Wang, K. Zhou, Y. Li, J. Catal. **237**, 426–430 (2006)
91. M.-F. Luo, X.-X. Yuan, X.-M. Zheng, Appl. Catal. A Gen. **175**, 121–129 (1998)
92. S. Scirè, C. Crisafulli, S. Giuffrida, C. Mazza, P.M. Riccobene, A. Pistone, G. Ventimiglia, C. Bongiorno, Appl. Catal. A Gen. **367**, 138–145 (2009)
93. N. Yi, R. Si, H. Saltsburg, M. Flytzani-Stephanopoulos, Appl. Catal. B Environ. **95**, 87–92 (2010)
94. L. González-Rovira, J.M. Sánchez-Amaya, M. López-Haro, E. del Rio, A.B. Hungría, P. Midgley, J.J. Calvino, S. Bernal, F.J. Botana, Nano Lett. **9**, 1395–1400 (2009)
95. R. Pérez-Hernández et al., Phys. Chem. Chem. Phys. **15**, 12702–12708 (2013)
96. R. Pérez-Hernández et al., Catal. Today **212**, 225–231 (2013)

Chapter 9
Effective Visible Light Photodegradation of Paraoxon with Pure and Doped TiO_2

A. K. P. D. Savio, J. Fletcher, K. Smith, R. Iyer, J. Bao, and F. C. Robles Hernández

9.1 Introduction

The titanium dioxide (TiO_2) allotropes are rutile, anatase, and brookite and have the following symmetries and structures: $P4_2/mnm$ (tetragonal), $I4_1/amd$ (body centered tetragonal), and P/cab (orthorhombic), respectively. Rutile can be obtained from heat-treated anatase under different conditions [1–5]. The TiO_2 is used for photocatalysis to degrade organic and biological substances. It is also effective as a reductor for corrosion protection among its other applications [1, 3]. In recent years the sonosynthesis of TiO_2 and its doping at relatively low temperatures have been demonstrated [1, 2, 4]. The band gap in TiO_2 can be manipulated in various ways, including but not limited to heat treatments, doping, mechanical alloying, type of synthesis, purity, etc. [1–9]. Yet, doping seems to be the most effective of these listed methods. Band gap tuning is key on the catalytic and photocatalytic effectiveness of TiO_2 species [10–12]. The presented work is used to demonstrate that band gap influenced catalysis, though there are other phenomena (e.g., plasmon effect) that may be more effective for photocatalysis [4].

A. K. P. D. Savio, J. Fletcher, and K. Smith contributed equally to this work.

A. K. P. D. Savio · J. Fletcher · F. C. Robles Hernández (✉)
Department of Mechanical Engineering Technology, College of Technology,
University of Houston, Houston, TX, USA
e-mail: fcrobles@uh.edu; fcrobles@central.uh.edu

K. Smith · R. Iyer
Center for Life Sciences Technology, University of Houston, Houston, TX, USA

J. Bao
Department of Electrical and Computer Engineering, University of Houston,
Houston, TX, USA

J. M. Domínguez-Esquivel, M. Ramos (eds.), *Advanced Catalytic Materials: Current Status and Future Progress*, https://doi.org/10.1007/978-3-030-25993-8_9

The chemical paraoxon is a potent neurotoxin and has been extensively used as an insecticide. Paraoxon belongs to the class of chemical compounds called organophosphates. Most organophosphorus pesticides are vinyl ester derivatives of phosphates and have been widely used as insecticides and chemical warfare agents. The widespread use of pesticide and its accumulation in the soil have been a cause of major health concern. The organophosphate compounds are potent cholinesterase inhibitors and irreversibly bind to acetylcholinesterase (AChE) by phosphorylating the active-site serine residue and rendering it inactive [13]. Inactive AChE prevents the degradation of acetylcholine; the accumulation of acetylcholine can quickly kill by causing convulsions, brain seizures, respiratory failure, and eventually death [13]. Several methods have been used to destroy these toxic compounds, including chemical hydrolysis, incineration, and microbial enzymes. The organophosphate pesticides were heavily used in the 1970s and 1980s [14]. The relative lack of persistence in the soil can be contributed to their degradation by microbial enzymes. The potential use of these microbial enzymes for pesticide detoxification had led to an interest in developing these hydrolases and potential remediation enzymes. However, the organophosphate enzymes belong to a structurally diverse family and challenges with reusability and stability need to be addressed to use these enzymes for bioremediation purposes.This work proposes a methodology to use doped TiO_2 as a catalyst to degrade paraoxon in the presence of visible (sunlight or commercial light bulb) light sources. The TiO_2 was synthesized and doped by sonochemistry followed by heat treatments to develop material with the specific crystalline structure to enhance the catalytic nature of TiO_2. The characterization methods used in this work include X-ray diffraction (XRD), electron (transmission and scanning) microscopy, UV-vis, Raman spectroscopy, and X-ray photoelectron spectroscopy (XPS).

9.2 Experimental

9.2.1 Synthesis of Doped TiO_2

The chemicals used in this work are described in Table 9.1. Deionized water (30 mL) is added dropwise to 150 mL of titanium isopropoxide ($Ti[OCH(CH_3)_2]_4$) during sonication. The temperature in the sonicator was monitored not to exceed 40 °C. The samples were doped with 0.1 at% of Al, C, Co, Fe, and Rh. The titanium isopropoxide is poured into a flask that was submerged in room-temperature water that was stirred thoroughly to keep a temperature of 40 °C through the entire synthesis. The sonication was assisted by a Misonix S-2000 apparatus operated with micro-tip using amplitude of 100%, 20 kHz, for 30 min delivering 15 J/s. The resulting colloid was placed on a hot plate at 60 °C for 24 h. The resultant powders are TiO_2 with organic residue that was dried until they reach a loose appearance. This follows an

Table 9.1 Chemical agents used in this work with their respective purity and vendors

Name	Formula	Purity (wt%)	Vendor
Titanium isopropoxide	$Ti[OCH(CH_3)_2]_4$	97.00	Sigma Aldrich
Dopant agents			
Aluminum chloride Anhydrous, metals basis	$AlCl_3$	99.99	Sigma Aldrich
Carbon soot	C	99.99	SERES
Cobalt (III)fluoride	CoF_3	99.99	Sigma Aldrich
Iron (III) nitrate Anhydrous, trace metal basis	$Fe(NO_3)_3$	99.99	Sigma Aldrich
Rhodium (III) nitrate ~36 wt% rhodium	$Rh(NO_3)_3$	99.99	Sigma Aldrich
Pesticide			
Paraoxon	$O_2NC_6H_4OP(O)(OC_2H_5)_2$	98.9	Supelco
Acetonitrile	C_2H_3N	99.5	Fluka
CSM: Carbon-selective media (prepared in lab, sterilized by autoclave)	MilliQ H_2O	94.5 mL	
	1 M NTA	200 µL	Sigma Aldrich
	20% (w/v) $MgSO_4$ $7H_2O$	100 µL	Sigma Aldrich
	4% (w/v) $CaNO_3$		
	0.5% (w/v) $FeSO_4$ $6H_2O$	100 µL	Sigma Aldrich
	Phosphate buffer solution (stock solution)	100 µL 5 mL	Sigma Aldrich Sigma Aldrich

organic residue removal by deionized water washing that is repeated five times. Each washing is accompanied by draining on micropore filter paper connected to a vacuum system via funnel flask. After the last washing procedure the powders are dried using the process described above.

9.2.2 Heat Treatment

The heat treatments were monitored via thermal analysis using a workstation consisting of a high-speed-high-resolution National Instruments data acquisition system (cFP 1804, Austin, TX) and a personal computer. The cFP 1804 data was connected to a battery of eight thermocouples that can be controlled remotely. The data collection is set to ten readings per second. Thermal analysis is used to determine the exact transition temperatures for TiO_2 following the procedures proposed by Robles-Hernandez et al. [15–17]. The pure and doped TiO_2 (Al, Co, Fe, and Rh) were heat treated at temperatures from 100 °C to 800 °C in a tube electric resistance furnace. All but C-doped samples were heat treated in air atmosphere for 12 h. Heat treatments for C-doped samples were conducted in helium at 100 torr to prevent interaction among carbon and oxygen.

9.2.3 Characterization

The XRD characterization was conducted on a SIEMENS Diffractometer D5000 equipped with a Cu tube and operated at 40 kV and 30 A with a corresponding $K_{\alpha} = 0.15406$ nm. The scanning electron microscopy (SEM) observations were carried out on a FEI XL-30FEG using a 15 kV in secondary electron mode. The samples were prepared depositing the powders directly on graphite tape and coated with gold. High-resolution transmission electron microscopy (HRTEM) samples were prepared by adding a pinch of powder on to a 3 mL of ethanol. The solution was sonicated for 1 min to form a suspension that was allowed to sediment until the liquid has a clear appearance. At that time two drops of the suspension were deposited on a Cu grid (300 mesh). The HRTEM was conducted on a JEOL 200 FX operated at 200 kV.

Raman spectroscopy was conducted on an XploRA™ apparatus, using a green laser (532 nm) on medium intensity and a shift of 1 cm^{-1}, a spot size of 1 μm, and a resolution of 0.5 cm^{-1}. Optical spectroscopy characterization was conducted using a Triax 320 monochromator in transmission mode equipped with a broad-spectrum xenon lamp and a UV-enhanced Si photodetector. The spectral measurements were performed using the diffused reflectance method in a wavelength range between 250 and 500 nm. The band gaps were determined with the Kubelka-Munk method [18]. The samples for Raman and optical spectroscopy were prepared by adding 0.01 g of each powder in 10 mil of deionized water. The mix was subjected to sonication for 10 min using an intensity of 15 J/s. The suspension was deposited on fuse silica glasses (4 mm in diameter) using a spinning-like approach followed by a drying procedure on a hot plate at 60 °C for 2 h. The process was repeated five times to thicken the film and obtain representative values.

The X-ray photoelectron spectroscopy (XPS) was conducted on a Physical Electronics XPS Instrument Model 5700. The XPS was operated via monochromatic Al-K_{α} X-ray source (1486.6 eV) at 350 W. The analyzed area, collection solid cone, and takeoff angle were set at 800 μm, 5°, and 45°, respectively. A pass energy of 11.75 eV was used to obtain a resolution of 0.51 eV or better. The XPS was conducted in a vacuum below 5×10^{-9} torr. The data analysis was conducted on Multipak™ software and the Shirley background subtraction routine had been applied throughout.

9.2.4 Degradation

Pure TiO_2 and doped TiO_2 were subjected to hydrolysis of the organophosphate compound paraoxon under sunlight and a commercial light bulb-assisted radiation. For simplicity the light bulb-assisted method will be identified in this manuscript as "assisted method." The experiment set was prepared using the minimal media, carbon-supplemented media (CSM). The pure and doped (C, Co, Fe, and Rh) TiO_2

were added to sterile 14 mL Flacon tubes at weights of 0.01, 0.04, 0.06, 0.07 and 0.08 g, followed by the addition of 10 mL of sterile CSM. To each sample tube 30 uL of paraoxon (100 mg/mL) was added; the tubes were then sealed and vortexed for 10 s. A metal powder control was made with 0.50 g of each respective metal powder and 10 mL of CSM (no pesticide addition). A paraoxon control was prepared with 10 mL of CSM and 30 μL of paraoxon (no TiO_2 additions). The sample set (with controls) was then placed in peg rack to allow for increased light exposure. The rack was then placed under the assisted radiation in a light box or placed on the counter to allow sunlight exposure. The temperature was measured during the experiments (approx. 29 °C) via K-thermocouple. A 500 μL aliquot was taken from each tube at different times. The aliquot was centrifuged at 13,400 rpm for 2 min at room temperature. The supernatant was then read by plate spectrophotometry at 200 μL per well (in duplicate) at a broad spectra range of 230–1000 nm.

9.3 Results

9.3.1 Materials: Synthesis and Characterization

Figure 9.1 shows the XRD and microscopic characterization of the pure TiO_2 in the as-synthesized and heat-treated conditions. The XRD results indicate that the as-synthesized product is quasi-amorphous and transform to anatase at relatively low temperatures [4]. The diffraction pattern at 300 °C shows the presence of pure anatase. The transformation to rutile is initiated at a temperature above 300 °C and completed at around 500 °C depending on the dopant. The samples were heat treated at temperatures as high as 800 °C to investigate their band gap, coarsening behavior, and phase transformation(s). Our observations indicated that the most appropriated characteristics for this work were identified when the materials were heat treated at 300 °C allowing the synthesis of pure anatase and preventing coarsening. The SEM micrographs show the effects of heat treatment in the macrostructure of the TiO_2 particles. From the SEM micrograph it is evident that the particles coarsen and become denser. The as-synthesized material is a quasi-amorphous phase with non-equilibrium stoichiometries and it is likely that it is the lack of oxygen with broken bonds that results in the wide reflections observed by XRD (Fig. 9.1a).

In Fig. 9.2 is presented the Raman spectroscopy analysis of the doped TiO_2 in the as-synthesized and heat-treated conditions. The as-synthesized C- and Co-doped samples present intense $E_{g(1)}$ and $E_{g(2)}$ Raman bands, respectively. We presume that the high intensity of the $E_{g(1)}$ band in the Co-doped sample is well resolved due to a short- to mid-range order [4]. The local nano-stoichiometry is strongly affecting the C-doped characteristics as observed in the Raman results that is due to phonon confinement effects on the $E_{g(1)}$ and $E_{g(2)}$ bands resulting in anomalies related to hydrostatic pressures [19]. We believe that the $E_{g(2)}$ band at 193 cm^{-1} (usually weak [20]) is well resolved and sharp in our case by the presence of interstitial C atoms that interact with the lattice building up hydrostatic stresses.

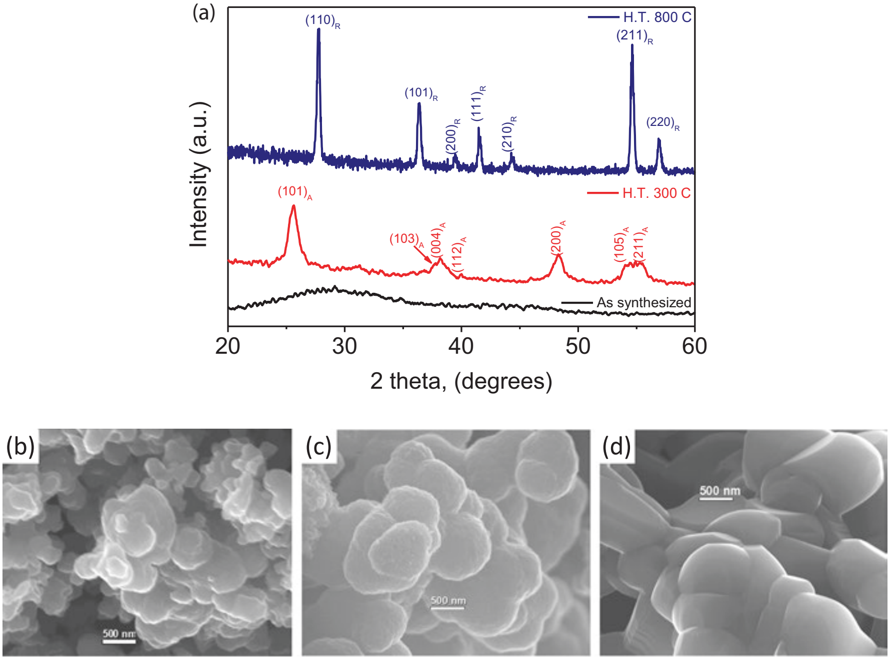

Fig. 9.1 (**a**) XRD and (**b**–**d**) scanning electron micrographs of the pure TiO_2 (undoped) in the (**b**) as-synthesized and (**c**, **d**) heat-treated conditions: (**c**) 300 °C and (**d**) 800 °C

Other identifiable Raman bands in Fig. 9.2 for anatase are E_g, B_{1g}, and the doublet A_{2g}. The E_g mode is identified by three bands (151, 193, and 630 cm^{-1}), while the B_{1g}, A_{1g}, and B_{1g} are at 400, 508, and 512 cm^{-1}, respectively [21]. None of the other bands are well resolved in any of the as-synthesized samples. When anatase is nanostructured the E_g band shows a red shift (from 144 cm^{-1}) that is in agreement with our current and previous work [22, 23]. In this work is observed that this shift in the Co-doped sample corresponds to particles with grain sizes of ~5 nm that agrees with our previous work [1, 2]. The heat treatment conditions were selected based on their effect on band gap. For instance, the heat-treated TiO_2 at low temperatures (below 300–400 °C) has a single-phase framework composed of anatase. At higher temperatures (above 500 °C) all samples transform to rutile. This is important because there are clear changes in band gap in samples with single-phase frameworks [4].

Figure 9.3 illustrates the band gap values for sono-synthesized samples for the pure TiO_2 and doped for different heat treatment temperatures. The values reported for the band gap herein are comparable to those reported in our previous work (2.8 eV [4]) and lower to those from commercial sources (3.0–3.2 eV [24]). The pure sample after heat treatment shows a widening effect on its band reaching values similar to those reported for commercial anatase. The increase in band gap is

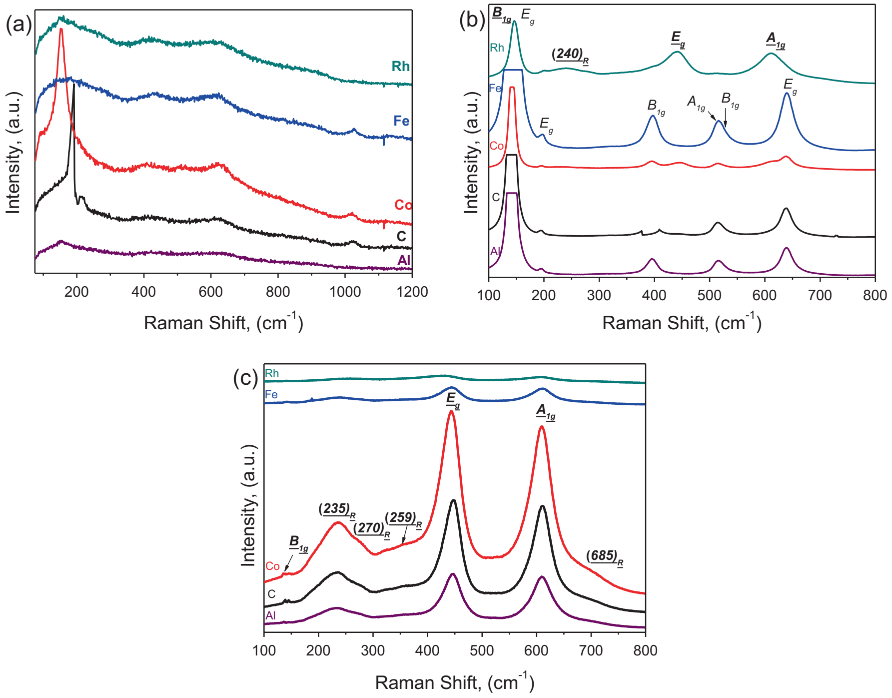

Fig. 9.2 Raman spectroscopy of the (**a**) as-synthesized and doped materials along with the (**b**, **c**) heat-treated ones at (**b**) 300 °C and (**c**) 800 °C. Note the spectra evolution from the quasi-amorphous material (**a**) to the synthesis of anatase followed by rutile for the as-synthesized and heat-treated conditions, respectively

attributed to the development of a dual-phase framework between anatase and rutile. It is of further interest to mention that heat treatment samples from 100 to 600 °C show an almost constant band gap. This range of temperature is characteristic of a dual-phase framework. After that the material transforms completely to rutile and the band gap shows significant changes depending on the dopant. The values of the band gap vary from 2.78 to 3.75 eV; the later value is comparable to that reported for rutile [25, 26]. Rh is to be effective to narrow the band gap.

In Fig. 9.3 is observed that Co and Al doping does not seem to have clear effect on band gap, except when heat treated above 600 °C. Opposite is the case for samples doped with Fe and C with respective band gaps of 3.94 and 4.17 eV. The band gap changes for the Fe-doped samples between 200 (3.69 eV) and 300 °C (3.67 eV) are directly attributed to phase transformations in the iron oxides at those temperatures; further details are available in [4, 27, 28]. Once the C-doped sample is heat treated between 100 and 600 °C its band gap decreases and is relatively constant at 3.27 ± 0.11 eV; above those temperatures the sample reaches values similar to those observed in rutile.

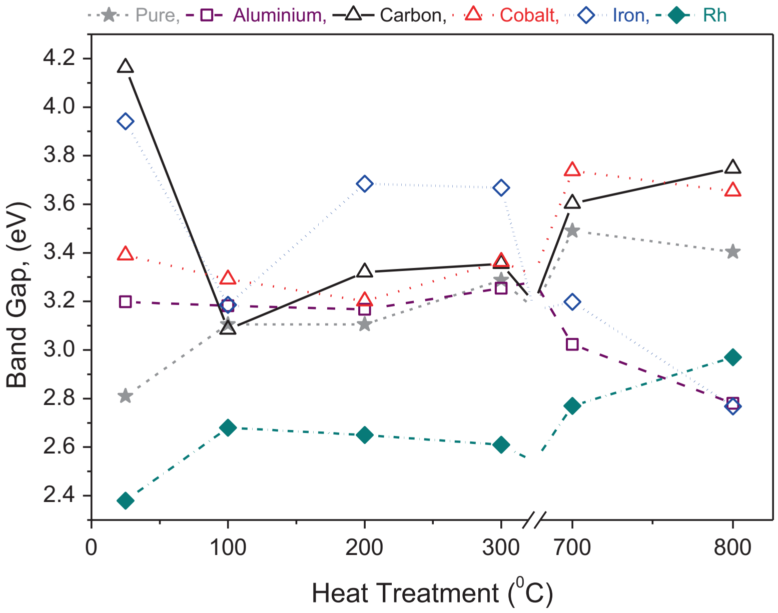

Fig. 9.3 Band gap results of the as-synthesized and heat-treated TiO_2 doped with various elements

9.3.2 Catalysis: Chemical Principles

Figure 9.4 shows the degradation sequence of paraoxon by the catalytic effect of doped TiO_2. The degradation is initiated by the degradation of paraoxon into the p-nitrophenol and diethyl phosphate (DEP). This degradation is important because the resultant products reduce its toxicity by two orders of magnitude or more [29]. In this work the catalytic degradation of paraoxon is measured by the quantification of *p*-nitrophenol via spectrometer. The degradation of the *p*-nitrophenol is the second step in the catalysis presented herein. This degradation can occur following two paths, by breaking into benzoquinone or hydroquinone that is less toxic substance [30]. This degradation is being investigated by means of enzymes, bacteria ozone, and UV light [29, 30]. In this work we demonstrate that TiO_2 is also effective to degrade paraoxon rapidly and in the presence of sunlight.

9.3.3 Catalysis: Degradation of Paraoxon

In the first set of experiments the degradation of paraoxon was conducted in the absence of TiO_2. As seen from Fig. 9.5 any changes in the absence of CSM are untraceable even after 6 days of exposure to sunlight. Those experiments are used

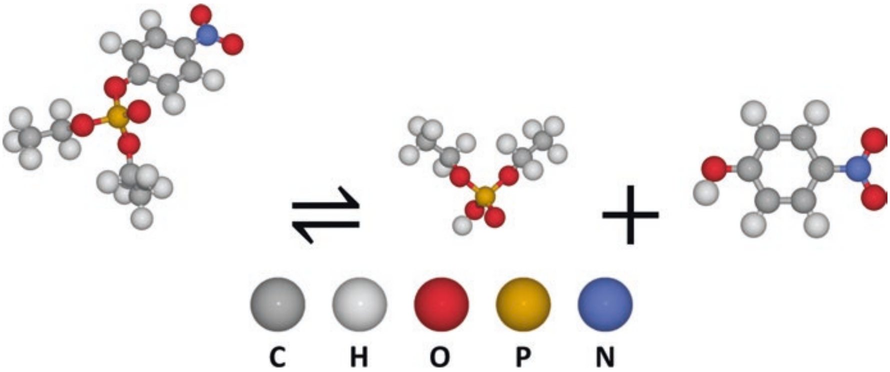

Fig. 9.4 Sketch of the chemical degradation of paraoxon onto *o*,*o*-diethylphosphate + *p*-nitrophenol by the catalytic effect of the doped TiO_2

to demonstrate the effectiveness on traceability of the degraded species (*p*-nitrophenol) of paraoxon (Fig. 9.5). It is important to clarify that in both experiments the degradation is taking place; however, it is only traceable when CSM is present. Further, the degradation traced in Fig. 9.5b occurs in a cumulative fashion in the first 3 days. After that the concentration and intensity of the degraded products decrease that may be attributed to a reverse reaction.

The results of adding 0.05 g of pure TiO_2 to the solutions with paraoxon and CSM and exposure to sunlight and the assisted method are presented in Fig. 9.6. From this figure it is apparent that both methods have different effects. The sunlight radiation has a continuous degradation effect after 6 days of exposure on paraoxon and this effect is clearer when compared to sunlight alone (Fig. 9.5b). In the assisted method (Fig. 9.6b) the degradation is enhanced. After 2 days of exposure the intensity reaches a higher value than that observed in Fig. 9.6a after 6 days. However, after the third day the intensity of the degraded species decays, which we attribute to a secondary degradation of the present species.

Figure 9.8a–f shows the degradation results of paraoxon in the presence of TiO_2 in the assisted method. This experiment was conducted using different additions of catalyst ranging from 0.01 to 0.08 g. The “control” sample has 0.5 g of pure TiO_2. These samples were tested under both methods for approximately 10 h starting in the morning and stopping in the evening, when the sunlight still has clarity. The sunlight is effective in degrading the paraoxon after exposure using 0.6–0.8 g of the Co-doped TiO_2. Samples tested in the assisted method show degradation even in smaller amounts of the catalyst (0.4 g). Furthermore, the use of 0.1 g of Co-doped TiO_2 does not seem to be effective to degrade paraoxon. This allows us to conclude that both the amount of catalyst and the light source have a direct effect on degradation effectiveness (Fig. 9.7).

In Fig. 9.8 only the results of paraoxon degradation using 0.08 g of catalyst are presented since they seem to be the most efficient. As seen in Fig. 9.8a–d the Co-doped TiO_2 seems to be the most effective catalyst. In 1 day the degradation of

Fig. 9.5 Results of a reference sample (**a**) with paraoxon in the absence of CSM (control) and (**b**) with paraoxon and CSM, both in the absence of TiO_2 exposure to sunlight for up to 6 days

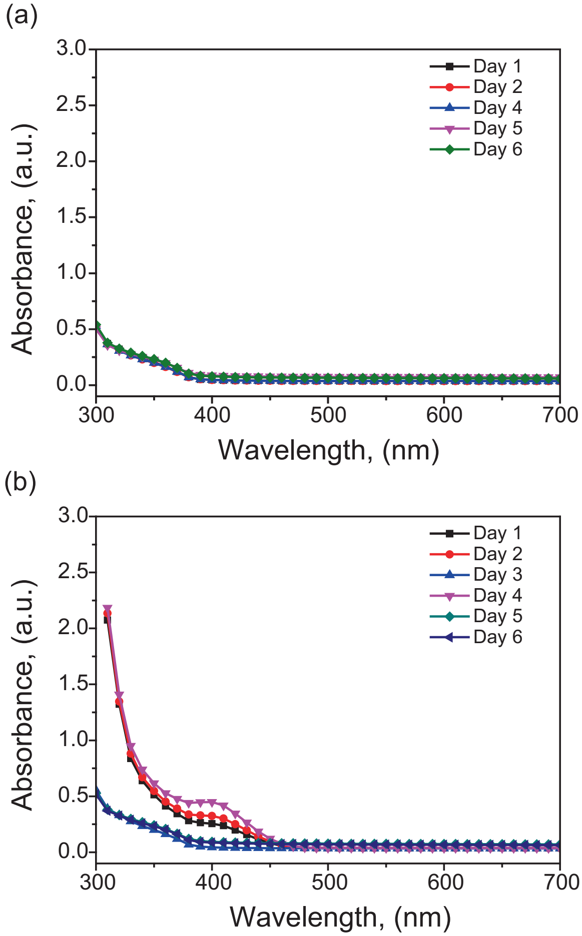

the paraoxon seems to be almost completed and it is completed by the second day. After the fourth day the presence of the degraded species seems again untraceable. In this case we attribute this effect to a second degree of degradation where the p-nitrophenol decomposes into p-benzoquinone or hydroquinone [31–33]. Further test is required to demonstrate the second degree of degradation.

Once the catalytic activity of the Co-doped TiO_2 is completed and a possible second degradation is occurring, the effect of Fe-doped TiO_2 becomes more evident (see Fig. 9.8a–f). This effect is observed after the first day, but it is until the second day when it clearly demonstrates to be the second most active catalyst. The Fe-doped TiO_2 has a rather steady reactivity during the third and fourth days and after the fifth day it is the dominant catalyst. The Rh-doped TiO_2 is also active from the first day; however, its efficiency is not like that observed in Fe-doped TiO_2 and Co-doped TiO_2. After the fourth day the traceability of *p*-nitrophenol is negligible in all cases but Fe-doped TiO_2 and Rh-doped TiO_2.

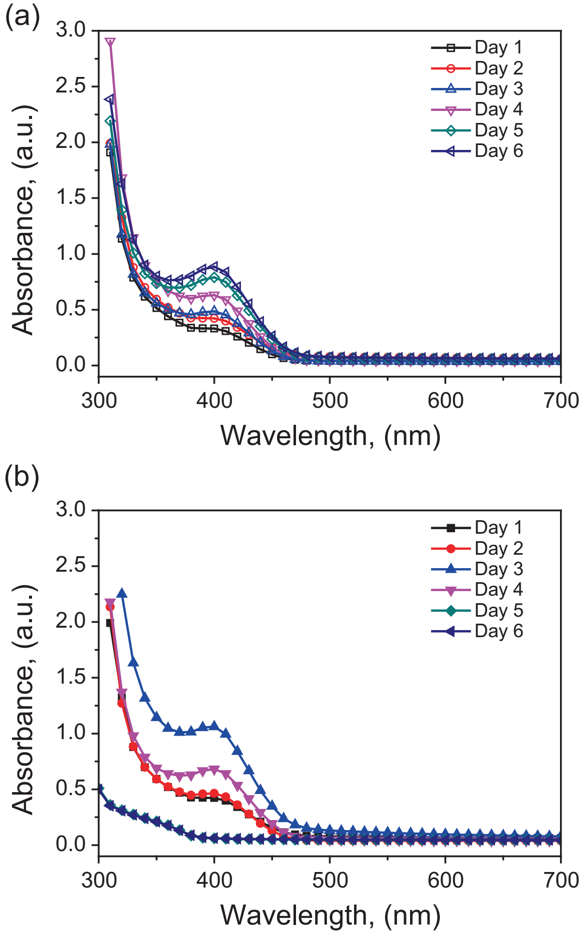

Fig. 9.6 Results of catalytic effects of pure TiO_2 on paraoxon under (**a**) sunlight and (**b**) UV-lamp conditions

All the tested catalysts, including pure TiO_2, are effective to degrade the paraoxon, but Fe and Co doped are the most effective. The Pt- and Rh-doped TiO_2 are usually reported as effective photocatalysts [34]; however, in our research we demonstrate that Co-doped TiO_2 has tremendous advantages. We did not observe clear advantages between C-doped TiO_2 and pure TiO_2. Further, the Rh-doped TiO_2 is effective over longer time periods. The use of pure TiO_2 for water purification and the removal of pesticides have been previously demonstrated [33, 35]. This work shows the positive effects of doping TiO_2 in particular with Fe and Co, both of which are commercial and affordable products.

The Co-doped TiO_2 experiments were conducted using 0.07 and 0.08 g of catalyst due to their clear effectiveness. Using 0.01 and 0.04 g similar effects were observed but in longer times (Fig. 9.9). Figure 9.9 shows that after 30 min the Co-doped TiO_2 starts degrading the paraoxon and *p*-nitrophenol is clearly measurable. The maximum reactivity in the examples presented in Fig. 9.9 takes place after

Fig. 9.7 Catalytic effectiveness of Co-doped TiO_2 additions exposed to (**a**) sunlight and (**b**) light bulb-assisted method for a 10 h of treatment

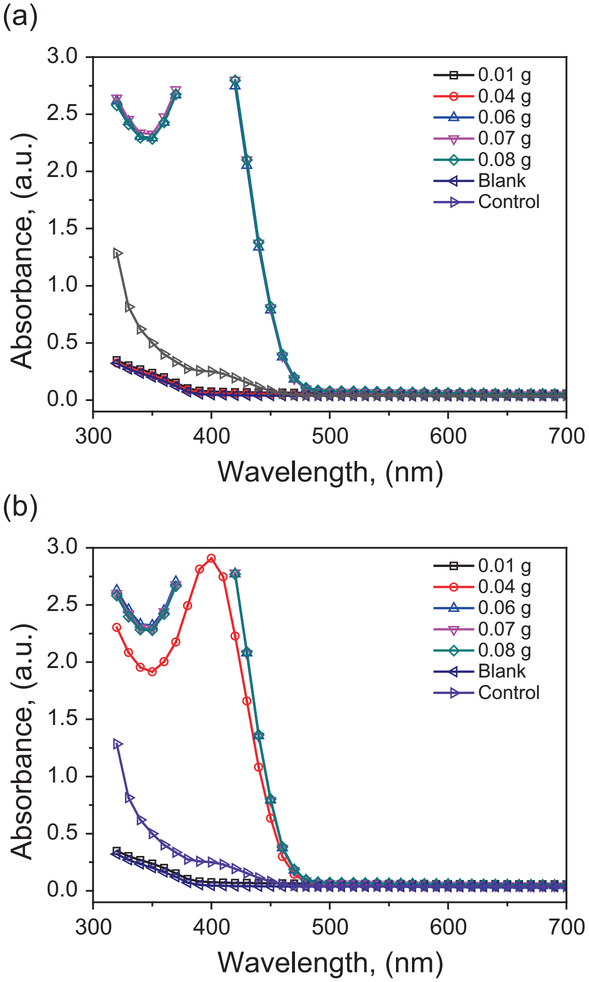

27 h and the difference among 0.07 and 0.08 g is also clear, but minor. Additionally, the results in Fig. 9.9 are in full agreement with those results presented in Fig. 9.8 and clearly complement the observations. The other catalysts were not tested at short times since they are not as efficient as the TiO_2-Co doped. In Fig. 9.9c are presented the results of varying the amounts of dopant from 0.04 to 0.08 g under sunlight. The amounts of 0.04 g of Co-doped TiO_2 have negligible effects to degrade paraoxon or may require significantly longer times.

Figure 9.10 depicts the resultant vials after the catalytic analysis for both sunlight and assisted method. From those vials it is clear that in the absence of CSM there is no possibility to measure the degree of degradation of paraoxon (Fig. 9.10f). On the contrary, all of the catalysts have a clear effect on the paraoxon degradation. The yellow color is a direct indication of the presence of the subspecies (namely

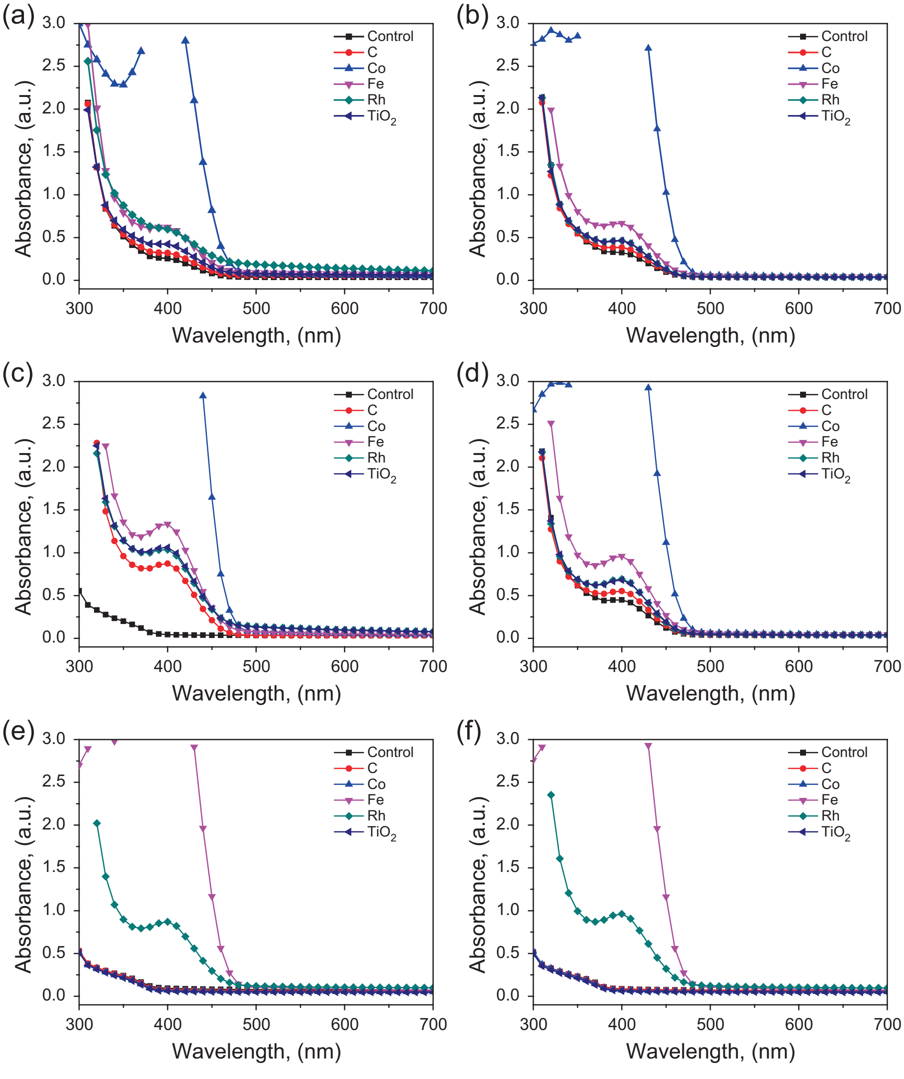

Fig. 9.8 Results of catalytic effects of pure TiO_2 and doped TiO_2 doped with C, Co, Fe, and Rh subjected to UV-lamp conditions for different times: (**a**) 1 day, (**b**) 2 days, (**c**) 3 days, (**d**) 4 days, (**e**) 5 days, (**f**) 6 days

p-nitrophenol) after degradation. It is also of interest to see that the degradation in the assisted method is evident, but sunlight is enough to degrade the paraoxon. As seen in previous figures, sunlight is also effective, but required longer times. A major finding, herein, is the fact that Co-doped TiO_2 is effective to degrade paraoxon under either sunlight or assisted method. This is of interest because this compound has a bandgap of 3.2 ± 0.1 eV that is equivalent to a wavelength of 390 nm and falls in the visible light ranges (blue and near UV). On the contrary

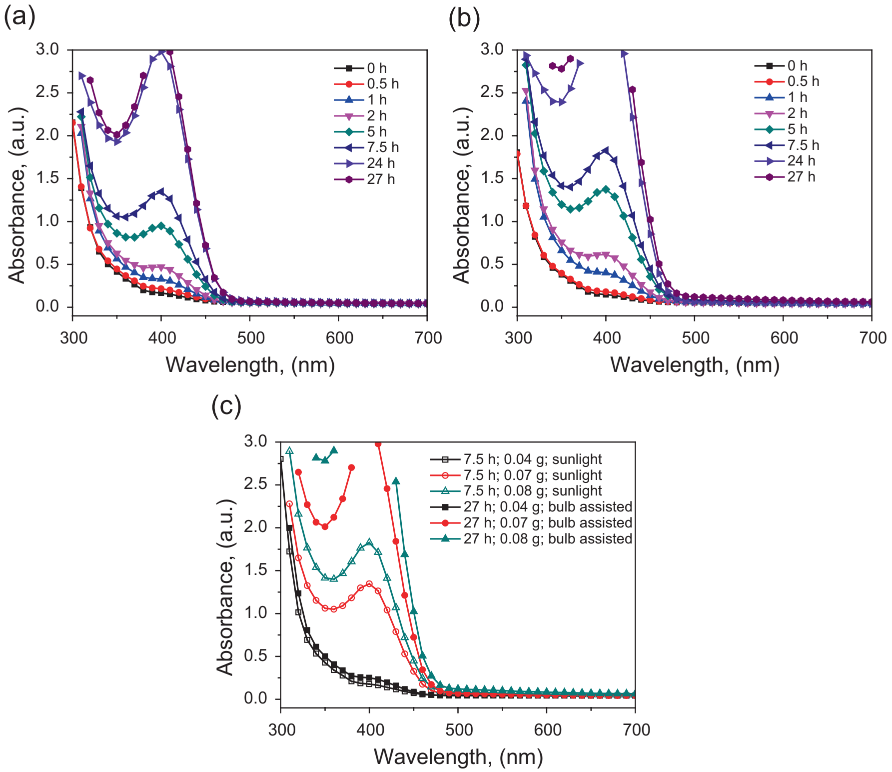

Fig. 9.9 Results of catalytic effects of cobalt-doped TiO_2 in short times using different amounts of catalyst and sunlight radiated: (**a**) 0.7 g and (**b**) 0.8 g, (**c**) effect of catalyst content on photodegradation of paraoxon at 7.5 h and 27 h

the Rh-doped TiO_2 has a band gap of 2.6 ± 0.1 eV (480 nm) and should be more effective than Co-toped TiO_2. This agrees with the idea of a degradation effect assisted by a plasmonic phenomenon that is further demonstrated with the presence of the decorating nano q-dots over the TiO_2 as seen in Fig. 9.10g.

9.4 Conclusions

In this work it is demonstrated that paraoxon can be degraded to less toxic substances using TiO_2. The importance of this catalytic demonstration is to prove that sunlight radiation is effective in degrading paraoxon with the proper dopant. In this work it is demonstrated that doping with Rh is more effective to decrease the band gap; however, Fe- or Co-doped TiO_2 is a more effective catalyst to degrade paraoxon. This phenomenon is attributed to the presence of q-dots that precipitate along the surface of the TiO_2 forming plasmonic sites that enhance the catalytic effectiveness of TiO_2. The investigated catalysts are able to degrade paraoxon using sunlight.

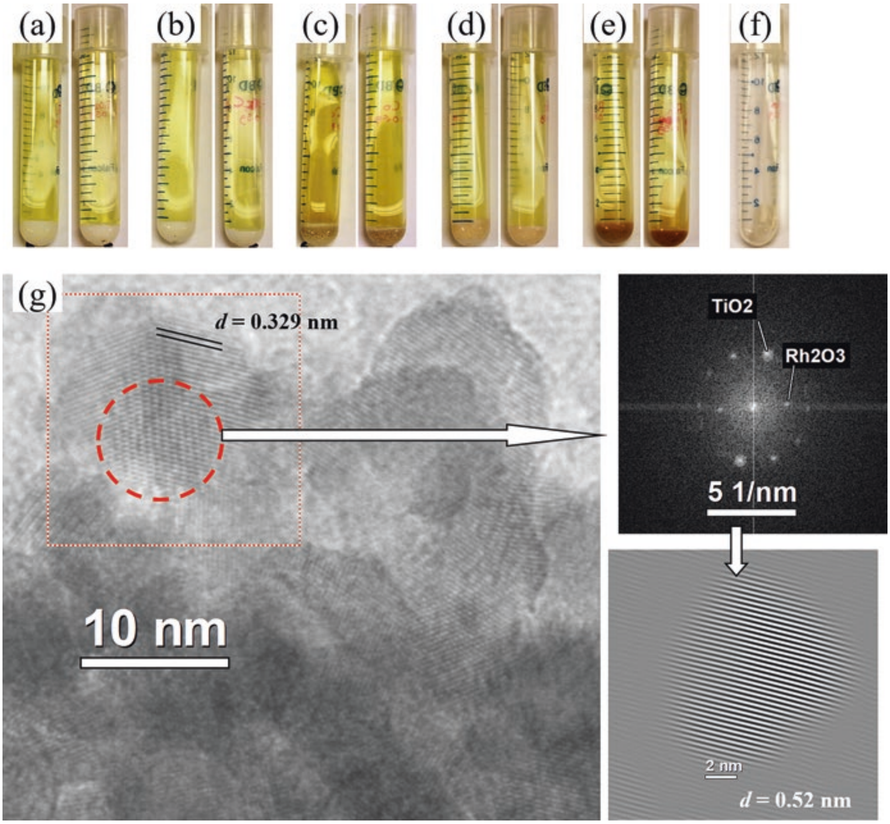

Fig. 9.10 Pictures of the vials used in the catalysis degradation of paraoxon after 6 days of treatment. The vials correspond to those exposed to the artificial light (lamp) and sunlight. The above images correspond to (**a**) pure, (**b**) C-doped, (**c**) Co-doped, (**d**) Fe-doped, (**e**) Rh-doped, (**f**) Co-doped without CSM, (**g**) HRTEM of the Rh-doped TiO_2 showing a particle of TiO_2 (dotted square) and a Rh_2O_3 (dotted circle). The insets on the right of (**g**) are used to filter the exact particle and measure the lattice constant with higher precision. The same procedure was used for TiO_2

Acknowledgements The authors would like to thank the University of Houston and the State of Texas for their invaluable support through the Star Up, Small grant, and HEAFS funding. The authors would like to thank Dr. L. Grabow and his student H. Doan for the molecular models in Fig. 9.4.

References

1. F.C. Robles Hernandez, L. Gonzalez-Reyes, I. Hernandez-Perez, Effect of coarsening of sonochemical synthesized anatase on BET surface characteristics. Chem. Eng. Sci. **66**(4), 721–728 (2011)
2. L. Gonzalez-Reyes, I. Hernandez-Perez, F.C.R. Hernandez, H.D. Rosales, E.M. Arce-Estrada, Sonochemical synthesis of nanostructured anatase and study of the kinetics among phase

transformation and coarsening as a function of heat treatment conditions. J. Eur. Ceram. Soc. **28**(8), 1585–1594 (2008)

3. U. Diebold, The surface science of titanium dioxide. Surf. Sci. Rep. **48**(5–8), 53–229 (2003)
4. A.K.P.D. Savio, J. Fletcher, F.C. Robles Hernández, Sonosynthesis of nanostructured TiO_2 doped with transition metals having variable bandgap. Ceram. Int. **39**(3), 2753–2765 (2013)
5. A.K.P.D. Savio, D. Starikov, A. Bensaoula, R. Pillai, L.L.D. Garcia, F.C.R. Hernandez, Tunable TiO_2 (anatase and rutile) materials manufactured by mechanical means. Ceram. Int. **38**(5), 3529–3535 (2012)
6. M.R. Hoffmann, S.T. Martin, W.Y. Choi, D.W. Bahnemann, Environmental applications of semiconductor photocatalysis. Chem. Rev. **95**(1), 69–96 (1995)
7. A. Fujishima, X.T. Zhang, Titanium dioxide photocatalysis: present situation and future approaches. C. R. Chim. **9**(5–6), 750–760 (2006)
8. J.H. Braun, Titanium dioxide—a review. J. Coating Technol. **69**(868), 59–72 (1997)
9. S. Ito, S. Inoue, H. Kawada, M. Hara, M. Iwasaki, H. Tada, Low-temperature synthesis of nanometer-sized crystalline TiO_2 particles and their photoinduced decomposition of formic acid. J. Colloid Interf. Sci. **216**(1), 59–64 (1999)
10. M. Hirano, C. Nakahara, K. Ota, M. Inagaki, Direct formation of zirconia-doped titania with stable anatase-type structure by thermal hydrolysis. J. Am. Ceram. Soc. **85**(5), 1333–1335 (2002)
11. A.J. Maira, K.L. Yeung, C.Y. Lee, P.L. Yue, C.K. Chan, Size effects in gas-phase photo-oxidation of trichloroethylene using nanometer-sized TiO_2 catalysts. J. Catal. **192**(1), 185–196 (2000)
12. C.K. Chan, J.F. Porter, Y.G. Li, W. Guo, C.M. Chan, Effects of calcination on the microstructures and photocatalytic properties of nanosized titanium dioxide powders prepared by vapor hydrolysis. J. Am. Ceram. Soc. **82**(3), 566–572 (1999)
13. S. Singh, N. Sharma, Neurological syndromes following organophosphate poisoning. Neurol. India **48**(4), 308–313 (2000)
14. X.H. Xu, A.B. Dailey, E.O. Talbott, V.A. Ilacqua, G. Kearney, N.R. Asal, Associations of serum concentrations of organochlorine pesticides with breast cancer and prostate cancer in US adults. Environ. Health Persp. **118**(1), 60–66 (2010)
15. F.C. Robles Hernandez, J.H. Sokolowski, Thermal analysis and microscopical characterization of Al-Si hypereutectic alloys. J. Alloy Compd. **419**(1–2), 180–190 (2006)
16. F.C. Robles Hernandez, J.H. Sokolowski, Effects and on-line prediction of electromagnetic stirring on microstructure refinement of the 319 Al-Si hypoeutectic alloy. J. Alloy Compd. **480**(2), 416–421 (2009)
17. F.C. Robles Hernandez, J.A. Neal, U.S. Aldea, Thermal characterization of poultry for the development of a comprehensive device to monitor safety and proper coking. J. Food Process Eng. **36**, 2 (2013)
18. M.A. Zanjanchi, H. Noei, M. Moghimi, Rapid determination of aluminum by UV-vis diffuse reflectance spectroscopy with application of suitable adsorbents. Talanta **70**(5), 933–939 (2006)
19. T. Ohsaka, S. Yamaoka, O. Shimomura, Effect of hydrostatic-pressure on the Raman-spectrum of anatase (TiO_2). Solid State Commun. **30**(6), 345–347 (1979)
20. V. Swamy, Size-dependent modifications of the first-order Raman spectra of nanostructured rutile TiO(2). Phys. Rev. B **77**(19), 195414 (2008)
21. U. Balachandran, N.G. Eror, Raman-spectra of titanium-dioxide. J. Solid State Chem. **42**(3), 276–282 (1982)
22. P.P. Lottici, D. Bersani, M. Braghini, A. Montenero, Raman-scattering characterization of gel-derived titania glass. J. Mater. Sci. **28**(1), 177–183 (1993)
23. A.K.P.D. Savio, D. Starikov, A. Bensaoula, R. Pillai, L.L. de la Torre García, F.C. Robles Hernández, Tunable TiO_2 (anatase and rutile) materials manufactured by mechanical means. Ceram. Int. **38**, 3529–3535 (2012)
24. T.P. Ang, J.Y. Law, Y.F. Han, Preparation, characterization of sulfur-doped nanosized TiO(2) and photocatalytic degradation of methylene blue under visible light. Catal. Lett. **139**(1–2), 77–84 (2010)

25. A. Amtout, R. Leonelli, Optical properties of rutile near its fundamental band gap. Phys. Rev. B Condens. Matter **51**(11), 6842–6851 (1995)
26. L. González-Reyes, I. Hernández-Pérez, L. Díaz-Barriga Arceo, H. Dorantes-Rosales, E. Arce-Estrada, R. Suárez-Parra, J.J. Cruz-Rivera, Temperature effects during Ostwald ripening on structural and bandgap properties of TiO_2 nanoparticles prepared by sonochemical synthesis. Mater. Sci. Eng. B **175**(1), 9–13 (2010)
27. A.K.P.D. Savio, Characterization protocol for titanium dioxide (anatase: rutile) use for photocatalytic applications, in: *Mechanical Engineering Technology*, Master of Science, University of Houston, Houston, 2011, pp. 158
28. S. Franger, P. Berthet, O. Dragos, R. Baddour-Hadjean, P. Bonville, J. Berthon, Large influence of the synthesis conditions on the physico-chemical properties of nanostructured Fe_3O_4. J. Nanopart. Res. **9**(3), 389–402 (2007)
29. S.V. Dzyadevych, A.P. Soldatkin, J.M. Chovelon, Assessment of the toxicity of methyl parathion and its photodegradation products in water samples using conductometric enzyme biosensors. Anal. Chim. Acta **459**(1), 33–41 (2002)
30. W. Kitagawa, N. Kimura, Y. Kamagata, A novel p-nitrophenol degradation gene cluster from a gram-positive bacterium, Rhodococcus opacus SAO101. J. Bacteriol. **186**(15), 4894–4902 (2004)
31. Y.L. Zheng, D.L. Liu, H. Xu, Y.L. Zhong, Y.Z. Yuan, L. Xiong, W.X. Li, Biodegradation of p-nitrophenol by Pseudomonas aeruginosa HS-D38 and analysis of metabolites with HPLC-ESI/MS. Int. Biodeterior. Biodegradation **63**(8), 1125–1129 (2009)
32. Y.L. Zheng, D.L. Liu, S.W. Liu, S.Y. Xu, Y.Z. Yuan, L. Xiong, Kinetics and mechanisms of p-nitrophenol biodegradation by Pseudomonas aeruginosa HS-D38. J. Environ. Sci. (China) **21**(9), 1194–1199 (2009)
33. J. Senthilnathan, L. Philip, Removal of mixed pesticides from drinking water system using surfactant-assisted nano-TiO_2. Water Air Soil Poll. **210**(1–4), 143–154 (2010)
34. C.T. Williams, K.Y. Chen, C.G. Takoudis, M.J. Weaver, Reduction kinetics of surface rhodium oxide by hydrogen and carbon monoxide at ambient gas pressures as probed by transient surface-enhanced Raman spectroscopy. J. Phys. Chem. B **102**(24), 4785–4794 (1998)
35. J. Senthilnathan, L. Philip, Removal of mixed pesticides from drinking water system by photodegradation using suspended and immobilized TiO_2. J. Environ. Sci. Health B **44**(3), 262–270 (2009)

Chapter 10
Ternary-Phase NiMoWS$_2$ Catalytic Material for Hydrodesulfurization

Brenda Torres, Lorena Alvarez-Contreras, Daniel Bahena-Uribe, Russell R. Chianelli, and Manuel Ramos

10.1 Introduction

Until nowadays, a continuous search for catalytic materials that are of high performance and are stable under industrial reaction conditions of hydro-processing remains a current activity by many research groups around the world. The main target is to achieve a catalytic material efficient enough for removal of heterogeneous atoms that are contained in crude oil refinement production of high-quality liquid fuels. As demanded by environmental legislation and regulations, one main component of that regulation is to achieve a sulfur content reduction from 50 to 10 ppm by 2020 mainly in automobile fuels [1]. One industrial scientific-based approach for hydro-processing crude oil has been the usage of transition metal sulfide catalytic materials due to its high stability at high pressures and temperatures,

---

B. Torres (✉) · R. R. Chianelli
Department of Chemistry and Biochemistry, University of Texas at El Paso,
El Paso, TX, USA
e-mail: btorres2@utep.edu; chianell@utep.edu

L. Alvarez-Contreras
Laboratorio Nacional de Nanotecnología, Centro de Investigación en Materiales Avanzados
S.C., Chihuahua, Mexico
e-mail: lorena.alvarez@cimav.edu.mx

D. Bahena-Uribe
Laboratorio Avanzado de Nanoscopía Electrónica, CINVESTAV, Ciudad de México, Mexico
e-mail: dbahenau@cinvestav.mx

M. Ramos
Departamento de Física y Matemáticas, Universidad Autónoma de Ciudad Juárez,
Chihuahua, Mexico
e-mail: manuel.ramos@uacj.mx

J. M. Domínguez-Esquivel, M. Ramos (eds.), *Advanced Catalytic Materials: Current Status and Future Progress*, https://doi.org/10.1007/978-3-030-25993-8_10

and catalytic activity performance [2]. Additionally, the catalytic activity can be tuned when adding cobalt- or nickel-“promoting” atoms into layered TMS structure; due to a change in its electronic structure as described by the Sabatier principle [3], and extensively studied and found through experimental and theoretical approaches by Lauritsen et al. [4] and Raybaud et al. [5] in so-called CoMoS and NiMoS catalytic systems. However, cobalt(nickel)-promoted chemical structure has reached its catalytic upper limit, when compared to industrially commercial catalytic material such as NEBULA® which is a ternary-phase catalytic material (3TM), as described in detail by Eijsbouts et al. [6]. Now ternary systems are mainly for oxidation purposes in the form of core-shell nanoparticles dispersed in high-temperature support (alumina, silica, zeolites, etc.) [7, 8] and low information can be found in the literature about ternary systems for hydro-treating purposes. The addition of more metallic chemical atoms into the catalytic phase causes an increase of pricing, making it less attractive for upscaling industrial applications. This is when unsupported systems take an important role, because of the decreased need for more chemical components to perform catalytic activity. Also, Ramirez et al. [9] state that supported material plays a role during chemical catalytic process, sometimes as promoter and on occasions as poison component. On the other hand, the catalytic activity can be understood by laboratory test for dibenzothiophene (DBT) molecule in established protocol reaction called hydrodesulphurization mainly referred to as HDS [10]. Nevertheless, in order to achieve more understanding beyond catalytic activity values a characterization process takes place; this characterization process is done by frequency spectra instrumentation and techniques, such as Raman or infrared (IR) spectra, which provides modes of vibration for atoms near edges in catalytic material [11, 12]. Moreover, the development of field emission electron microscopy in combination with energy-disperse surface spectroscopy can allow direct measurements of atomistic structure and noble understanding of structure/function relationships as completed by Ramos et al. [13] in catalytic unsupported molybdenum disulfide catalytic materials. Here, authors present a hydrothermal synthesis ternary-phase nickel molybdenum-tungsten disulfide ($NiMoWS_2$) catalytic material from thiosalts at aqueous environment in combination with extensive structural and catalytic test for HDS reactions.

10.2 Experimental Methods

10.2.1 Synthesis of Ternary-Phase Catalyst

A solution of ammonium thiotungstate $(NH4)_2WoS_4$ is prepared in a minimum amount of water at room conditions and mixed with a solution of ammonium thiomolybdate $(NH4)_2MoS_4$ also prepared in a minimum amount of water at room conditions. This solution is added to an aqueous solution of $NiCl_2$ under stirring and a fine black precipitate is rapidly formed. The final material is vacuum filtered to obtain a precursor paste according to the next chemical equations:

$$\left(\mathrm{NH4}\right)_2 \mathrm{MoS}_4 + \left(\mathrm{NH4}\right)_2 \mathrm{WS}_4 \rightarrow 2\left(\mathrm{NH}_4\right)_2 \mathrm{WMoS}_4 \tag{10.1}$$

$$2\left(\mathrm{NH4}\right)_2 \mathrm{WMoS}_4 + 0.5\mathrm{NiCl}_2 \rightarrow \mathrm{Ni}_{0.5} / \left[\left(\mathrm{NH}_4\right)_2 \mathrm{WMoS}_4\right]_2 + 2\mathrm{NH}_4\mathrm{Cl} \tag{10.2}$$

Five grams of trimetallic precursor were added to 50 mL of water; the solution is placed inside a 0.6 L Parr reactor Model 4650 at room temperature. The reactor is purged with nitrogen gas. The temperature is then raised to 300 °C and the pressure is increased to 1200 psi. These conditions are maintained for 2 h. After that, the reactor was let to cool down to room temperature. Once depressurized the sulfide catalyst is recovered from the reactor and washed with isopropanol.

10.2.2 Catalytic Activity Using HDS Reaction and Selectivity

The HDS of DBT is carried out in a Parr reactor-type batch of high-pressure Model 4522. One gram of catalytic sample is placed in a batch reactor with HDS reactant (5.0% vol. of DBT in decaline). The reactor is pressurized to 3.1 MPa with hydrogen and heated to 623 K at a rate of 10 K/min. After reaching working temperature, sampling for chromatographic analysis is performed to determine the conversion versus time dependence. The reaction runtime was 5 h. The reaction products were analyzed using a Perkin Elmer Auto-System chromatograph with a 9 ft. × 1/8 i.d. packed column OV17 3% over Chromosorb 80/100. The main reaction products from the HDS of DBT are biphenyl (BP) and cyclohexylbenzene (CHB). The selectivity for the main products (BP, CHB) was calculated by the following equation:

$$\mathrm{HYD} / \mathrm{DDS} = \left[\mathrm{THDBT}\right] + \left[\mathrm{CHB}\right] / \left[\mathrm{BF}\right] \tag{10.3}$$

where tetrahydrodibenzothiophene (THDBT) and cyclohexylbenzene (CHB) are the concentration of the hydrogenation products (HYD), whereas biphenyl (BF) is the direct desulfurization product (DDS), obtained after 5 h of reaction.

10.2.3 Textural Properties

Nitrogen adsorption isotherms were measured using a Quantachrome AUTOSORB-1 surface area analyzer. The specific surface area was determined using BET method, while the pore size distribution was obtained using BJH method.

10.2.4 Sample Preparation for HRTEM

Approximately 0.5 g of sample was dissolved using isopropanol in a glass vial with the mixtures under ultrasonic bath for 10 min. Just one drop of the solution for each sample was placed onto a 200 mesh Cu/C grid and dried at 120 °C for 30 s to evaporate all isopropanol. Observations were performed in a JEOL® model ARM-200F with an operational voltage of 200 kV equipped with a Cs corrector (CEOS GmbH) and FEGSTEM/TEM unit. Images were processed using Digital Micrograph® package.

10.3 Results and Discussion

The aim of this research work is to achieve hydrothermal synthesis of highly active catalytic unsupported material in order to compete with supported commercial catalyst, which is made out of low-dimension materials supported in a high-temperature matrix like alumina oxide (Al_2O_3), zirconia oxide (ZrO_2), and ceria oxide (CeO_2), which in many cases can also contribute to the homogenous distribution [14] of the catalytic material and provide some electronic structure promotion as described by Diaz-Garcia et al. when studying the electronic effects of the support in NiMo catalyst [15]. Previous work performed on this topic had found that unsupported molybdenum disulfide catalyst possesses high surface area, ideal for molecular conversion and chemical reactivity; the preparation of ternary-phase catalyst from thiomolybdate salt precursors has been used before with high success as reported by Huirache-Acuña et al. [16]. Textural properties of unsupported ternary-phase catalyst were evaluated by N_2 physisorption at −196 °C; the results are listed in Table 10.1; for comparison purposes MoS_2 and $NiMoS_2$ catalysts were included; those were synthesized using the same method and same equipment was used for $NiMoWS_2$. While the pore diameter can be considered practically the same for those three catalysts, as the same synthesis conditions were used, the addition of nickel as promoter enhances dramatically the specific surface area. Meanwhile the incorporation of tungsten metal decreased, thus making a reduction in the number of pores present. This modified porosity correlates with the presence of tungsten metal in the solid.

Pore size diameter and N_2 adsorption hysteresis loops shown in Fig. 10.1 reveal predominance of mesopores and limited amount of macropores. The isotherms are

Table 10.1 Textural properties of the as-synthesized catalytic materials

Catalyst	Precursors	Specific surface area ($m^2\ g^{-1}$)	Pore diameter (Å)
MoS_2	$(NH4)_2MoS_4$ precursor (82.7 bars, 300 °C)	101.32	37
$NiMoS_2$	(NH4)2MoS4 + $NiCl_2$ (82.7 bars, 300 °C)	301.22	35
$NiMoWS_2$	$(NH4)_2MoS_4$ + $(NH4)_2WS_4$ + $NiCl_2$ (82.7 bars, 300 °C)	143.89	38

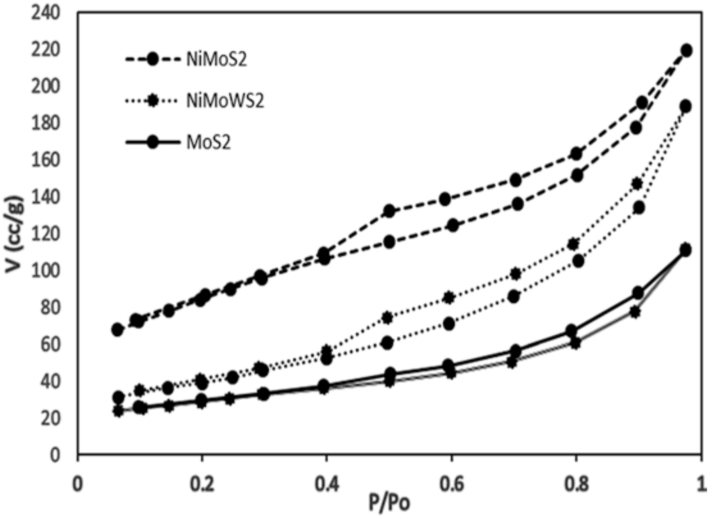

Fig. 10.1 Representative adsorption desorption isotherms of nitrogen at 77 K

type IV, with H3 hysteresis loops, which do not exhibit any limiting adsorption at high *p/p*^{o}, as is observed with aggregates of platelike particle with slit-shaped pores as studied by Sing et al. [17].

Hydrodesulfurization (HDS) reaction is a standard protocol to achieve evaluation of catalytic activity by reacting dibenzothiophene (DBT) molecule under pressure and temperature conditions as described by Alvarez et al. [18]; pseudo zero-order reaction kinetics equations are used to describe the reaction rate of HDS reaction in a batch reactor. A pseudo zero-order HDS reaction kinetics analysis of the relationship between the conversion and the rate constant showed that the standard deviation of the estimated reaction rate constant was about 2% in all cases. In our HDS catalytic tests, the main reaction products of DBT are biphenyl (BP) and cyclohexylbenzene (CHB). Table 10.2 shows the comparison of DBT HDS activity and HYD/DDS ratios of unsupported catalysts prepared by hydrothermal technique.

The results show that the specific reaction rate for the ternary catalyst NiMoWS$_2$ is greater than its counterpart materials, showing a high conversation percentage of DBT of 89%; also the hydrogenation ratio is highest than its counterpart materials that does not contain nickel metal. With NiMoWS$_2$ being the most active material in this study, we can say that it has the highest concentration of available coordinative unsaturated sites (CUS); this statement is in agreement with the TEM findings that show high bending curvatures at the edge of NiMoWS$_2$ microtube.

In order to correlate the activity to morphological structure/functionality a series of high-resolution images were taken with the aid of Cs-corrected transmission electron microscopy; the results indicate a microtube configuration with well-defined walls made out of two-dimensional layered transition metal chalcogenide

Table 10.2 Comparison of DBT HDS activity and HYD/DDS ratios of unsupported catalysts prepared by hydrothermal technique

Catalyst	Method of preparation	Rate constants (10^{-7} mol s^{-1} g^{-1})	HYD/DDS ratio	%DBT conversion
MoS_2	ATM precursor (Patm, 400 °C)	1.7	0.40	9
MoS_2	ATM precursor (82.7 bars, 300 °C)	12.0	0.39	47
$NiMoS_2$	Ni/ATM precursor (82.7 bars, 300 °C)	20.0	0.95	76
$NiMoWS_2$	Ni/ATM-ATT precursor (82.7 bars, 300 °C)	25.0	0.99	89
CoMo/ Al_2O_3	Commercial (no method of prep. available)	15.0	0.40	41

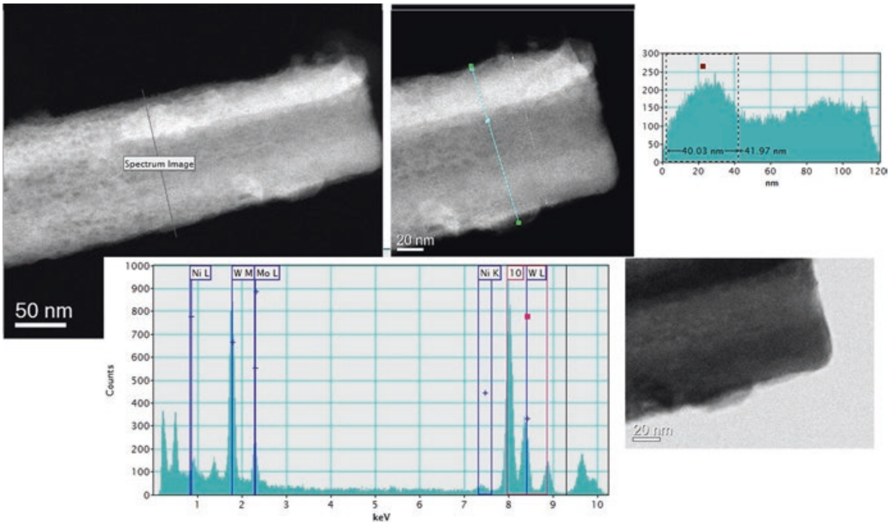

Fig. 10.2 Scanning transmission electron micrograph taken with the aid of Cs-corrected instrument. Dark-field image indicates some porosity over the walls of microtube and from the measurements a ~40 nm wall thickness is confirmed with nickel, tungsten, and molybdenum atoms present as indicated from EELS spectra

material as presented in Fig. 10.2. The tube wall thickness is about ~40 nm; it was possible to determine curvatures of laminar two-dimensional structures at edges with typical 0.649 nm between layers and 0.324 nm between atoms corresponding to Mo-Mo in the single crystallographic structure.

The energy electron loss spectra indicate the presence of nickel, tungsten, and molybdenum species; however, it does not provide the location of chemical species at the ternary-phase walls of the microtube. By a closer look as presented in Fig. 10.3, it is possible to observe the characteristic fringes with high bending

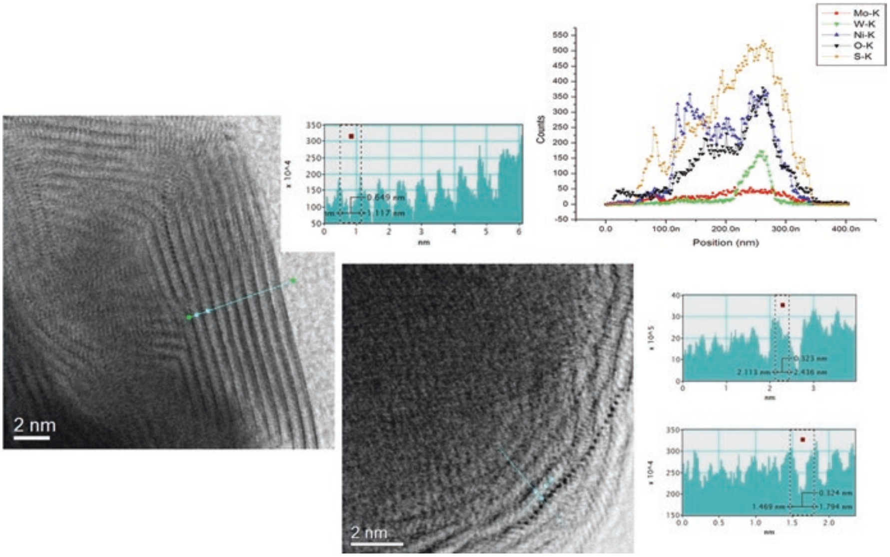

Fig. 10.3 Closer observation of edge corresponding to Fig. 10.2, using STEM instrument. It is possible to determine interlayer distance of 0.649 nm as shown in inset and 0.32 nm for interatomic distances over the edge of layers both presented in inset profiles

curvatures at the edge of microtube along with energy-disperse spectra indicating tungsten, sulfur, nickel, and molybdenum species as present in the sample; the oxygen was added as calibration species but it is not presented in the chemical structure of the sample.

10.4 Conclusions

A successful synthesis using salt solutions of ammonium thiotungstate (NH4)$_2$WoS$_4$ and ammonium thiomolybdate (NH4)$_2$MoS$_4$ to prepare a ternary-phase catalytic material under hydrothermal conditions is presented here. The products were studied using conventional hydrodesulfurization reaction for dibenzothiophene (DBT) molecule and indicate a conversion rate $k = 25.2 \times 10^{-7}$ mol/g s. From Cs-corrected scanning transmission electron microscopy it was possible to determine a microtube-like morphology with wall thickness of ~40 nm and high bending curvatures of layered two-dimensional structures are observed at the edges of tube, which can be possible sites of high DBT conversion.

Acknowledgements Principal author thank Department of Chemistry and Biochemistry of University of Texas at El Paso and Centro de Investigación en Materiales Avanzados-Chihuahua for usage of laboratory facilities. M. A. Ramos thank Kleberg Advanced Microscopy Centre of University of Texas at San Antonio for usage of Cs-corrected STEM instrument as well as Universidad Autónoma de Ciudad Juárez for economical support.

References

1. J. Saul, U.N. sets rules to cut sulfur emissions by ships from 2020, REUTERS, Environment. October 27, 2016. https://www.reuters.com/article/us-shipping-environment-sulphur
2. T.A. Pecoraro, R.R. Chianelli, Hydrodesulfurization catalysis by transition metal sulfides. J. Catal. **67**(2), 430–445 (1981)
3. R.R. Chianelli, G. Berhault, P. Raybaud, S. Kasztelan, J. Hafner, H. Toulhoat, Periodic trends in hydrodesulfurization: in support of the Sabatier principle. Appl. Catal. A **227**, 83–96 (2002)
4. J.V. Lauritsen, S. Helveg, E. Lægsgaard, I. Stensgaard, B.S. Clausen, H. Topsøe, F. Besenbacher, Atomic-scale structure of Co–Mo–S nanoclusters in hydrotreating catalysts. J. Catal. **197**, 1–5 (2001)
5. P. Raybaud, J. Hafner, G. Kresse, H. Toulhoat, Structural and electronic properties of the MoS_2(10Γ0) edge-surface. Surf. Sci. **407**, 237 (1998)
6. S. Eijsbouts, F. Plantenga, B. Leliveld, Y. Inoue, K. Fujita, STARS and NEBULA—new generations of hydroprocessing catalysts for the production of ultra low sulfur diesel. Prepr. Pap.-Am. Chem. Soc. Div. Fuel Chem. **48**(2), 494 (2003)
7. S.H. Noh, B. Han, T. Ohsaka, First-principles computational study of highly stable and active ternary PtCuNi nanocatalyst for oxygen reduction reaction. Nano Res. **8**, 3394 (2015). https://doi.org/10.1007/s12274-015-0839-2
8. D. Ferrer, A. Torres-Castro, X. Gao, S. Sepúlveda-Guzmán, U. Ortiz-Méndez, M. José-Yacamán, Three-layer core/shell structure in Au−Pd bimetallic nanoparticles. Nano Lett. **7**(6), 1701–1705 (2007)
9. J. Ramírez, F. Sánchez-Minero, Support effects in the hydrotreatment of model molecules. Catal. Today **130**, 267–271 (2008)
10. H. Topsøe, B.S. Clausen, F.E. Massoth, *Hydrotreating Catalysis, Science and Technology* (Springer-Verlag, Berlin, 1996). ISBN 3-540-60380-8
11. E. Stavitskia, B.M. Weckhuysen, Infrared and Raman imaging of heterogeneous catalysts. Chem. Soc. Rev. **39**, 4557–4559 (2010)
12. K. Castillo, F. Manciu, J.G. Parsons, R.R. Chianelli, Synthesis and characterization of 1,2,3,4 tetrahydroquinoline intercalated into MoS_2 in search of cleaner fuels. J. Mater. Res. **22**(10), 2747–2757 (2007)
13. M.A. Ramos, G. Berhault, D.A. Ferrer, B. Torres, R.R. Chianelli, Combined HRTEM and molecular modeling of the MoS_2-Co_9S_8 interface to understand the promotion effect in bulk HDS catalytic structures. Catal. Sci. Technol. **2**, 164–178 (2012)
14. T. Klimova, M. Calderón, J. Ramírez, Ni and Mo interaction with Al-containing MCM-41 support and its effect on the catalytic behavior in DBT hydrodesulfurization. Appl. Catal. A Gen. **240**(1–2), 29–40 (2018)
15. L. Díaz-García, V. Santes, T. Viveros-García, A. Sánchez-Trujillo, J. Ramírez-Salgado, C. Ornelas, E. Rodríguez-Castellón, Electronic binding of sulfur sites into Al_2O_3-ZrO_2 supports for NiMoS configuration and their application for hydrodesulfurization. Catal. Today **282**(2), 230–239 (2017)
16. R. Huirache-Acuña, B. Pawelec, C.V. Loricera, E.M. Rivera-Muñoz, R. Nava, B. Torres, J.L.G. Fierro, Comparison of the morphology and HDS activity of ternary Ni(Co)-Mo-W catalysts supported on Al-HMS and Al-SBA-16 substrates. Appl. Catal. B Environ. **125**, 473–485 (2012)
17. K.S.W. Sing, D.H. Everett, R.A.W. Haul, L. Moscou, R.A. Pierotti, J. Rouquerol, T. Siemieniewska, Reporting physisorption data for gas/solid systems with special reference to the determination of surface area and porosity. Pure Appl. Chem. **57**, 603 (1985)
18. H. Nava, C. Ornelas, A. Aguilar, G. Berhault, S. Fuentes, G. Alonso, Cobalt-molybdenum sulfide catalysts prepared by in situ activation of bimetallic (Co-Mo) alkylthiomolybdates. Catal. Lett. **86**, 257–265 (2003)

Index

J. M. Domínguez-Esquivel, M. Ramos (eds.), *Advanced Catalytic Materials: Current Status and Future Progress*, https://doi.org/10.1007/978-3-030-25993-8